imec 2023

Proceedings

10th & 11th MAY, 2023 KARACHI PAKISTAN

12th INTERNATIONAL MECHANICAL ENGINEERING CONFERENCE

Theme: Role of Mechanical Engineering in Economic Uplift and Sustainability

Jointly Organized by

The Institution of Engineers Pakistan Karachi Centre

NED University of Engineering & Technology, Karachi

NED International Alumni Network (NEDIAN) Association, Pakistan

In Collaboration With

Federation of Engineering Institutions of South & Central Asia (FEISCA)

Federation of Engineering Institutions of Islamic Countries (FEIIC)

Mehran University of Engineering and Technology Jamshoro

Balochistan University of Engineering & Technology Khuzdar

Balochistan University of Information Technology Engineering & Management Sciences, Quetta

Dawood University of Engineering & Technology, Karachi

DHA Suffa University Karachi

Hamdard University Karachi

Quaid-e-Awam University of Engineering Science &Technology, Nawabshah

Nazeer Hussain University Karachi

Pakistan Navy Engineering College - NUST Karachi

Shaheed Zulfikar Ali Bhutto Institute of Science & Technology, Karachi

The American Society of Heating, Refrigerating and Air-Conditioning Engineers

Pakistan Society of Plumbing Professionals, Karachi

(Copyrights © Reserved with IMEC 2023 Committee)

Conference Proceedings
International Mechanical Engineering Conference 2023

Table of Contents

(Copyrights © Reserved with IMEC 2023 Committee)

(Copyrights © Reserved with IMEC 2023 Committee)

NUMERICAL INVESTIGATION OF A NOVEL DESIGN OF CROSS AXIS WIND TURBINE WITH IMPROVED EFFICIENCY

Faheem Abbas[1], Usama Ali[1], Adnan Rasheed[1], Mumtaz A. Qaisrani[1,*], M. Basit Shafiq[2], Usman Allauddin[3], Muhammad Umar Farooq[1], Shajar Abbas[1], Ali Zulkarnain[1]

[1]Institute of Mechanical and Manufacturing Engineering, Khwaja Fareed University of Engineering and Information Technology, Rahim Yar Khan, Pakistan.
[2]Department of Mechanical Engineering, National University of Technology, Islamabad, Pakistan
[3]Department of Mechanical Engineering, NED University of Engineering and Technology, Karachi

*Corresponding author. *E-mail address:* mumtazahmed@kfueit.edu.pk (Mumtaz A. Qaisrani)

ABSTRACT

Wind energy is viewed as a growing renewable energy source, as opposed to fossil fuels, which are finite and create harmful emissions. Modern wind turbines, such as horizontal axis wind turbines (HAWTs) and vertical axis wind turbines (VAWTs), have significant drawbacks that reduce their effectiveness. In order to maximize wind energy output, a cross axis wind turbine (CAWT) has been developed to overcome the aforementioned problems. CAWT has a unique design that combines the horizontal and vertical blades arranged in a cross-axis pattern. In this paper, Computational Fluid Dynamics (CFD) is used to analyze the aerodynamic performance of various airfoil shapes for CAWT. The study aims to identify the airfoil with the maximum lift coefficient, which is essential for maximizing the wind turbine's output. Findings indicated that, among the evaluated airfoils, FX 63-137 had highest lift coefficient. By employing this airfoil shape to horizontal blades of CAWT might potentially maximize energy output.

Keywords: Cross axis wind turbine, CFD, NACA 0015, FX63-137.

1 INTRODUCTION

The growth of a nation's economy, industry, and society are all reliant on its access to energy. Fossil fuels presently provide for around 80% of the world's energy needs. In recent years, environmental degradation has been linked in large part to the excessive use of fossil fuels [1]. Renewable energy has emerged as a critical component of energy policy debates and attempts to mitigateclimate change. It includes a range of renewable resources like solar, wind, hydro, geothermal, and biomass. Due to their abilityto minimize adverse environmental effects and lower greenhouse gas emissions, these sources have received significant recognition [2]. Based on global energy policy, wind energy has become a well-liked renewable source of energy. According to a report published in EIA, wind energy has recently contributed 3% of the world's energy sources [3]. Utilizing wind energy lessens reliance on fossil fuel supplies. The need for energy is rising quickly along the world's population. Energy consumption in emerging countries will increase by 65% from 2010 to 2040 [4]. In recent years, wind energy has become more affordable than other energy sources, making

it a more enticing option for the generation of power [5]. Wind turbines are equipment that generates electricity by harnessing the kinetic energy of the wind. Horizontal Axis Wind Turbines (HAWTs) and Vertical Axis Wind Turbines (VAWTs) are the two basic varieties. Wind energy is produced quite efficiently by the HAWTs[6]. However, yaw mechanisms are needed to align themselves properly, and their transmissions need to be maintained and repaired often. Additionally, it will cost more to improve the tower construction that supports the bulky nacelle[7].

The usage of HAWTs in urban contexts is hampered by the excessive noise[8]. The VAWT is safer, lighter, and can be used in winds blowing from any horizontal direction because it doesn't need yaw mechanism to spin it to face wind direction. VAWTs are better suited for urban settings since its gearbox and generator are located at a lower height because its rotor size may be changed horizontally without impacting its total height[9], [10]. The VAWT need a beginning power to rotate for capturing wind energy. Due to wind hitting the rotor blades from all sides, the VAWT is less efficient than the HAWT. The installation of VAWTs on rooftops was determined to be certainly advantageous[11]. Additionally, VAWT is quieter than HAWT, which is even more significant in cities[12]. VAWT and the HAWT both have a number of problems to solve these drawbacks CAWT was developed. No matter which way the wind is blowing, CAWT can fully use wind energy without the use of an orientation mechanism, and it also has improved self-starting capabilities. Although CAWT used the same amount of area as the VAWT, it had more lift force generating surfaces. Due to the high density of high-rise structures, metropolitan regions' wind characteristics are greatly impacted. CAWT provide an advantage in terms of turbine performance in such metropolitan areas since it can capture wind energy regardless of its direction, leading in increased power production performance.

2 NUMERICAL STUDY

In this study Simulations were run at various angle of attacks with constant wind speed, and the resulting velocity and pressure profiles were examined.

Table 1. Computational conditions for the numerical study

Input	Value	Input	Value
Wind Speed	10 m/s	Density	1.225 kg/m^3
Mach number	0.0292	Kinematic viscosity	1.5×10^{-5} m^2/s
Reynolds number	6.8×10^5	Angle of Attack	0^o to 30^o
Temperature	300 K	Airfoil chord length	1 m
Pressure	101325 Pa	Viscous model	SST K-omega

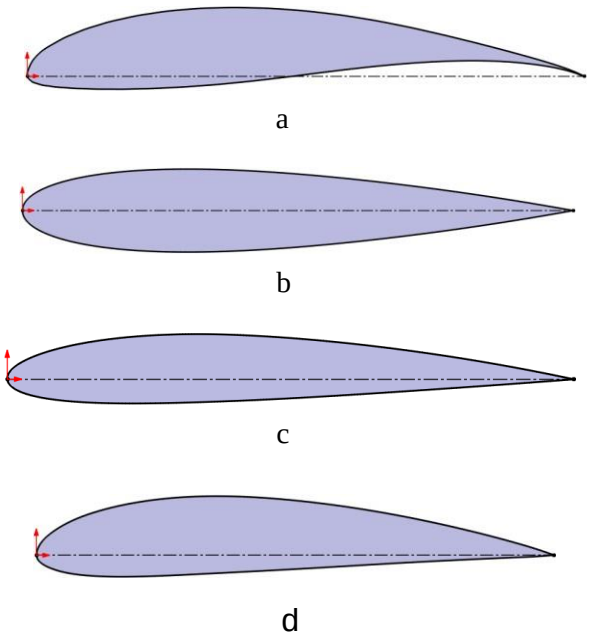

Figure 1. Airfoil profiles
a) FX 63-137, b) NACA 0015,
c) NACA 2412, d) NACA 4415

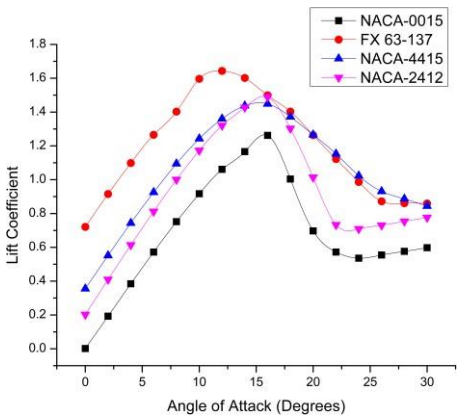

Figure 2. Lift coefficient of different airfoil shapes

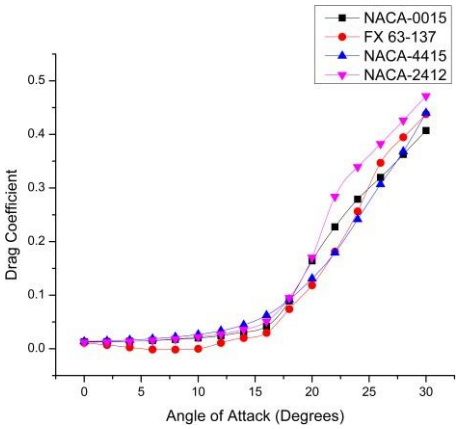

Figure 3. Drag coefficient of different airfoil shapes at various angle of attacks

Lift coefficient is a crucial factor during the designing of airfoil blades. It is found, FX 63-137 airfoil has comparatively high lift coefficient in comparison to the other airfoils mentioned. At AOA of 14º, lift coefficient of FX 63-137 is around 1.6. NACA 0015 had a maximum lift coefficient of around 1.2 at AOA of 16º. NACA 4415 and NACA 2412 had maximum lift coefficients around 1.4 at AOA of 14º.A detailed comparison is shown in figure 2. It is crucial to keep in mind that these numbers are based on certain simulation settings and might change depending on variables like the Reynolds number, turbulence severity, airfoil size, and wind speed etc.

Drag coefficient, indicates the resistance that object experience during moving through a fluid. Based on simulation results from AOA of 0º to 30º, NACA 2412 has maximum drag coefficient among the mentioned airfoils as shown in figure 3. This means that this airfoil will experience the greatest drag force when moving through air, compared to the other airfoils. However, drag coefficient is important factor that affect the overall aerodynamic performance and the choice of airfoil profile depends on many other factors, such as lift, stability, and control.

3 PORPOSED NOVEL DESIGN

Previously, NACA 0015 airfoils were used to construct the cross-axis wind turbine blades. Due to its ability to effectively balance lift and drag, NACA 0015 is a common airfoil shape used in wind turbines[13]. In this study, it is found that CAWT may function more effectively and produce more power from the same amount of wind by swapping the horizontal blades by FX 63-137 airfoils as depicted in figure 4.

Figure 4. CAD model of the Cross Axis Wind Turbine (CAWT)

3.1 Meshing

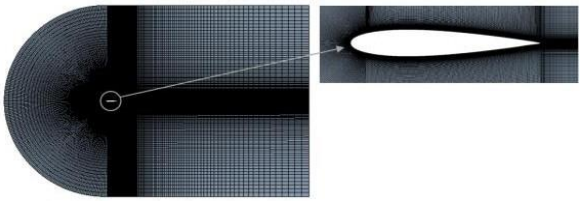

Figure 5. Meshing of airfoil

Meshing of an airfoil blade is an important stage in computational fluid dynamics (CFD) simulations since it impacts the precision and dependability of the results generated using software such as ANSYS FLUENT. Meshing is the technique of partitioning a computational domain into tiny parts that describe the geometry of an airfoil blade. A well-designed mesh with the proper size, shape, and resolution can capture the complicated flow mechanics surrounding the airfoil, resulting in precise and dependable results.

The domain size of the airfoil blade was set 15 times of the chord length with inlet 7.5 times as shown in figure 5. Mesh was generated using ANSYS FLUENT software with C-grid topology to effectively resolve the boundary layer. There were 200401 nodes and 199502 elements. To determine the lift and drag coefficients at various angle of attack (AOA), turbulent flow was simulated using the κ-ω based SST model in ANSYS Fluent with an input velocity of 10 m/s. The residual type was set to RMS, and the residual goal value was set at $1x10^{-6}$.

3.2 Results and Discussion

The contours of pressure and velocity must be considered while analyzing the forms of airfoils. The specific contours will depend on the airfoil's shape and design parameters, and can be used to assess factors such as lift and drag coefficients, stall characteristics, and overall efficiency. The air velocity peaks at the topmost point of the leading edge and gradually declines as it advances towards the boundary layer separation point close to the upper surface of the trailing edge. The air velocity remains maximum for NACA 2412 and minimum for NACA 4415. The least pressure is observed for NACA 4415, NACA 0015 and FX 63-137 are 60.4 Pa, 60.5 Pa and 60.5 Pa respectively. The least pressure around the upper surface suggests a high lift coefficient and in turn better performance as shown in figure 6 and 7.

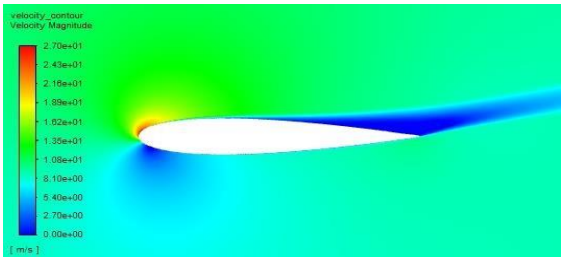

a

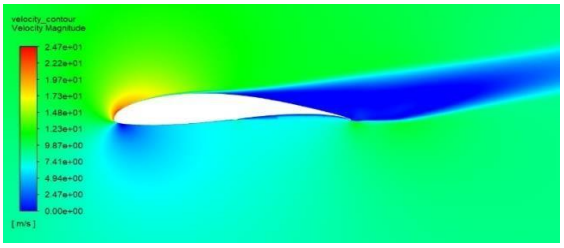

b

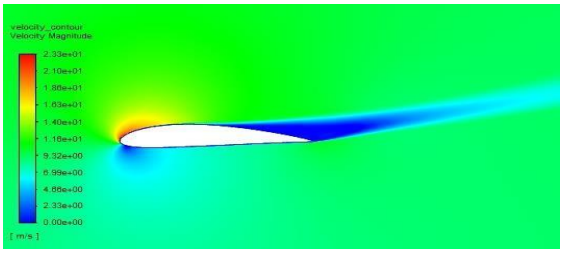

c

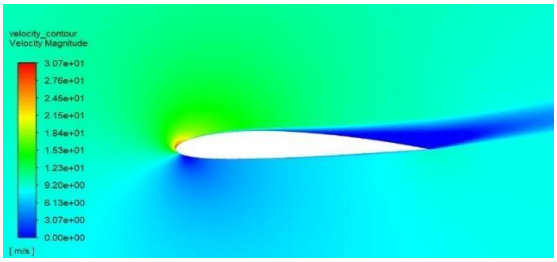

d

Figure 6. Velocity contours

a) NACA-0015 at AOA of 16^{o}

b) FX 63-137 at AOA of 14^{o}

c) NACA-4415 at AOA of16^{o}

d) NACA-2412 at AOA of 16^{o}

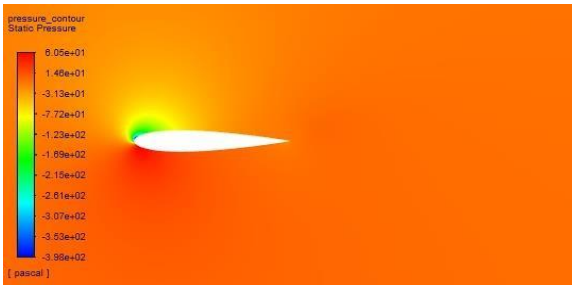

a

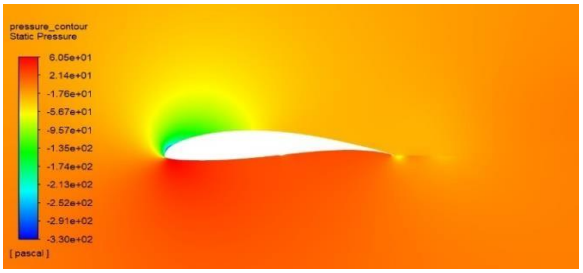

b

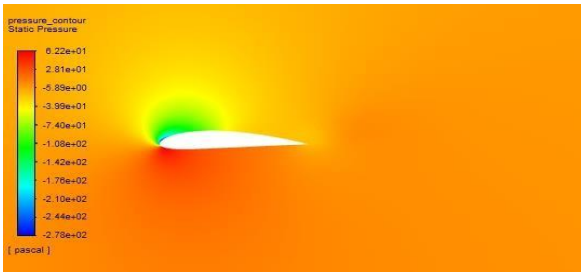

c

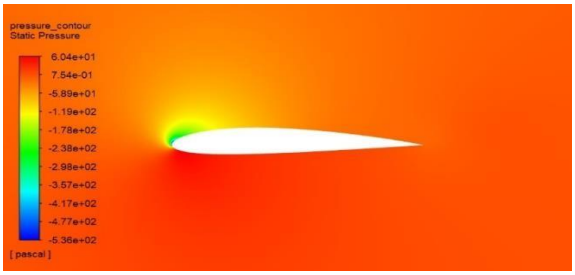

d

Figure 7. Pressure contours
a) NACA-0015 at AOA of 16º
b) FX 63-137 at AOA of 14º
c) NACA-4415 at AOA of 16º
d) NACA-2412 at AOA of 16º

4 CONCLUSIONS

Computational Fluid Dynamics (CFD) simulations are used to analyse the lift and drag coefficients of various airfoils, as well as to observe and monitor the flow field pattern around the body. The data show that increasing the angle of attack causes an increase in the lift and drag coefficients. As Reynolds' number rises, there is a steady reduction in the drag coefficient but lift coefficient grows marginally and then starts to decline. Airfoil experiences significant negative pressure, contributing to much of the lift. It is found that FX 63-137 and NACA 2412 has maximum lift and drag coefficients respectively among the mentioned airfoils. It is discovered that CAWT may function more effectively and produce more power from the same amount of wind by swapping the horizontal blades by FX 63-137 airfoils.

REFERENCES

[1]. M. Irfan, Z.-Y. Zhao, H. Li, and A. Rehman, "The influence of consumers' intention factors on willingness to pay for renewable energy: a structural equation modeling approach," *Environ. Sci. Pollut. Res.*, vol. 27, no. 17, pp. 21747–21761, 2020, doi: 10.1007/s11356-020-08592-9.

[2]. Qaisrani, M. A., Wei, J., Fang, J., Jin, Y., Wan, Z., & Khalid, M. (2019). Heat losses and thermal stresses of an external cylindrical water/steam solar tower receiver. Applied Thermal Engineering, 163, 114241.

[3]. T. Kober, H.-W. Schiffer, M. Densing, and E. Panos, "Global energy perspectives to 2060– WEC's World Energy Scenarios 2019," *Energy Strateg. Rev.*, vol. 31, p. 100523, 2020.

[4]. R. Selin, "The outlook for energy: a view to 2040," 2013.

[5]. M. F. Howland, S. K. Lele, and J. O. Dabiri, "Wind farm power optimization through wake steering," *Proc. Natl. Acad. Sci.*, vol. 116, no. 29, pp. 14495–14500, Jul. 2019, doi: 10.1073/pnas.1903680116.

[6]. K. Pope, I. Dincer, and G. F. Naterer, "Energy and exergy efficiency comparison of horizontal and vertical axis wind turbines," *Renew. Energy*, vol. 35, no. 9, pp. 2102–2113, 2010, doi: https://doi.org/10.1016/j.renene.2010.02.013.

[7]. N. A. Ahmed and M. Cameron, "The challenges and possible solutions of horizontal axis wind turbines as a clean energy solution for the future," *Renew. Sustain. Energy Rev.*, vol. 38, pp. 439–460, 2014, doi: https://doi.org/10.1016/j.rser.2014.06.004.

[8]. W. T. Chong, A. Fazlizan, S. C. Poh, K. C. Pan, W. P. Hew, and F. B. Hsiao, "The design, simulation and testing of an urban vertical axis wind turbine with the omni-direction-guide-vane," *Appl. Energy*, vol. 112, pp. 601–609, 2013.

[9]. W. T. Chong *et al.*, "Performance investigation of a power augmented vertical axis wind turbine for urban high-rise application," *Renew. Energy*, vol. 51, pp. 388–397, 2013, doi: https://doi.org/10.1016/j.renene.2012.09.033.

[10]. W. T. Chong *et al.*, "Cross-Axis-Wind-Turbine: A Complementary Design to Push the Limit of Wind Turbine Technology," *Energy Procedia*, vol. 105, pp. 973–979, 2017, doi: 10.1016/j.egypro.2017.03.430.

[11]. S. Mertens, "The Energy Yield of Roof Mounted Wind Turbines," *Wind Eng.*, vol. 27, no. 6, pp. 507–518, Dec. 2003, doi: 10.1260/030952403773617472.

[12]. "HAWT versus VAWT: Small VAWTs find a clear niche," *Refocus*, vol. 4, no. 4, pp. 44– 46, 2003, doi: https://doi.org/10.1016/S1471-0846(03)00433-5.

[13]. W.-T. Chong *et al.*, "Cross axis wind turbine: Pushing the limit of wind turbine technology with complementary design," *Appl. Energy*, vol. 207, pp. 78–95, 2017, doi: https://doi.org/10.1016/j.apenergy.2017.06.099.

DESIGN OPTIMIZATION AND PERFORMANCE ASSESSMENT OF A NOVEL SAVONIUS WIND TURBINE

Saqlain Saeed[1], Saqlain Ali[1], Khizar Hayat[1], Muhammad Zahid[1], Mumtaz A. Qaisrani[1,*], Basit Shafiq[2], Adnan Rasheed[1], Muhammad Umer Farooq[1], Usman Allaudin[3]

[1]Institute of Mechanical and Manufacturing Engineering, Khwaja Fareed University of Engineering & Technology, Rahim Yar Khan, Pakistan

[2]Department of Mechanical Engineering, National University of Technology, Islamabad, Pakistan

[3]Department of Mechanical Engineering, NED. University of Engineering and Technology, Karachi.

[*]Corresponding author. *E-mail address*: mumtaz.ahmed@kfueit.edu.pk (Mumtaz A. Qaisrani)

ABSTRACT

The effectiveness of a modified Savonius wind turbine design was examined in this study and computationally analyzed. A 3-dimensional rotor blade model is proposed and examined using ANSYS-Fluent and the Shear Stress Transport (SST) k-omega turbulence model. The redesigned turbine design is contrasted with the industry-standard reference design, and the coefficient of power (CP) is assessed for a single spin at various tip speed ratios (TSR). The proposed design outperforms the reference design at TSR 0.7, which is the best TSR for both designs. The updated turbine design's optimized torque is 0.15 N-m, 17.2% more torque than the conventional design. The findings imply that the modified Savonius wind turbine design can perform better than conventional designs.

Keywords: Savonius wind turbine, Novel Blade Design, Aerodynamics wind blade

1 INTRODUCTION

In this modern era, having access to power is a basic requirement for everyone. Renewable energy sources, including wind, should be used to improve the uneven supply of electricity in developing nations. Low wind speeds are no problem for the Savonius wind turbine, and manufacturing costs are not too high.

Although it performs less well than other turbine types, it offers benefits including easy construction and little speed control requirements as stated by [1]. Rural areas in developing nations with a lack of electricity and low-income populations can benefit from the Savonius turbine.

By changing the Savonius turbine's performance, researchers have experimented with changing the blade shape, blade contour, and other factors. It was possible to improve performance by adding two curtains to the Savonius rotor as studied by [2]. In comparison to other turbine types, the Savonius-type turbine has a number of benefits, including a simple structure, self-starting at low-speed wind and operational skills, and less noise pollution [3].

Few earlier studies included a modified design because they were primarily concerned with the examination of traditional Savonius wind turbines. Although there were many opportunities to enhance these models, the performance of these upgraded blades was subpar. In this study, the performance of the reference model is evaluated in relation to the aerodynamic characteristics of a proposed improved design.

Keeping in mind the study of earlier writers, we modified the rotor's blades to introduce a novel Savonius wind turbine design. The rotor's slots and flapper reduce negative drag on the blades' convex side, enabling the turbine to run more quickly and generate more power, which accounts for the increase in Cp.

Our analysis demonstrates the potential for the proposed upgraded Savonius wind turbine design to significantly increase both performance and efficiency. The updated design can attain a higher maximum CP than earlier designs by reducing the negative drag on the blades' convex side, which might persuade more people to switch to wind energy as a sustainable energy source.

2 NUMERICAL SIMULATIONS

Using Shear-Stress Transport (SST) k-omega turbulence models, ANSYS-Fluent commercial software was utilised to analyse turbulent flow.

2.1 Geometry

The Savonius blade used in this investigation has the following measurements: blade diameter of 200 mm, aperture of 40 mm, rotor radius of 200 mm, 220 mm endplate radius, and 2 mm extent [4]. The geometry of the Savonius wind turbine was created using CAD software. The new geometry keeps the same rotor diameter, endplate diameter, and blade thickness, as illustrated in Figure 1 while venting slits of 100mm length and 70mm width and flapper length and width of 110mm and 70mm respectively were introduced.

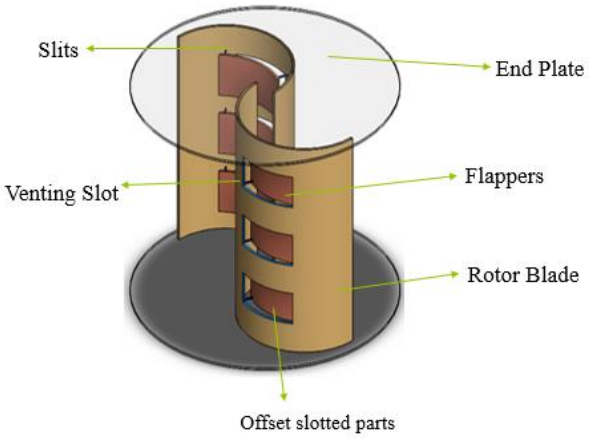

Figure 1. Modified blade rotor

2.2 Computational Domain

Figure 2 depicts the arithmetical area was split into two subdomains: rotating and stationary. The enclosure dimensions were determined using a numerical study [5]. The rotating domain's rotor grid components are a part of the best-quality subdomain. Cells on the outside region (stationary domain) are included in the secondary subdomain with low resolution. The turbine's spinning cell zone size was kept constant. Measuring from the rotor's centre to the left boundary, the outflow zone was scheduled to be 10 times the breadth of the rotor, whereas the entrance zone was intended to be 5 times that size. Flow could enter a fully formed condition since the size of the machine domain as a whole prevented any obstruction or sidewall effects. Boundary restrictions thereby made sure that a huge computing domain did not skew the computational results.

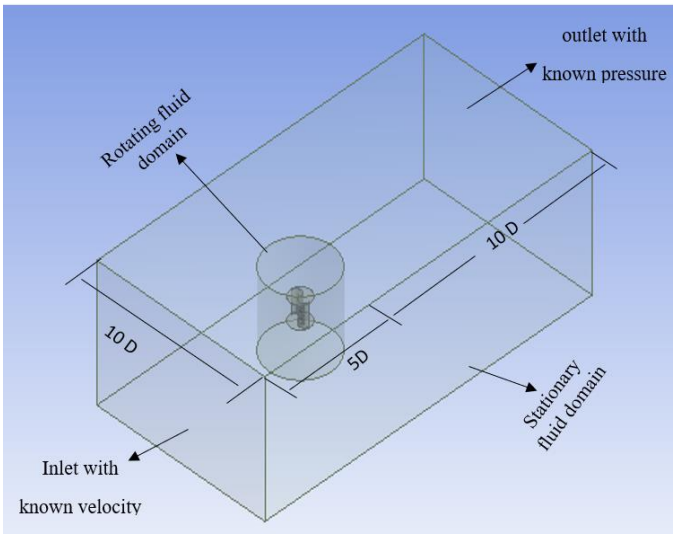

Figure 2. Complete domain for the numerical simulations

2.3 Mesh Creation

A key technique in CFD analysis is mesh creation. Correct mesh independence investigation is performed for better mesh production. With the use of the drag force coefficient and torque, we examined coarse, fine, and medium meshes as well as mesh refinement in our mesh study. Tetrahedron mesh generation requires little time. Specific areas of the computational domain were given appropriate names.

2.4 Boundary Condition

Inlet velocity is 7 m/s and turbulence intensity are 5%. Fluid flow (Ansys) is utilized in the simulation. to solve the unstable Reynold Navier, stoke equation, a pressure-based, the K-omega model for turbulence was used, along with wall treatment for boundary layer and. the sliding mesh is employed. For each degree of turbine rotation, the time step and size were computed [6].

Table 1. Boundary conditions

Parameter	Specification
Turbulence model	k-omega Standard
Fluid	Air
Density	1.225 kg/m^3
Turbulence intensity	5%
Inlet velocity	7 m/s
Solver	Pressure based
Convergence criteria	Momentum and pressure are both second-order upwind.

Table 1 shows the boundary conditions used for the simulation. The air utilised had a density of 1.225 kg/m^3. Inlet velocity of 7 m/s and turbulence intensity of 5%. Solver is unsteady and pressure based, and the CFD boundary conditions are presented in Table 1. The air had a density of 1.225 kg/m^3. 7 m/s inlet velocity and 5% turbulence intensity. The CFD algorithm and the unstable, pressure-based solver are connected. Analysis was conducted using a sliding mesh, and the discretization approach involved a second-order equation.

3 RESULTS

This study's objective is to ascertain how the tip speed ratio impacts Savonius wind turbines with slotted blade efficiency, the effect of slotted blades and slits on the pressure of the convex and concave sides of blades, and the drag coefficient on both sides.

The torque, power coefficient, and tip speed ratio values can be used to gauge the efficiency of a turbine. The rotor's mechanical power as well as the mechanical energy found in wind is compared to get the power coefficient. Analysing torque using simulations in ANSYS. The tip speed ratio, on the other hand, the proportion of wind speed to the speed of the blade tips of wind turbines. Figure 2. compares the simple Savonius model with the modified blade model using a graph between the TSR and power coefficient. The graph demonstrates that the innovative model performs better than the traditional model. The maximum Cp for the novel design was found at TSR 0.7, or 0.231, which is 27% higher than the maximum Cp for the traditional design. The graph shows an increasing trend of Cp value first and maximum value at TSR 0.7 and then decreasing trend, which means at this TSR, Cp for a unique design can be realised.

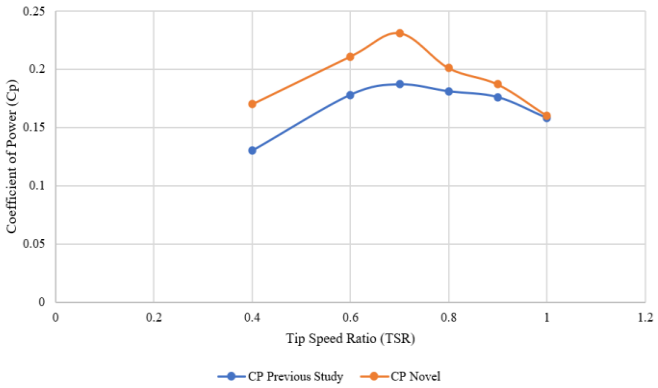

Figure 3. Plot of TSR against Cp

Figure 4. depicts a pressure contour comparison between the normal Savonius blade and the modified blade. Simple Savonius analysis shows that higher pressure is generated on the convex side. The pressure contour plots demonstrate that there is a pressure difference between the rotor's two sides. The red and blue areas on the blade represent larger and lesser pressure rises, respectively. Compared to the altered blade, the original blade has a more rounded blade shape, which has venting slots and flappers attached to it, Consequently, the original blade's pressure increase is relatively greater than the modified blade's. The distinction between these two blades is made by this form of optimization. In the region where venting slots and flappers are inserted, less pressure is generated, causing the drag coefficient on the convex side to drop, which is known as negative drag. The rotor's torque increases as the negative drag decreases, improving the power coefficient value.

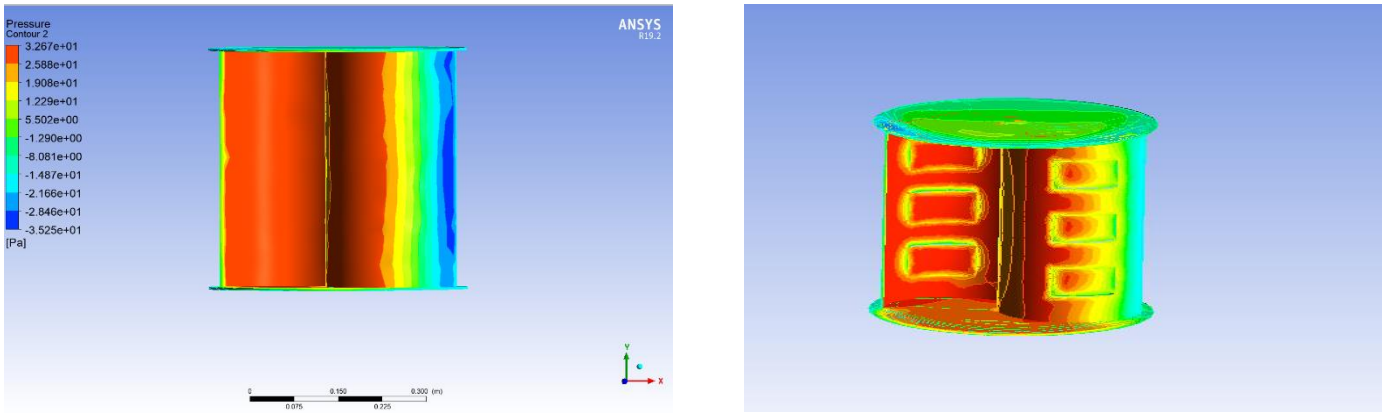

Figure 4. Comparison between pressure contours

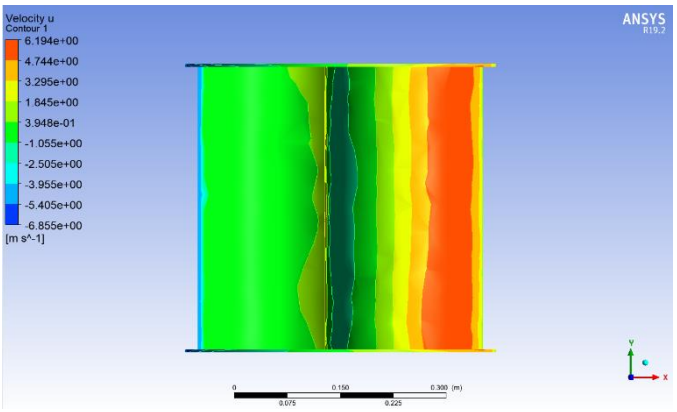

Figure 5. Velocity Contours simple

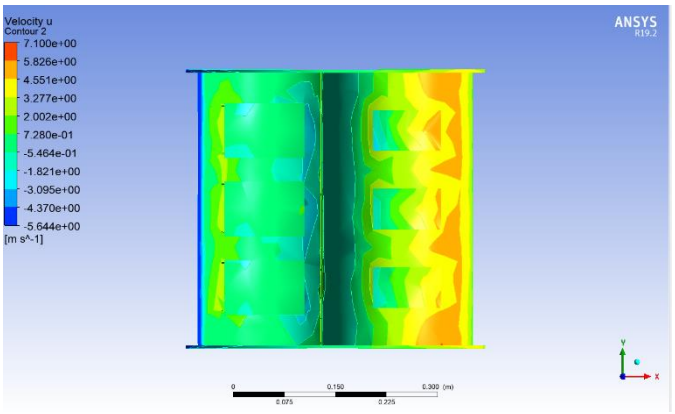

Figure 6. Velocity Contours novel

Figures 5 and 6 depict the velocity profiles of a typical semi-circular Savonius blade and a modified blade design, respectively. According to the comparison, the redesigned rotor's velocity has decreased where the venting slots are attached. At the edges of slits, Fewer velocity curves are most common. The concave side of the blade's velocity remained unchanged, but the venting slots on its convex side observed a fall in speed as the air went through them.

4 CONCLUSIONS

This study illustrates the impact of modifying the Savonius turbine's blade to increase rotor efficiency. Additionally, we examined the pressure, velocity contours, and impact of TSR on the rotor's torque. The Finite Element Method calculates equations involving mass and momentum conservation. Based on an acceptable correlation with earlier investigations, The mandated geometries of the blade's behavior were examined using the turbulence model SST k-omega. The refining occurs at a specified TSR value (TSR 0.7), and findings reveal a 27% increase in the total power coefficients. These results have been put to the test to verify the modifications made by the most recent blade model. The results of the consequences also demonstrate that the model significantly boosts the power coefficient.

ACKNOWLEDGEMENTS

We would like to thank Institute of Mechanical and Manufacturing Engineering at KFUEIT for providing the resources and Mr. Muhammad Tayyab for helping in the laboratory work.

REFERENCES

[1]. Al-Bahadly, I. (2009) Building a wind turbine for a rural home. *Energy for Sustainable Development*, 13, pp. 159–165.

[2]. R. D. Maldonado, b*, E. Huerta, J. E. Coronac, O. Cehb, A. I. León-Castillo, M. P. Gómez-Acosta, E. Mendoza-Andradea, Design, simulation, and construction of a Savonius wind rotor for subsidized houses in Mexico, 57 (2014) 691 – 697

[3]. Al-Faruk, A. Sharifian, Geometrical optimization of a swirling Savonius wind turbine using an open jet wind tunnel, *Alexandria Eng. J.* (2016).

[4]. Dominicus Danardono Dwi Prija Tjahjanaa,∗ , Zainal Arifina, Suyitno Suyitnoa, Wibawa Endra Juwanaa, Aditya Rio Prabowoa, Catur Harsito b, Experimental study of the effect of slotted blades on the Savonius wind turbine performance, *ScienceDirect*, 11 (2021) 100249

[5]. G. Sakti a, c, T. Yuwono b, Numerical and experimental investigation of the effect of a circular cylinder as passive control on the Savonius wind turbine performance, *journal of southwest jiaotong university*, 10.35741/issn.0258-2724.56.6.7

[6]. Satrio, D., Utama, Ikap, And Mukhtasor (2018) The influence of time step setting on the CFD simulation result of vertical axis tidal current turbine. *Journal of Mechanical Engineering and Sciences*, 12, pp. 3399-3409.

DESULFURIZATION OF DIESEL OIL FOR THE UPGRADATION TO EURO V EMISSION STANDARD

Muhammad Ali[1,*], Muzaffar Ali[1], M Shahrukh Atta[1], Usama Asghar[1], Sadeed Ullah Khan Jano[2], Haris Khan[1], M Iftikhar Ul Hassan[1]

[1]Mechanical Engineering Department, University of Engineering & Technology, Taxila, Pakistan

[2]Software Engineering Department, Foundation University School of Science & Technology, Islamabad, Pakistan

[*]Corresponding Author. Tel.: +92-311-1767611

E-mail Address: muhammadalyy22@gmail.com (Muhammad Ali)

ABSTRACT

The current research work investigates the usage of task specified ionic liquids (ILs) for the removal of dibenzothiophene (DBT) from diesel oil and upgrading the fuel to meet the euro V emission standard having 10 ppm sulfur content. Model oil for current research was produced by adding DBT in n-dodecane separately. A number of experimental variables were taken into account while determining the desulfurization efficiency such as temperature, time, volume ratio of IL to model oil, and amount of H_2O_2. DBT was effectively extracted from the model oil using a pyridinium based ionic liquid i.e. n-hexyl-pyridinium tetrafluoroborate $[C_6P_y][BF_4]$, exhibiting an equilibrium within 60 minutes of EDS reaction and the removal time of 40 mins was examined to be optimal, which resulted in the highest sulfur removal for DBT. A sulfur extraction rate of nearly 74% is achieved within just 10 minutes of OEDS (containing 1 % v/v H_2O_2) under the same effective conditions as that of EDS. Temperature directly affects the kinetic rate constant of the DBT removal reaction, which results in higher DBT removal efficiency and 40^oC was selected as the highest temperature. A high volume fraction of IL to model oil (1:1) directed to a remarkable increase of 7.18 % in desulfurization efficiency from 70 % (unreacted H_2O_2) to 77.18 % (with H_2O_2). Desulfurization efficiency was further increased by 4.3% when H_2O_2 concentrations ranged from 1 % v/v to 10 % v/v. Furthermore, findings from this experimental research indicates that $[C_6P_y][BF_4]$ is capable of being regenerated and can be reused up to 8 cycles without a significant loss in desulfurization efficiency.

Keywords: Ionic Liquid; Euro V; Diesel Oil; Desulfurization Efficiency; DBT Extraction

1 INTRODUCTION

With the development of the automobile industry and global petrochemical industry, diesel sulfur oxide (SOx) emissions have led to an increased level of air pollution rapidly. As a result of these emissions combining with rainwater, sulfurous acid is produced, popularly referred to as acid rain. To reduce toxic gas emissions, environmental authorities limited sulfur compounds in fuel oil to 10 parts per million [1].

The sulfur compounds in fuel oil cannot be completely extracted by any current method. It has been widely used to eliminate sulfur compounds through two major extraction strategies, i.e. hydrodesulfurization (HDS) and non-hydrodesulfurization (adsorption, oxidative, and extractive desulfurization) [2]. In spite of the fact that HDS is very effective in removing aliphatic sulfur compounds, some aromatic sulfur compounds, i.e. benzothiophene (BT), dibenzothiophene (DBT) and their derivatives, are difficult to eliminate using HDS. The development of more cost-effective methods is required to desulfurize aromatic sulfur compounds from crude oil [3]. Ionic liquids (ILs) may show significant potential as a means of removing refractory sulfur compounds at ambient pressures and temperatures. An IL is a molten salt with a melting point below 100°C, which is usually composed of

inorganic/organic anions and large asymmetric cations. [4]

Since Euro II standard diesel fuel is still being used in Pakistan despite the fact that better standards are available. There are no safety standards for vehicles in Pakistan and the lack of policies and implementations are the reason Pakistan still relies on Euro II. It might be different when adopting Euro V, but credible sources like Environmental Protection Agency (EPA) claims that the reason for this adaptation is that Euro II fuel will be phased out globally. Thus, the Euro II fuel might become unavailable in the near future, that's why it was necessary to adapt the new standard [5]. In this research, ionic liquids will be investigated for removing dibenzothiophene from diesel fuel and upgrading the fuel to Euro V emission standards, i.e. ≤ 10 parts per million. In order to achieve this, hexyl pyridinium based ILs were used [6].

2 EXPERIMENTAL

Model fuel for current research was produced by adding dibenzothiophene (DBT) in n-dodecane separately to attain a 500 parts per million sulfur content. Desulfurization studies were carried out in 50 mL glass volumetric flasks. For these experimental studies, the volume proportions of ionic liquids to model oil were 1:1, 1:2, 1:3, and 1:4. The model fuel was added with different amounts of ionic liquid, each of which was magnetically stirred vigorously at a definite temperature having the uncertainty of about (±0.1°C). There was a particular selection of temperatures and time intervals. A two phase mixture was formed after allowing the biphasic mixture to settle for 15 minutes.

After the reaction was completed and the reaction mixture settled, the two layers were separated by a separatory funnel. A stainless-steel syringe was used to withdraw the top layer model oil for sulfur content analysis. A UV-Vis-IR spectrophotometer with a wavelength of χmax 284 nm was used to findout the concentration of DBT in model oil samples with Agilent Cary 6000i UV-Vis-IR Spectrophotometer. The calibration curves were generated using mixture with DBT concentrations of 500 ppm, 400 ppm, 300 ppm, 200 ppm, 100 ppm, and 1ppm in n-dodecane. The UV-vis spectrophotometry was preferred over other generally used procedures for different reasons. It was chosen over High Performance Liquid Chromatography (HPLC) as the volatile model oil solvent (n-dodecane) may possibly evaporate during the HPLC timeframe, probably leading to experimental incorrectness.
As a result, the DBT removal efficiency was calculated as net sulfur removal based on the initial and final content of sulfur of the diesel oil. [7]

$$\eta = \left(\frac{[DBT]_i - [DBT]_f}{[DBT]_i}\right) \times 100 \qquad (1)$$

Where, η is removal efficiency, $[DBT]_i$ and $[DBT]_f$ are the initial and final content of sulfur of the diesel oil.

Each measurement of sulfur content in model oil was averaged across three measurements. Calculated values had an uncertainty of 0.5%. Likewise the sulfur distribution coefficient, K_N values were taken into account. As a measure of sulfur concentration, K_N is the ratio between the ILs phase and the model oil phase

To determine how ILs interacts with sulfur molecules, K_N values need to be measured. ILs has a higher affinity for sulfur molecules when their KN values are higher.

$$K_N = \left(\frac{C_0 - C_f}{C_f}\right)\frac{m_{IL}}{m_{diesel}} \qquad (2)$$

Where, C_0 and C_f reflect to the initial and final equilibrium concentrations of model oil respectively. m_{IL} is mass of Ionic Liquid in grams m_{diesel} is the mass of diesel in grams.

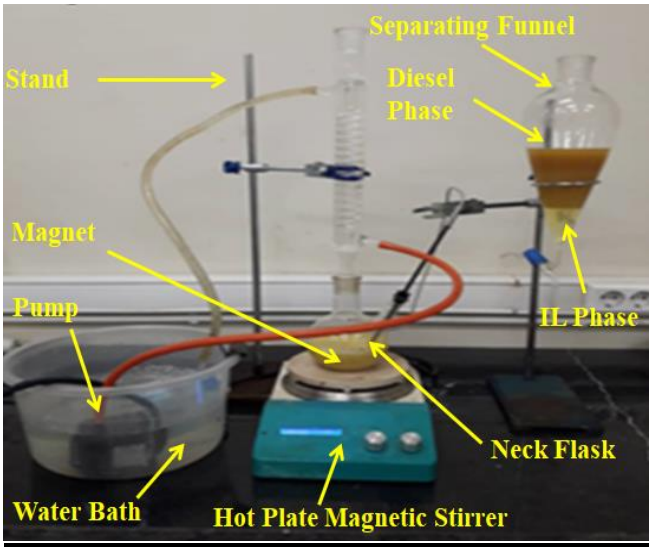

Figure 1. Experimental Setup

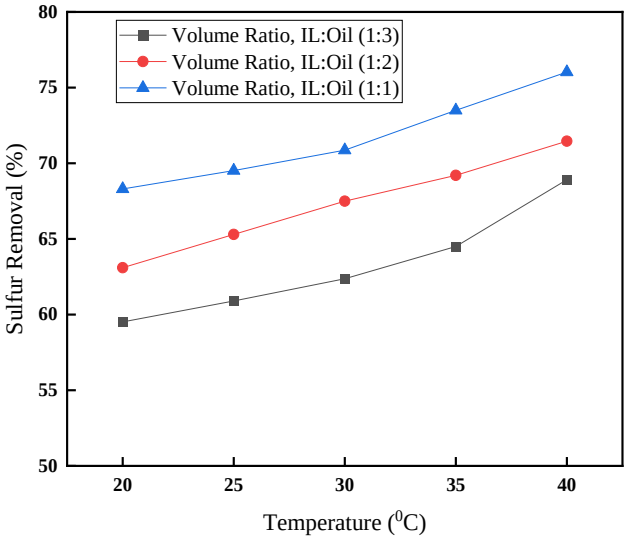

Figure 2. Extraction Desulfurization Efficiency at Different Temperatures

3 RESULTS AND DISCUSSIONS

3.1 Effect of Extraction Temperature

Reaction temperature is an important factor in the EDS process. By changing the temperature range from 20°C to 40°C, outcome of temperature on DBT extraction from diesel (having 500 ppm DBT content) was investigated. In addition, three different ratios of IL to oil were used, i.e. 1:1, 1:2, and 1:3. Figure 2 shows the findings from these experiments.

Higher desulfurization efficiency was detected at higher temperatures regardless of the ILs to the diesel oil volume ratio. Owing to the direct effect of reaction temperature on the kinetic rate constant, rate of reaction and the desulfurization efficiency are increased by increasing the temperature of the reaction. In this study, the highest desulfurization efficiency was attained at the maximum temperature of 40°C. For the Ionic Liquid to diesel oil volume fractions of 1:1, 1:2, and 1:3, the efficiencies of desulfurization during this temperature were 77%, 71%, and 68%, respectively.

Consequently, desulfurization efficiency displayed a direct relation as it reduced with a decrease in the volume fraction of IL to model oil, as greater DBT concentration makes IL almost saturated in the reaction mixture. Thus, the highest desulfurization efficiency was detected for the volume ratio of IL to model oil of 1:1. As a result, efficiency of desulfurization was 67%, 70% and 77% at the temperatures of 20.0°C, 30.0°C and 40.0°C, respectively.

3.2 Effect of Extraction Time

A DBT concentration of 500 ppm at 40°C was allowed to examine the effect of extraction time on DBT removal. Figure shows that during first 45 minutes, the DBT removal efficiency increases swiftly with time for EDS. After almost 45 minutes, the percentage of desulfurization becomes slow, and it is approximately established after 1 hour, resulting in a final DBT removal efficiency of 75 % after 60 minutes. A sulfur removal rate of nearly 74% is achieved within just 10 minutes of OEDS (containing 1 % v/v H_2O_2) under the same effective conditions as that of EDS. After 60 minutes (1 hour) phase equilibrium was reached with 79.6% desulfurization efficiency.

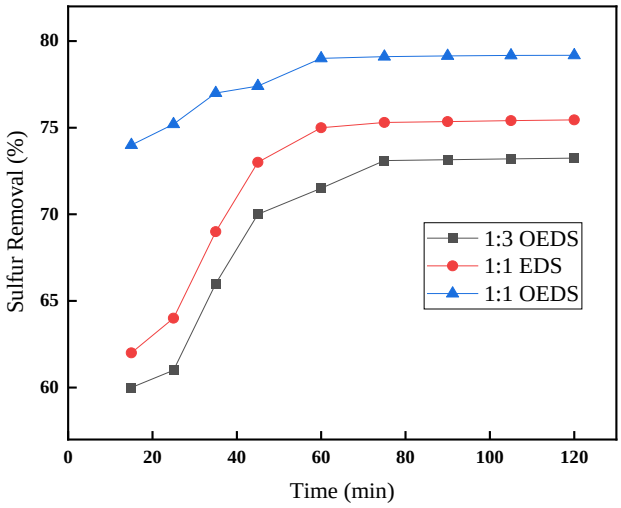

Figure 3. Extraction Desulfurization Efficiency at Different Time Intervals

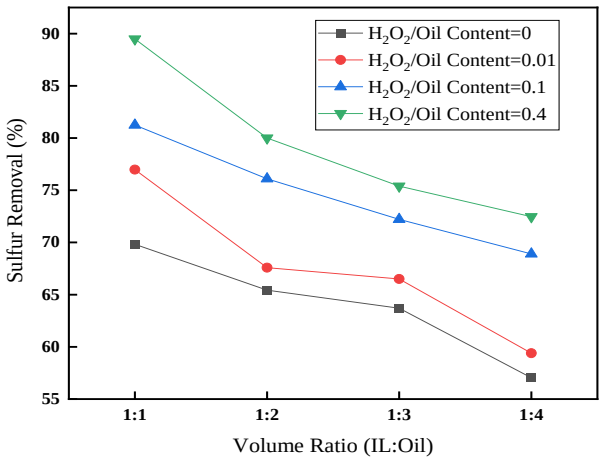

Figure 4. Extraction Desulfurization Efficiency at Different Volume Ratios of H_2O_2 and Oil

A comparison of ionic liquid to model oil ratios for OEDS research suggests that as the volume ratio falls from 1:1 to 1:3, DBT removal rate falls by 21% (74 % for 1:1 ratio, 58 % for 1:3) at the same time due to the fact that model oil has three times as much DBT. As phase equilibrium was reached, the difference in DBT removal efficiencies at two volume ratios gradually decreased over time.

3.3 Effect of Oxidant (H_2O_2) Quantity

DBT removal efficiency increases with a rise in the quantity of H_2O_2 added to the system. It was found that the highest desulfurization efficiency was obtained when H_2O_2 was added at the maximum rate (40.0 % v/v) to all unlike volume ratios of IL and model oil studied. A slight difference in H_2O_2 amount influenced desulfurization efficiency was observed when unlike IL to model fuel volume ratios were taken into account. It was found that pouring just a 1 % v/v of H_2O_2 to model oil at a volume ratio 1:1 resulted in a 7.18 % increase in DBT removal efficiency from 70 % (unreacted H_2O_2) to 77.18 % (with H_2O_2). Desulfurization efficiency was further increased by 4.3% when H_2O_2 concentrations ranged from 1.0 to 10.0 %.

When IL and diesel fuel were mixed in low volumes (1:4), DBT removal efficiency increased from 56 % (without H_2O_2) to 58.9 % after pouring 1 % v/v of H_2O_2. Nevertheless, notable rise of 9.7 % in DBT removal efficiency was attained when quantity of $H_2O_2$was amplified from 1 to 10 % v/v.

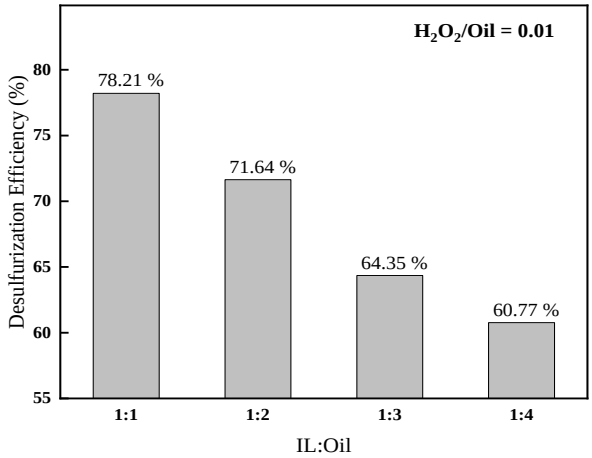

Figure 5. Extraction Desulfurization Efficiency at H_2O_2/Oil = 0.01

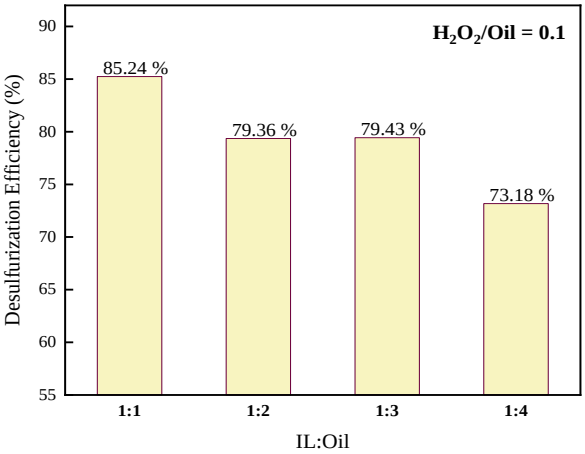

Figure 6. Extraction Desulfurization Efficiency at H_2O_2/Oil = 0.1

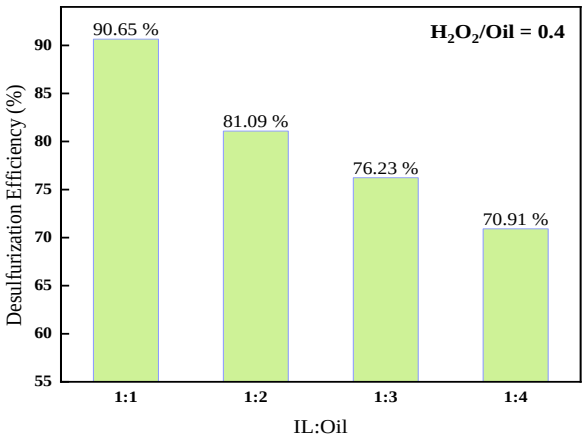

Figure 7. Extraction Desulfurization Efficiency at H_2O_2/Oil = 0.4

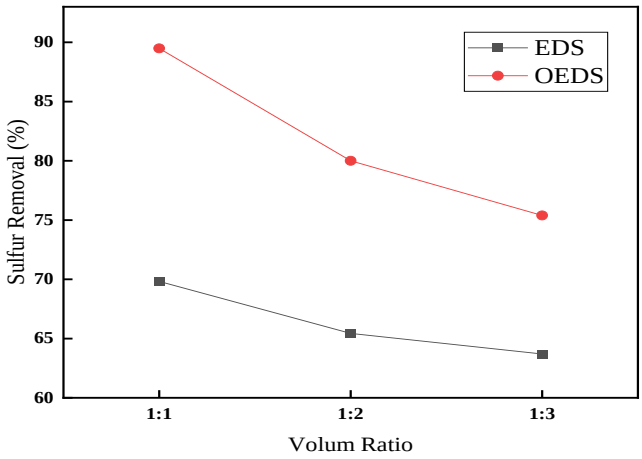

Figure 8. Extraction Desulfurization Efficiency at Definite Volume Ratios EDS & OEDS

3.4 Effect of Volume Ratio of IL to Model Oil

EDS and OEDS were both studied for their effect on desulfurization efficiency by adjusting the IL to model oil volume ratio. Three IL to model oil volume ratios were experienced, i.e. 1:1, 1:2 and 1:3, at a temperature of 40°C and a 30 % oxygen to sulfur ratio. The following figure shows the DBT removal efficiency of EDS and OEDS for different proportions of Ionic Liquid to model oil. When the volume ratio of IL to oil is reduced, desulfurization rate decreases. As the volume ratio falls from 1:1 to 1:3, the efficiency drops by 15 % from 88.5 to 74.7 %, for OEDS. As the volume fraction drops from 1:1 to 1:3, DBT removal rate for EDS decreases by only 9 % (from 68.7 % to 64 %) with all the other operating states lasting the similar in physical world engineering applications.

An ideal ratio of IL to oil must be designated in order to maintain a balance between DBT removal efficiency and production capacity. The same trend was observed in the following figure that EDS exhibited lower DBT removal efficiency than OEDS. The trend remained the same for all the total three volume ratios verified between Ionic Liquid to model oil. As a result of a decrease in the IL to oil volume ratio, gap between the EDS process and OEDS reduced, from 18.67% (88.6 % - 68.7 %) at a 1:1 ratio to 11.62 % (76 % - 62.90 %) at a 1:3 ratio.

3.5 Desulfurization of DBT from Diesel Oil with [C_6Py][BF_4]

This study verified the ability of n-hexyl-pyridinium tetrafluoroborate [HxPy][BF_4] to extract hydrocarbon feedstocks from diesel fuel containing 500 parts per million DBT. Based on a stable volume ratio (1:1) of Ionic Liquid to diesel oil, the figure illustrates that the results were obtained for desulfurizing DBT for 10.0 min, 15 min, 20.0 min, 25 min, 30.0 min, 35.0 min, 40.0 min, and 45.0 min at 40°C.

[HxP_y][BF_4] has a significantly lower ability to extract DBT from diesel fuel than it does from model fuel. Under the similar conditions, DBT extracted from real diesel oil (peak desulfurization at 60%) is significantly lower than that removed from the model oil (n-dodecane) by using IL [C_6P_y][BF_4]. Because diesel oil contains a variety of hydrocarbons, such as aromatic, paraffinic, alkyl aromatic, and polyaromatic hydrocarbons, which may partially mix with IL.

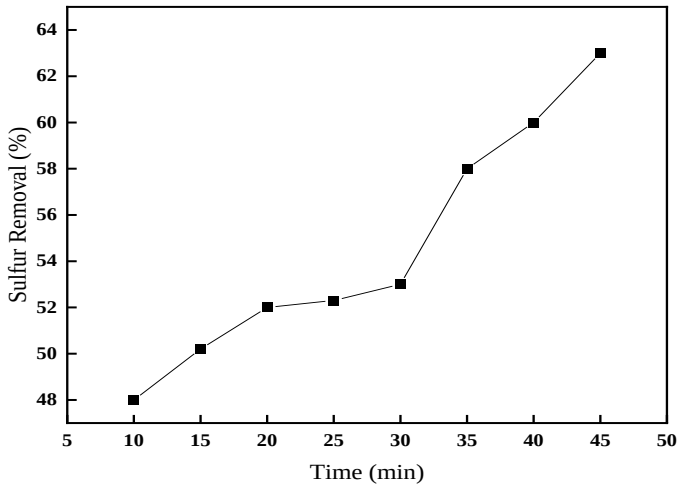

Figure 9. Desulfurization of DBT from Diesel Oil

3.6 Recycling of the Ionic Liquid

The Ionic Liquid [C_6Py][BF4] was recycled up to 8 times and after each recycling stage, it was examined for its efficiency of desulfurization in a model oil. Each recycling step results in a different variation in efficiency of desulfurization as shown in figure 10. The desulfurization efficiency of the IL varied only minimally over the 8 cycles, indicating that recycling did not significantly affect its ability to remove sulfur from the model oil. The reduction in desulfurization efficiency was observed with an increase in recycling and reuses cycles, reducing to 75% by the 8th cycle.

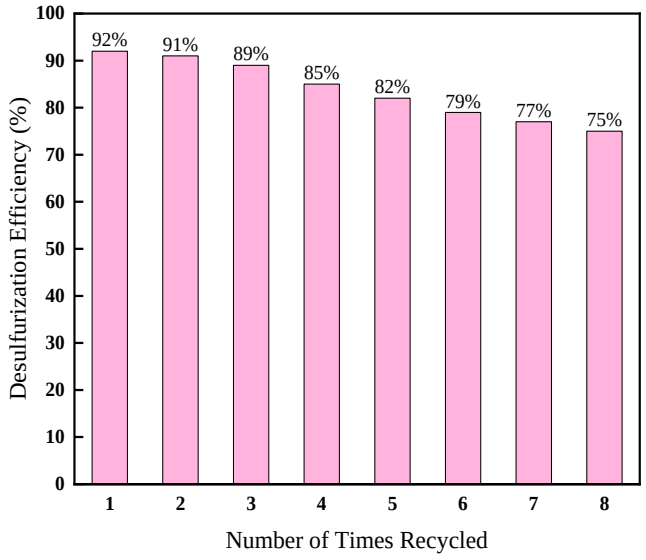

Figure 10. Recycling of the Ionic Liquid

4 CONCLUSIONS

In this research, pyridinium-based ILs [C_6P_y][BF_4] was used as extractant under different experimental conditions to extract DBT from model oils (dibenzothiophene in n-dodecane) and diesel oil. Several reaction parameters were examined, including the type of IL applications, extraction temperature, extraction time, volume ratio (IL:Oil), and amount of H_2O_2 for desulfurization efficiency. Under ambient temperature (room temperature), DBT concentrations were 500 ppm initially. Temperature directly affects the kinetic rate constant of the DBT removal reaction, which results in higher DBT removal efficiency. In order to save energy and lower operating costs, the maximum temperature was set to 40 ^oC. In EDS, the removal time of 40 mins was examined to be optimal, which resulted in the highest sulfur removal for DBT. A sulfur removal rate of nearly 74% is achieved within just 10 minutes of OEDS (containing 1 % v/v H_2O_2) under the same effective conditions as that of EDS. Phase equilibrium was reached after 60 minutes with 79.6% desulfurization efficiency. In order to increase desulfurization efficiency, the volume ratio of IL to oil (1:1) was increased to a high level by increasing the amount of H_2O_2.

Under the same conditions, DBT extracted from actual diesel oil is significantly lower than that removed from the model fuel (n-dodecane). As the amount of ionic liquid decreased, the efficiency of [C_6P_y][BF_4] decreased, indicating that a large amount of DBT almost saturated the ionic liquid. At the first recycling, the efficiency of decaying DBT from diesel oil was lower than the efficiency of decaying DBT from model oil. A higher number of recycling & reuse cycles resulted in a decrease in desulfurization (removal of DBT from n-dodecane) efficiency, reducing to 75% by 8th cycle. There is no significant loss in desulfurization efficiency when [C_6P_y][BF_4] is reused up to 8 times.

ACKNOWLEDGEMENTS

We are grateful to Mechanical Engineering Department of University of Engineering and Technology Taxila, Pakistan for providing us opportunity to conduct this research work and for all of the resources and support they provided.

REFERENCES

[1]. Kulkarni, Prashant S., and Carlos AM Afonso. "Deep desulfurization of diesel fuel using ionic liquids: current status and future challenges." *Green Chemistry* 12.7, 2021.

[2]. Bösmann, Andreas, et al. "Deep desulfurization of diesel fuel by extraction with ionic liquids." *Chemical Communications* 23, 2020.

[3]. Xuemei, Chu, et al. "Desulfurization of diesel fuel by extraction with [BF4]−-based ionic liquids." *Chinese Journal of Chemical Engineering* 16.6, 2020.

[4]. Jiang, Bin, et al. "Efficient oxidative desulfurization of diesel fuel using amide-based ionic liquids." *Chemical Engineering Journal* 283, 2019.

[5]. Chen, Xiaochun, et al. "Using functional acidic ionic liquids as both extractant and catalyst in oxidative desulfurization of diesel fuel: An investigation of real feedstock." *Fuel* 146, 2019.

[6]. Ban, Li-Li, et al. "Deep extractive desulfurization of diesel fuels by FeCl3/ionic liquids." *Chinese Chemical Letters* 24.8, 2018.

[7]. Anantharaj, R., and Tamal Banerjee. "COSMO-RS based predictions for the desulphurization of diesel oil using ionic liquids: Effect of cation and anion combination." *Fuel processing* 92.1, 2018.

PERFORMANCE AND EMISSIONS ANALYSIS OF A DIESEL ENGINE FUELED BY DIESEL MIXTURES WITH MANGANESE OXIDE AND CARBON NANOTUBES FUEL ADDITIVES

Muhammad Sarfraz Ali[1,*], Sadia Saleem[2], Rozeena Aslam[1], Hamza Akhtar[1], Muhammad Imran[1], Talha Nadeem Hassan[1], Abdul Rehman[1], Muhammad Faheem Nazar[1], Anees ur Rehman[1]

[1]Mechanical Engineering Department, Swedish College of Engineering & Technology, Rahim Yar Khan, Pakistan

[2]Institute of Computer Science and Information Technology, The Women University, Multan, Pakistan

*Corresponding author. Tel.: +92-345-8329528

E-mail address: sarfrazali@piet.edu.pk (Muhammad Sarfraz Ali)

ABSTRACT

To improve the quality of the air we breathe, internal combustion engine emission standards are getting stricter and stricter. Modern diesel emission control technologies concentrate on reducing particulate matter and nitrogen oxide emissions. Diesel emissions were said to be reduced with nanoparticle additions. Diesel fuel can burn cleanly because of engine advancement and diesel fuel formulation. The experimental study is concentrated on the impact of adding nanoparticles to diesel fuel, such as manganese oxide and multi-walled carbon nanotubes. Manganese oxide and multiwalled carbon nanotubes were added to pure diesel in a concentration of 90 ppm each. The experiments were carried out on a four-stroke diesel engine. The performance and emission parameters were recorded at engine speeds of 1200, 1400, 1600, 1800, 2000, and 2200 rpm. The performance of diesel fuel with nanoparticles addition showed a significant improvement. The brake thermal efficiency of the diesel engine increased by 10.62% when both manganese oxide and carbon nanotubes were added to pure diesel in a concentration of 90 ppm each. Diesel fuel with a nanoparticle addition demonstrated significantly lower levels of pollution emissions in exhaust emissions. The unburned hydrocarbons decrease maximum by 8.43% when carbon nanotubes were blended with pure diesel. Carbon monoxide emissions were reduced by 20.34% with carbon nanotubes at an engine speed of 1800 rpm. There was a 6.2% reduction in NO_x emissions when both manganese oxide and carbon nanotubes were used at a concentration of 90 ppm each.

Keywords: Diesel Engine; Nanoparticles; Manganese oxide; Multiwalled carbon nanotubes; Emissions; Performance

1 INTRODUCTION

Diesel engines work by squeezing air at very high pressures and then spraying a minor quantity of fuel into this highly compressed air to provide their tremendous performance and outstanding fuel economy. Excessive emissions of particulate matter (PM) and nitrogen oxides (NO_X) continue to be a technical difficulty for diesel engines [1,2]. Future emission regulations will be helped by the new fields of technology, such as fuel post-combustion emission control devices. Using fuel additives to reduce the number of particles smaller than 2.5 μm was a cost-effective strategy. The highest decline in freezing point with organic manganese was recorded at 15 ℃, and the ideal dosage rate was found 700 ppm [3].

Significant trends were observed in the freezing point fall when the metal dosage was applied. Various metal additives were used with diesel to improve the quality of the fuel to achieve more complete fuel combustion and produce fewer exhaust emissions. The principle of this additive action comprises the effect of a catalyst on the burning of unburned hydrocarbons [4]. The soot ignition temperature is lowered with the use of transitional or noble metals as fuel additives. According to the function for which they were intended, diesel additives can also be divided into

three categories: (i) pre-flame additive (ii) flame additive and (iii) post-flame additive [5].

As soon as the additive amount surpasses a predetermined threshold, additional particles start to form. The soot emissions aspect and engine type were the only variables that affect the additive dose limit (turbocharged and normally aspirated engines behave similarly). While lower additive dosages were advantageous, a more focused benefit was shown with higher additive concentrations [6].

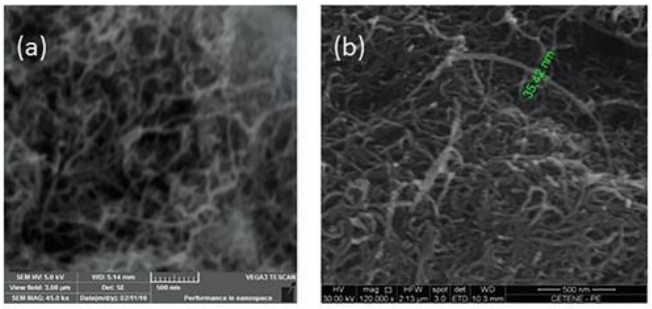

Figure 1. (a) SEM images of MnO (b) MWCNTs

The nano additive was released mostly in the particle phase rather than the gaseous phase. All of the additives have metal as their primary component, which is released as oxide in the exhaust. Although additives don't have much of an impact on soot suppression, they were helpful for trap regeneration. One of the most alluring ways to minimize PM was to add catalytic chemicals to petrol. Fuel is supplemented with additives to increase engine performance and lower emissions. Almost all methods for reducing emissions at the source from diesel engines lead to a compromise in the amounts of UHC, particulates, and NO_X [7]. At the combustion and injection stage, the engine manufacturer has several tools at their disposal to accurately handle the emissions of any particular contaminant.

The subsequent actualities and patterns were relevant, (i) particulate emissions reduction and better air-fuel mixing due to the increase in injection speed; (ii) the increase in injection pressure was beneficial as well; and (iii) Using the injector with pintles as flat reduces the residuals and reduces the emissions of unburned hydrocarbons and particulate matters [8]. The additive approach demands a diesel fuel everlasting addition that would be used in all cars, barring those with filters. The majority of fuel additives were metal-organic compounds that were entirely dissolved in diesel fuel. Diesel fuel is given a metal additive to: (i) reduce the ignition delay; (ii) stabilize and act as an anti-oxidizer; and (iii) act as a surface-active agent [9].

Diesel emissions were efficiently reduced by metal-based additions in two ways. Initially, the metals either interact in a straight line with the carbon molecules in the soot to lower the oxidation temperature or interact with water to procedure radicals of hydroxyl, which accelerate the oxidation of soot [10]. If the additives were employed in the diesel engine after combustion, the nanoparticles serve as an oxidation nucleus for soot.

The potential of engine exhaust particles to enter and simply linger in the respiratory alveolar, with detrimental health effects, puts them even in little quantities always under suspicion. Out of all the varieties of dust that can be found in the atmosphere, diesel particulates have been shown to match the size of particles that were most easily retained for the longest time in the respiratory system [11].

Preceding studies illustrate that nanoparticle additives have an important effect on the performance and emission of the diesel engine. In the current study, the experimental work was carried out on a single-cylinder, four-stroke diesel engine. Manganese oxide and multi-walled carbon nanotubes were blended with pure diesel at a concentration of 90 ppm each. The performance and emission parameters were recorded at engine speeds of 1200, 1400, 1600, 1800, 2000, and 2200 rpm. The performance of diesel fuel with nanoparticles addition showed a significant improvement. The BTE of the diesel engine increased by 10.62% when both manganese oxide and carbon nanotubes were added to pure diesel in a concentration of 90 ppm each. Diesel fuel with a nanoparticle addition demonstrated significantly lower levels of pollution emissions in exhaust emissions. The unburned hydrocarbons decrease maximum by 8.43% when carbon nanotubes were blended with pure diesel. Carbon monoxide emissions were reduced by 20.34% with carbon nanotubes at an engine speed of 1800 rpm. There was a 6.2% reduction in NO_x emissions when both manganese oxide and carbon nanotubes were used at a concentration of 90 ppm each.

2 FUEL PREPARATION

In the current study, manganese oxide (MnO) and multi-walled carbon nanotubes were used with pure diesel (D)in the diesel engine. Manganese oxide (MnO) and multi-walled carbon nanotubes were blended with pure diesel (D) in a concentration of 90

ppm each. The design of the experiment is shown in Table 1. To create a homogeneous emulsion fuel, the MnO and CNTs introduced to pure diesel were stirred using a magnetic stirrer for 30 minutes. The addition of manganese oxide (MnO) and carbon nanotubes (CNTs) to pure diesel can improve its quality. Amido group-containing carbon nanotubes (CNTs) were highly reactive and may interact with a variety of substances.

Table 1. Design of experiment

Name	Diesel (%)	MnO (ppm)	CNTs (ppm)
D	100	0	0
DMnO	100	90	0
DCNTs	100	0	90
DMnOCNTs	100	90	90

3 EXPERIMENTAL SETUP

On a four-stroke, single-cylinder, air-cooled diesel engine, the performance and emission characteristics were evaluated by using diesel mixtures with manganese oxide and multi-walled carbon nanotubes. Figure 2 displays the schematic diagram of the experimental setup. The engine had a Bore (70 mm) and Stroke (98mm) of a Compression Ratio of 17.5:1, and a Rated Power of 4 kW was used for the experiments. The engine was coupled to an electric dynamometer to apply load. The experiments were carried out at engine speeds of 1200, 1400, 1600, 1800, 2000, and 2200 rpm.

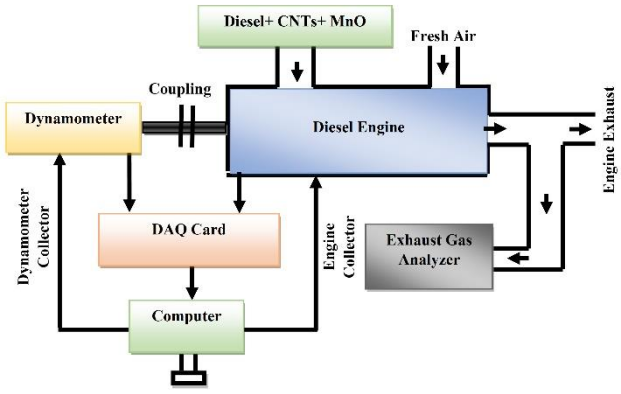

Figure 2. Schematic diagram of the experimental setup

The tests were conducted using manganese oxide and multi-walled carbon nanotube fuel blends with pure diesel. In the first test, pure diesel was used in the engine and performance and emission characteristics were recorded for reference. After that manganese oxide and multiwalled carbon nanotubes were blended separately with the pure diesel at a concentration of 90 ppm and the result was recorded. After that, both manganese oxide and multiwalled carbon nanotubes in a concentration of 90 ppm were blended with the pure diesel and results were recorded. Before every next test, the engine was run with pure diesel for at least 10 minutes so that the residuals of the previous fuel blend could clean from the fuel line. Every test was repeated three times and the average value was used for comparison. Performance parameters i.e., BTE and emission characteristics i.e., NO_X, UHC, and CO were assessed. An exhaust gas analyzer was used to measure the exhaust emissions.

4 RESULTS AND DISCUSSIONS

4.1 Brake Thermal Efficiency

Figure 3 shows the fluctuation in the engine's brake thermal efficiency. By shortening the ignition delay, the addition of manganese oxide to pure diesel improves combustion efficiency. At an engine speed of 2200 rpm, the best maximum thermal efficiency was found since it rises as the engine speed rises. Additionally, the BTE increased by mixing nanoparticles with pure diesel. More complete combustion caused by the presence of too much oxygen in the engine cylinder increases brake thermal efficiency. [12]. The maximum increase in BTE was achieved when both the manganese oxide and carbon nanotubes were used at a concentration of 90 ppm each with pure diesel. With this combination, there was an increase of 10.62% in BTE when compared to pure diesel.

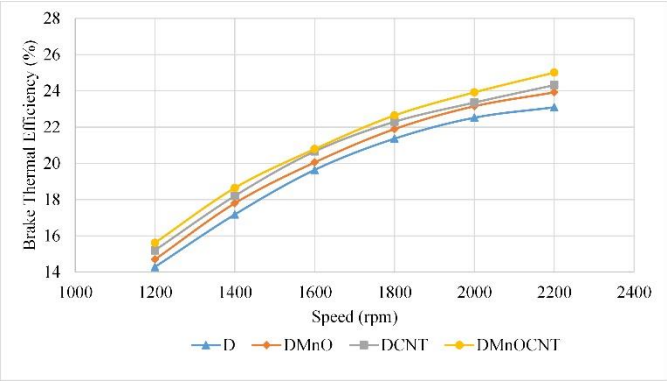

Figure 3. Variation of brake thermal efficiency with speed

4.2 UHC Emissions

The unburned hydrocarbon emissions for the DI diesel engine were lower at the engine speed of 1200 rpm. It increases with an increase of engine speed up to 1600 rpm. Maximum unburned hydrocarbon emissions were at speed of 1600 rpm. After that, it can be realised that there is a decline in unburned

hydrocarbon at higher speeds. Thus, attention has been focused on unburned hydrocarbon emissions while the engine is idling. Figure 4 displays the engine's emission pattern for unburned hydrocarbons. With the addition of nanoparticles to the pure diesel fuel, the unburned hydrocarbons decrease [13]. The maximum decrease in unburned hydrocarbons was 8.43 % when carbon nanotubes in a concentration of 90 ppm were blended with pure diesel.

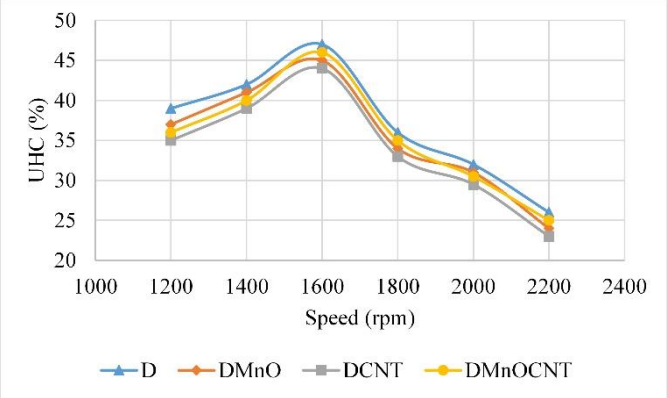

Figure 4. Variation of unburned hydrocarbon with speed

4.3 CO Emissions

Incomplete combustion results in the production of carbon monoxide, which is made worse due to the absence of oxidants, a low temperature, and a long staying period. The engine's carbon monoxide emissions are shown in Figure 5. The emissions of carbon monoxide were trending downward when metal oxide additives were catalytically oxidized in abundant oxygen [14]. As can be seen from the graph, carbon monoxide emissions were reduced by 20.34% with carbon nanotubes at an engine speed of 1800 rpm.

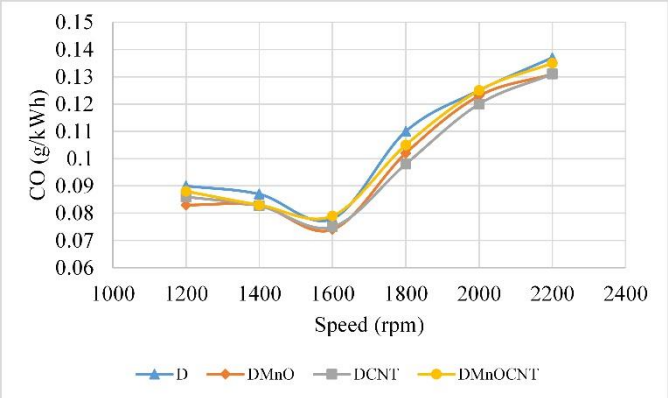

Figure 5. Variation of carbon monoxide with speed

4.4 NO_x Emissions

It has been discovered that NO_x emissions were on the decline when diesel fuel contains nanoparticle additives. There was a change of 1-1.4% in the cetane number of diesel fuel due to nanoparticles which has an impact on emissions. Compared to fuels with lower cetane numbers, those with higher cetane numbers have lesser premixed fuel fractions and fewer NO_x emissions [6]. Figure 6 illustrates the engine's nitrogen oxide (NO_X) emission. The data indicates a 6.2% reduction in NO_x emissions when both manganese oxide and carbon nanotubes were used at a concentration of 90 ppm each.

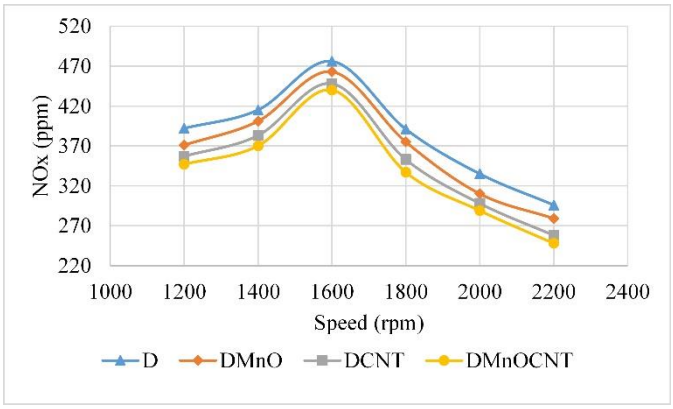

Figure 6. Variation of nitrogen oxide emissions with speed.

5 CONCLUSIONS

From the results of the experimental study, manganese has the strongest impact on lowering engine exhaust emissions. Since manganese is not considered to be a contaminant, it is frequently employed as a doping agent in diesel fuel. Diesel fuel that has been infused with a manganese oxide and carbon nanotubes additive somewhat improves an engine's performance. The BTE of the diesel engine increased by 10.62% when both manganese oxide and carbon nanotubes were added to pure diesel in a concentration of 90 ppm each.

Measurements of the exhaust emissions for the fuel with the manganese oxide and carbon nanotube additives show a significant decrease. The unburned hydrocarbons decrease maximum by 8.43% when carbon nanotubes were blended with pure diesel. Carbon monoxide emissions were reduced by 20.34% with carbon nanotubes at the engine speed of 1800 rpm. There was a 6.2% reduction in NO_x emissions when both manganese oxide and carbon nanotubes were used at a concentration of 90 ppm each.

If additives were used, they must be kept from venturing into the surrounding air by suitable traps.

ACKNOWLEDGEMENTS

The Authors would like to thank the management of the Swedish College of Engineering and Technology, Rahim Yar Khan, for supporting this experimental study.

REFERENCES

[1]. H. Solmaz, S. M. S. Ardebili, A. Calam, E. Yılmaz, and D. İpci, "Prediction of performance and exhaust emissions of a CI engine fueled with multi-wall carbon nanotube doped biodiesel-diesel blends using response surface method," *Energy*, vol. 227, 2021, doi: 10.1016/j.energy.2021.120518.

[2]. M. Mirzajanzadeh *et al.*, "A novel soluble nano-catalysts in diesel-biodiesel fuel blends to improve diesel engines performance and reduce exhaust emissions," *Fuel*, vol. 139, no. x, pp. 374–382, 2015, doi: 10.1016/j.fuel.2014.09.008.

[3]. M. Ghanbari, G. Najafi, B. Ghobadian, T. Yusaf, A. P. Carlucci, and M. Kiani Deh Kiani, "Performance and emission characteristics of a CI engine using nanoparticles additives in biodiesel-diesel blends and modelling with GP approach," *Fuel*, vol. 202, pp. 699–716, 2017, doi: 10.1016/j.fuel.2017.04.117.

[4]. G. R. Kannan, R. Karvembu, and R. Anand, "Effect of metal-based additive on performance emission and combustion characteristics of diesel engine fuelled with biodiesel," *Appl. Energy*, vol. 88, no. 11, pp. 3694–3703, 2011, doi: 10.1016/j.apenergy.2011.04.043.

[5]. A. F. Chen, M. Akmal Adzmi, A. Adam, M. F. Othman, M. K. Kamaruzzaman, and A. G. Mrwan, "Combustion characteristics, engine performances and emissions of a diesel engine using nanoparticle-diesel fuel blends with aluminium oxide, carbon nanotubes and silicon oxide," *Energy Convers. Manag.*, vol. 171, no. June, pp. 461–477, 2018, doi: 10.1016/j.enconman.2018.06.004.

[6]. A. Heidari-Maleni, T. M. Gundoshmian, B. Karimi, A. Jahanbakhshi, and B. Ghobadian, "A novel fuel based on biocompatible nanoparticles and ethanol-biodiesel blends to improve diesel engines performance and reduce exhaust emissions," *Fuel*, vol. 276, no. April, p. 118079, 2020, doi: 10.1016/j.fuel.2020.118079.

[7]. V. Arul Mozhi Selvan, R. B. Anand, and M. Udayakumar, "Effect of cerium oxide nanoparticles and carbon nanotubes as fuel-borne additives in diesterol blends on the performance, combustion and emission characteristics of a variable compression ratio engine," *Fuel*, vol. 130, pp. 160–167, 2014, doi: 10.1016/j.fuel.2014.04.034.

[8]. A. I. EL-Seesy and H. Hassan, "Investigation of the effect of adding graphene oxide, graphene nanoplatelet, and multiwalled carbon nanotube additives with n-butanol-Jatropha methyl ester on a diesel engine performance," *Renew. Energy*, vol. 132, pp. 558–574, 2019, doi: 10.1016/j.renene.2018.08.026.

[9]. D. Balasubramanian, A. T. Hoang, I. Papla Venugopal, A. Shanmugam, J. Gao, and T. Wongwuttanasatian, "Numerical and experimental evaluation on the pooled effect of waste cooking oil biodiesel/diesel blends and exhaust gas recirculation in a twin-cylinder diesel engine," *Fuel*, vol. 287, no. August 2020, p. 119815, 2021, doi: 10.1016/j.fuel.2020.119815.

[10]. A. Taghizadeh-Alisaraei and A. Rezaei-Asl, "The effect of added ethanol to diesel fuel on performance, vibration, combustion and knocking of a CI engine," *Fuel*, vol. 185, pp. 718–733, 2016, doi: 10.1016/j.fuel.2016.08.041.

[11]. M. Kapetanović, A. Núñez, N. van Oort, and R. M. P. Goverde, "Reducing fuel consumption and related emissions through optimal sizing of energy storage systems for diesel-electric trains," *Appl. Energy*, vol. 294, no. November 2020, 2021, doi: 10.1016/j.apenergy.2021.117018.

[12]. O. M. I. Nwafor, G. Rice, and A. I. Ogbonna, "Effect of advanced injection timing on the performance of rapeseed oil in diesel engines," *Renew. energy*, vol. 21, no. 3, pp. 433–444, 2000, doi: 10.1016/S0960-1481(00)00037-9.

[13]. A. Pourahmadiyan, P. Ahmadi, and E. Kjeang, "Dynamic simulation and life cycle greenhouse gas impact assessment of CNG, LNG, and diesel-powered transit buses in British Columbia, Canada," *Transp. Res. Part*

D Transp. Environ., vol. 92, no. February, p. 102724, 2021, doi: 10.1016/j.trd.2021.102724.

[14]. S. H. Hosseini, A. Taghizadeh-Alisaraei, B. Ghobadian, and A. Abbaszadeh-Mayvan, "Performance and emission characteristics of a CI engine fuelled with carbon nanotubes and diesel-biodiesel blends," *Renew. Energy*, vol. 111, pp. 201–213, 2017, doi: 10.1016/j.renene.2017.04.013.

MODELING OF SURFACE ROUGHNESS AND OPTIMIZATION OF CUTTING PARAMETERS FOR MILLING OF 42CrMo4 BY COATED CARBIDE TOOL INSERTS

Hamza Khalid[1,*], Mirza Jahanzaib[1], Muhammad Jawad[1], Uroosa Malik[2]
[1]Engineering Management Department, University of Engineering & Technology, Taxila, Pakistan.
[2]Department of Mechanical Engineering, College of Electrical & Mechanical Engineering (NUST), Rawalpindi, Pakistan

[*]Corresponding author. Tel.: +92-333-5715457;
E-mail address: hamzakhalidtz97@hotmail.com (Hamza Khalid)

ABSTRACT

Machining is considered as the backbone of the manufacturing sector. By the advancement of technology and its implementation in the field of manufacturing, establishment of optimized cutting parameters for machining of various materials is the basic requirement for high quality and energy efficient machining with minimum cost and time. Surface roughness in machining (normally denoted by 'R_a') is not only the main indicator for the surface quality but also helps in achieving close dimensional tolerances of machined parts. The parameters which control surface roughness include rate of feed (*f*), spindle speed (*v*), depth of cut (DoC), material of insert and tool holder, tool geometry and cutting oils etc. With the introduction of automation and Artificial Intelligence (AI) and Machine Learning in the machining sector, accurate predictive models using techniques such as Response Surface Methodology (RSM) will help in selecting optimum parameters of machining to achieve desired surface roughness. This will ultimately help in enhancing productivity quality, efficiency and economy. In this research, average surface roughness (R_a) mathematical model has been developed for milling very popular steel type namely 42CrMo4 in free forged and hardened form using mechanical cutter clamped with multilayer coated carbide inserts TPKN-2204. A sequence of experiments using the response surface methodology (RSM) have been conducted to obtain a relationship between milling parameters (i.e., *f, v* & DoC) and R_a. Contour plots and surface plots of interactions among the cutting parameters have been developed for 42CrMo4 which identify that a target R_a can be achieved through optimum combination of the above mentioned milling parameters with a confidence interval of 95%. The confirmation of validity of the developed model has been done afterwards through conducting three experiments with an avg. prediction error of 2.08%.

Keywords: Surface roughness; dimensional tolerances; cutting parameters; Response Surface Methodology (RSM)

1 INTRODUCTION

Surface roughness is often termed by machinists as its similar opposite word as 'surface finish'. Lower the value of R_a, higher will be the surface finish. A fine surface finish is of great importance, especially in automobile, aerospace and defense sectors where critical machinery/equipment requires fine surfaced components. It has previously been established experimentally that fatigue life of machined parts is decreased by the high value of surface roughness [1]. 42CrMo4 is 1% chromium molybdenum through hardened steel and possess good tensile resistance and shock resistant properties combined with ductility. Its wear resistance can be considerably increased by hardening or nitriding. considering this, 42CrMo4 has a wide range of practical engineering applications comprising components related to power transmission, gears, bearing surfaces, high strength parts related to turbines, compressors etc. and

manufacturing of critical components related to machine building industry, automotive, aerospace and defense and power sectors etc. Metal forgings are extensively used in the machining as well as in forming industry [6–7], Their use in the industry range from automotive sector [8], to other engineering sectors like transport, aerospace & precision industries [9–11]. These forgings include shafts of gas, water and steam turbines, rotors for generators related to wind and gas power [12]. Forged steels are improved mechanical properties of the material. These properties include hardness, wear resistance, toughness, and high strength [13, 14]. Free forging is normally implemented in forging heavy duty materials in minimum production time. 42CrMo4 is a very popular material with forging whose mechanical properties are enhanced exponentially by hot forging. Tool inserts are commonly manufactured from carbide, Cubic Boron Nitride CBN), micro grain carbide, cermet-based inserts, cobalt based, silicon nitride and ceramic based inserts. Coatings on the inserts help increase resistance to wear and insert life. Normally used Coatings for the inserts, comprise titanium nitride (TiN), titanium carbonitride (TiCN), titanium aluminum nitride (TiAlN), aluminum oxide (Al2O3), chromium nitride and zirconium nitride etc. Literature review regarding parameters effecting surface finish has been conducted [2–5]. The scholars focused on the machining issues during various conditions, surface finish relation with cutting tools specifications and type and geometry of inserts used on the tool holders, insert failure, and machining of heat treated materials. Parameters for cutting tools include cutting tool angles, type of insert coatings, cutting tool/insert geometry (like nose radii & chip breakers etc.), process of manufacturing, material of inserts, and type of cutting fluid used. Naseli et al. [5], studied the effects of the approach and rake angles of Al2O3 coated inserts on the R_a for steel AISI 1040. The nose radius of tool is also a major factor affecting finish of the machined surface. Beauchamp et al [15] through his research concluded that a smoother surface is produced by a larger nose radius at low *f* values and at high speeds. It is noteworthy that more than 80% of the total machining that is performed in the industry is by using coated carbide based inserts [16]. Tooling with coated carbide inserts is becoming more and more popular in present day machining and are replacing the uncoated carbide tools. The impact of uncoated and multilayer coated carbide inserts on the surface roughness of hardened AISI 4340 steel was examined by Sahoo and Sahoo [16]. Carbide inserts with multilayer coatings turned out to function better. The use of cutting oils is to lubrication and heat dissipation of the interface connecting the tool and the job to improve machinability is widespread throughout all industrial sectors [17]. Tool wear and R_a were studied in relation to various cutting oil levels and machining parameters by Sujan Debnath et al [17] by using Taguchi methodology. Using a mild steel bar, they experimented with a carbide based inserts coated with TiCN-Al2O3-TiN during a CNC turning operation. According to the findings, the job's R_a was mostly determined by feed rate/ Cutting fluid's flow rate also made a significant contribution. Xavior et al [18] examined the impact of the coolants on R_a while turning AISI-304 steel with carbide based inserts. They compared coconut oil and other coolants. The results showed that when compared to the other two forms of oils used as coolants, coconut oil gave long lasting tool life and better surface quality. Surface roughness is affected by machining parameters in addition to tool and cutting fluid factors. Surface roughness in machining operations is related by Equation (1) [19]:

$$R_a = \frac{f^2}{32r} \qquad (1)$$

Where, '*f*' is the rate of feed and '*r*' is the nose radius of insert/tool. There have been concerns about the given model shown in Eq. 1. For instance, the model gives no account for manufacturing flaws such as tool vibrations and adhesion of chips. To increase surface roughness and tool life, certain geometries are required for some tools, such as Cubic Boron Nitride (CBN). Surface roughness values obtained from trials using slow *f* values do not match with the theoretical values [5]. Yet, it has been demonstrated through experimentation that raising the *f* increases R_a values, whilst lowering the *f* and raising the *v* has the opposite effect, thereby improving the surface quality of

the component/job. Surface roughness, cutting pressures and tool life were among the performance metrics that were investigated by Chinchanikar and Choudhury [20] while turning of AISI 4340 steel hardened to 35 & 45 HRC. Findings concluded that there was a substantial interaction between "*f* and *v*" and "*f* and DoC" for the R_a model. R_a was noticeably impacted by higher feed and cut depth. Using various cutting tools, Lima et al. [21] examined the machinability AISI 4340 that were hardened prior to machining. Inserts made of coated carbide and Polycrystalline Cubic Boron Nitride (PCBN) were used for steel AISI 4340 hardened at 42 and 48 HRC, respectively. For steel hardened to 42 HRC, it was discovered that as *v* was increased to 120 m/min, the surface finish substantially improved, but as speed was increased further, R_a began degrading. Surface finish improved by increasing *v* for steel hardened to 48 HRC. Conversely, the surface finish was affected adversely by feed rate throughout its range while DoC had almost no effect on R_a up to 1.5mm. Suresh et al. [22] examined the surface roughness (R_a) of steel AISI 4340 that had been hardened to 48 HRC. It was discovered that a low *f* rates in conjunction with a fast *v* values produced the lowest R_a value. Using coated carbide multilayered inserts, Sahoo and Sahoo [23] investigated the impact of machining settings on R_a and flank wear for steel AISI 4340 which was heat treated to 47 HRC. Taguchi and RSM were both applied in this study. Findings showed that feed had the biggest impact on Ra, followed by speed and depth of cut. *f* and DoC have been shown to interact significantly as well. Noordin et al. Nalbant et al. [24] investigated the impact of *f*, *v* on PVD coated, CVD coated, and uncoated carbide tools on surface roughness for steel AISI 1030. For coated carbide inserts, the results showed that R_a fell as *v* increased. R_a, however, rose by increasing *v* for tools clamped with uncoated carbide inserts. Both coated and uncoated carbide inserts showed a linear relationship between *f* and R_a. Also, the R_a value was decreased by decreasing heat conductivity and friction coefficient values.

Costa et al [25] studied the impact of austenitizing time and austenitizing temperatures on the microstructural development of 42CrMo4. According to the findings, 42CrMo4 could only achieve a fully recrystallized microstructure after being austenitized at 1200 °C for 200 min. Results showed that, as the austenitizing time and temperature increase, the micro-hardness values decreased in accordance with the reduction in resultant force. Çalık et al [26] studied how heat treatment affected the microstructure and mechanical strength characteristics of 42CrMo4 steel by annealing samples for 120 minutes at 860°C, quenching them in oil for 120 minutes, and then tempering them for 120 minutes at 480–570°C. In contrast to untreated 42CrMo4 steel, which mostly comprises of pearlite and ferrite, quenched 42CrMo4 steel was discovered to have a martensitic microstructure. At the conclusion of the quenching procedure, they saw that the measured yield stress, UTS, hardness, and impact energy had increased while the elongation had decreased.

It can be concluded from the above discussion that R_a is directly impacted by cutting tools, type of cutting inserts, machining parameters, cutting fluids, and machining settings.

Additionally, it can be seen that when the carbon content & hardness of the material changes, the influence of machining parameters (i.e., *f*, *v*, and DoC) on R_a varies. Mechanical qualities are influenced by carbon content as well as the type and concentration of various alloying elements. This influences the material's machinability, which in turn determines the machining parameters. It has been observed that no working on research has been stated in the technical literature on the milling of Free Forged and Heat Treated 42CrMo4 and the optimization of cutting parameters through RSM. Aim of this research is to investigate the effects of machining (milling) parameters on surface roughness for 42CrMo4 steel through Carbide based inserts, mathematical model development, and the optimization of these parameters through Response Surface Methodology (RSM).

2 EXPERIMENTAL DETAILS

This section describes the description and specifications of material used, methodology of experimentation adopted, details of experimental and testing apparatus, the manufacturing processes of test samples preparation.

2.1 Experimental Apparatus

Dry milling tests have been performed on 42CrMo4 steel blocks with dimensions 100 x 50 x 50mm (L x W x H). Test runs have been diligently carried out.

Table 1. Heat Treatment Parameters

Process	Austenitizing		Quenching			Tempering	
Parameters	Time (min)	Temp ⁰ C	Medium	Time (min)	Temp ⁰ C	Time (min)	Temp ⁰ C
Reading	950	60	Oil	30-40	30	120	550

To prevent results from being contaminated Inserts were changed after machining each sample. The material was Casted, and then heated to Austenitic Temperature (1150 ~ 1200^{0}C) on a Gas Fired Furnace. Material was then Free Forged on 150kg Hammer Press and then shaped to cuboids of required sizes including machining allowance. Material was then rough machined and through hardened by was Oil Quenching and tempered to achieve hardness of 32HRC in a gas fired Furnace. Heat Treatment parameters are given in Table 1. The chemical composition tests were conducted through spectroscopy and wet analysis techniques. Observed Chemical Composition of the material is given in Table 2. For Milling, the heat treated samples were clamped on the bed of a Knee Type (Bridgeport Type) Milling Machine TSINFA WN736D with 11kW spindle drive motor 1.5kW feed motor. A just clean cut of 2mm was first performed on the outer surface to prepare the test samples for the actual test runs. Tests runs were performed on 20 samples by finish milling them according to parameters obtained by application of Central Composite Design (CCD) as given in Table 4. The tool used for the milling was 90^0 TPKN Face Mill Cutter by Teknik with diameter 125mm incorporating 6 coated carbides milling inserts TPKN 2204 PDTR-HPN TT7080 with positive rake angle and 90^0 lead angle. Material of the insert was Tungsten Carbide and the coating was MT-TiCN + Al2O3 + TiN coated through chemical vapor deposition (CVD) method. Microstructure test

Samples were prepared in the same lot with the heat treated material. The samples were grinded, polished and etched subsequently. A metallurgical microscope was used for capturing the work piece's microstructure. Figure 1 shows the microstructure of 42CrMo4 steel captured at X350 with 2% Nital Solution. Tensile Test Specimens were made on lathe machine and the tensile tests were conducted on 100Ton Tensile testing machine. Mechanical properties of the 42CrMo4 obtained after Tensile and Hardness Tests are enlisted in Table 3 below.

2.2 Design Space for Experimentation

The goal of this research is to optimize the

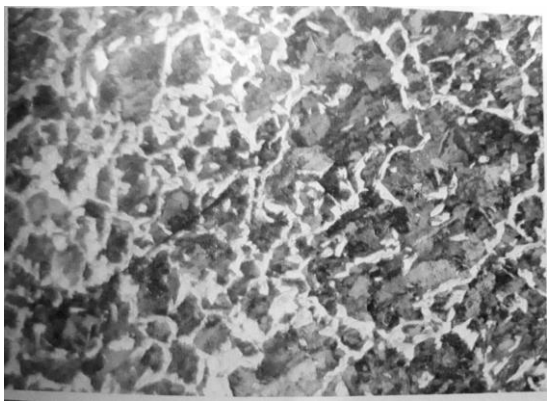

Figure 1. Microstructure of 42CrMo4 at X350

Table 3. Mechanical Properties of 42CrMo4 Forging Sample

Properties	Yield Strength (MPa)	Tensile Strength (MPa)	Elongation (%)	Reduction of Area (%)	Hardness (HRC)
Readings	672	882	16	50.09	32

Table 2. Chemical Composition of 42CrMo4

Elements	C%	Mn%	Si%	P%	S%	Ni%	Cr%	Mo%	Cu%	Al%
% Reading	0.4	0.68	0.32	0.025	0.023	0.16	0.94	0.18	0.23	0.029

milling parameters in order to get the desired R_a values. Selected design space (given in Table 4) is based on medium-finish cuts and has been reformed from the Sandvik handbook [27].
Parametric ranges are selected on the basis of shop floor machining experience, type and capacity of machine tool used, type of milling cutter, inserts and considering dry machining operation. Previous researchers have utilized comparable ranges for investigating surface roughness [20, 28, 21]. Berend Denkena et al [29] also applied cutting parameters of similar ranges during his experiments.

Table 4. Levels of the Independent Variables

Factors	Levels				
	Lowest	Low	Centre	High	Highest
Speed (*v*) (m/min)	78.115	118	176.5	235	274.8849
Feed (*f*) (mm/min)	18.7274	23.5	30.5	37.5	42.2725
DoC (mm)	0.3295	0.5	0.75	1	1.1704

3 EXPERIMENTAL DESIGN

R_a is optimized using the response surface methodology. RSM uses statistical and mathematical techniques to study the response when the components alter simultaneously. Regression analysis and experiment design were used to create the model according to Montgomery's Design and Analysis of Experiments guide [30]. The findings are modelled using the following equations to fit either a first-order or a second-order model.

$$y = \beta_o + \beta_1 x_1 + \beta_2 x_2 + \beta_k x_k + \varepsilon \quad (2)$$

$$y = \beta_o + \sum_{i=1} \beta_i x_i + \sum \beta_{ii} x_i^2 + \sum_{i<j} \sum \beta_{ij}^{x_i x_j} + \varepsilon \quad (3)$$

Where, β_o, β_i, β_{ii}, and β_{ij} are parameters of approximating functions, where y = response variable and x_i = input variable.

3.1 Central Composite Design (CCD)

CCD was the base for all experimental runs. Eight corner points which are also called factorial or cube points, six center points, and six axial points or star points are employed in each of the twenty experimental runs. Pure error is determined by adding center points. To gain a sense of the quadratic connection between the answer and the independent variables, star points are added (Figure 2).

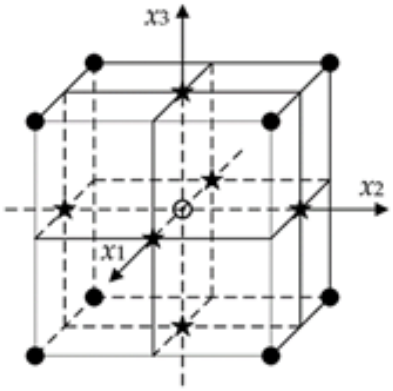

Figure 2. Central Composition Design with Three Factors

The parameters to be used for modelling are detailed here. *v*, *f*, and DoC, all three of which are coded as X1, X2, and X3. These will be used to determine R_a. Table 5 displays the design matrix together with the responses and standard deviation. 20 Experimental runs were conducted as per varying the three parameters as shown in the Table 5. Then the surface roughness readings were entered and simulated to get the results in Minitab Software.

Table 5. Design Matrix

Exp. No.	Input Variables						Output Variable
	Speed	Feed	DoC	Coding			R_a
	m/min	mm/rev	mm	X1	X2	X3	mm
1	118	23.5	0.5	-1	-1	-1	3.85
2	235	23.5	0.5	1	-1	-1	4.12
3	118	37.5	0.5	-1	1	-1	6.14
4	235	37.5	0.5	1	1	-1	5.9
5	118	23.5	1	-1	-1	1	4.194
6	235	23.5	1	1	-1	1	3.67
7	118	37.5	1	-1	1	1	3.99
8	235	37.5	1	1	1	1	3.37
9	78.11512	30.5	0.75	-1.6818	0	0	5.2
10	274.8849	30.5	0.75	1.6818	0	0	3.53
11	176.5	18.7275	0.75	0	-1.6818	0	3.72
12	176.5	42.2725	0.75	0	1.6818	0	5.37
13	176.5	30.5	0.32955	0	0	-1.6818	3.95
14	176.5	30.5	1.17045	0	0	1.6818	3.234
15	176.5	30.5	0.75	0	0	0	4.04
16	176.5	30.5	0.75	0	0	0	4.12
17	176.5	30.5	0.75	0	0	0	4.42
18	176.5	30.5	0.75	0	0	0	4.09
19	176.5	30.5	0.75	0	0	0	4.07
20	176.5	30.5	0.75	0	0	0	4.1

3.2 Mathematical Model

Twenty tests employed by CCD were used to create the mathematical model. Minitab Software has been used to code a mathematical link between surface roughness and milling parameters (*f*, *v*, and DoC). Based on Eq. (3), the Second Order model for R_a has been developed. Eq. (4) below provides the response surface equation for R_a in terms of actual parametric variables.

Response Surface/Regression Equation

$$\begin{aligned} \text{Surface Roughness } (R_a) = {} & -1.97 - 0.0051\ \text{Speed} + 0.104\ \text{Feed} \\ & + 13.44\ \text{DOC} + 0.000038\ \text{Speed*Speed} + \\ & 0.00394\ \text{Feed*Feed} - 2.31\ \text{DOC*DOC} - \\ & 0.000185\ \text{Speed*Feed} - \\ & 0.01003\ \text{Speed*DOC} - 0.3267\ \text{Feed*DOC} \end{aligned} \quad (4)$$

Analysis of Variance (ANOVA)

Table 6 displays the Analysis of Variance (ANOVA) results for the model. ANOVA analysis was implemented to the test findings at a 95% Confidence Interval in order to ascertain the impact of control variables/parameters on R_a. Minitab software was used to conduct an ANOVA analysis and the RSM. The F- and P-values in Table 6 make it clear that the feed rate is the primary and significant parameter that affects surface roughness followed by DoC and speed. Interactions among the parameters show that the interaction between feed and DoC is observed to be significant.

Table 6. ANOVA

Source	DF	Adj SS	Adj MS	F-Value	P-Value
Model	9	10.6839	1.18710	9.75	0.001
Linear	3	6.6982	2.23274	18.34	0.000
Speed	1	1.1267	1.12667	9.25	0.012
Feed	1	2.9441	2.94414	24.18	0.001
DOC	1	2.6274	2.62740	21.58	0.001
Square	3	1.1523	0.38410	3.15	0.073
Speed*Speed	1	0.2405	0.24054	1.98	0.190
Feed*Feed	1	0.5359	0.53589	4.40	0.062
DOC*DOC	1	0.2993	0.29926	2.46	0.148
2-Way Interaction	3	2.8334	0.94446	7.76	0.006
Speed*Feed	1	0.0459	0.04590	0.38	0.553
Speed*DOC	1	0.1723	0.17228	1.41	0.262
Feed*DOC	1	2.6152	2.61518	21.48	0.001
Error	10	1.2177	0.12177		
Lack-of-Fit	5	1.1199	0.22398	5.45	0.07
Pure Error	5	0.0978	0.01956		
Total	19	11.9016			

Coefficient of determination (R^2) in Model Summary (Table 7) is basically a measure of degree of fit.

Given value of R^2 in the summary table shows that 89.77 % of the total variations are explained by the model. The value of R^2 which is obtained after adjustment of the terms (size) of model is 80.56 %.

Table 7. Model Summary

S	R^2	R^2 (adj)
0.348955	89.77%	80.56%

4 RESULTS AND DISCUSSION

Graphs are obtained as a result of the experimentation and application of the RSM. The RSM and analysis of the data demonstrate the impact of the milling parameters and their interactions on the R_a. Figure 3 shows the primary effects of cutting parameters on surface roughness.

4.1 Individual Plots of R_a

Surface Roughness Vs Speed

Figure 3 (a), Slope of line on R_a versus Speed plot (left most) shows that there is a considerable decrease in values of R_a when speed (rpm) is increased from 100 rpm to 200 rpm hence surface roughness value decreases by increasing speed of the milling cutter. In other words, surface quality (or finish) improves by increasing speed. But further increasing speed over 200 rpm, the cutting speed has no effect on R_a. Hence it can be deduced that the relationship between spindle speed of the milling tool and the surface roughness is inverse to some extant i.e., from small to medium speeds, but R_a becomes constant in high spindle speeds.

Surface Roughness Vs Feed

Figure 3 (b), R_a is increased exponentially when feed rate (mm/min) is changed from 20 to 40 mm/min as evident from R_a versus Feed Plot. Hence surface quality improves by decreasing feed rate (or R_a increases by increasing feed). It may be noted from the plot that after a lowest limit of feed, its effect on surface roughness becomes minimum, but at higher feed rates, R_a increases exponentially. It is deduced from the plot that the surface becomes smooth at low feeds.

Surface Roughness Vs Depth of Cut

Figure 3 (c) explains the relationship between depth of cut (DoC) and R_a. It is evident from the graph that R_a is relatively less effected by DoC (mm) i.e., a uniform behaviour is observed when DoC is increased from 0.25 to 0.5 mm (Right most Figure 3) and then decreases by further increasing DoC. Hence, we can deduce that the DoC has a little influence on surface roughness (R_a) when it is in low values i.e., <0.7mm but its above 0.75mm it has an inverse effect on the surface roughness.

Summary

It is observed by comparing the individual graphs that the best possible condition for achieving high surface finish/surface quality (low value of R_a) is to maintain low feed, medium to high speeds and high values of depth of cuts.

4.2 Interaction Plots

Interaction Plots are shown in Figure 4. The interaction graph shows that the interaction between Feed and DoC gives a significant response. We can clearly see from the interaction plots that the combination of feed and depth of cut (DoC) has a significant response on the surface roughness. Therefore, while machining 42CrMo4, feed and DoC should be in check for the best desired response.

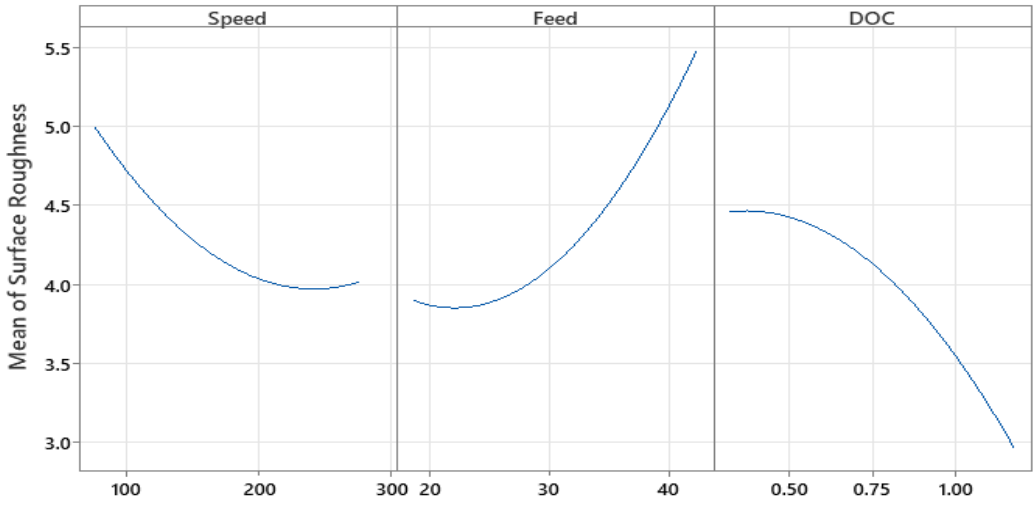

Figure 3. Main Effects Plot for Surface Roughness against (a) Speed, (b) Feed and (c) DoC

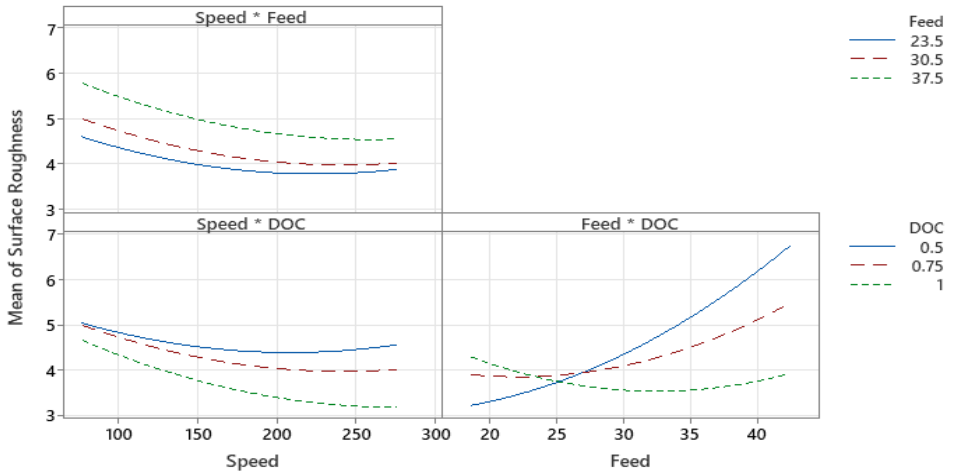

Figure 4. Interaction Plots of Parameters with R_a

4.3 Surface Plots

Three dimensional response surface plots are shown in Figure 5, 6 and 7. It is evident from the plots shown in the figures that the surfaces are curved depicting significant interactions among parameters. The following can be observed from the surface plots.

Figure 5 shows the interaction of *v* and *f* on R_a. The upward curve towards high feed and low speed shows that we get high values of R_a by applying high values of feeds and low values of cutting speeds. A similar trend was observed by Mirza Jahanzaib et al [28] while turning HSLA (4340) steel by coated carbide inserts.

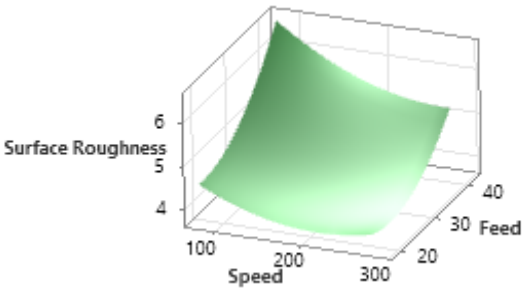

Figure 5. Interaction Plot of R_a with *v* & *f*

The interaction between DoC and speed is depicted in Figure 6. It can be seen that the surface curves downwards at high values of cutting speed whereas it goes upwards at high values of DoC. This means that R_a decreases on high values of speed but increases as DoC increases. Similar observations were made by Omar Zurita et al [32] while turning AISI-1020 steel by carbide insert tool.

The relationship between feed and depth of cut against R_a is depicted in Figure 7. It can be seen that R_a reduces on low values of feed and is unchanged by DoC to some values but increases

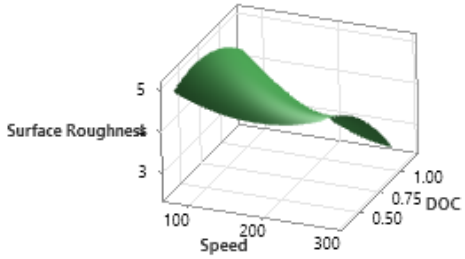

Figure 6. Interaction Plot of R_a with *v* & DoC

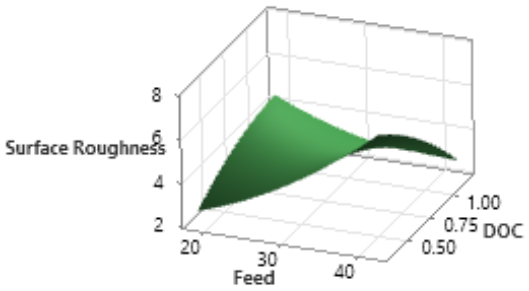

Figure 7. Interaction Plot of R_a with f & DoC

as the DoC increases. Mirza Jahanzaib et al [28] observed same trend followed by these parameters in their research for feed and unchanging DoC. But the results deviate from the mentioned research in case of high values of DoC.

4.4 Contour Plots

In order to optimize the Ra for specific ranges of speed, feed, and DoC, three-dimensional contour plots can be used. These plots show and help optimize the milling parameters versus R_a, that is essential for productivity and quality as there is a tradeoff. Depending on the design and functional requirements, the required values of surface finish on particular parts of a part or

project can vary. From contour plots, it is clear that the ideal combination of speed, feed, and depth of cut can result in a surface roughness of less than 3m. Figure 8's contour plots make it clear that a target surface roughness (R_a) value

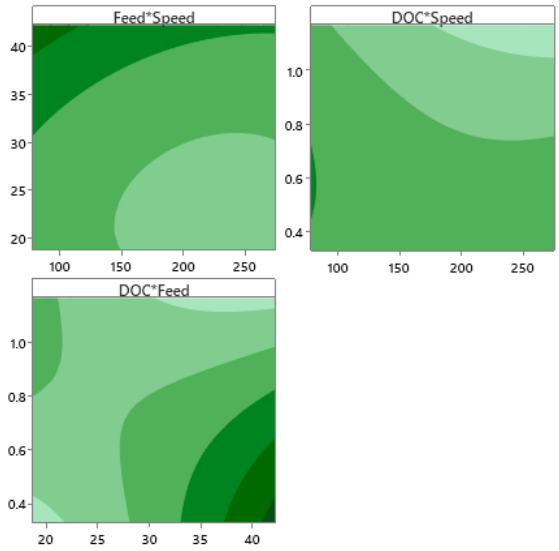

Figure 8. Contour Plots

of less than 3 mm can be reached by setting the speed between 200 and 250 rpm and the depth of cut between 0.8 and 1.2 mm; the feed, however, should be kept between 20 and 30 mm per minute.

4.5 Optimization

Optimization of the cutting parameters done on Minitab is enlisted in Table 8. It is evident from Table 8 that a target R_a value of less than 2.2531µm can be attained by maintaining the speed to 274.885 rpm, and DoC to 1.17mm; however, feed should be set to 18.7275 mm/min. The maximum speed of 250 m/min and the depth of cut of 1.2 mm must be chosen in order to meet the goal of the shortest machining time. Other combinations in the design space can also reach similar target R_a values, ensuring optimal productivity without sacrificing the needed level of surface finish. This leads to the conclusion that the ideal combination can be attained for design ranges of cutting conditions for 42CrMo4 steel.

4.6 Validation of Mathematical Models

Three further experiments were done to verify the model. These test runs are not part of the CCD data collection. These experimental runs are carried out on parameters using the model's projected values. The accuracy of the model is determined using the Table 9. Table 9 makes it evident that the experimental and projected values. are remarkably comparable. An average prediction error of 2.08% was found after the validation of data.

Table 8. Optimization

Solution	Speed	Feed	DOC	Surface Roughness Fit	Composite Desirability
1	274.885	18.7275	1.17045	2.2531	1

4.7 Productivity and Quality

Productivity have been measured on optimal parametric combination through material removal rate (MRR). The MRR has been calculated from following equation. [31]

$$MRR = \left[\frac{Wi - Wf}{\rho * t}\right] \quad (5)$$

Where Wi = Initial Weight, Wf = Final Weight ρ = density of material and t = machining time. MRR for the optimized parameters given in Table 8 was measured to be = 109503mm^3/min. where Wi = 1.9625kg, Wf = 1.9165kg and t = 5.33min.

4.8 Utilization of Results

- Appropriate combinations of cutting parameters can be identified using this model to achieve the required surface finish on widely used material like 42CrMo4 which have extensive industrial applications.
- By using this model, surface roughness (R_a) prior to practical machining can be forecasted.
- Cutting parameters can also be selected for the most efficient and swift machining of

Table 9. Validation of Results

Sr. No.	Parameters	Parameter Levels	R_a Value (Predicted)	R_a Values (Experimental)			Average R_a (Exp)	Prediction Error
				Exp -1	Exp-2	Exp-3		R_a (Pred) – Ave R_a (Exp) / R_a (Pred)
1	Feed (mm/min)	18.7275	2.2531µm	2.201	2.378	2.323	2.300	0.02081 = 2.081%
2	Speed (rpm)	274.885						
3	DoC (mm)	1.17						

these materials while maintaining the surface roughness (R_a) in a given range.

5 CONCLUSION

Following conclusions can be drawn from the results;

- After analyzing the ANOVA findings, it was established that the feed parameter had the greatest impact on R_a, followed by the depth of cut and then the interaction between feed and DoC. When the impact of cutting parameters on surface roughness was evaluated in terms of P significance value ($p<0.05$), feed and depth of cut were shown to be more important than speed.
- In the analysis-aided optimization, it was discovered that putting the speed at roughly 200–250 rpm and the depth of cut at 0.8–1.2 mm would allow for the best R_a value of less than 3 mm; the feed, however, should be set at 18–30 mm/min.
- In milling experiments, the surface roughness values rose as feed increased and fell with the decrease in speed resulting in an improved surface finish. Hence, we can conclude that the R_a is directly proportional to feed rate.
- An increase in depth of cut will not affect the R_a of 42CrMo4 to some extent but will reduce the surface roughness if DoC is further increased thereby improving the surface quality. Hence, we can conclude that DoC and R_a are also inversely proportional to some extent.
- Increasing speed also has an inverse effect on surface roughness to some extent. This effect becomes low for high values of speed.
- It can therefore be deduced that for high surface quality in the milling of free forged 42CrMo4 hardened to 32 HRC. The best possible scenario would be to keep the feeds low thereby increasing depth of cut and spindle speeds for high productivity and surface quality.
- Following the validation testing, a prediction error of 2.08% in R_a was obtained when the estimated results and experimental data were compared.

REFERENCES

[1]. Sharma VS, Dhiman S, Sehgal R, Sharma SK (2008) Estimation of cutting forces and surface roughness for hard turning using neural networks. J. Intell. Manuf. 19:473–483

[2]. Asiltürk I, Akkuş H (2011) Determining the effect of cutting parameters on surface roughness in hard turning using the Taguchi method. Measurement 44(9):1697–1704.

[3]. Boothroyd, G., and Knight, W.A. (2005), Fundamentals of machining and Machine tools (3rd ed.), Taylor and Francis Group: CRC Press.

[4]. Lalwani DI, Mehta NK, Jain PK (2008) Experimental investigations of cutting parameters influence on cutting forces and surface roughness in finish hard turning of MDN250 steel. J Mater Process Technol 206:167–179.

[5]. Neşeli, S., Yaldız, S., and Türkeş, E. (2011), "Optimization of tool geometry parameters for turning operations based on the response surface methodology", Measurement, 44(3), 580–587.

[6]. Nakhaie D, Benhangi PH, Fazeli F, et al. (2012) Controlled forging of a Nb containing microalloyed steel for automotive applications. Metall Mater Trans A 43: 5209–5217.

[7]. Di Schino A, Kenny JM, Salvatori I, et al. (2001) Modelling primary recrystrallization and grain growth in a low nickel austenitic stainless steel. J Mater Sci 36: 593–601.

[8]. Shen G, Furrer D (2000) Manufacturing of aerospace forgings. J Mat Process Tech 8: 189–195.

[9]. Schafrik RE, Walsson S (2008) Challenges for high temperature materials in the new millennium, Superalloys 2008-Proceedings of the 11th International Symposium on Superalloys, 3–9.

[10]. Di Schino A (2017) Analysis of phase transformation in high strength low alloyed steels. Metalurgija 56: 349–352.

[11]. Dindorf R, Wos P (2020) Energy-saving hot open die forging process of heavy steel forgings on an industrial hydraulic forging press. Energies 13: 1620.

[12]. Di Schino A (2021) Microstructure and mechanical properties of forged steels. Metals 11: 32.

[13]. Di Schino A (2016) Analysis of heat treatment effect on microstructural features evolution in a micro-alloyed martensitic steel. Acta Metall Slovaca 22: 266–270.

[14]. Mancini S, Langellotto L, Di Nunzio PE, et al. (2020) Defect reduction and quality optimization by modelling plastic deformation and metallurgical evolution in ferritic stainless steels. Metals 10: 186.

[15]. Beauchamp, Y., Thomas, M., Youssef, A., and Jacques, Masounave. (1996) "Investigation of cutting parameter effects on surface roughness in lathe boring operation by use of a full factorial design." Computers and Industrial Engineering, Vol. 31, No.3-4, pp.645-651.

[16]. Sahoo AK, Sahoo B (2012) Experimental investigations on machinability aspects in finish hard turning of AISI 4340 steel using uncoated and multilayer coated carbide inserts. Measurement 45:2153– 2165

[17]. Sujan Debnath, Moola Mohan Reddy, Qua Sok Yi (2015), "Influence of cutting fluid conditions and cutting parameters on surface roughness and tool wear in turning process using Taguchi method" https://doi.org/10.1016/j.measurement.2015.09.011, Measurement Volume 78, January 2016, Pages 111-119

[18]. Xavior MA, Adithan M (2009) Determining the influence of cutting fluids on tool wear and surface roughness during

[19]. Bhuvnesh Bhardwaj, Rajesh Kumar, Pradeep K Singh 2013, September. Surface roughness (R_a) prediction model for turning of AISI 1019 steel using response surface methodology and Box–Cox transformation, Journal of Engineering Manufacture, Volume: 228 issue: 2, pp. 223–232

[20]. Chinchanikar S, Choudhury SK (2013) Effect of work material hardness and cutting parameters on performance of coated carbide tool when turning hardened steel: an optimization approach. Measurement 46(4):1572–1584.

[21]. Lima JG, Avila RF, Abrao AM, Faustino M, Davim JP (2005) Hard turning: AISI 4340 high strength low alloy steel and AISI D2 coldwork tool steel. Mater Proc Technol. 169:388–395.

[22]. Suresh R, Basavarajappa S, Gaitonde VN, Samuel GL (2012) Machinability investigations on hardened AISI 4340 steel using coated carbide insert. Int. J Refract Met Hard Mater33:75–86]

[23]. Sahoo AK, Sahoo B (2013) Performance studies of multilayer hard surface coatings (TiN/TiCN/Al2O3/TiN) of indexable carbide inserts in hard machining: part-I (an experimental approach). Measurement 46(8):2854–2867

[24]. Nalbant M, Gokkaya H, Toktas I, Sur G (2009) The experimental investigation of the effects of uncoated, PVD- and CVD-coated cemented carbide inserts and cutting parameters on surface roughness in CNC turning and its prediction using artificial neural networks. Robot Comp.Int.Manuf. 25:211–223.

[25]. L. L. Costa, A. M. G Brito, A. Rosiak, L. Schaeffer (2020), Microstructure evolution of 42CrMo4 during hot forging process of hollow shafts for wind turbines, The International Journal of Advanced Manufacturing Technology 106:511–517

[26]. Çalık, O. Dokuzlar, N. Uçar b (January 2020), The effect of heat treatment on mechanical properties of 42CrMo4 steel, Journal of Achievements in Materials and Manufacturing Engineering Volume 98, Issue 1.

[27]. Sandvik Coromant (Firm). (2010), Metal cutting technologyTechnical guide, Sandvik, Coromant, Sweden.

[28]. Muhammad Azam & Mirza Jahanzaib & Ahmad Wasim & Salman Hussain 2014, December. Surface roughness modeling using RSM for HSLA steel by coated carbide tools. The International Journal of Advanced Manufacturing

Technology, DOI 10.1007/s00170-014-6707-5.

[29]. Berend Denkena, Jens Koehler, Michael Rehe (2012) Influence of the Honed Cutting Edge on Tool Wear and SurfaceIntegrity in Slot Milling of 42CrMo4 Steel. 5th CIRP Conference on High Performance Cutting 2012

[30]. Montgomery, D.C. (2004), Design and analysis of experiments (5th Ed.), New York: John Wiley & Sons

[31]. Hassan Javid, Mirza Jahanzaib Muhammad Jawad, Muhammad, Asad Ali, Muhammad Umar Farooq, Catalin I. Pruncu & Salman Hussain (2021) Parametric analysis of turning HSLA steel under minimum quantity lubrication (MQL) and nanofluids-based minimum quantity lubrication (NF-MQL): a concept of one-step sustainable machining. The International Journal of Advanced Manuf. Technology https://doi.org/10.1007/s00170-021-07776-y.

[32]. Omar Zurita, Verónica Di-Graci, María Capace (2017), Effect of cutting parameters on surface roughness in turning of annealed AISI-1020 steel, Revista Facultad de Ingeniería (Rev. Fac. Ing.) Vol. 27 (47), pp. 111-118.

SIMULATION-BASED MODAL ANALYSIS OF CRACKED CANTILEVER BEAM

Ahmad Naveed[1,*], Muhammad Usman[1], Muhammad Bu Ali[1], Muhammad Haseeb[1], Zain Abbas Tahir[1], Ali Husnain Ahmad Tabassum[1], Haseeb Arshad[1]
[1]University of Engineering & Technology, Lahore, Pakistan

Corresponding Author. *E-mail address*: ahmadnaveed@uet.edu.pk (Ahmad Naveed)

ABSTRACT

Any structure with a crack is likely to crumble based on the type of vibration. The resonance created by the natural frequency leads to the failure of the structure. In this modal analysis study, twenty-seven models of a cracked cantilever beam with the crack parameters; crack location, depth, and height have been created on SolidWorks, and its simulations have been done to study its natural frequency over six modes. An uncracked beam has also been compared to analyze the study. As the cross-section area of the beam is square, the frequency of the two modes is similar because it has symmetry. And is clear from the study that the beam's natural frequency reduces due to the presence of the crack. A statistical analysis has been performed on Minitab software to analyze which parameter affects the most of the natural frequency of cracked cantilever beam.

Keywords: Modal analysis, Natural frequency; Vibration; Cracked beam

1 INTRODUCTION

Modal analysis is a method to depict a structure in terms of its natural characteristics: frequency, damping, and mode shapes. The modal analysis yields different frequencies of vibration for several mode shapes. For a cracked structure, modal analysis is vital as a crack creates discontinuities in a structure. Discontinuities in a structure cause unique physical characteristics regarding the failure of specific structures. A crack in the structural member presents local flexibility that influences the vibration response. The modal analysis includes the process of determining the modal parameters of a structure to showcase its response. Any change in the physical properties of the model due to damage is directly proportional to changes in the model parameters. Recently, vibration-based structural damage identification has gained much interest in engineering research. [1]

Cantilevers are considered one of the important components in engineering applications. Examples of these applications are the cantilevers used in mechanical and aerospace models such as fixed-wing aircraft, helicopter fan blades, and solar arrays. Moreover, civil construction engineering uses these structures in cantilever bridges and balconies. Machinery and construction structures should be more flexible and capable of withstanding high-stress levels. Hence, the best cantilever beam designs are based on optimizing multi-objectives: maximum strength and long lifespan coupled with minimum weight and cost-effectiveness. Several non-destructive techniques are available to detect faults and defects in a structure. Their use and reliability consequently became essential factors in evaluating the investigated structure's safety. Many engineers and scientists have devoted their time and efforts to developing new, more reliable, efficient, and less tedious detection techniques. These beams might have internal voids and unevenly dispersed material surfaces shaped as a structural defect prompt failure. A significant factor in evaluating the safety of the examined structure is its utilization and reliability. [2]

A crack is an advanced formed fracture failure mode when a component or machine part is subjected to extreme load. Cracks are present in structures due to various reasons. [3] The presence of a crack could cause a local variation in the stiffness and affect the mechanical behavior of the entire structure to a considerable extent. Cracks present in vibrating or rotating components could lead to catastrophic failure. For these reasons, there is a need to understand the dynamics of cracked structures. The modal analysis yields natural frequencies, and mode shapes of cracked beams can provide insight into the extent of the damage. [4] If a crack appears in the structure, it will cause failure. It also affects the natural frequency of the structure. Changes in vibrational parameters are required to be analyzed to identify the crack. The location and depth of the crack are essential parameters to change the vibrational parameters of the structure. [5]

In this study, the natural frequencies of a cracked beam have been investigated. During the study, the natural frequency of both uncracked and cracked cantilever beams was observed. For cracked cantilever beams, three criteria, such as different sizes of crack openings, different crack locations, and different crack depths, have been considered to visualize the importance of natural frequency at different modes. In the end, different cases have been compared, and the deductive decision has been provided using both dimensional and non-dimensional data compilation.

2 LITERATURE REVIEW

Engineering structures must operate under high-loading conditions, which may lead to catastrophic failures or cracks in overstressed zones. The presence of cracks in a structural member, such as a beam, causes local variations in stiffness, the magnitude of which mainly depends on the location and depth of the cracks. In the past, there have been considerable attempts to understand the dynamics of a cracked beam.

Banerjee, J.R. and S. Guo [6] Investigated the dynamic behavior of a cracked beam by using the dynamic stiffness method through the application of compliance properties of the crack. The cracked beam is essentially idealized by connecting two Bernoulli-Euler beams at the crack location, which leads to a non-linear eigenvalue problem for which the Wittrick-Williams algorithm is used as a solution technique to yield natural frequencies and mode shapes of the cracked beam. Agarwalla, D. and D. Parhi explored that the rigid structures in our environment develop irregularities and inconsistency after some time. These inconsistencies lead to the development of cracks.[7]. Elshamy, M., W. Crosby, and M. Elhadary analyze a transverse crack introduced in a cantilever beam that will introduce more flexibility and elasticity in the cantilever beams. The system stiffness is also affected. As a result, the natural frequency is decreased. [8]. Ostachowicz, W. and M. Krawczuk find out that variation in the system stiffness also affects the dynamics properties of the structure up to a significant extent.[9] Hong-Ping, Z., H. Bo, and C. Xiao-qiang studied that any discontinuities and irregularities in a structure can affect the natural frequency of the structure as it is sensitive to disruption in the structure.[10] Ahiwale D concluded that the crack could be detected in the Cantilever beam by observing the natural frequency and modes as they vary directly to crack depth and location.[11] .Cawley, P. and R.D. Adams observed that the difference in natural frequency of any structure offers possibilities of locating the damage done to the structure and also the extent of the damage. [12] Anifantis, N., N. Aspragathos, and A. Dimarogonas put forward a way to detect cracks in structures after an earthquake by observing the vibrations of the structure.[13] Shifrin, E. and R. Ruotolo evaluated the natural frequency of the crack beam. Cracks were considered massless

springs, and a continuous mathematics model of the beam was used.[14]. Shan, Q. and R. Dewhurst invested their time in the detection of cracks and other surface irregularities by employing ultrasonic rays.[15]. Arundas, P. and U. Dewangan Devaloped a non destructive model using Ultrasonic rays. They find that the distance between the crack and the fixed end increases, increasing the ultrasonic pulse velocity.[16] Through Hamilton's principle, Behzad, M., A. Meghdari, A. Ebrahimi develops equations of motions and co-related boundary equations of open edge Euler-Bernoulli beams.[17]. Parhi, D.R. and S. Choudhury researched in smart crack detection methodologies. They find the location of crack using fuzzy controller and genectic controller.[18] . Chang, C.-C. and L.-W. Chen predicted the crack depth and location on a beams based on the spatial wavelet analysis. [19] .Qian, G.-L., S.-N. Gu, and J.-S. Jiang proposed a crack detection method by observing the diffrence in displacement of crack and uncracked cantilever beams in finite element analysis.[20]. Rizos, P., N. Aspragathos, and A. Dimarogonas identified the location of the crack up to some accuracy, analytically and non-destructively. They observed the frequency and amplitude of a crack cantilever beam.[21]. Owolabi, G., A. Swamidas, and R. Seshadri observed the change in the frequency and amplitude of vibrations of the supported and fixed beams due to introductions of crack in the stuctures. [22]. Kisa, M. and M.A. Gurel calculated the natural frequency and mode shapes of a cicular cantilever beam, multiple cracks were introduced in the surface. They found a correlation between the beam location and depth with the frequency and modes. [23] . Chaudhari, J. and C. Patil find out the frequency of crack and un crack Cantilever beams by employing Euller's equations. They Simulated the Modal in Ansys and observed negligible differences between the two calculations. [24]. Chaphalkar, S., S.N. Khetre, and A.M. Meshram studied the vibration analysis of the fixed beam using the FEA(finate Element Analysis) using ANSYS program. They came to an outcome that FEA values using ANSYS is in tuned with analytical values.[25]. Jassim, Z. performed analytical, experimental, and theoretical modal analyses on cantilever beams led to the conclusion that the Damage Magnitude Index (DMI) must be based on frequency and mode shape (MAC), and that the damage localization can be determined by using mode shape (COMAC) and Curvature Change Index (CCI).[2] . Mekalke, G.C. and A. Sutar performed modal analysis on cantilever beams made up of different metals, They observed the frequency response change with material. They also cocluded that error between calcultion perforn on ANSYS program and analytically, icreases with the frequency. [26]. Barad, K.H., D. Sharma, and V. Vyas observed that the depth ratio of crack also defines the significant of it's effect on the natural beam. Crack with larger depth ratio cause more reduction in frequency than the crack with smaller depth ratio. They also observed the effect of distance of crack and the fixed end of beam on natural frequency.[27]. Talekar, N. and M. Kotambkarobserved the modal analysis of Cantilever beams made up of composite materials with diffrenet length to thickness ratio.[28]. Lee, H.-H, Szabó, B. and I. Babuška provided an effective guide to perform modal analysis.[29, 30].

3 METHODOLOGY

When a structure starts to vibrate at its natural frequency, it can behave unpredictably. That's why it is recommended to have the natural frequency of the structure or machine way higher than its working frequency. Continuous vibrations can sometimes cause crack formation in the structures, or creep can cause these. The problem starts there because when a crack is formed in the structure, this will cause the structure to have a low natural frequency than that of its original one.

This study observed modal analysis of a simple "Cantilever Beam" structure (without cracks and with cracks) and calculated its natural frequency. First, the cantilever beam was modeled in SolidWorks, visible in Fig.1 The model's dimensions are given in the following table 1. Then SLDPRT file of the SolidWorks is converted into the .step file, as it's the standard format to be used with the Ansys analysis software.

For the uncracked beam study, first, convert the SLDPRT file into the step file to import it into the ANSYS 2022 R1 for the simulation. The module is named "Modal" in the ANSYS Workbench. Structural steel has been used for the cantilever beam. The mesh size selected for this study is 7 mm for simulation visible in Fig.2 fixed one end of the cantilever beam, known as the "Fixed Support" in the ANSYS. Then, after doing all these steps, in the solution section, find the total deformation six times and change the number of mode selections to 1 for the first deformation and mode 2 for the second deformation, and up to so on for all the six total deformation results. In this result section, the frequencies have been obtained to analyze it for our study.

Table 1 Dimensions of Cantilever Beam

Parameter	Value (mm)
Length	1000
Height	50
Thickness	50

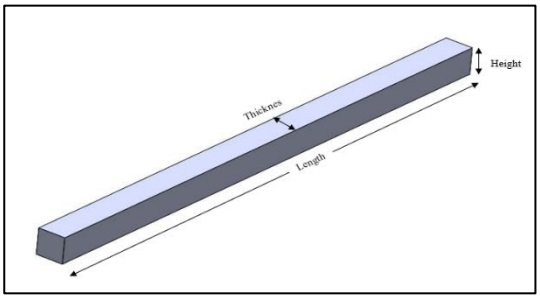

Figure 1. Length, Thickness, Height of cantilever beam

After getting a reference point for our modes using the uncracked beam, a crack was introduced in the beam. Three different parameters for the cracks are incorporated, i.e., crack opening, depth, and its position on the beam. For the position, there were three positions in the study, i.e., tip, mid, and the root, which are depicted in Fig.3. Now this study has further continued to see the effect of a given parameter on natural frequency keeping all other parameters constant, i.e., the effect of crack depth keeping crack opening and its position constant, the impact of crack opening keeping crack depth and position constant then the effect of crack position keeping crack opening and depth constant.

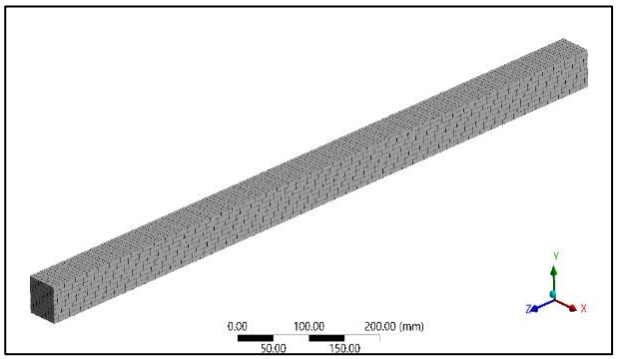

Figure 2. Mesh size is 7 mm

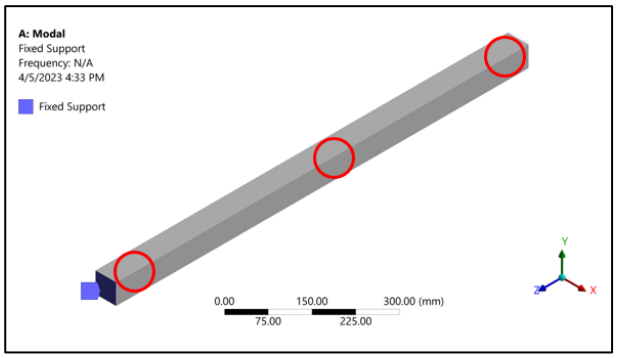

Figure 3. From left to right root, mid and tip

As given in Table 2, three different levels of these parameters were used, so a total of 27 combinations of these parameters were made having dimensions as stated in Table 3. Modeled all these combinations and, after simulating, analyzed the results of these models to investigate their combined behavior in Minitab statistical software.

4 RESULTS AND DISCUSSION

Table 2. Crack Variable of cantilever beam

Crack Variables		
Position	**Crack Opening (degrees)**	**Depth (mm)**
Root	20	10
Mid	40	20
Tip	60	30

First of all, for the reference values, the modal analysis was performed for an uncracked beam, and the results for all modes as shown in the following Table 4 to compare it with all the modes of the possible combinations of a cracked beam.

After the simulation of the uncracked beam for reference. Checked the effect of one parameter on the natural frequencies by keeping the remaining two parameters constant. The

Table 4. Uncracked beam's modal

Uncracked Cantilever Beam	
Mode	Frequency (Hz)
1	40.785
2	40.785
3	252.67
4	252.67
5	695.01
6	695.01

results are provided in the Table 5, where there are three different sections, name of each section is giving the other constant. This is done to see the individual effect of parameters. Created 27 CAD models using the Dimensions provided in the Table 3. Then those 27 models were simulated to get the results for the mode frequencies, this is done to see the combine effect of the parameters. For each model, result

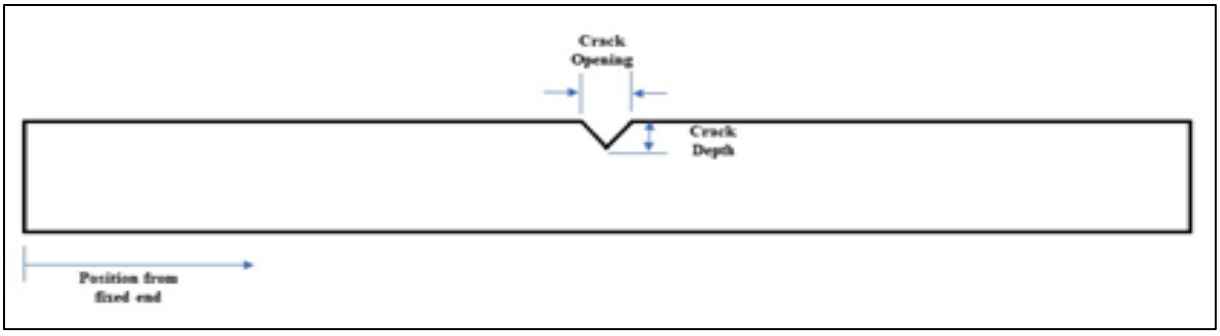

Figure 4. Cracked cantilever beam

Table 3. Multi level factorial design

Combinations	Position	Opening (degrees)	Depth (mm)	Combinations	Position	Opening (degrees)	Depth (mm)	Combinations	Position	Opening (degrees)	Depth (mm)
1	990	20	10	10	500	60	10	19	990	40	30
2	10	60	20	11	500	20	20	20	500	40	30
3	500	40	10	12	500	20	30	21	990	60	30
4	500	60	20	13	10	60	10	22	10	20	20
5	990	20	20	14	500	20	10	23	10	20	10
6	10	60	30	15	990	40	20	24	990	20	30
7	990	40	10	16	500	40	20	25	500	60	30
8	990	60	20	17	10	40	10	26	10	20	30
9	990	60	10	18	10	40	20	27	10	40	30

of 6 model frequencies were extracted. Table 5 provides the detail results for each combination by three different categories. Fig.5 provides the visual depiction of all 6 frequency modes for combination 6.

From graphs in Fig.7 were generated from the mode frequencies' results from all 27 combinations. From the graphs, it has been concluded that the minimum natural frequency has been achieved by combination no. 6 having the values of crack variables; crack position is at root, crack opening of 60° and crack depth of 30 mm. Irrespective of the mode number, getting the same trend in all modes, i.e., if a particular mode of specific combination is at certain level w.r.t other combination it will be same for different modes of same combination just having one exception of mode 3 of combination 6.

As, there is software that is used named "Minitab" which is basically a leading statistical software which helps to explore the statistical concepts and spend less time to doing the tedious calculations. However, with the improvements it is not only used in the advanced courses also it is the leading software which is used in the world for the improvement of quality.

From the Fig. 6 which is generated using Minitab, and from it, this is visible that for a given Depth, changing the position from root to tip at a given depth changes the mode value in inverse relation. It means that as we go towards the root, it affects the mode maximum, and its value is minimum at a given depth, e.g., 30 mm. This trend is followed. Increasing the opening angle from 20 to 40 degrees gives a mixed result depending upon the crack depth.

Table 5. Effect of changing one crack parameter

Variable Position

Crack Variables			Frequency (Hz)					
Position	**Crack Opening (°)**	**Crack Depth (mm)**	**Mode 1**	**Mode 2**	**Mode 3**	**Mode 4**	**Mode 5**	**Mode 6**
10	20	10	39.643	40.417	246.43	250.66	679.91	690.13
990	20	10	40.814	40.814	252.83	252.84	695.43	695.44
500	20	10	40.614	40.731	248.21	251.23	694.9	695
Variable Crack Opening								
Position	**Crack Opening (°)**	**Crack Depth (mm)**	**Mode 1**	**Mode 2**	**Mode 3**	**Mode 4**	**Mode 5**	**Mode 6**
500	60	10	40.629	40.74	248.6	251.48	694.88	695.01
500	40	10	40.65	40.736	248.49	251.37	694.89	695.01
500	20	10	40.614	140.731	248.21	251.23	694.9	695
Variable Crack Depth								
Position	**Crack Opening (°)**	**Crack Depth (mm)**	**Mode 1**	**Mode 2**	**Mode 3**	**Mode 4**	**Mode 5**	**Mode 6**
500	20	30	38.238	40.278	205.07	240.45	689.8	694.14
500	20	20	40.005	40.579	234.26	247.41	694.2	694.8
500	20	10	40.614	40.731	248.21	251.23	694.9	695

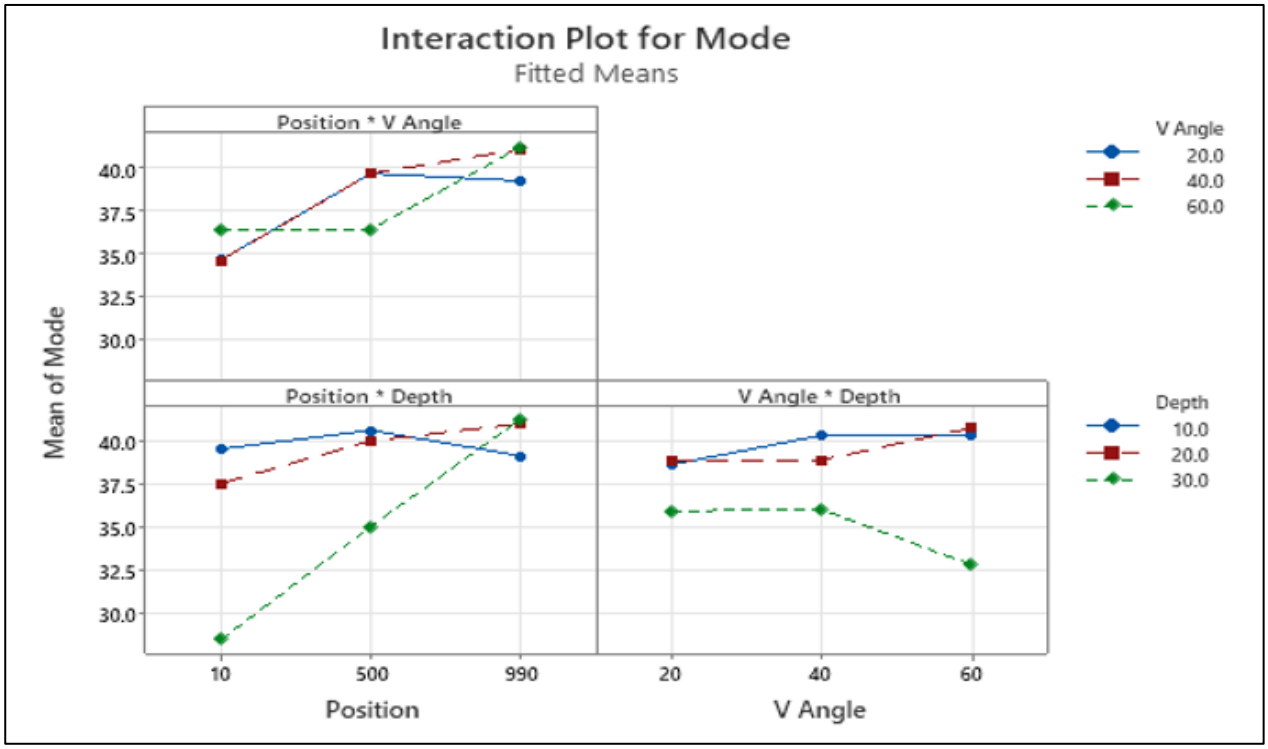

Figure 6. Interaction plots for mode

When the crack depth is minimal, the effect shows that frequency is higher at a higher angle, and frequency is lower at a higher angle when the crack depth is more elevated. This is because at minimum crack depth, increasing the opening angle creates a relatively flat small surface like that of an indent, which does not affect a crack. On to this, when depth is higher, having a wider opening will create a big crack and affect the mode frequency, so it becomes much lower than others at low crack depths. Changing the position from root to tip for a given opening angle increases mode frequency from root to tip, and depth 40 has the minimum mode frequency.

The Fig.8 showing mean effect plots, it is visible that the position has a maximum effect on the mode frequency compared to other factors. But crack depth is catching upon it with a minimum margin. So, if higher crack depth values are used, it can have more effect than position on the mode frequency. On the other hand, the crack opening has the minimum impact according to the given plot. This may be because its effect is somewhat balanced by the depth, as mentioned earlier.

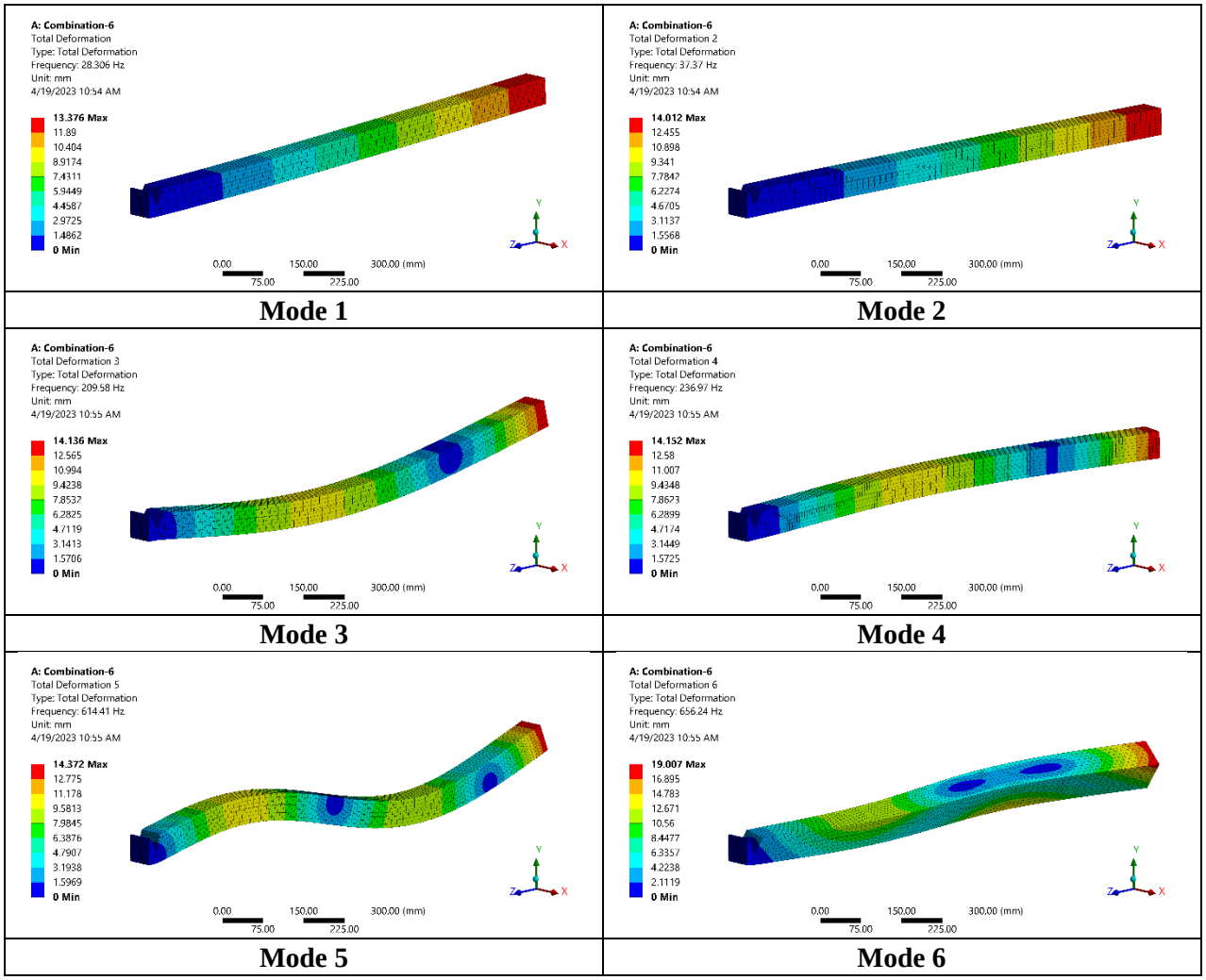

Figure 5. Result of 6 modes of modal frequencies

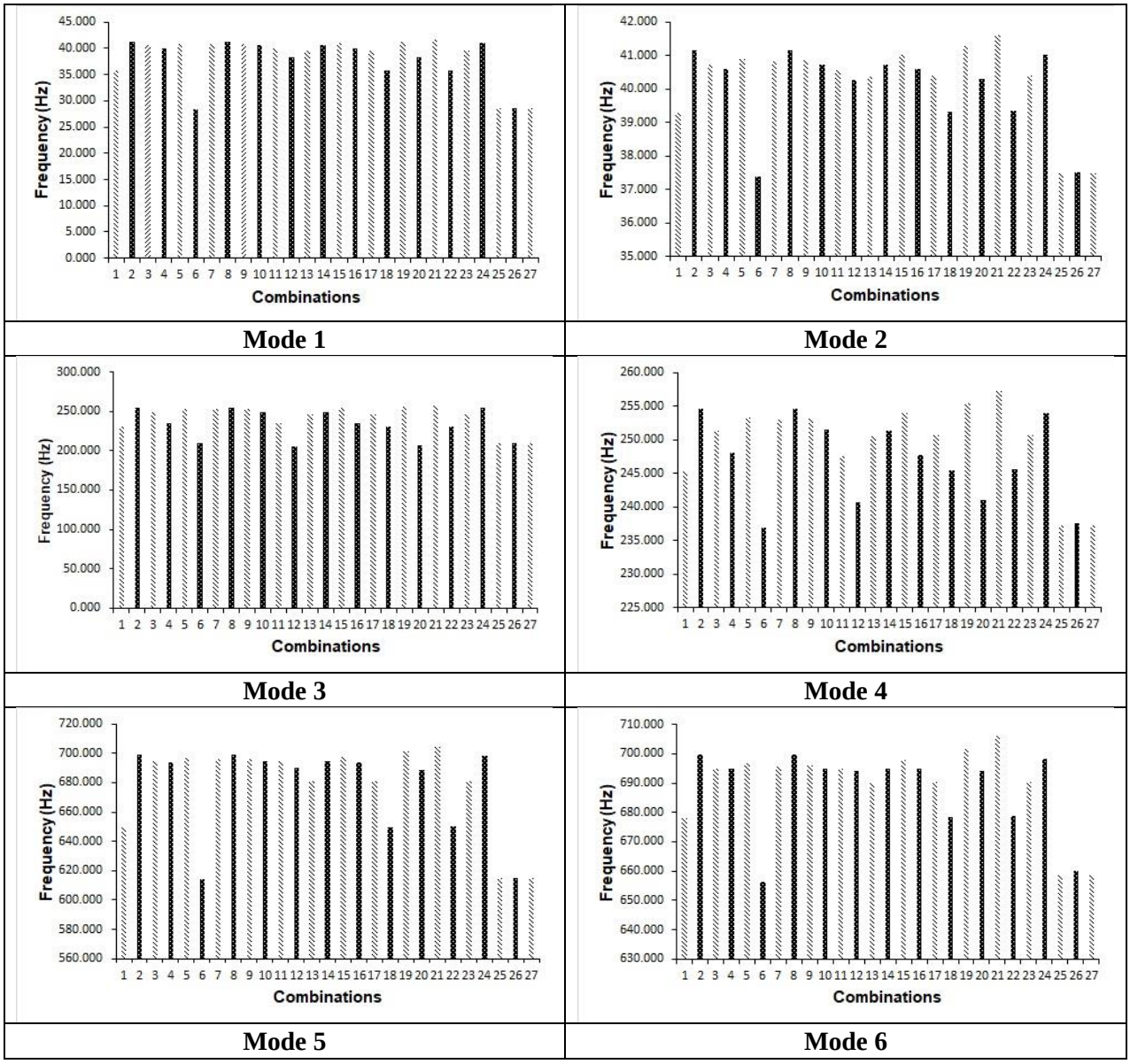

Figure 7. Modal frequencies of all 27 combinations

Table 6. Effect of Correlation

	Position	V Angle	Depth	Mode 1	Mode 2	Mode 3	Mode 4	Mode 5
V Angle	0.000							
Depth	0.000	0.000						
Mode 1	0.501	0.014	-0.457					
Mode 2	0.538	0.045	-0.367	0.993				
Mode 3	0.465	0.143	-0.524	0.809	0.805			
Mode 4	0.524	0.135	-0.445	0.892	0.901	0.978		
Mode 5	0.533	0.043	-0.346	0.982	0.987	0.740	0.842	
Mode 6	0.540	0.033	-0.318	0.985	0.996	0.752	0.862	0.992

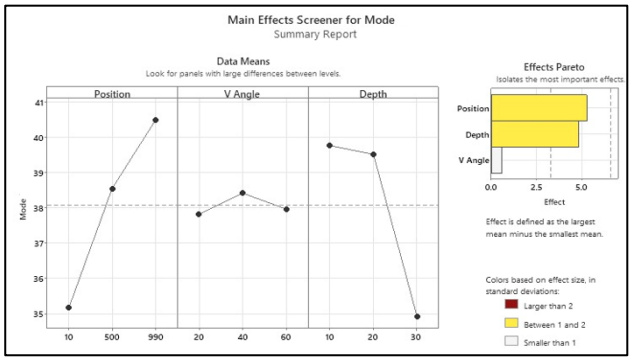

Figure 8. Main effect for the modes

5 CONCLUSIONS

All the factors studied affect the mode frequency, but their effect level is different. The position's effect is like that, at the tip, it has a minimum effect, and the mode frequency is as close as to the mode frequency of the uncracked beam, but when the crack is near the root, it highly affects the mode frequency and minimum value of mode frequency is obtained as compared to the uncracked beam.

For crack depth, increasing the depth decreases the mode frequency; an inverse relationship between two higher crack depths with large openings has maximum effect.

The effect of the crack opening is countered by the depth (like sometimes combination can go toward flatness), which reduces its overall correlation with the mode frequency, but when the conditions are favorable, it can be effective.

REFERENCES

[1]. Z. Zhou, "Vibration-based damage detection of simple bridge superstructures," 2006.

[2]. Z. Jassim, N. Ali, F. Mustapha, and N. A. Jalil, "A review on the vibration analysis for a damage occurrence of a cantilever beam," *Engineering Failure Analysis,* vol. 31, pp. 442-461, 2013.

[3]. M. K. Kumar, M. A. Pasha, M. A. Khan, and C. N. Nagaraju, "Modal Analysis of a Cracked Cantilever Beam Using ANSYS Workbench," *International Journal of Prevention and Control of Industrial Pollution,* vol. 4, no. 1, pp. 24-30, 2018.

[4]. M. Chati, R. Rand, and S. Mukherjee, "Modal analysis of a cracked beam," *Journal of sound and vibration,* vol. 207, no. 2, pp. 249-270, 1997.

[5]. C. Ramachandran and R. Ponnudurai, "Modal analysis of beam with varying crack depth," *International Journal of Engineering Research and Technololgy,* pp. 452-458, 2017.

[6]. J. R. Banerjee and S. Guo, "On the dynamics of cracked beams," in *50th AIAA/ASME/ASCE/AHS/ASC Structures, Structural Dynamics, and Materials Conference 17th AIAA/ASME/AHS Adaptive Structures Conference 11th AIAA No*, 2009, p. 2429.

[7]. D. Agarwalla and D. Parhi, "Effect of crack on modal parameters of a cantilever beam subjected to vibration," *Procedia Engineering,* vol. 51, pp. 665-669, 2013.

[8]. M. Elshamy, W. Crosby, and M. Elhadary, "Crack detection of a cantilever beam by natural frequency tracking using experimental and finite element analysis," *Alexandria engineering journal,* vol. 57, no. 4, pp. 3755-3766, 2018.

[9]. W. Ostachowicz and M. Krawczuk, "Analysis of the effect of cracks on the natural frequencies of a cantilever beam," *Journal of sound and vibration,* vol. 150, no. 2, pp. 191-201, 1991.

[10]. Z. Hong-Ping, H. Bo, and C. Xiao-qiang, "Detection of structural damage through changes in frequency," *Wuhan University Journal of Natural Sciences,* vol. 10, no. 6, pp. 1069-1073, 2005.

[11]. D. Ahiwale, H. Madake, N. Phadtare, A. Jarande, and D. Jambhale, "Modal analysis of cracked cantilever beam using ANSYS software," *Materials Today: Proceedings,* vol. 56, pp. 165-170, 2022.

[12]. P. Cawley and R. D. Adams, "The location of defects in structures from measurements of natural frequencies," *The Journal of Strain Analysis for Engineering Design,* vol. 14, no. 2, pp. 49-57, 1979.

[13]. N. Anifantis, N. Aspragathos, and A. Dimarogonas, "Diagnosis of cracks on concrete frames due to earthquakes by vibration response analysis," in *Moscow: Third International Symposium of the International Measurements Federation (IMEKO)*, 1983.

[14]. E. Shifrin and R. Ruotolo, "Natural frequencies of a beam with an arbitrary number of cracks," *Journal of Sound and vibration,* vol. 222, no. 3, pp. 409-423, 1999.

[15]. Q. Shan and R. Dewhurst, "Surface breaking fatigue crack detection using laser ultrasound," *Applied physics letters,* vol. 62, no. 21, pp. 2649-2651, 1993.

[16]. P. Arundas and U. Dewangan, "Prediction of crack locations using non destructive tests," *Indian Journal of Science and Technology,* vol. 9, no. 34, pp. 1-6, 2016.

[17]. M. Behzad, A. Meghdari, and A. Ebrahimi, "A new approach for vibration analysis of a cracked beam," 2005.

[18]. D. R. Parhi and S. Choudhury, "Analysis of smart crack detection methodologies in various structures," *Journal of Engineering and Technology Research,* vol. 3, no. 5, pp. 139-147, 2011.

[19]. C.-C. Chang and L.-W. Chen, "Detection of the location and size of cracks in the multiple cracked beam by spatial wavelet based approach," *Mechanical Systems and Signal Processing,* vol. 19, no. 1, pp. 139-155, 2005.

[20]. G.-L. Qian, S.-N. Gu, and J.-S. Jiang, "The dynamic behaviour and crack detection of a beam with a crack," *Journal of sound and vibration,* vol. 138, no. 2, pp. 233-243, 1990.

[21]. P. Rizos, N. Aspragathos, and A. Dimarogonas, "Identification of crack location and magnitude in a cantilever beam from the vibration modes," *Journal of sound and vibration,* vol. 138, no. 3, pp. 381-388, 1990.

[22]. G. Owolabi, A. Swamidas, and R. Seshadri, "Crack detection in beams using changes in frequencies and amplitudes of frequency response functions," *Journal of sound and vibration,* vol. 265, no. 1, pp. 1-22, 2003.

[23]. M. Kisa and M. A. Gurel, "Modal analysis of multi-cracked beams with circular cross section," *Engineering Fracture Mechanics,* vol. 73, no. 8, pp. 963-977, 2006.

[24]. J. Chaudhari and C. Patil, "Study of static and modal analysis of un-crack and crack cantilever beam using FEA," *International Journal of Engineering Research,* vol. 5, no. 4, 2016.

[25]. S. Chaphalkar, S. N. Khetre, and A. M. Meshram, "Modal analysis of cantilever beam structure using finite element analysis and experimental analysis," *American journal of engineering research,* vol. 4, no. 10, pp. 178-185, 2015.

[26]. G. C. Mekalke and A. Sutar, "Modal analysis of cantilever beam for various cases and its analytical and fea analysis," *International journal of engineering technology, management and applied sciences,* vol. 4, no. 2, pp. 60-66, 2016.

[27]. K. H. Barad, D. Sharma, and V. Vyas, "Crack detection in cantilever beam by frequency based method," *procedia engineering,* vol. 51, pp. 770-775, 2013.

[28]. N. Talekar and M. Kotambkar, "Modal analysis of four layered composite cantilever beam with lay-up sequence and length-to-thickness ratio," *Materials Today: Proceedings,* vol. 21, pp. 1176-1194, 2020.

[29]. H.-H. Lee, *Finite Element Simulations with ANSYS Workbench 2022: Theory, Applications, Case Studies*. SDC publications, 2022.

[30]. B. Szabó and I. Babuška, "Finite Element Analysis: Method, Verification and Validation," 2021.

DESIGN, FABRICATION AND STUDY OF REINFORCED ARC WELD JOINTS

Muhammad Saad Suleman[1,*], Murtaza Mehdi[1], Shahzaib Nazim[1]
[1]Mechanical Engineering Department, NED University of Engineering & Technology, Karachi, Pakistan

[*]Corresponding author. Tel.: +92-349-7012337;
E-mail address: saad.16032000@gmail.com (Muhammad Saad Suleman)

ABSTRACT

This study investigates the effects of using smooth and knurled high-carbon spring steel pins (ASTM A228) as reinforcement in arc welding of ASTM A36 structural steel. The purpose of this study is to compare the mechanical properties of welded samples with and without reinforcement, and to determine the effect of surface roughness of the reinforcement pins. Three sets of samples were prepared: solid metal, welded metal without reinforcement, and welded metal with reinforcement pins. Tensile tests were performed on each set of samples using ASTM E8 standard test methods. The results showed that the use of reinforcement pins significantly improved the mechanical properties of the welded joints, and the knurled pins provided better reinforcement than smooth pins. The increase in surface roughness of the reinforcement pins resulted in improved mechanical properties of the welded joints. These findings suggest that high-carbon spring steel pins with surface roughness can be a promising reinforcement material for arc welding of structural steel.

Keywords: Arc Welding; Reinforcement; Spring steel pins

1 INTRODUCTION

Welding is a widely used process in industry for joining two or more metal pieces. The use of welding has increased significantly over the years due to the benefits it provides, including improved strength and durability of the joint [1,2]. In recent years, research has been focused on developing new welding techniques and materials that can provide better results in terms of strength and quality of the joint.

Studies like the one presented in this conference paper play an important role in advancing the field of welding. The results of this study indicate that high-carbon spring steel pins(ASTM A228) with surface roughness can significantly improve the mechanical properties of the welded joints. This finding can have practical implications for industries that use welding for joining structural steel. By incorporating such reinforcement materials, they can improve the strength and durability of the welded joints, leading to better and safer products. Arc welding is one of the most commonly used welding techniques [3], where an electric arc is used to melt and fuse the metal pieces together. In this process, a shielding gas is used to protect the weld pool from atmospheric contamination [4]. Argon gas is a commonly used shielding gas in arc welding because of its non-reactive nature and ability to produce a stable arc [5].

The quality and strength of welded joints are critical in many applications. The use of reinforcement in welding can improve the strength and durability of welded joints. In this study, we investigated the use of high carbon spring wire pins(ASTM A228) as reinforcement in arc welding. The pins were inserted into the weld pool during the welding process to reinforce the joint. Similar methods are used by few researchers to produce metal matrix composites [6].

The objective of this study was to evaluate the effectiveness of using spring steel pins as reinforcement in arc welding. Three sets of samples were prepared: welded metal samples without reinforcement, welded metal samples with smooth pins reinforcement, and welded metal samples with rough spring steel pins reinforcement. The effect of pin roughness was also studied by using a knurling tool to create rough pins and observing the roughness pattern using a microscope. Tensile tests were performed on the samples to compare the strength and ductility of the different types of

samples. The results of the study show promising improvements in the strength and ductility of the welded joints with the use of spring steel pin reinforcement. The results also indicate that pin roughness can further improve the strength of the joints. This paper presents the details of the experimental setup, results, and conclusions of the study. The findings of this study can be useful in improving the quality and reliability of welded joints in various industrial applications.

2 EXPERIMENTAL SETUP

To investigate the effect of using smooth and knurled high-carbon spring steel pins as reinforcement in arc welding of ASTM A36 structural steel, a set of experiments was conducted. The experimental setup consisted of the following steps:

2.1 Materials

ASTM A36 structural steel was used as the base metal and high-carbon spring steel wire (ASTM A228) was used as the reinforcement material. The diameter of the pins was 4.8 mm.

Reinforcement Pins:

Smooth and knurled pins were used as reinforcement in welded joints. The knurling tool used had a pitch of 1.5 mm.

Microscopic Study:

Microscopic study of Pins showed that roughness pattern was created by a 1.5mm pitch knurling tool and had 11 teeths per pin and a working depth of 0.5mm.

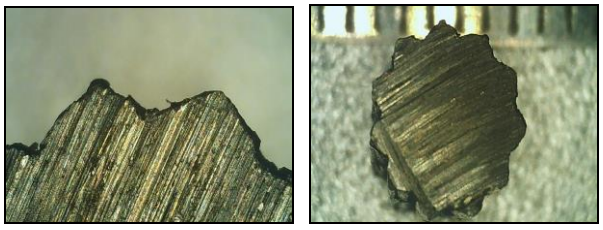

Figure 1. Microscopic Top view of a knurled spring steel pin

2.2 Sample Preparation Using Argon Metal Arc Welding

Three sets of samples were prepared for each case. These were welded metal samples without reinforcement and welded metal samples with smooth and knurled reinforcement pins. The samples were prepared using a standard plate size of 0.5-inch thickness and ASTM E8 standard for tensile testing.

The welding was done using an argon gas shielded arc welding process. The welding parameters such as voltage, current, and travel speed were kept constant during the welding process.

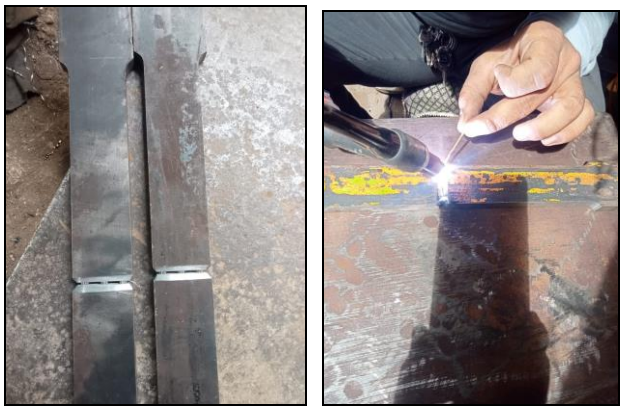

Figure 2. Argon Gas Welding on samples

2.3 Tensile Testing

Tensile tests were performed on each set of samples using the ASTM E8 standard test method. The tensile testing machine was calibrated according to the ASTM standards.

Figure 3. Tensile Test and Fractured Samples

3 DATA ANALYSIS

The mechanical properties of the samples were analyzed based on the results obtained from the tensile testing. The data obtained was analyzed using statistical methods to determine the significance of the effect of reinforcement on the welded joints.

Once the samples were prepared, they were subjected to tensile tests using a universal testing

machine. The tests were performed according to ASTM E8 standard test methods for tension testing of metallic materials. The samples were mounted on the testing machine, and a load was applied to the samples at a constant rate of deformation. The load and displacement were measured using load cells and extensometers, respectively. The tensile tests were performed until the sample fractured, and the maximum load and displacement at fracture were recorded. The data obtained from the tensile tests were analyzed to determine the mechanical properties of the samples, including yield strength, ultimate tensile strength, and elongation.

Overall, the experimental setup ensured the accuracy and reliability of the results and allowed for the comparison of the mechanical properties of the different sets of samples. The results of the tensile tests were used to evaluate the effectiveness of using high-carbon spring steel pins as reinforcement in arc welding of structural steel.

4 CALCULATION AND RESULTS

The process of measuring the tensile strength involves the use of a universal testing machine, which provides an output data of force and corresponding elongation, also known as stroke. This data is then analysed to determine the maximum force that was exerted on the sample during the tensile test. The next step involves calculating the cross-sectional area of the sample, which is the area perpendicular to the applied force. This is achieved by measuring the width and thickness of the sample and multiplying them together. With the maximum force and the cross-sectional area known, the tensile strength can be calculated. In order to find the tensile strength of the joints following formula was used:

For a cross-sectional area of 40mm x 25mm = 1000 mm^2 = 0.001 m^2

Tensile Strength= Maximum Load/ Cross-sectional Area

So, the Tensile Strength calculated with respect to the maximum load are given in Table 1

Table 1. Tensile Strength of Samples

Sample Type	**Maximum Load(kN)**	**Tensile Strength(MPa)**
Without Reinforcement	161	161
Without Reinforcement	168	168
Without Reinforcement	165	165
Smooth Pins Reinforcement	169	169
Smooth Pins Reinforcement	162	162
Smooth Pins Reinforcement	170	170
Rough (Knurled) Pins Reinforcement	184	184
Rough (Knurled) Pins Reinforcement	188	188
Rough (Knurled) Pins Reinforcement	189	189

By taking average of the 3 values we found tensile strengths for samples without reinforcement, with smooth pins reinforcement, knurled pin reinforcement as 164.6MPa, 167MPa, 187MPa respectively.

By comparing the difference in the tensile strength values and representing it in percentage we found that percentage improvement in smooth and knurled pins reinforcement is 1.46% and 13.6% respectively.

5 CONCLUSION

In conclusion, this study investigated the use of smooth and knurled high-carbon spring steel pins as reinforcement in arc welding of ASTM A36 structural steel. The results showed that the use of reinforcement pins significantly improved the mechanical properties of the welded joints, and the knurled pins provided better reinforcement than smooth pins. The increase in surface roughness of the reinforcement pins resulted in improved mechanical properties of the welded joints. The percentage improvement in tensile strength values for smooth and knurled pins reinforcement was found to be 1.46% and 13.6% respectively. These findings suggest that high-carbon spring steel pins with surface roughness can be a promising reinforcement material for arc welding of structural steel, and further research can be done to optimize the process parameters and investigate the effect of different types of reinforcement materials.

REFERENCES

[1]. Moreira RCS, Kovalenko O, Souza D, Reis RP. Metal matrix composite material reinforced with metal wire and produced with gas metal arc welding. Journal of

Composite Materials. 2019;53(28-30):4411-4426.

[2]. Deekshant Varshney, Kaushal Kumar, Application and use of different aluminium alloys with respect to workability, strength and welding parameter optimization, Ain Shams Engineering Journal,Volume 12, Issue 1, 2021, Pages 1143-1152, ISSN 2090-4479

[3]. Chiocca, A.; Frendo, F.; Bertini, L. Evaluation of Heat Sources for the Simulation of the Temperature Distribution in Gas Metal Arc Welded Joints. Metals 2019, 9, 1142.

[4]. Cai, X.; Dong, B.; Lin, S.; Murphy, A.B.; Fan, C.; Yang, C. Heat Source Characteristics of Ternary-Gas-Shielded Tandem Narrow-Gap GMAW. Materials 2019, 12, 1397.

[5]. Dutra, J.C., Gonçalves e Silva, R.H., Riffel, K.C. et al. High-performance GMAW process for deep penetration applications. Weld World 64, 999–1009 (2020).

[6]. Moreira RCS, Kovalenko O, Souza D, Reis RP. Metal matrix composite material reinforced with metal wire and produced with gas metal arc welding. Journal of Composite Materials. 2019;53(28-30):4411-4426.

A NOVEL STUDY ON PERFORMANCE EVALUATION OF SINGLE FLOW DOUBLE PASS SOLAR AIR HEATER WITH PHASE CHANGE MATERIALS

Zeeshan Rasool[1], Muhammad Imran Akram[1], Rabeet Yousaf[1], Muhammad Sarfraz Ali[1,2,*], Sadia Saleem[3]

[1]Mechanical Engineering Department, Pakistan Institute of Engineering & Technology, Multan, Pakistan

[2]Mechanical Engineering Department, Swedish College of Engineering & Technology, Rahim Yar Khan, Pakistan

[3]Institute of Computer Science and Information Technology, The Women University, Multan, Pakistan

[*]Corresponding author. Tel.: +92-345-8329528

E-mail address: sarfrazali@piet.edu.pk (Muhammad Sarfraz Ali)

ABSTRACT

Solar air heater (SAH) collects heat from the sun's rays, transfer it to the working substance, and then use the heated fluid for a variety of purposes. The performance of a double-pass SAH is compared and examined in the current paper using a V-corrugated absorber panel. For storing extra solar energy and releasing it at night, this work's goal is to construct and test a double-pass solar SAH with a thermal energy storage system in Multan, Pakistan. To assess the efficiency of a double-pass SAH the air flows at different masses ranging between 0.03 kg/s to 0.05 kg/s, and experimental work was carried out. When the air flows at the rate of 0.03 kg/s, the phase change material's extreme temperature changes between the input and output air flow was 31 °C. For the equal flow of air, the average effectiveness of double-pass SAH comprised with thermal storage is more than that of the double-pass SAH without thermal storage. Low mass flow rates can offer heat for a longer period by making use of the storage system's maximal capacity. Additionally, 0.03 kg/s is the suggested range for air mass flow rate that provides an acceptable efficiency and beneficial heat gain.

Keywords: Radiations; Phase change material; Paraffin wax, Copper oxide nanoparticles; Solar air heater

1 INTRODUCTION

In contemporary times, a country's prosperity is determined by how much energy it consumes, and this relationship directly affects its GDP. As a result, the need for energy resources is growing every day. Technologies for sustainable energy are extremely important for a bright future. Because they provide an endless source of energy. The efficient use, conversion, and storage of sustainable energy is the solution to the global energy dilemma. Work in this area is being done by researchers. Solar energy is a renewable resource that can be used for a variety of purposes, including space heating, direct radiation drying, and power generation. Another significant use of solar energy is in solar air warmers.

Simple devices called solar air heaters use incident solar radiation to produce green energy for a variety of uses. The SAH gadget absorbs solar energy, transforms it into heat in the air, and then delivers the heated air for usage. An absorber plate, one or more air passages, insulation for the solar collector's bottom and lateral sides, and one or more crystal clear covers make up a solar air heater. For the air supply, a blower is not required. Airflow channel configuration and airflow channel design are the two main categories for solar air heaters. The first type is associated with the configuration of the airflow passage. System efficiency increases by changing the configuration of the airflow passage. This category also expresses in three sub-titles. The sub-

categories are single pass and single flow, single flow and double pass, and double flow and single pass. The subsequent type is related to the design of the airflow channel. The system efficiency improved by changing the design of the airflow passage. This category is also expressed in two sub-categories: flat plate, and v-corrugated plate. The effectiveness of a double-flow, single-pass solar air heater with phase change materials is investigated in research as shown in Figure 1.

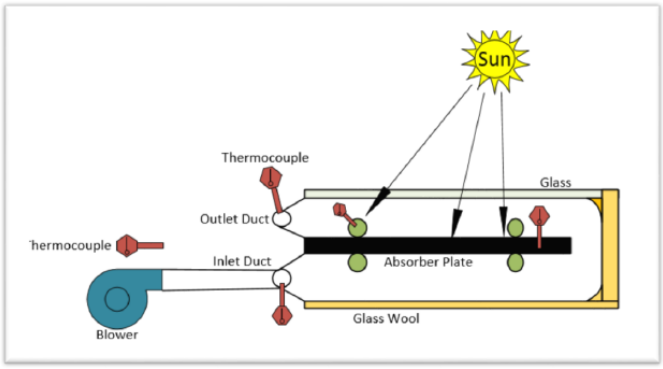

Figure 1. Single pass double flow solar air heater with phase change materials

A phase-changing material, or PCM for short, is an extremely hot type of fusion component with the ability to solidify and melt above a particular temperature, storing and releasing huge quantities of energy. Due to the fact that heat is captured when a substance changes from a solid to a liquid or vice versa, PCMs are classed as latent heat storage units.

Researchers have put a lot of effort into finding ways to deal with the alternating nature of solar energy availability. A double pass SAH heater with and without a storage media was the subject of experiment research by Ali et al. [1], who also employed Al and Cu rods as thermal enhancers. According to the results, arrangements with a storage material offer productivity for 1.5 and 2 hours after sunset. A double pass SAH's capacity to store heat with three distinct arrangements was explored by Krishnananth et al. [2]. They discovered that the SAH PCM capsule placed on top of the SAH is the most effective configuration. For use at night, Khadraoui et al. [3] investigated the behaviour of a solar dryer without latent storage units (including PCM). According to reports, compared to ISD, DSD produces less favourable drying conditions. Additionally, ISD's daily exergy and energy efficiency was 33.9% and 8.5%, respectively. In a review of research on new strategies and developments for using PCMs in solar systems, A.K. Pandey et al. [4] came to the conclusion that no one type of PCM is best for the desired outputs. Regarding the use of PCMs, a solid plan must be made, as must variations.

Experimental research by Fatih et al. [5] has shown that increasing the heat transfer area increases the thermal efficacy of solar air collectors. Solar air collectors made of baffled and flat plates were the subject of experiments by Vivek Singh et al. [6]. Due to an enhanced airflow channel, baffled solar air collectors were found to be 16–21% more thermally efficient. According to Abdullah et al. [7], the circular cross-sectional area configuration had the highest efficiency of 80% for the three configurations of half-circle, semi-circle and circular with an isosceles triangle. SAHs were the subject of a thorough review of research by Kabeel et al. [8]. It was claimed that setups with fins, baffles, and artificially roughened surfaces produce higher thermal efficiency. Additionally, compared to blackened SAHs, Ni-Sn-coated solar air heaters have a 30.01% greater yearly efficiency. To examine the impact of different limitations, such as airflow rate, sun intensity, and temperature on the performance of SAH with a flat plate, Taki et al. [9] carried out a theoretical and experimental study. It was claimed that colouring the back of the absorber plate black might boost effectiveness by 10%. By using the phase-changing material with high latent heat capacities, Khadraoui et al. [10] conducted an investigational study to increase the effectiveness of a straightforwardly constructed solar air heater. It was discovered that the outlet temperature rose during overnight use. Additionally, daily energy effectiveness for solar air heaters with PCM has gotten up to 33%, compared to 17% for arrangements without PCM. Moradi et al. [11] used paraffin wax layers of 2 cm and 4 cm to explore a single-pass SAH numerically and experimentally. SAH with a 4 cm layer was proven to produce more

ideal outcomes. Ammari [12] created a mathematical model to determine the flat SAH thermal performance. It was projected that the thermal performance of this flat SAH would be better than that of the majority of heaters of this type.

Significant research is being done to build solar air heaters that have improved heat transfer rates from storage mediums and overall thermal performance. From a review of the literature, it is clear that double-pass SAH is more effective than single-pass ones and that storage mediums boost the average thermal efficiencies of SAHs Because the problem of decreased conduction of storage channels has a tendency to lower overall efficiency, research in the same area is being done by keeping contact between storage channels and materials with stronger conductivity like Copper and Aluminium. The storage capacity of SAHs may soon be solved by organic phase shift materials, while the problem of reduced conductivity may be solved by keeping contact with higher conductivity materials.

2 MATERIALS AND METHODS

2.1 Experimental procedures

In order to explore the heat absorbing and releasing process of the double-pass solar air heater with and without PCM, the experimental set-up was created and constructed. Both June and July 2019 were used for the measurements. Testing for the charging process takes place from 8:00 am to 8:00 pm. (local time). A portion of the total solar light that the transparent cover transmits during the day is captured by the collector's black absorber plate. Along with mass flow rate, sun irradiation, ambient temperature, entrance and exit air temperatures, air temperatures inside the SAHs, and temperature of the absorbing plate, these variables are measured during the experiment.

The performance of DPSAH is examined for four setups, i.e. flat plate without PCM, flat plate with PCM, corrugated plate without PCM, and corrugated plate with PCM. The DPSAH uses an air blower to circulate air and a speed controller that was directly connected to the blower allowed for the creation of various mass flow rates. The DPSAH's functionality in each setup. The effectiveness of the four DPSAH configurations is assessed using four mass flow rates of air such as 0.03, 0.04, and 0.05 kg/s. The best performance parameters are determined by conducting the tests three times on three different days, collecting the average values of the results, and comparing them to the various configurations. The air and absorber plate temperature within the heaters is measured using temperature sensors. The Arduino UNO is connected to the temperature sensors, and the result is displayed on an LED and saved to an SD card. A solar metre was used to calculate the total sun irradiation.

Configuration 1

In configuration 1 there is no thermal storage material is used to store energy after sunset as shown in Figure 2. The flat plate of copper is used as a collector plate. In this configuration, the cool air inlet from the lower channel and hot air exits from the upper channel.

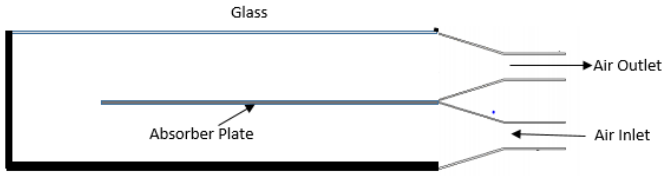

Figure 2. Solar air heater with flat plate and no PCM

Configuration 2

In configuration 2 the thermal storage material is used to store energy after sunset as shown in Figure 3. The flat plate of copper is used as a collector plate. The TSM is stored in circular finned aluminium pipes. TSM the extra working hour. In this configuration the cool air inlet from the lower channel and hot air exits from the upper channel.

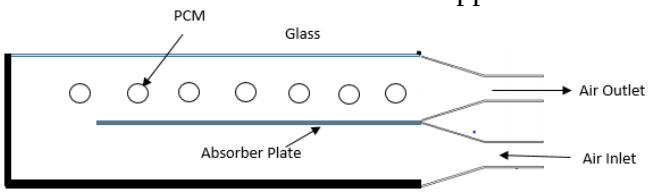

Figure 3. Solar air heater with flat plate and PCM

Configuration 3

In configuration 3 there is no thermal material is used to store energy after sunset as shown in Fig 4. The v-corrugated plate of copper is used as a collector plate to increase the thermal contact of air. In this

configuration, the cool air inlet from the lower channel and hot air exits from the upper channel.

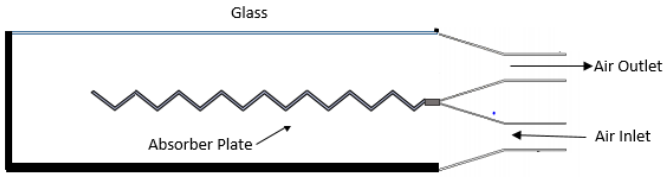

Figure 4. Solar air heater with v-corrugated plate and no PCM

Configuration 4

In configuration 4 the thermal material is used to store energy after sunset as shown in Fig. 5. For better performance of DPSAH the v-corrugated plate of copper is used as a collector plate. The TSM is stored in circular finned aluminium pipes. TSM the extra working hour. In this configuration the cool air inlet from the lower channel and hot air exits from the upper channel.

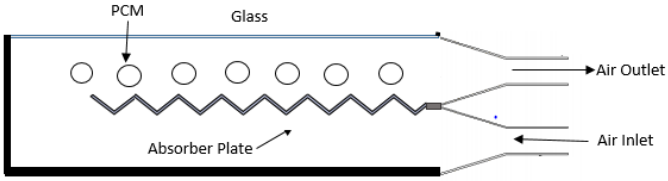

Figure 5. Solar air heater with v-corrugated plate and PCM

2.2 Experimental setup

A two-pass SAH made of mild steel was built for this experimental investigation. The dimensions of a double-pass solar air heater were 1800mm long, 600mm wide, and 290mm tall. Black paint was applied to the 1mm thick aluminium absorber plate to trap as much radiation as possible. Figure 6 shows how the collector's top side was protected from convective losses with a 4 mm glass plate and how the bottom and lateral sides were insulated with 20 mm thick glass wool to minimise heat losses to the atmosphere.

Figure 6. Solar air heater

A conical intake and exit portion were added to the collector in order to maintain an evenly dispersed flow inside. Air was circulated in the opposite direction through the upper channel between the absorber plate and the top glass cover after being driven through the lower channel in the double pass collector between the rear plate and the absorber plate.

A detailed technical description of the collector and pipes utilised for thermal storage shown in Figure 7 may be found in Tables 1 and 2. A double-pass solar air heater was used in conjunction with the phase change material thermal storage technology to boost system performance. To store the extra thermal energy, eight aluminium capsules (each 50 mm in diameter and 500 mm in length) containing paraffin wax with a concentration of copper oxide (Nano Particle) were utilised. The plate which absorbs solar radiations was coloured black to absorb the highest temperature, thermocouples were installed in various locations and connected to the Arduino, a digital-led was used for display, and an SD card module was used to store various values according to the time change. V-corrugated plates are utilised to improve the thermal contact of air. The corrugate is maintained at a 60-degree angle.

Table 1. Design Parameters for Collector of Solar Air Heater

Sr. No.	Design material/parameter	Specification
1	Absorber plate	Width: 600 mm, length: 1700 mm
2	Collector glazing	Plane glass with 4 mm thickness
3	Area of Glass	3657.6mm2

Figure 7. Aluminium Circular finned thermal storage pipe

Table 2. Design Parameters for storage capsules of Solar Air Heater

Sr. No.	Design material/parameter	Specification
1	Weight paraffin per capsule	475g
2	Total no. of pipes	8
3	Pipe length	500mm
4	Pipe, outer diameter	50mm
5	Pipe, inner diameter	40mm

2.3 Thermal storage material

The thermal storage material is used to store thermal energy. The paraffin wax with 0.7% concentration of copper oxide nanoparticle is used as thermal storage material.

Paraffin wax

A combination of hydrocarbon molecules with between 20 and 40 carbon atoms makes up paraffin wax, a soft, colourless substance. At room temperature, it is solid, but beyond around 37 °C, it starts to melt, and its boiling point is above 370 °C. The storage of heat also makes use of paraffin wax. It starts to store heat when its temperature exceeds room temperature and melting temperature. The properties of the paraffin fix are shown in Table 3.

Table 3. Properties of paraffin fix

Sr. No.	Properties	Values
1	Specific heat capacity	2.14 J/g. K
2	Fusion heat	220 J g−1
3	Melting temperature	50 ºC

Copper oxide nanoparticles

There are two types of nanoparticles, simple nanoparticles and hybrid nanoparticles. Simple nanoparticles are consisting of a single element, but hybrid is consisting of two or more elements. In the current decade, due to advancements in the field of nanotechnology, nanoparticles are evolved as a good option for heat transfer applications. Nanoparticles are extremely small particles of oxides, nitrides and carbides of metals with a size of less than 100 nm. Nanoparticles are available in different sizes. The properties of nanoparticles depend upon the composition of particles. The thermal properties of nanoparticles include viscosity, thermal conductivity, density and specific heat are shown in Table 4.

Table 4. Properties of copper oxide nanoparticles

Sr. No.	Specifications	Values
1	Appearance	Brownish black powder
2	Purity	+98%
3	Grain size	60 nm
4	Thermal conductivity	20 W/m K
5	Specific heat	535.6 j/kg K
6	Density	6500 kg/m^3

3 RESULTS AND DISCUSSIONS

The current experimental study was conducted on four different configurations as explained before. Primary parameters of importance were recorded and noted which temperature measurements in this study are basically. Using mathematical relationships, such as energy storage, input and output, other factors that are just as crucial as the core ones were developed. For each configuration, experimentation is performed at three different flow rates. For the first and third types of configuration, the experimental data was collected from 8:00 AM to 5:00 PM. While, for the second and fourth kinds of configuration, the data was collected from 8:00 AM to 8:00 PM.

The double-pass solar air heater was oriented southward to receive the most sun radiation at Multan's local latitude of 32.20 degrees. Line Figures are used in the current study to present experimental data. Figures can be divided into two types. 1st one depicts a single parameter under experimental study while 2nd one shows multi parameters under experimental study. These Figures provide oversight of different parameters related to experimental configurations being studied.

3.1 Configuration 1

For configuration 1, the flat plate is used to absorb the solar radiation and there is no thermal storage used to store energy. Three different flow rates are used such as 0.03kg/s, 0.04kg/s and 0.05kg/s Following Figures depict the different parameters under study for this configuration in the first week of June 2019.

We conclude the result from different flow rates in this experimentation that at 0.03kg/s value of flow rate has a higher value of temperature difference as compared to other flow rates. Figure 8 shows that a flow rate of 0.03kg/s has a temperature difference of 21 ℃, and a flow rate of 0.05kg/s have a temperature difference is 16 ℃.

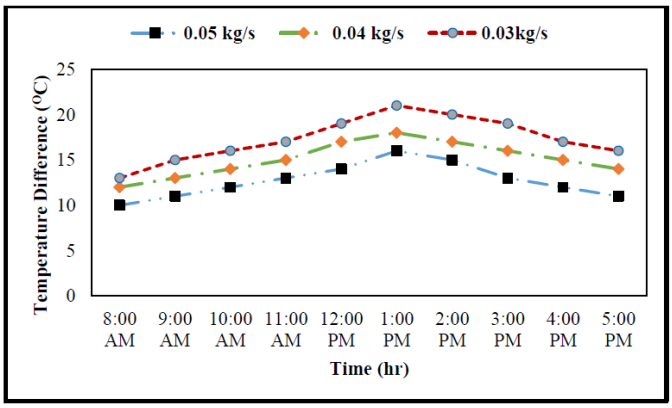

Figure 8. Temperature difference at a different flow rate for configuration 1

Figure 9 provides that a higher flow rate has maximum efficiency and a lower flow rate has low efficiency at a flow rate of 0.05kg/s have maximum efficiency and at a flow rate of 0.03kg/s.

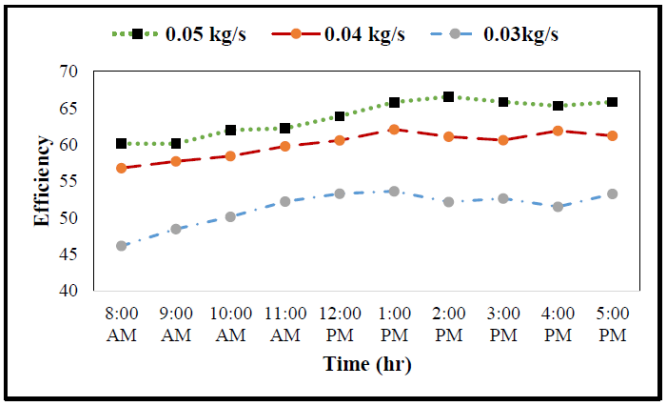

Figure 9. Efficiencies comparison at a different flow rate for Configuration 1

3.2 Configuration 2

For configuration 2, Thermal storage material is filled in circular finned aluminium tubes which are used to store energy. In total, eight tubes filled with thermal storage material were used during experimentation. These tubes were basically in suspension condition in the upper pass of DPSAH, so that, air could perform convection on all surface areas. The following Figures depict the different parameters under study for this configuration in the third week of June 2019.

We conclude the result from different flow rates in this experimentation that at 0.03kg/s value of flow rate has a higher value of temperature difference as compared to other flow rates. Figure 10 shows that a flow rate of 0.03kg/s has a temperature difference of 23 ℃, and a flow rate of 0.05kg/s have a temperature difference is 18 ℃.

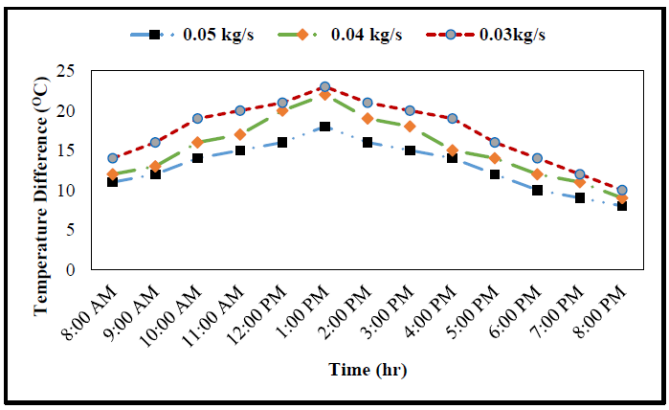

Figure 10. Temperature difference at a different flow rate for configuration 2

Figure 11 provides that a higher flow rate has maximum efficiency and a lower flow rate has low efficiency at a flow rate of 0.05kg/s have maximum efficiency and at a flow rate of 0.03kg/s.

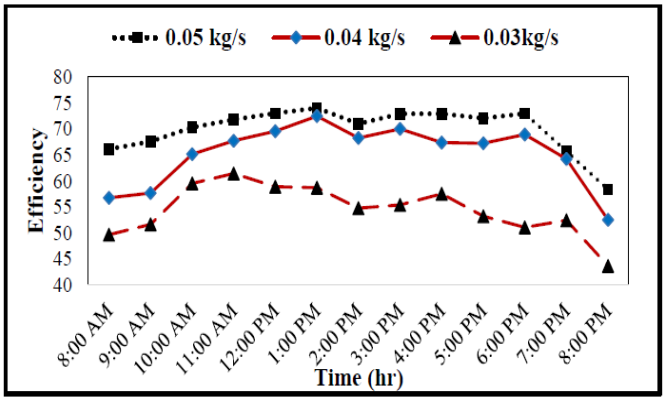

Figure 11. Efficiencies comparison at a different flow rate for configuration 2

3.3 Configuration 3

For 3rd configuration, the V-corrugated plate is used to absorb solar radiation and there is no thermal storage is used to store energy. The V-corrugated plate increases the heat transfer rate between the collector and air. Three different flow rates are used such as 0.03kg/s, 0.04kg/s and 0.05kg/s in experimentation. The following Figures depict the different parameters under study for this configuration in the first week of July 2019.

We conclude the result from different flow rates in this experimentation that at 0.03kg/s value of flow rate has a higher value of temperature difference as compared to other flow rates. Figure 12 shows that a flow rate of 0.03kg/s has a temperature difference of 24 ℃, and a flow rate of 0.05kg/s have a temperature difference is 19 ℃.

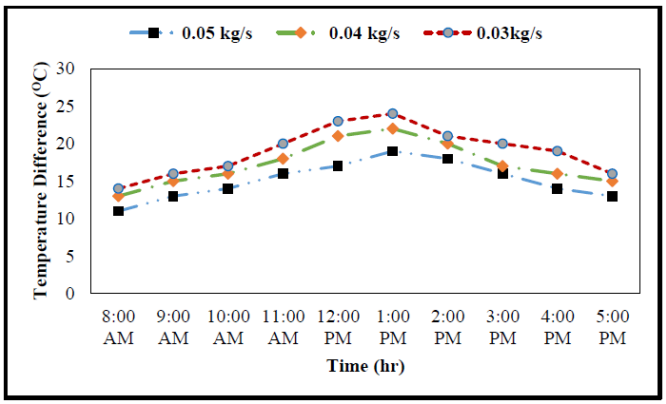

Figure 12. Temperature difference at a different flow rate for configuration 3

Figure 13 provides that a higher flow rate has maximum efficiency and a lower flow rate has low efficiency at a flow rate of 0.05kg/s have maximum efficiency and at a flow rate of 0.03kg/s.

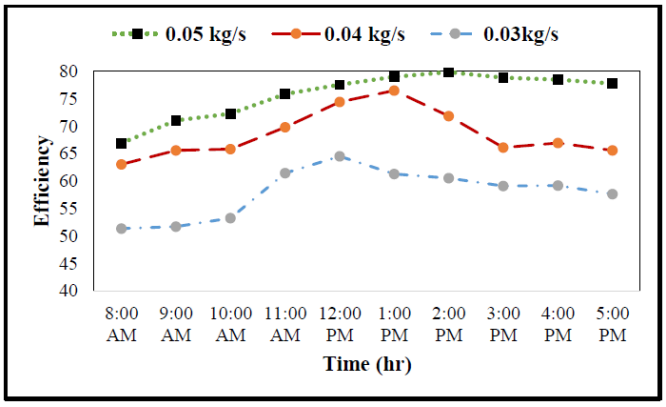

Figure 13. Efficiencies comparison at a different flow rate for configuration 3

3.4 Configuration 4

For configuration 4, the V-corrugated plate is used to absorb the solar radiation and there is thermal storage is used to store energy. The V-corrugated plate increases the heat transfer rate between the collector and air. Thermal storage material is filled in circular finned aluminium tubes which are used to store energy. In total, eight tubes filled with thermal storage material were used during experimentation. These tubes were basically in suspension condition in the upper pass of DPSAH, so that, air could perform convection on all surface areas. The following Figures depict the different parameters under study for the third week of July 2019.

We conclude result from different flow rates in this experimentation that 0.03kg/s value of flow rate has a higher value temperature difference as compared to other flow rates Figure 14 shows that at a flow rate 0.03kg/s have a temperature difference of 31℃,

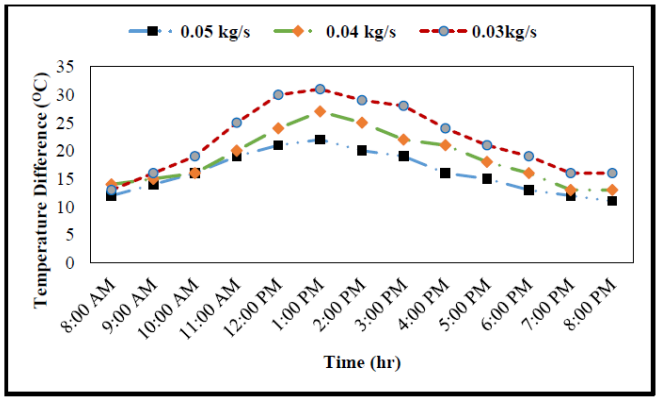

Fig. 14. Temperature difference at a different flow rate for configuration 4

at flow rate 0.05kg/s have temperature difference is 22℃.

Figure 15 provides that a higher flow rate has maximum efficiency and a lower flow rate has low efficiency at a flow rate of 0.05kg/s have maximum efficiency and at a flow rate of 0.03kg/s.

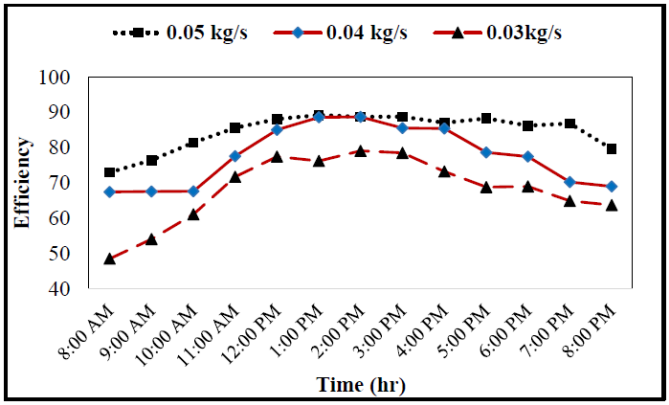

Figure 15. Efficiencies comparison at a different flow rate for configuration 4

3.5 Comparison of all configurations

The succeeding Figures are depicting the comparison between all three configurations for different parameters recorded or calculated during the experimentation study. Figure 16 shows the variation in solar radiation intensity for all three configurations. Figure lines tell that solar radiation intensity was best available for configuration 4 variation for all configurations. This difference in solar radiations is majorly due to the intermittent nature of weather conditions as even partial clouds can largely reduce the intensity of solar radiations on the ground.

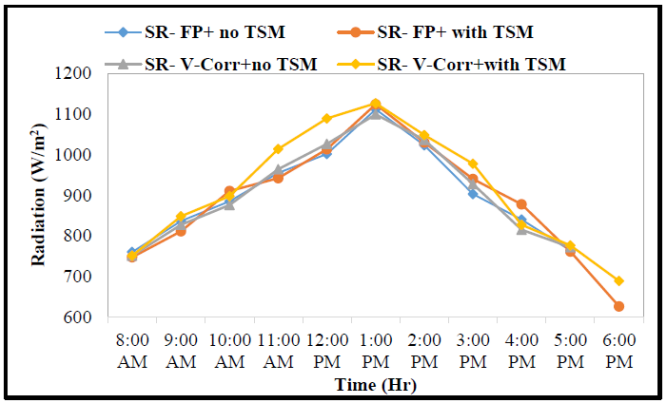

Figure 16. Solar Radiation of all Configuration

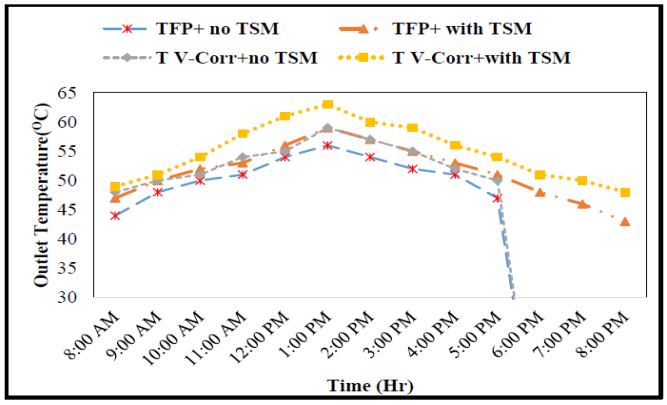

Figure 17. Outlet Temperature of all configurations at 0.05 kg/s flow rate

Figure 17 shows the comparison between the temperature rises achieved by using all four configurations for DPSAH at a flow rate of 0.05kg/s. It can be seen that for configuration 1, with no thermal energy storage medium, the temperature outlet is smaller at the beginning of the day, as equated to other configurations because all of the energy is available for heating since no thermal energy storage medium is used for this configuration and we have temperature outlet up to 5:00 P.M only. For configuration 2, with higher melting point paraffin wax filled in circular aluminium finned tubes as a thermal storage medium, we have a high outlet temperature as compared to configuration 1 because the thermal contact of air increases. As, is obvious from the Figure that around 1:00 P.M. because of the effect of the thermal storage medium, a reasonably high outlet temperature is achieved as compared to configuration 1. Also, we have prolonged heating hours reaching up to 7:30 P.M due to the thermal storage medium which was up to 5:00 P.M in the case of configuration 1. In configuration 3 the temperature outlet increases because here v-corrugated plate is a collector plate. The temperature rises due to the increase of thermal contact of air and collector. In configuration 4, v-corrugated plate and higher melting point paraffin wax with the concentration of copper oxide nanoparticle filled in circular aluminium finned tubes as a thermal storage medium, we have high outlet temperature as compared to other configurations because thermal contact of air increases. As, is obvious from the Figure that around 1:00 P.M. because of the effect of the thermal storage medium, a reasonably high outlet temperature is achieved as compared to configuration 2. Also, we have prolonged heating hours reaching 8:00 P.M. due to the thermal storage medium which was up to 5:00 P.M. in the case of configurations 1 and 3.

Figure 18 shows the differentiation of outlet temperature for all four configurations for DPSAH at a flow rate of 0.04kg/s. For configuration 1 outlet temperature is smaller as compared to other configurations and we have a temperature outlet up to 5:00 P.M only. For configuration 2, with higher melting point paraffin wax filled in circular aluminium finned tubes as a thermal storage medium, we have a high outlet temperature as compared to configuration 1 because the thermal contact of air increases. As, is obvious from the Figure that around 1:00 P.M. because of the effect of the thermal storage medium, a reasonably high outlet temperature is achieved as compared to configuration 1. Also, we have prolonged heating hours reaching 8:00 P.M. due to the thermal storage medium which was up to 5:00 P.M. in the case of configuration 1. In configuration 3 the outlet temperature is almost the same compared to configuration 2 due to the internment condition of the weather but later temperature starts increasing. The temperature rises due to the increase of thermal contact of air and collector. In configuration 4, v-corrugated plate and higher melting point paraffin wax with the concentration of copper oxide nanoparticle filled in circular aluminium finned tubes as a thermal storage medium, we have high outlet temperature as compared to other configurations because thermal contact of air increase Also, we have prolonged heating hours reaching till to 8:00 P.M due to thermal storage medium which was up to 5:00 P.M in case of configuration 1 and 3.

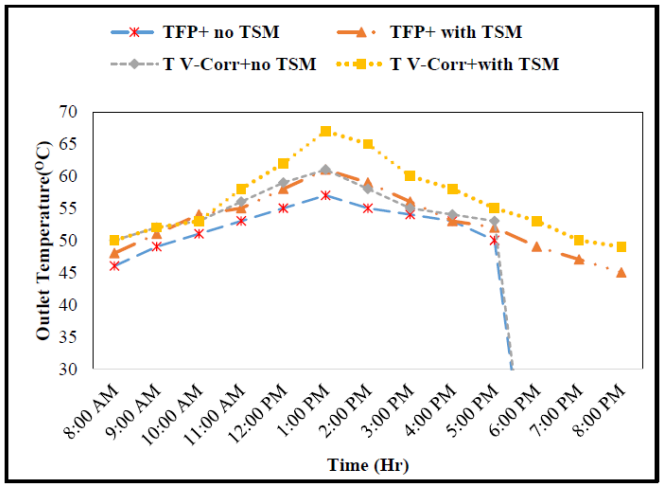

Figure 18. Outlet Temperature of all configurations at 0.04 kg/s flow rate

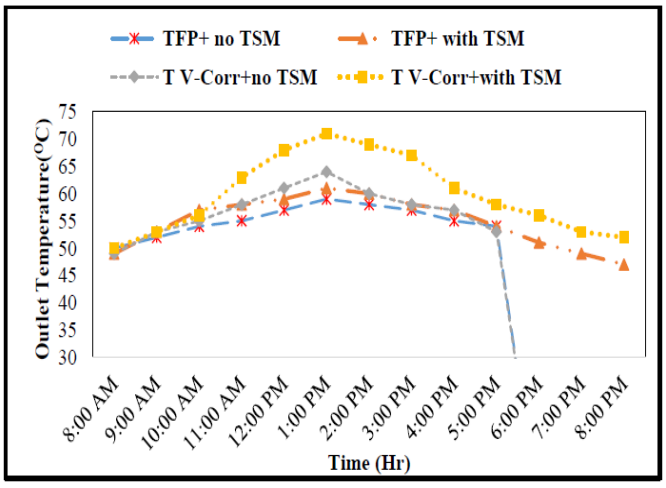

Figure 19. Outlet Temperature of all configurations at 0.03 kg/s flow rate

Figure 19 illustrates the result of air outlet temperature for all configurations of DPSAH at a flow rate of 0.03kg/s. For configuration 1 outlet temperature is higher as compared to configuration 2 and we have temperature outlets up to 5:00 P.M only. For configuration 2, the outlet temperature is as compared to configuration 2 because of higher melting point paraffin wax filled in circular aluminium finned tubes as a thermal storage medium and thermal contact of air increase. Also, we have prolonged heating hours reaching 8:00 P.M. due to the thermal storage medium which was up to 5:00 P.M. in the case of configuration 1. In configuration 3 the outlet temperature is smaller at the start of the day compared to configuration 2 due to the internment condition of the weather but later temperature starts increasing. The temperature rises due to the increase of thermal contact of air and collector. In configuration 4, v-corrugated plate and higher melting point paraffin wax with the concentration of copper oxide nanoparticle filled in circular aluminium finned tubes as a thermal storage medium, we have high outlet temperature as compared to other configurations because thermal contact of air increase Also, we have prolonged heating hours reaching till to 8:00 P.M due to thermal storage medium which was up to 5:00 P.M in case of configuration 1 and 3.

4 CONCLUSIONS

DPSAH was investigated experimentally for four different configurations from 8:00 AM to 5:00 PM for the 1st and 3rd configurations while experimental results were conducted for the 2nd and 4th configurations from 8:00 AM to 8:00 PM due to an increased amount of thermal energy stored in the thermal storage medium. In 1st and 3rd configuration, no thermal storage medium was used while in 2nd and 4th configurations, paraffin wax with a concentration of 0.7 % copper oxide (Nanoparticle) was filled in circular aluminium finned tubes as the thermal storage medium in the upper pass. The maximum efficiency achieved is 91 % in the 4th configuration.

For configurations 1st and 3rd, with no thermal energy storage medium, the temperature difference is smaller, as compared to other configurations because all of the energy is available for heating with no thermal energy storage medium is used for these configurations and we have temperature difference up to 5:00 P.M only. For configurations 2nd and 4th, paraffin wax with the concentration of copper oxide (Nano-particle) as a thermal storage medium in the upper pass only, we have a high-temperature difference as compared to configurations 1st and 3rd because some of the solar energy is being stored in thermal storage materials for release at low input times later. Reasonably, high-temperature differences are achieved as compared to configurations 1st and 3rd. Moreover, we have prolonged heating hours reaching up to 8:00 P.M due to the thermal storage medium which was up to 5:00 P.M in the case of configurations 1st and 3rd. From the result, it is observed that the maximum temperature difference and outlet temperature are measured at noon time.

ACKNOWLEDGEMENTS

The Authors would like to thank the management of the Pakistan Institute of Engineering and Technology, Multan, for supporting this experimental study.

REFERENCES

[1]. H. M. Ali, A. I. Bhatti, and M. Ali, "An experimental investigation of performance of a double pass solar air heater with thermal storage medium," *Therm. Sci.*, vol. 19, no. 5, pp. 1699–1708, 2015, doi: 10.2298/TSCI140824140A.

[2]. S. S. Krishnananth and K. Kalidasa Murugavel, "Experimental study on double pass solar air heater with thermal energy storage," *J. King Saud Univ. - Eng. Sci.*, vol. 25, no. 2, pp. 135–140, 2013, doi: 10.1016/j.jksues.2012.05.004.

[3]. A. El Khadraoui, S. Bouadila, S. Kooli, A. Farhat, and A. Guizani, "Thermal behavior of indirect solar dryer: Nocturnal usage of solar air collector with PCM," *J. Clean. Prod.*, vol. 148, pp. 37–48, 2017, doi: 10.1016/j.jclepro.2017.01.149.

[4]. A. K. Pandey, M. S. Hossain, V. V. Tyagi, N. Abd Rahim, J. A. L. Selvaraj, and A. Sari, "Novel approaches and recent developments on potential applications of phase change materials in solar energy," *Renew. Sustain. Energy Rev.*, vol. 82, no. September 2017, pp. 281–323, 2018, doi: 10.1016/j.rser.2017.09.043.

[5]. F. Bayrak and H. F. Oztop, "Experimental Analysis of Thermal Performance of Solar Air Collectors With Aluminum Foam Obstacles KapaliHücreliAlüminyum Köpük EngellerSahip Hava Isitmali GüneKollektörlerinin Isil Performansinin DeneyseAnalizi," *J. Therm. Sci. Technol.*, vol. 35, pp. 11–20, 2015.

[6]. Anandh.A Baskar.R, "Experimental Investigation of Double Pass Solar Air Heater with Baffled Absorber Plate," vol. 3, no. November, pp. 420–423, 2017, doi: 10.13140/RG.2.2.13409.20322.

[7]. A. S. Abdullah, Y. A. F. El-Samadony, and Z. M. Omara, "Performance evaluation of plastic solar air heater with different cross sectional configuration," *Appl. Therm. Eng.*, vol. 121, pp. 218–223, 2017, doi: 10.1016/j.applthermaleng.2017.04.067.

[8]. A. E. Kabeel, M. H. Hamed, Z. M. Omara, and A. W. Kandeal, "Solar air heaters: Design configurations, improvement methods and applications – A detailed review," *Renew. Sustain. Energy Rev.*, vol. 70, no. November 2015, pp. 1189–1206, 2017, doi: 10.1016/j.rser.2016.12.021.

[9]. M. Taki Al-Kamil and A. A. Al-Ghareeb, "Effect of thermal radiation inside solar air heaters," *Energy Convers. Manag.*, vol. 38, no. 14, pp. 1451–1458, 1997, doi: 10.1016/S0196-8904(96)00050-7.

[10]. A. El Khadraoui, S. Bouadila, S. Kooli, A. Guizani, and A. Farhat, "Solar air heater with phase change material: An energy analysis and a comparative study," *Appl. Therm. Eng.*, vol. 107, pp. 1057–1064, 2016, doi: 10.1016/j.applthermaleng.2016.07.004.

[11]. R. Moradi, A. Kianifar, and S. Wongwises, "Optimization of a solar air heater with phase change materials: Experimental and numerical study," *Exp. Therm. Fluid Sci.*, vol. 89, no. January, pp. 41–49, 2017, doi: 10.1016/j.expthermflusci.2017.07.011.

[12]. H. D. Ammari, "A mathematical model of thermal performance of a solar air heater with slats," *Renew. Energy*, vol. 28, no. 10, pp. 1597–1615, 2003, doi: 10.1016/S0960-1481(02)00253-7.

NUMERICAL INVESTIGATION OF SMALL-SCALE WIND TURBINE FOR COMMERCIAL BUILDINGS

Osama Qadeer[1], M. Usman Khan[1], M. Basit Shafiq[1,*], Usman Allauddin[2], Mumtaz A. Qaisrani[3], Liaquat Ali Khan[1]

[1]Mechanical Engineering Department, National University of Technology, Islamabad, Pakistan

[2]Mechanical Engineering Department, NED University of Engineering and Technology, Karachi, Pakistan

[3]Institute of Mechanical and Manufacturing Engineering, Khwaja Fareed University of Engineering and Information Technology, Rahim Yar Khan, Pakistan

[*]Corresponding author. Tel.: +92-336-5430556

E-mail address: basitshafiq@nutech.edu.pk (M. Basit Shafiq)

ABSTRACT

Due to the increasing demands for energy, depletion of fossil fuels, and climate change, wind turbines appear to be good alternatives to extract energy from wind because of its availability at the cheapest. This study seeks to conduct a numerical analysis of small Savonius wind turbines that could contribute to the energy consumption of commercial buildings. In this study, the drag-type VAWT, Savonius wind turbine, with twist angle of 45 degrees is employed for the analysis of the consequence of velocity on the coefficient of performance and torque coefficient for the commercial buildings of Islamabad. Numerical results were carried out with wind speed ranging from 2m/s to 3.25m/s with step of 0.25m/s. Results obtained shows that the maximum coefficient of performance (C_p) for Savonius wind turbine obtained can never be more than 0.3. Maximum coefficient of torque (C_t) was obtained at wind speed of 2.5m/s and power of turbines increases with increase in speed of wind, hence more wind energy can be converted into electrical energy at high speeds.

1 INTRODUCTION

The use of renewable energy is spreading day by day to fulfill the increasing demands of energy because of its abundance and environment friendliness [1]. Wind as a renewable energy source is getting more and more attention to producing electricity by converting its kinetic energy into electricity [2]. A rotating mechanical device known as a wind turbine converts kinetic wind energy into electrical energy. They come in various sizes and have either vertical or horizontal axis.[3]. Vertical Axis Wind turbines are the turbines having axis perpendicular to the wind speed. These turbines are mostly preferred for small scale applications because of their noiseless operation and ability to operate regardless of direction of wind [4].

Savonius wind turbines are a particular kind of VAWTs regarded as the most streamlined turbine in comparison to other turbines, making its working principle simple to comprehend. The curvature of blades means that when they move in the opposite direction to the direction of wind, they will drag less, but when they move in the same direction, they will drag the most. The Savonius turbine's spinning motion is caused by this variation in dragging.

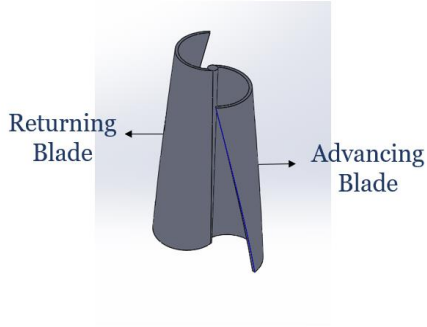

Figure 1. Isometric view of the Rotor

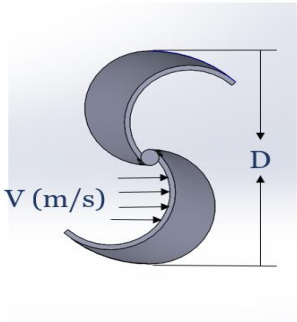

Figure 2. Top View of the Rotor

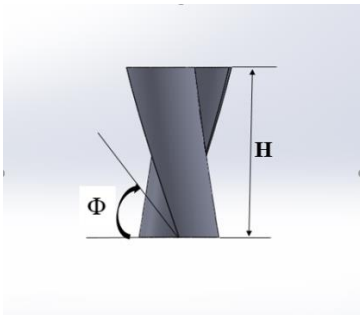

Figure 3. Side View of the Rotor

Xu et al. [4] examined that Wind energy can be captured by vertically oriented wind turbines in all directions. They are appropriate for the intricate flow patterns found in urban settings. According to the study, the average power output of a turbine array inside an urban location is always higher compared to a single wind turbine. Absi et al. [5] examined that, Savonius turbines are a form of wind turbine with a vertical axis that may be preferred for power generation and off-grid applications since they may be used in limited locations and places with little wind. By increasing the rotor's overlap ratio, a series of 2D unstable simulations (using CFD-Fluent version 19.1) were carried out. Lee et al. [6] carried-out study aimed to understand the performance and shape characteristics of a helical Savonius wind turbine at various helical angles. Results showed that the maximum power coefficient values occurred at the twist angle of 45^o, whereas it decreased by 25.5% at 90^o and 135^o. Promdee and Photong [7] examined the impact of wind speeds and angles on the capacity of a Savonius turbine with two wind tunnels to generate voltage. The testing findings demonstrated that large amounts of generated voltages were produced at wind angles from 23.2 to 35.5 degrees, with wind angles of 0 to 90 degrees producing the maximum voltage at 30 degrees. The generated voltage increases with increasing wind speed. Frikha et al. [8] analyzed the impact of incidence angle on the Savonius wind rotor's aerodynamic structure. The angle of incidence of the incurved Savonius rotor has a direct impact on the local characteristics, according to numerical results on velocity fields, pressure, and turbulence characteristics. Saad et al. [9] investigations were conducted into the impact of several design factors, such as angle of twist, overlap ratio, endplate size ratio, and wind velocity, on the Savonius wind turbine's performance. Findings showed that, in comparison to other designs, the turbines rotor with an angle of twist of 45°, an overlapping ratio of zero, and a plates size ratio of 1.1 achieves the best output power. Brusca et al. [10] analyzed the relationship between performance and aspect ratio of a H-Rotor wind turbine (power coefficient). As changes in a vertical-axis wind turbine's aspect ratio affect Reynolds numbers. Findings showed that as the aspect ratio decreases, the Reynolds number increases, improving the performance of wind turbines. C.M. Parker and M.C. Leftwich [11] examined the impact of the ratio of tip speed at large Reynolds numbers on a wind turbine with a vertical axis. Irrespective of the tip speed ratio, time averaged data indicated an asymmetrical wake behind turbine, with a bigger speed deficit for a greater tip speed ratio. Findings indicated that changes in the ratio of tip speed are more sensitive to the wake shape than changes in Reynolds number.

With the passage of time the demand of electricity is increasing and along with that the cost of electricity is increasing because of hike

in prices of fuel being imported to generate electricity. So, it the need of time to come up with a solution that will help to solve this problem or atleast reduce the impacts of this issue. Hence, the research is undertaken to check the potential of electricity generation in Islamabad starting from small model and then utilize the results to manufacture a large scale model for application for commercial buildings afterwards. Hence, All the numerical analysis are performed keeping in view the location of Islamabad as height of commercial buildings varies from 10m to 50m and in this range velocity of air varies from 2.2m/s to 4.68m/s [12].

2 PROJECT DESIGN

A small model of wind turbine was designed by using solid works 2017 and simulation was done on Ansys Workbench 19.2.

2.1 Design Parameters

Design Parameters utilized for the analytical calculations include:

Power Coefficient

Power coefficient is the measure of the rotors' power in relation to the available wind power. Mathematically,

$$C_p = {T\omega}/{0.5\rho A v^3} \quad (1)$$

Where, C_p is Power Coefficient, H stands for the rotor's height, T for its torque, D for its diameter, ω for its angular velocity, v for its wind speed, ρ for its air density, and A for its area, which is calculated by taking product of its height and its width.

Tip Speed Ratio

The difference between the tangential velocity of a blade's tip and the speed of the wind is known as the tip-speed ratio (TSR) for wind turbines.

Mathematically,

$$\lambda = {\omega R}/{v} \quad (2)$$

Where λ stands for Tip speed ratio and R is rotor's radius.

Torque Coefficient

The torque coefficient is the difference between the rotor's actual torque and its theoretical torque.

$$C_T = {T}/{0.5\rho A v^2} \quad (3)$$

Where C_T is the Torque coefficient.

Aspect Ratio

The height-to-diameter ratio of the rotor is known as the aspect ratio. Mathematically,

$$AR = {H}/{D} \quad (4)$$

Where AR is the Aspect ratio.

Overlap Ratio

The ratio of the blades' eccentricity, or distance from one another, to their radius.

Mathematically,

$$OR = {(e-a)}/{R} \quad (5)$$

Where a is the diameter of the central shaft, e is the eccentricity, or the distance between the blades, and OR is the overlapping ratio. [6]

3 ANALYTICAL CALCULATIONS

All the calculations are done according to wind data available for Islamabad at height of 50 meters.

The Max C_p for Savonius wind turbine = 0.3

Optimum Tip Speed Ratio for Savonius is between 0.7 to 0.8

Optimal Savonius turbine aspect ratio is 1.5

Density of air = 1.225 kg/m3

Height of Turbine = 0.2 m

Diameter of turbine = 0.133m

4 SIMULATION

The simulation is carried out for the scaled model of our rotor by keeping the area constant and changing the velocity of air. The velocities of air used are 2 m/s, 2.5 m/s, and 3 m/s. The simulation is done on Ansys Fluent.

4.1 Geometry of the Rotor

The geometry of the rotor is designed using SolidWorks using the following dimensions.

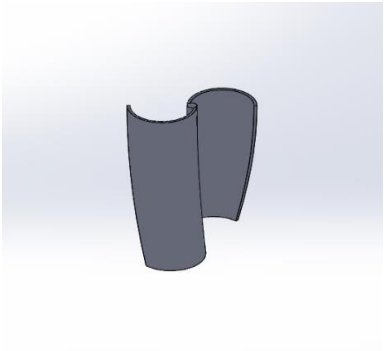

Figure 4. Isometric view of the Rotor

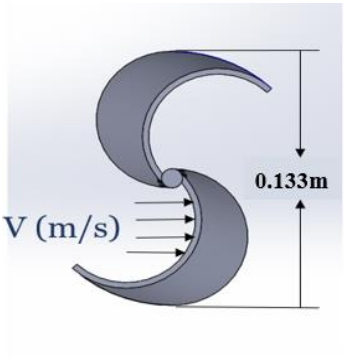

Figure 5. Top View of the Rotor

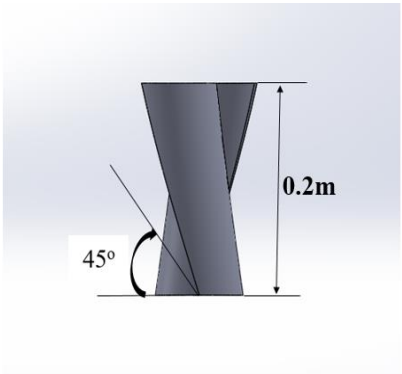

Figure 6. Side View of the Rotor

Table 1. Rotor Geometry Parameters

Height of Rotor	H	0.2m
Diameter of Rotor	D	0.133m
Thickness of Blade	t	0.002m
Diameter of Rod	d	0.01m
Twist Angle	φ	45º

4.2 Meshing of tshe Geometry

The quality of the mesh depends upon various factors such as skewness, orthogonality, aspect ratio which is important in CFD problem for the accuracy and convergence of the solution. As we are concerned about the torque and the angular velocity at turbine walls so a mesh with less skewness and high orthogonality is generated near the walls to get most accurate results. The total no. of nodes was **5915901** and the total no. of elements were **3786184**. Pictures of the meshing are attached below

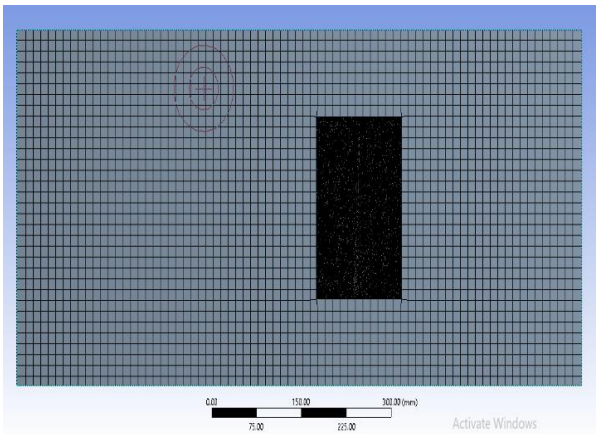

Figure 7. Front View of the mesh

In the picture given above the rectangular box shows the control volume region of the geometry and the smaller rectangle with darker region shows the turbine blades/rotor.

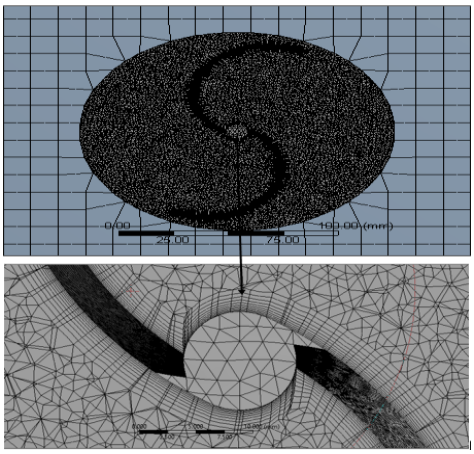

Figure 8. Closer view of boundary layer mesh

In order to ensure the quality of mesh we find out the skewness, orthogonality and aspect ratio of the mesh which comes out to be 0.2, 0.79 and 3.03. These values come out to be the good quality mesh according to mesh quality criteria [13].

5.3. SST K-ω Model

The SST k-omega model combines the benefits of two popular models, the k-omega and k-epsilon models. K-omega is suited for flow region near the wall where k-epsilon is best suited for flow region away from wall. It is particularly useful for simulating turbulent boundary layers and separated flows [14].

5 COMPARISON OF ANALYTICAL AND NUMERICAL RESULTS

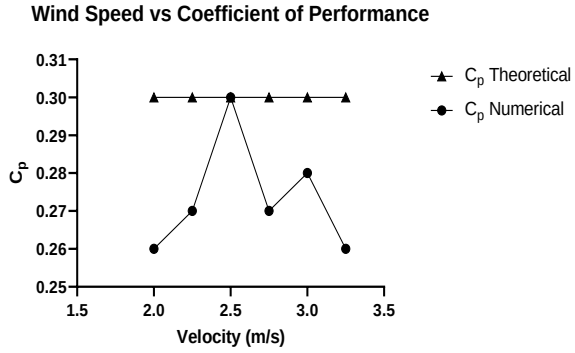

Figure 9. Relation between Velocity and C_p

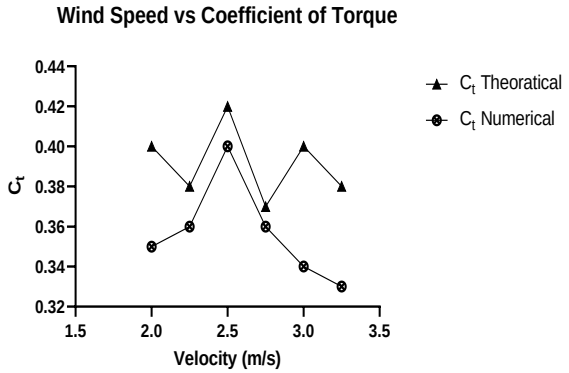

Figure 10. Relation between Velocity and Ct

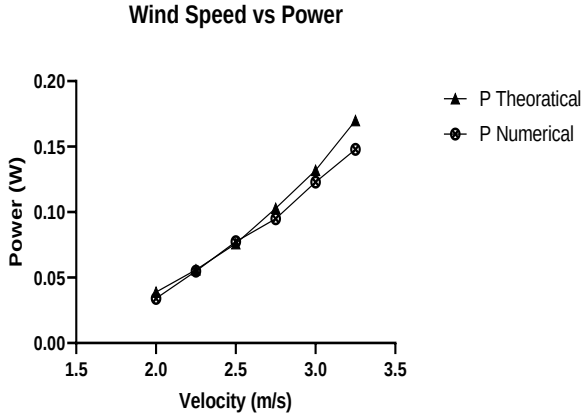

Figure 11. Relation between Velocity and Power

6 RESULTS DISCUSSIONS

From the results obtained in Figure 20, it can be seen that as the coefficient of performance of the turbine does not exceeds beyond a maximum theoretical Cp of savonius wind turbine which is 0.30. Cp of wind turbine being a dimensionless number shows how efficiently a turbine convert wind energy into electrical energy which is proportional to size, wind velocity and the properties of the fluid [15].

Results in Figure 21 shows that as we increased the speed of wind the Ct of turbine increases and then it decreases, this is because as we initially increases the wind speed the tip speed ratio increases upto 0.8 at which it gives maximum Ct after which as the TSR increases, Ct of the turbine decreased as turbine angular velocity increases causing torque to decrease [16] .

From the results obtained in Figure 22, It is evident that the power output of the turbine increases as the wind speed rises. As the power

output of the turbine is directly proportionate to area, wind velocity and fluid properties. As we raise the wind speed, the power of the turbine noticeably increases since the power output of the turbine increases with cube of velocity.

8 CONCLUSION

To determine the various parameters, a numerical study of the Savonius wind turbine was conducted that effect the performance of the wind turbines. Savonius wind turbine was selected because of its power generation capability at low wind speed [17]. We observed that how increase in velocity effects the savonius turbine's performance and the C_p of this turbine cannot increase beyond 0.3 which is the maximum power that can be obtained using savonius wind tubrine. Maximum Ct was obtained at 2.5 m/s which is 0.40 after which angular velocity increases rapidly causing Ct of the turbine to decrease. Also power output increases with wind speed and we can extract most of the useful wind energy from areas having high wind speed to be used as electrical energy.

REFERENCES

[1]. M. A. Qaisrani *et al.*, "Thermal losses evaluation of an external rectangular receiver in a windy environment," *Solar Energy*, vol. 184, pp. 281–291, May 2019, doi: 10.1016/J.SOLENER.2019.03.103.

[2]. M. Elgendi, M. AlMallahi, A. Abdelkhalig, and M. Y. E. Selim, "A review of wind turbines in complex terrain," *International Journal of Thermofluids*, vol. 17, p. 100289, Feb. 2023, doi: 10.1016/J.IJFT.2023.100289.

[3]. M. O. L. Hansen, "Aerodynamics of wind turbines: Third edition," *Aerodynamics of Wind Turbines: Third Edition*, pp. 1–173, May 2015, doi: 10.4324/9781315769981.

[4]. W. Xu, Y. Li, G. Li, S. Li, C. Zhang, and F. Wang, "High-resolution numerical simulation of the performance of vertical axis wind turbines in urban area: Part II, array of vertical axis wind turbines between buildings," *Renew Energy*, vol. 176, pp. 25–39, Oct. 2021, doi: 10.1016/j.renene.2021.05.011.

[5]. S. Meri Al Absi, A. Hasan Jabbar, S. Oudah Mezan, B. Ahmed Al-Rawi, and S. Thajeel Alattabi, "An experimental test of the performance enhancement of a Savonius turbine by modifying the inner surface of a blade," in *Materials Today: Proceedings*, Elsevier Ltd, 2021, pp. 2233–2240. doi: 10.1016/j.matpr.2020.12.309.

[6]. J. H. Lee, Y. T. Lee, and H. C. Lim, "Effect of twist angle on the performance of Savonius wind turbine," *Renew Energy*, vol. 89, pp. 231–244, Apr. 2016, doi: 10.1016/j.renene.2015.12.012.

[7]. C. Promdee and C. Photong, "Effects of Wind Angles and Wind Speeds on Voltage Generation of Savonius Wind Turbine with Double Wind Tunnels," in *Procedia Computer Science*, Elsevier B.V., 2016, pp. 401–404. doi: 10.1016/j.procs.2016.05.044.

[8]. S. Frikha, Z. Driss, H. Kchaou, and M. S. Abid, "Study of the Incidence Angle Effect on a Savonius Wind Rotor Aerodynamic Structure," in *CFD Techniques and Energy Applications*, Springer International Publishing, 2018, pp. 161–177. doi: 10.1007/978-3-319-70950-5_8.

[9]. A. S. Saad, I. I. El-Sharkawy, S. Ookawara, and M. Ahmed, "Performance enhancement of twisted-bladed Savonius vertical axis wind turbines," *Energy Convers Manag*, vol. 209, Apr. 2020, doi: 10.1016/j.enconman.2020.112673.

[10]. S. Brusca, R. Lanzafame, and M. Messina, "Design of a vertical-axis wind turbine: how the aspect ratio affects the turbine's performance," *International Journal of Energy and Environmental Engineering*, vol. 5, no. 4, pp. 333–340, Dec. 2014, doi: 10.1007/s40095-014-0129-x.

[11]. C. M. Parker and M. C. Leftwich, "The effect of tip speed ratio on a vertical axis wind turbine at high Reynolds numbers,"

Exp Fluids, vol. 57, no. 5, May 2016, doi: 10.1007/s00348-016-2155-3.

[12]. "MERRA-2." https://gmao.gsfc.nasa.gov/reanalysis/MERRA-2/ (accessed Apr. 13, 2023).

[13]. "Skewness and orthogonal quality mesh metrics spectrums. | Download Scientific Diagram." https://www.researchgate.net/figure/Skewness-and-orthogonal-quality-mesh-metrics-spectrums_fig2_320786408 (accessed Apr. 13, 2023).

[14]. "Help: SST K-Omega Turbulence Models." https://help.autodesk.com/view/SCDSE/2014/ENU/?guid=GUID-0F5C4828-9F91-46B6-A16A-2578D72DCFCC (accessed Apr. 13, 2023).

[15]. N. Van Bang and D. Rozehnal, "Determination of performance parameters of vertical axis wind turbines in wind tunnel," *MATEC Web of Conferences*, vol. 107, May 2017, doi: 10.1051/MATECCONF/201710700076.

[16]. K. A. H. Al-Gburi, B. A. J. Al-quraishi, F. B. Ismail Alnaimi, E. S. Tan, and A. H. S. Al-Safi, "Experimental and Simulation Investigation of Performance of Scaled Model for a Rotor of a Savonius Wind Turbine," *Energies (Basel)*, vol. 15, no. 23, Dec. 2022, doi: 10.3390/en15238808.

[17]. S. Meri Al Absi, A. Hasan Jabbar, S. Oudah Mezan, B. Ahmed Al-Rawi, and S. Thajeel Alattabi, "An experimental test of the performance enhancement of a Savonius turbine by modifying the inner surface of a blade," in *Materials Today: Proceedings*, 2021, vol. 42, pp. 2233–2240. doi: 10.1016/j.matpr.2020.12.309.

EFFECT OF FLOW RATE ON VARIOUS PARAMETERS OF ARCHIMEDES SCREW WATER TURBINE USING EXPERIMENTAL AND CFD ANALYSIS

Muhammad Ahsan Pervaiz Khan[1,*], Ali Raza[1], Dr. Muhammad Khurram[1], Saqib Naseer[2], Rizwan Shahid[2]

[1]Mechanical Engineering Department, National University of Technology (NUTECH) Islamabad, Pakistan

[2]Mechanical Engineering Department, NFC Institute of Engineering and Fertilizer Research centre, Faisalabad, Pakistan

[*]Corresponding author. Tel.: +92-334-6171761

E-mail address: ahsan.pervaiz@nutech.edu.pk (Muhammad Ahsan Pervaiz Khan)

ABSTRACT

Archimedes screw water turbine (ASWT) is the efficient technology to harness energy from water flowing at a low head. This turbine is usually installed where changing of flow rate is significant. This study investigates, how the power output of Archimedes Screw Turbines (AST) is affected at different flow rates. Computational Fluid Dynamics (CFD) simulations on ANSYS Fluent are performed to analyse the effect of flow rate on power output that is comprised of analysis of angular velocity, pressure, and torque. The experimental results of power output and efficiency at varying flow rates are compared to ANSYS numerical results and final the results are shown in plotted graphs. From CFD analysis, the maximum power output value at flow rate (42 L/s) is 175.26 watts, while corresponding experimental values of power output on the same flow rate (42 L/s) is 168 watts. Similarly, the efficiency which is obtained from numerical result is 92.17 % at the flow rate of 36 (L/s) while the corresponding experimental values of the efficiency on the same flow rate (36 L/s) is 90.8 %. Since, there are minor variations between experimental and numerical results which validate the model.

Keywords: CFD; Torque; Angular velocity; Pressure

1 INTRODUCTION

Hydropower is considered the renewable and clean electricity generation resource. It is highly efficient because the maintenance costs are very low [1]. The power obtained from a turbine depends upon the volume flow rate of water which is being passed through the screw and the head (i.e. highest difference above and below the turbine). The amount of potential energy available is proportional to the head. A major drawback while obtaining energy from a dam is the cost and resources required to plan and built a hydropower plant [2]. While Archimedes Screw turbine requires less cost as compared to a dam. Archimedes was credited due to invention of a screw that has been used as a pump initially to lift water for irrigation and drainage [3].

Moreover, ASWTs are fish friendly, small aquatic creatures can pass through the screws without any harm while maintaining the function of the Archimedes Screw Generator (ASG) itself. A study showed more than 98% of fish passed through the screw unharmed [4]. Initial ASWT experiments were conducted by Brada in the 1990s [5]. After that almost 400 ASWT units have been installed across Europe, with one in North America, which is grid-connected [6].

Our main objectives which will be discussed are CFD analysis to predict the power output for the specified prototype at a prescribed flow rate at a given location and experimental Validation with numerical results.

2 GOVERNING EQUATIONS

To calculate the power output, the formulas that are being used are: [7]

$P_{output}=T_{total} \times \omega$

Where,

$T_{total}=L\frac{LN}{P}$

$T=\int_{r=R_i}^{r=R_o} \cdot \int_{\theta=0}^{\theta=2\pi} dT$

$dT=(P_1-P_2)(\frac{P}{2\pi})\, rdrd\theta$

$Z_1= rcos\theta cos\beta - \frac{P}{2\pi} rdrd\theta$

Where z_1 =downstream flighting surface

$Z_2 = r\cos\theta\cos\beta - [\frac{P}{2\pi} - \frac{P}{N}]\sin\beta$

Where z_2=upstream of flighting surface

$\theta = 2[\frac{\omega}{P}]$

$\omega = \frac{P}{N}$

$Z_{wl} = Z_{min} + f[z_{max} - z_{min}]$

Where,

Z_{wl} = water level

f=fill level

$Z_{min} = -R_{\circ}\cos\beta - \frac{P}{2}\sin\beta$

$Z_{max} = R_i\cos\beta - P\sin\beta$

$f = \frac{\cos\beta\ D_{\circ}}{(0.5)\cos\beta[D_{\circ} + Di] - \sin\beta\ P}$

$P = \begin{Bmatrix} \rho g(Zwl - z) \\ 0 \end{Bmatrix}$ Where, $z \geq Zwl$

$Q = NV\omega\ 2\pi$

$V = \int_{r=R_i}^{r=R_{\circ}} \cdot \int_{\theta=0}^{\theta=2\pi} dv$

Where,

$dv = \begin{Bmatrix} 0 \\ \frac{Zwl - z1}{z2 - z1} \\ \frac{P}{N} drd\theta \end{Bmatrix} \frac{P}{N} drd\theta$

Where,

$z_2 > Z_{wl}$, $z_1 > Z_{wl}$

$z_2 > Z_{wl}$, z_1

$z_2 < Z_{wl}$, $z_1 < Z_{wl}$

$Pavail = \rho Qgh$

$\eta = \frac{Pout}{Pavail}$ X 100

3 GEOMETRY OF SCREW

The geometry of this Screw is as following which is according to our specific location, located in District Faisalabad, Punjab, Pakistan.

Table 1. Geometry Parameters

Parameters	Values	Units
Outer dia	4	Inches
Inner dia	8	Inches
Number of blades	3	----------
Pitch	13	Inches

3.1 CFD Parameters

The parameters that were used to run simulations on the Archimedes Screw Turbine include model, algorithm, scheme and boundary conditions, etc. and their further details follow.

Table 2. Ansys Parameters

Model	k-epsilon model
Approach	Moving Frame of reference (MRF)
Pressure Velocity Coupling (scheme)	Coupled
Special Discretization Gradient	Least Squares Cell Based
Pressure Scheme	Second Order
Momentum	Second Order Upwind
Turbulent K.E	Second Order Upwind
Specific Dissipation Rate	Second Order Upwind
Transition Formulation	Second Order Implicit
Convergence Criteria	$1e{-}4$

The modelling of turbulent structures in the flow field is the most crucial step to be taken in the computation process. This turbulent structure happens throughout a range of timescales and lengths, making it difficult to develop a model that can account for every scenario. For the simulation of turbulent flow, there are many different turbulence models available.

The study's model is an adaptation of the standard k-epsilon. The turbulent flow analysis method used by the k-epsilon turbulence model is known as the field of fluctuation velocity. Due to the rapid flow rate and uneven motion of the fluid particles, this turbulent flow results in turulence or uncontrolled effects. Moving speed has fluctuated as a result of numerous mixed changes on the move, including species of momentum, energy, and concentration. The K-Epsilon model adds two transport equations, which are based on k and ε variables and are given in [8]

$\frac{\partial}{\partial t}(pk) + \frac{\partial}{\partial Xj}(pkUj) = \frac{\partial}{\partial Xj}[(\mu + \frac{\mu t}{\sigma k})\frac{\partial k}{\partial Xj}] + Gk + Gb - \rho\varepsilon - YM + Sk$

$\frac{\partial}{\partial t}(pk) + \frac{\partial}{\partial Xj}(pkUj) = \frac{\partial}{\partial Xj}[(\mu + \frac{\mu t}{\sigma k})\frac{\partial k}{\partial Xj}]$
$+\rho C_1 S\varepsilon - \rho C_2 \frac{\varepsilon 2}{k + \sqrt{v\varepsilon}} + C1_{\varepsilon}\frac{\varepsilon}{k}C_3 G_b + S\varepsilon$

Boundary Conditions

These are the boundary conditions that are being used in the analysis.

Table 3. Boundary Conditions

Sr. No.	Region	Boundary condition
1	Inlet	Mass Flow Inlet
2	Outlet	Pressure outlet
3	Wall	Wall
4	Turbine	Wall
5	Flow domain	Interior

Contours

After the setup, calculations were performed on 1000 iterations, and after the iterations following results has been obtained.

A. Pressure Contours

After the opening post process, pressure contours on t h e turbine location according to the pressure range of the experimental site are created. The results are shown below in figure 1.

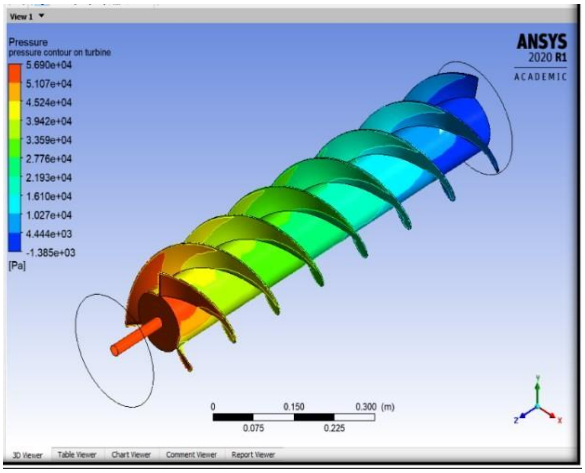

Figure 1. Pressure Contour of Screw Blades

B. Velocity magnitude contour

After creating the pressure contours the velocity contours on the turbine location with variable velocity in an instant frameare created according to the pressure range of the experimental site as it can be shown in the following figure 2.

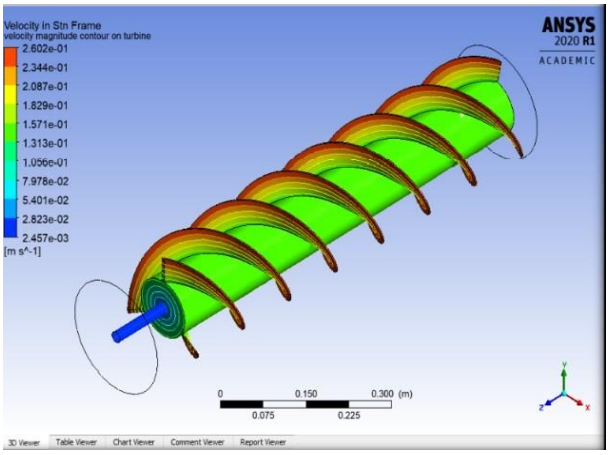

Figure 2. Velocity Contour of Screw Blades

C. Selection of location (plane)

In the post process, the location plane at YZ & X axis is selected to validate the Bernoulli relation at specific locationson the turbine as shown in figure 3.

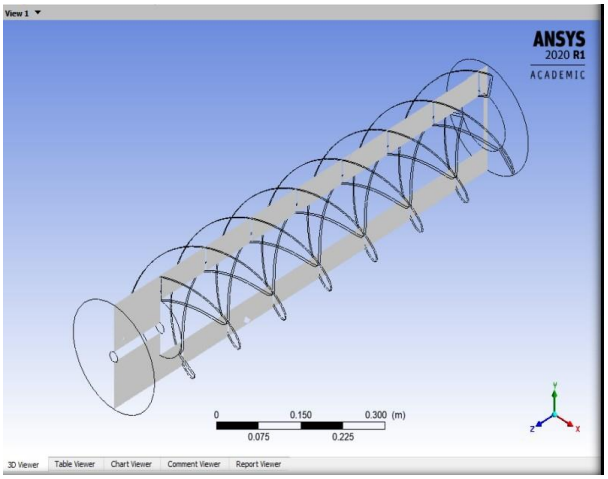

Figure 3. Plane Selection on turbine blade

D. Pressure and velocity contours at the selected plane

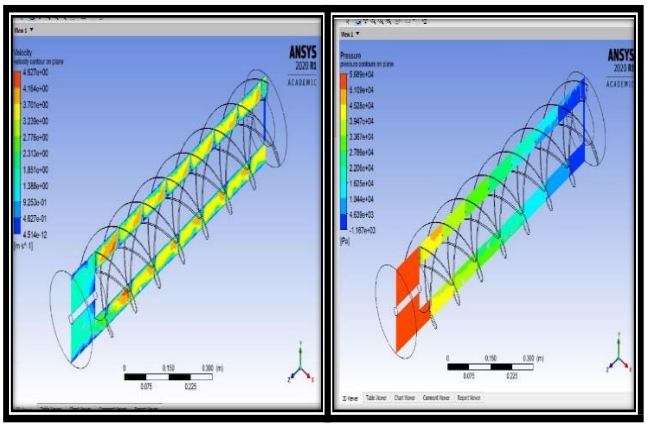

Figure 4. Pressure and velocity contours on selected planes

From figure 4, it is clear that the pressure and velocity contours are inverse to each other, which

means that the point where the velocity contour is maximum, and the pressure contours are minimum and this relation validates the Bernoulli principle.

E. Streamlines

In post process, to show the direction of water flows upon turbine blades streamline counters have been created which are shown in figure 5 below;

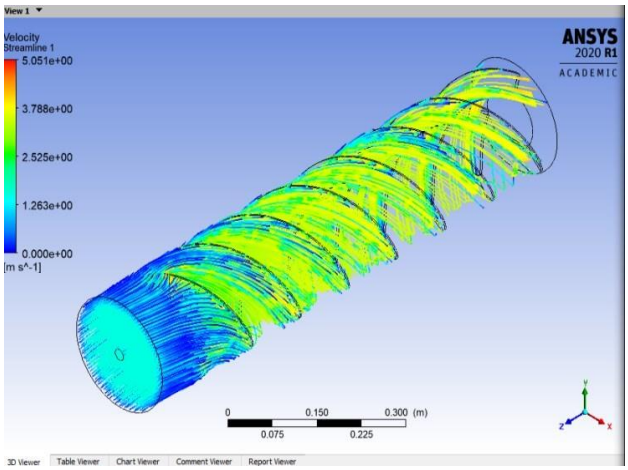

Figure 5. Streamlines of water flow across the turbine

4 RESULTS AND DISCUSSION

The numerical results that have been obtained from Ansys will now be represented in graphs and that will explain the relationship between torque and flow rate at different angular velocities. Similarly, the variation of output power & efficiency with respect to flow rate will be shown with the help of graphs.

The graphs which will be discussed are as follows

a) Torque vs flow rate at ω = 20 rad/sec
b) Torque vs flow rate at ω = 26.1799 rad/sec
c) Torque vs flow rate at ω = 30 rad/sec
d) Output power vs flow rate
e) Efficiency vs flow rate
f) Angular velocity vs power output at Q=28(l/s)
g) Angular velocity vs Efficiency at Q=28(l/s)

Torque vs flow rate at ω = 20 rad/sec

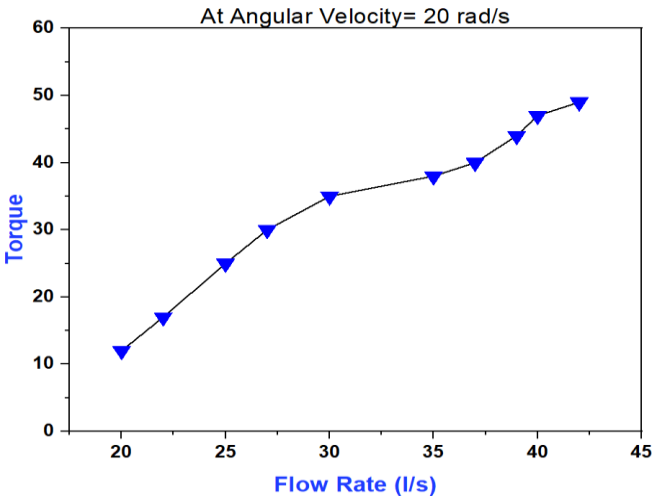

Figure 6. Torque vs Flow Rate at ω = **20 *rad/sec***

From figure 6, it can be seen that there is a linear relationship between torque and flow rate at an angular velocity of 20 rad/sec which actually explains the direct relation between torque and flow rate. From deduced results, the maximum value of torque occurs at 42(l/s) which is 48 Nm

Torque vs flow rate at ω = 26. 1799 *rad/sec*

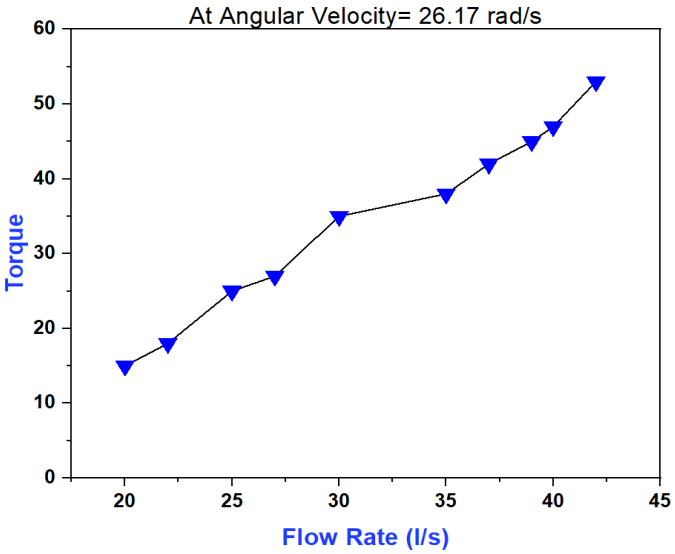

Figure 7. Torque vs Flow Rate ω = **26.17 *rad/sec***

From figure 7, it can be clearly predicted that after changing the value of angular velocity from 20 to 26.17(rad/sec) there will be no effect on the trend between torque and flow rate. So, according to the graph, there is a direct relation between torque and flow rate but this graph shows an increment in torque values at the same flow rate that was given in the previous graph. From the graph, it can be seen

clearly that the maximum value of torque on the same flow rate 42(l/s) is 53(Nm) which was 48 (Nm) at ω=20 rad/sec at the same flowrate.

Torque vs flow rate at ω = 30 rad/sec:

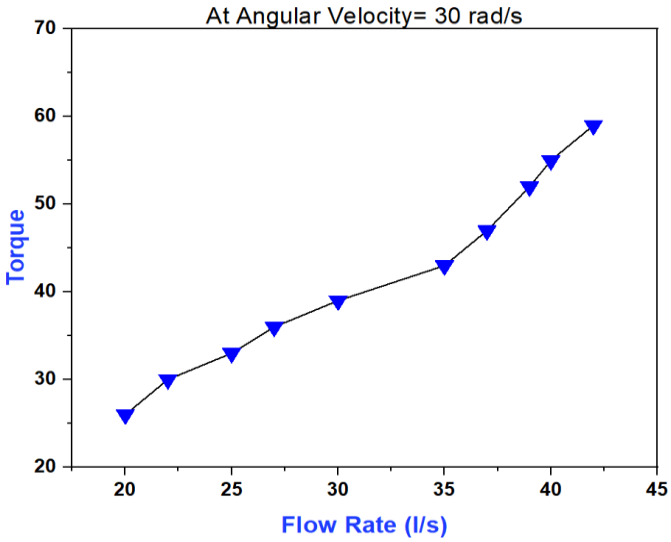

Figure 8. Torque vs Flow Rate ω = 30 rad/sec

From figure 8, again trend between torque and flow rate remains the same even at an angular velocity of 30(rad/sec). There is a jump in torque values rate as compared to values on lower values of angular velocities at the same flow rate. Here, at 42(l/s) the value of torque is 59 (Nm) which was 48Nm and 53 Nm at ω=20 rad/sec and ω=26.17 rad/sec respectively.

Output power vs flow rate:

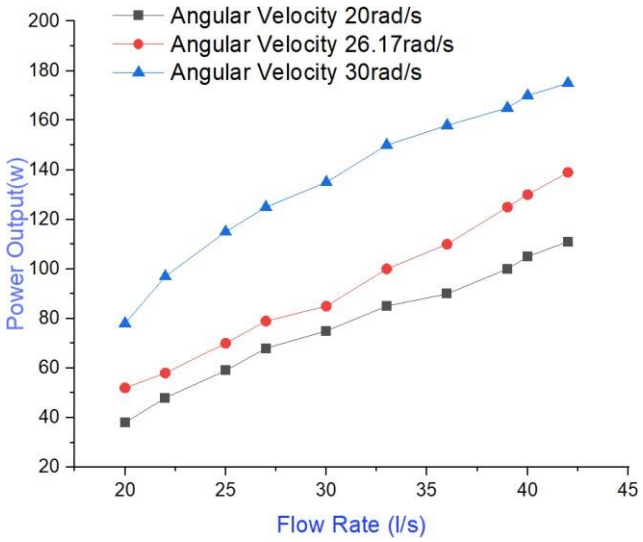

Figure 9. Power output vs Flow Rate

Figure 9 actually shows the comparison between power output obtained at different flow rates at three different constant angular velocities whose values are ω=20 rad/sec, ω=26.17 rad/sec, and $\omega = 30\ rad/sec$ respectively. From the graph, it can be seen that at $\omega = 30\ rad/sec$, the power output is maximum at a flow rate of 42 L/s, which is 175.1487 watts.

Efficiency vs flow rate:

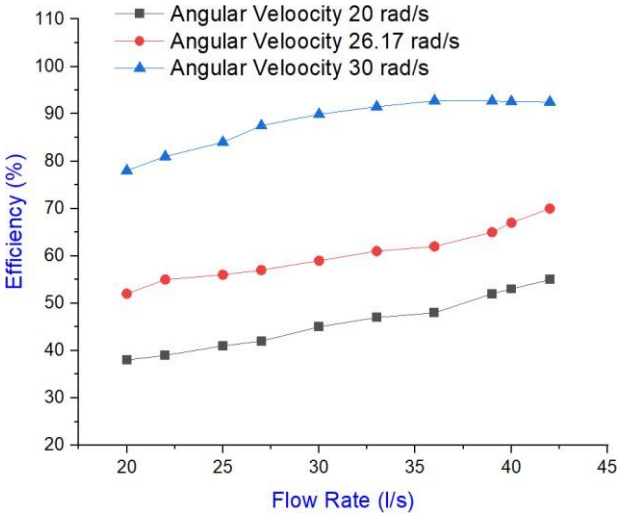

Figure 10. Efficiency vs Flow Rate

Figure 10 actually shows the comparison between efficiency obtained at different flow rates at three different constant angular velocities whose values are ω=20 rad/sec, ω=26.17 rad/sec and $\omega = 30\ rad/sec$ respectively. From the graph, it can be seen that at ω = 30 rad/sec, efficiency is maximum at a flow rate of 36 L/s, which is 92.76%. From graph it can be observed that at higher values of angular velocities the efficiency increases till specific limit then trend line becomesconstant even at higher flow rates. It is basically because of design limitation of this turbine. This is actually a prototype turbine which can work up to specific limit of flow rate.

Angular velocity vs Power Output:

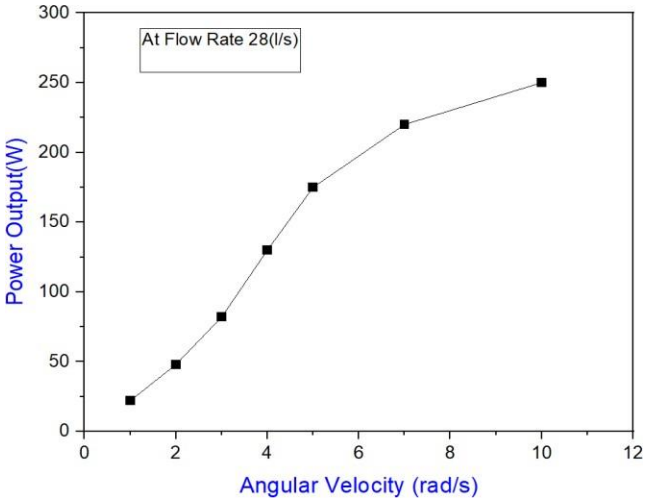

Figure 11. Power Output Vs Angular Velocity (rad/sec)

Figure 11 basically helps us to understand the dependence of power output on angular velocities. From the graph, it can be seen that there is direct relation between power output and angular velocities. From graph it can be seen that the maximum output power is 260 watts at 15 rad/s on a constant flow rate of 28 L/s.

Angular Velocity Vs Efficiency:

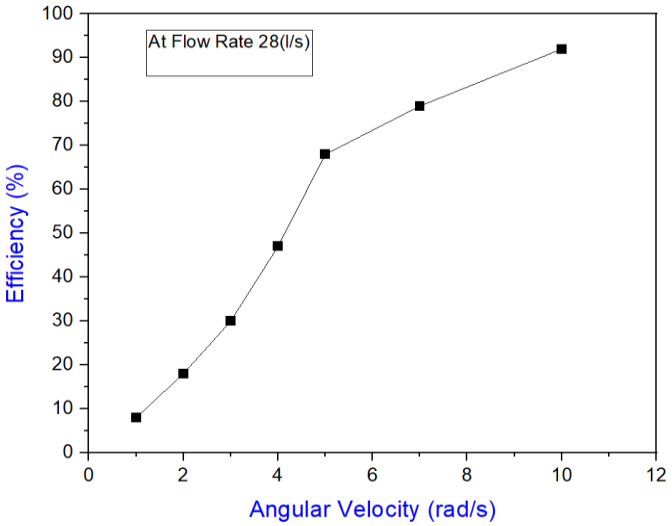

Figure 12. Power Output Vs Angular Velocity (rad/sec)

Similarly, figure 12 predicts that how efficiency will changeat different angular velocities of turbine screw. From the graph it can be seen that efficiency is directly proportional to angular velocity and maximum efficiency is 93% at 15 rad/s on a constant flow rate of 28 L/s.

Flow Rate vs Power Output:

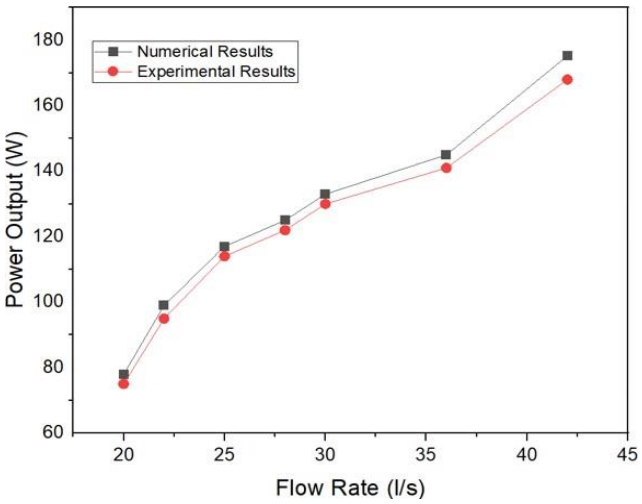

Figure 13. Power Output Vs Flow Rate (L/sec)

This is the comparison between numerical and experimental results. Both experimental and numerical results shows directrelation between flow rate and power output. The maximum experimental value is 170.261 watt while, maximum numerical result is 175.14 watt at constant flow rate of 42 L/s. The difference between the experimental and numerical values is some loses which occur during experiments.

Flow rate vs Efficiency:

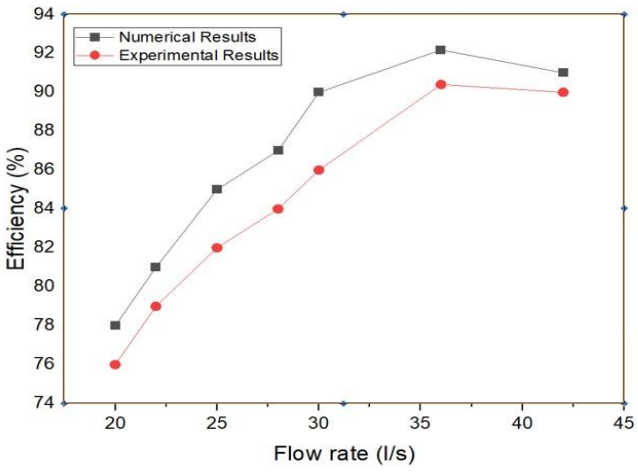

Figure 14. Efficiency Vs Flow Rate (L/sec)

This is the comparison between numerical results and Experimental results at a constant angular velocity of 30 rad/sec. This graph predicts the model validation as there is coherence between experimental and numerical results. The maximum experimental and numerical values are 92.17% and 90.25 % at 36 (L/s) respectively.

5 CONCLUSION

CFD analysis of this ASWT is performed that predicts the output power of ASWT and then experimentation has been done at the selected site. It is also observed that power output increases with increase in flow rate and maximum power output achieved at 42 (L/s) which is 170.26 watts, whereas the efficiency of 90.25 % at flow rate of 36 (L/s) achieved from experimental results. While, on the basis of numerical results, maximum power output which is obtained is 175.14 watts at flow rate of 42 (L/s) and maximum efficiency is 92.17% at flow rate of 36(L/s) achieved. Similarly, there is also direct relation between power output and angular velocity where maximum power output occurred at 15 rad/s which gives 260 watt and efficiency of 93%. It is observed that there is a small difference between numerical and experimental results which is justifiable.

REFERENCES

[1]. Hatch, E. (2008). Low head hydro market assessment: main report: vol. 1.

[2]. Lyons, M. (2014). Lab testing and modeling of Archimedes screw turbines (Doctoral dissertation, University of Guelph).

[3]. Rorres, C. (2000). The turn of the screw: Optimal design of an Archimedes screw. Journal of hydraulic engineering, 126(1), 72-80.

[4]. McNabb, C. D., Liston, C. R., & Borthwick, S. M. (2003). Passage of juvenile chinook salmon and other fish species through archimedes lifts and a hidrostal pump at red bluff, California. Transactions of the American Fisheries Society, 132(2), 326-334.

[5]. Brada, K. (1999). Spiral turbine enables power generation by small hydropower plants; Wasserkraftschnecke ermoeglicht Stromerzeugung ueber Kleinkraftwerke. MM- Maschinenmarkt, 105.

[6]. Lashofer, A., Hawle, W., & Pelikan, B. (2012). State of technology and design guidelines for the Archimedes screw turbine. Proceedings of the Hydro.

[7]. Kotronis, I. K. (2016). Low Head Hydropower: A Performance Improvement Study for Archimedes Screw Turbines Using Mathematical Modelling (Doctoral dissertation, Lancaster University (United Kingdom)).

[8]. Raza, A., Mehboob, H., Miran, S., Arif, W., & Rizvi,

[9]. S. F. J. (2020). Investigation on the characteristics of biodiesel droplets in the engine cylinder. Energies, 13(14), 3637.

ENVIRONMENTAL AND FINANCIAL FEASIBILITY OF A SOLAR-POWERED AIR-CONDITIONING SYSTEM FOR A PASSENGER TRAIN IN PAKISTAN

Haris Riaz[1,*], Muhammad Asim Ghaffar[1], Salman Aziz[1], Ahmad Bilal[1]
[1]Mechanical Engineering Department, University of Engineering & Technology, Lahore, Pakistan

[*]Corresponding author. Ph.: +92-309-6743842
E-mail address: harisriazofficial2@gmail.com (Haris Riaz)

ABSTRACT

The study focuses on designing a stand-alone solar system for the air-conditioning system of a passenger train, specifically the 10DN Allama Iqbal Express which travels from Sialkot to Karachi. The maximum cooling load of the passenger train cabin was calculated using the HAP software, and a compressor was selected based on ASHRAE MT RGT 95° F Standard, requiring a power input of 9.95 kW. The stand-alone solar system was designed in PVsyst software for a power requirement of 10.95 kW, including a factor of safety for power production and inverter power loss. An inverter was introduced to provide AC to the compressor.

Carbon emission reduction and payback period for the usage months of the system were calculated, and the results showed that the stand-alone solar system resulted in the reduction of 17.4 metric tonnes of carbon emissions. Furthermore, the payback period of 4 years and 4 months indicated that the system can be financially viable over its lifespan. Overall, this study highlights the environmental and financial feasibility and potential benefits of using stand-alone solar systems for passenger trains in Pakistan, underscoring the importance of considering renewable energy sources for powering trains.

Keywords: stand-alone solar system; Hourly Analysis Program (HAP); PVsyst

1 INTRODUCTION

The increasing energy demand worldwide has had a negative impact on the environment due to the use of traditional energy sources. This has led to a growing interest in the use of renewable energy sources, one of the most promising alternatives being solar energy. Solar energy has gained significant attention in recent years in the transportation sector as a potential solution to reducing greenhouse gas emissions and mitigating the impacts of climate change.

Pakistan has heavily relied on imported oil to meet its energy needs, resulting in a significant trade deficit. The primary energy supply consists of 33.1% natural gas, 22.6% oil, and 18.2% coal.[1] In 2020, Pakistan imported petroleum products of USD 10.31 billion,[2] and its trade deficit stood at USD 21.11 billion.[3] This heavy reliance on imported oil not only leads to a trade deficit but also exposes the country to the volatility of international oil prices.

Shifting towards renewable energy sources could help reduce Pakistan's oil consumption, ultimately lowering the oil import bill and the trade deficit. Additionally, it could stimulate local job creation and provide economic benefits in the long run. The adoption of renewable energy sources will also reduce carbon emissions, contributing to a cleaner and healthier environment.

The transportation sector in Pakistan is responsible for a significant amount of the country's greenhouse gas emissions due to its heavy reliance on fossil fuels.[4] Thus, there is a need to explore alternative energy sources for transportation systems in Pakistan. Several studies have explored the feasibility of using solar energy in the transportation sector. Research by Jaffery et. al (2012) found that a solar-powered high-speed passenger rail system is a viable alternative to the existing non-renewable fossil fuel-based rail system in Pakistan, offering numerous benefits, including reduced traffic congestion, improved air quality, and decreased reliance on imported fuels.[5] Similarly, a study by

Omar et. al (2021) explores the feasibility of implementing solar panels as an alternative source of electricity for the Light Rail Transit (LRT) System in Malaysia, proposing the use of solar PV technology to reduce energy pollution and climate change impact. The study shows that the use of solar panels as a renewable energy source could be a viable solution for the LRT System, with potential benefits, including reduced environmental impact and improved sustainability.[6]

Furthermore, Kilic et. al (2017) explore the feasibility of using photovoltaic (PV) technology for the interior lighting of urban rail vehicles to reduce greenhouse gas emissions, and the study proposes the use of PV panels for urban rail vehicles as a means of reducing greenhouse gas emissions.[7] Similarly, Vasisht et. al (2017) report on the performance of solar photovoltaic modules mounted on the rooftop of a rail coach of The Indian Railways. The statistical model developed in the study enables The Indian Railways to calculate the benefits of operating solar rail coaches on various routes.[8] Research conducted by Nazir et. al (2019) proposes a solution to the high energy consumption of electric railways, i.e., a grid-tied PV solar plant with battery storage. The study suggests installing solar panels along the ballast-less tracks of a high-speed rail network to generate electricity from sunlight.[9] Another study by Loannidis et. al (2019) investigates the application of a solar-powered bus route to a small-scale transportation system, such as a university campus, presenting three scenarios for harnessing solar power, and investigating their optimal technical configuration, energy generation, and capital costs.[10]

Moreover, S.H.I. Jaffery (2014) proposes the utilization of solar energy for the development of a solar-powered railway transport system in Pakistan, to meet the country's energy demands and aid economic growth. The study aims to utilize renewable energy resources within the country to combat the ever-increasing energy deficit that has led to the severe economic slowdown in Pakistan. The feasibility of a solar-powered air-conditioning system for a passenger train in Pakistan is investigated, with the study assessing the potential of a solar-powered air-conditioning system to reduce greenhouse gas emissions and operating costs compared to traditional air-conditioning systems.[11] Overall, these studies highlight the potential of solar energy in the transportation sector as a viable solution to reduce greenhouse gas emissions, improve air quality, and decrease reliance on imported fuels.

The study aims to evaluate the feasibility of a solar-powered air-conditioning system for a passenger train in Pakistan. The need for sustainable energy sources has increased significantly in recent years due to the depletion of non-renewable energy resources and their negative effects on the environment. As the transportation sector is a major contributor to global carbon emissions, the use of renewable energy sources has become increasingly important. Solar energy, in particular, has gained attention as a promising alternative to traditional fossil fuels.

The focus of this study is on designing a stand-alone solar system that can meet the power requirements of an air-conditioning system for a passenger train cabin in Pakistan. The use of such a system would offer a reliable source of cooling for passengers during train travel while also reducing the train's carbon emissions. The study also aims to assess the financial and environmental feasibility of the system by calculating its carbon emission reduction and payback period for the usage months.

The results of this study are expected to contribute to the development of sustainable and environmentally friendly transportation systems in Pakistan. The study emphasizes the importance of considering renewable energy sources for powering trains and highlights the potential for reducing carbon emissions and promoting sustainable transportation solutions. As such, this research is novel and significant and may provide valuable insights into the feasibility and potential benefits of using stand-alone solar systems for passenger trains.

2 METHODOLOGY

This study aims to assess the viability of implementing a solar-assisted air conditioning system in Pakistan from both environmental and financial perspectives. To accomplish this goal, a train cabin was chosen, and the cooling load was calculated utilizing HAP software for the summer season (Apr-Sep). After determining the cooling load requirement, a compressor capable of producing the required level of cooling for an air-conditioning system was chosen. The selection of the compressor was essential for estimating the electric power needed to maintain the required level of cooling within the train cabin. Subsequently, the PV system was designed using PVsyst software to generate the necessary electric power. The reduction in carbon emissions resulting from the consumption

of electric power generated by the PV system was then calculated. Also, the financial feasibility of the system was assessed by calculating the payback period.

The methodology is described in detail in the following sections.

Table 1. Construction of train cabin [12]

Sr. #	Name	Quantity	Area (m^2)
1	Roof	1	79.56
2	Floor	1	79.56
3	Side Walls	2	113.1
4	Doors	4	2.9
5	Windows	24	0.69

2.1 Train Cabin Dimensions

The train cabin CHN YZ25G was selected for the cooling load calculations. The construction and material properties details of the train cabin are given in Tables 1 and 2.

2.2 Modelling System in HAP

The train cabin is modelled in HAP by feeding all the construction, material properties and other details.

Route & Scheduling

The train route of 10DN Allama Iqbal Express was selected for analysis which travels from Sialkot to Karachi. It takes approximately 24 hours to complete this journey. During the journey, the train passes by several cities which are mentioned in Table 2. Figure 1 shows the train route on the map.

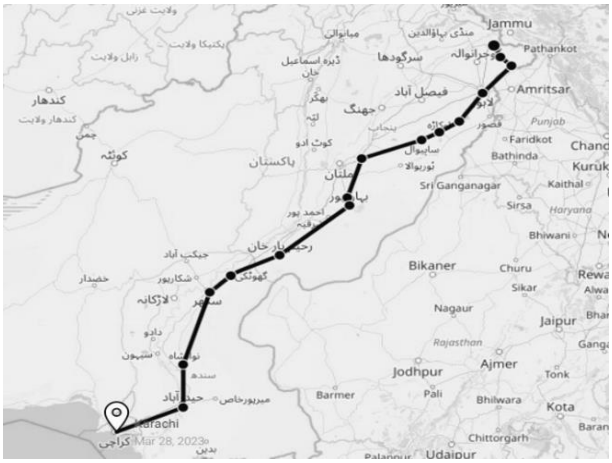

Figure 1. Train route on map

Cabin Direction

The train cabin is a dynamic system that undergoes movement and directional changes during operation. To account for these dynamic effects, the cooling load analysis of the train cabin was performed by rotating it in eight different directions with a 45-degree resolution. These directions include North, South, East, West, South-East, South-West, North-East, and North-West. By considering the impact of train cabin movement in the cooling load analysis, a more accurate assessment of the cooling load requirements can be obtained, which is essential for ensuring the efficient and effective operation of the train cabin's air-conditioning system.

2.3 Cities Selection

The Hourly Analysis Program (HAP) only contains weather data for Karachi city and does not contain weather information for other cities in Pakistan. However, the available weather data for Karachi is outdated. As a result, we manually input the dry bulb temperature, coincident wet bulb temperature, elevation, and maximum and minimum design dry bulb and wet bulb temperatures for summer months into the HAP software to estimate the cooling load for various cities on our train route. This approach enables us to calculate the cooling load requirements for different locations with greater accuracy and specificity, even when weather data is not readily available or up to date in the software. Such precise calculations are crucial for determining the accurate cooling load.

Table 2. List of Major Cities on the train route

Sr. no.	Cities
1	Sialkot
2	Pasror
3	Narowal
4	Lahore
5	Pattoki
6	Okara
7	Sahiwal
8	Khanewal
9	Lodhran
10	Bahawalpur
11	Rahimyar Khan
12	Nawab Shah
13	Hyderabad
14	Karachi

2.4 Compressor Selection

The selection of the compressor was based on the cooling load requirements using Danfoss software, which is designed to comply with the ASHRAE

Table 3. Construction and Material Properties of Train Cabin [12]

Layer	Material	Thickness (mm)	Density (kg/m)	Specific Heat (kJ/kg.K)	Thermal Conductivity (W/m.K)	Weight (kg/m^3)
Outboard	Steel	2	7850	0.48	50	15.7
Middle	Glass Wool	74	200	1.22	0.08	14.8
Inboard	Wood	20	300	01.89	0.093	6

(American Society of Heating, Refrigerating and Air-Conditioning Engineers) MT RGT 95º F rating conditions standard. This standard specifies the operating parameters of air conditioning systems and is appropriate for the climatic conditions of the cities included in our route. By utilizing this standard, we can ensure that the compressor is chosen according to the specific cooling requirements of our system and that it is capable of operating efficiently and effectively under a range of environmental conditions. This approach allows us to estimate the power required by the air-conditioning system to operate for our required application. The specification of the selected compressor is mentioned in Table 4.

Table 4. Specification of Compressor [13]

Type	Variable-Speed Scroll Compressor
Model & Manufacturer	Danfoss VZH117CGM
Refrigerant	R454B
Power Input (for Max. Cooling)	9.95 kW
Swept Volume	116.9 cm^3
Nominal Speed at 50Hz	3000 RPM
Max. Cooling Capacity	44.3 kW
Phase	3
Compressor Power Supply	50Hz 380-480V

2.5 PVsyst Analysis

The HAP software was used to calculate the cooling load, which will be used as a basis for designing our solar system. It enabled us to estimate the power required by the compressor to achieve the necessary level of cooling. Since the train travels through multiple cities on its route, it was crucial to establish a consistent basis for calculating power generation. To accomplish this, we gathered data on solar irradiance for the cities on our train route from the web application "POWER | Data Access Viewer" by

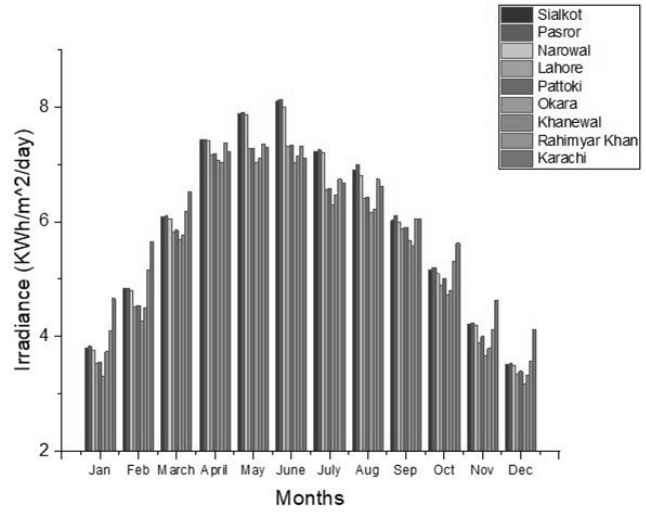

Figure 2. Monthly Solar Irradiance Data for Selected Cities on Train Route [14]

NASA.[14] Figure 2 displays the result of the comparison.

From Figure 2, it is evident that the mean overall irradiance for Lahore city is lower compared to other cities throughout the year. Using this information as a basis, we designed the PV system using PVsyst software for Lahore city, to introduce a factor of safety in power production. Lahore was chosen due to its relatively low irradiance, as meeting our power requirements in a city with minimal irradiance would ensure that the system could generate adequate power in other cities with higher irradiance.

The design process begins by selecting the 'Stand-Alone' system design and importing the meteo file for Lahore city. The next step is to determine the optimal orientation of the solar panels. Due to the movement of the train, a tilt angle at a specific degree according to a specific location and direction would not be feasible for the entire route. Therefore, the

solar panels are given a fixed tilt angle of 0 degrees and an azimuth angle of 0 degrees with the panels facing due south. Once the panel orientation is established, the power requirements of the system, are defined. Following this, appropriate batteries and PV panels are selected based on the parameters suggested by PVsyst software. By utilizing the software's recommendations and optimizing the system design, we can ensure that the solar system generates adequate power to meet our air conditioning system's requirements.

2.6 Inverter Selection

The inverter also needs to be selected as it is responsible for providing AC to the compressor to enable its operation. When selecting the inverter, it is important to ensure that its rated power is higher than that of the compressor. Moreover, it must be compatible with the current and voltage being supplied through the battery to ensure the efficient operation of the system.

2.7 Carbon Emissions

To calculate the reduction in carbon emissions resulting from the installation of a PV system to power the air-conditioning system, the number of litres of fuel saved is calculated. Typically, a diesel generator consumes 0.32 litres of diesel per kWh of energy production at its rated power, which can be used to determine the number of litres of fuel saved by using the solar-powered air-conditioning system.[15] According to the US Environmental Protection Agency (EPA) report, 1 litre of diesel when burnt generates 734 grams of carbon content.[16] Thus, once the number of litres of fuel saved is determined, the corresponding reduction in carbon emissions can be calculated.

2.8 Payback Period

The payback period can be calculated by determining the total investment cost and the savings per month using Equation 1.

$$PP = \frac{C_i}{S_m} \quad (1)$$

Where 'PP' is the payback period in months, C_i is the total cost of investment (USD), and S_m is the saving per month (USD/month).

3 RESULTS & DISCUSSION

3.1 Cooling Load using Carrier HAP

Cooling load for 9 selected cities on the route was calculated using the HAP for eight different directions, i.e., N, S, E, W, NE, NW, SE, and SW. The results for these selected cities corresponding to the mentioned directions are summarized in Figure 3.

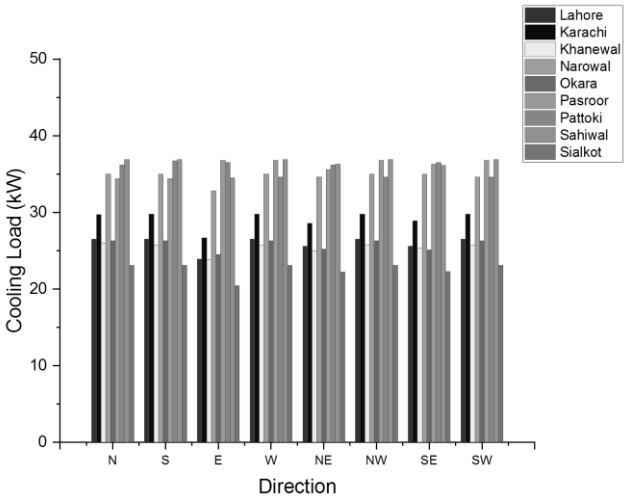

Figure 3. Cooling Load Requirements for the cities on train route in all directions

The cooling load analysis revealed that the city of Sahiwal in the West and Northwest directions had the highest peak load of 36.9 kW. This maximum load value was used as a reference to determine the air-conditioning system's required input power. Applying a Factor of Safety (FOS) of 1.2, we selected a compressor with a maximum cooling capacity of 44.3 kW, which will be powered by the solar system. The breakdown of the cooling load by type is presented in Figure 4, which shows that the occupants contribute the most to the load, followed by the windows and walls, respectively.

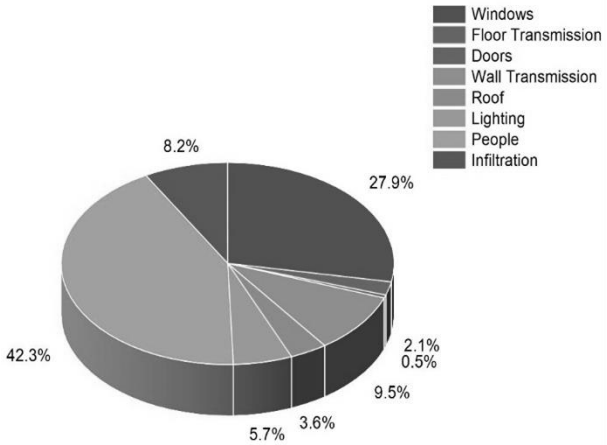

Figure 4. Breakdown of Cooling Load Requirement by Load Type

3.2 PVsyst

The power requirement for the compressor was estimated, and then a PV system was designed using PVsyst software. The PV system is found to be working with a performance ratio of 74.4% and a solar fraction of 1 during the summer months (April-September) as shown in Figures 5 and 6. A solar fraction of 1 indicates that the PV system can meet the air-conditioning system's power requirements during the summer months. This performance is even more remarkable since the city with the lowest irradiance was selected, indicating even higher PV system performance in other cities. Based on the PVsyst software, the suggested installation involves 72 AE 400DGLM6 PV modules with a nominal power of 400 W each, with 3 strings of 24 modules in series to make a total nominal power of 28.8 kW. PVsyst also recommended using 6 LG Chem JH4 SR19_2P battery racks in parallel with a total nominal capacity of 889 Ah and employing a Universal MPPT Controller compatible with the system. The total area covered by the modules is 144 m^2, which indicates that the modules will cover the roofs of two train cabins.

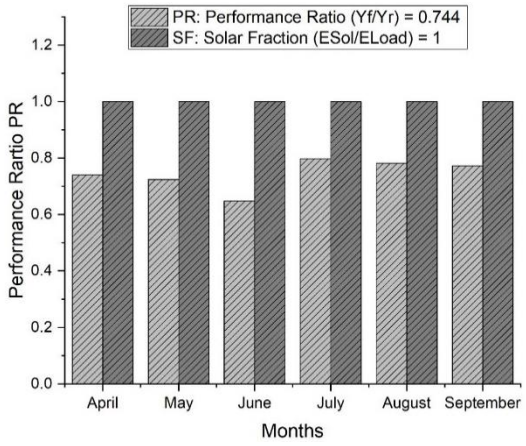

Figure 5. Performance Ratio and Solar Fraction of PV System in usage months

3.3 Inverter Selection

The selected inverter for the air-conditioning system is the ***15kW Fronius Symo Advanced Lite 15.0-3 480V 3-Phase Inverter***. It is selected due to its compatibility with both the battery and compressor and has a rated power of 15 kW, which is higher than the compressor's power rating of 9.95 kW.

3.4 Carbon Emissions

The installation of a PV system to power the air-conditioning system in a single train cabin resulted in a significant reduction of 17.4 metric tonnes of carbon emissions in usage months (Apr-Sep). Given that a typical train usually consists of three air-conditioned cabins, utilizing PV systems for the other two cabins of the same train and for other trains operated by Pakistan Railways, has the potential to achieve a substantial reduction in carbon emissions, amounting to hundreds of metric tonnes.

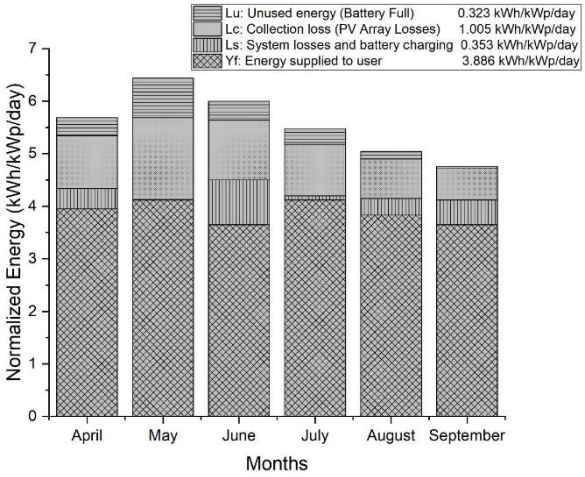

Figure 6. Normalized Energy Production by PV system in usage months

3.5 Payback Period

The investment cost and savings generated per month for the proposed solar-powered air-conditioning system are detailed in Tables 5 and 6, respectively. The prices of the components were estimated based on the local market. By using Equation 1, the payback period for the system is calculated to be 25 usage months. However, as the system is only used for 6 months, the payback period extends to 4 years and 4 months. Figure 7 demonstrates the cash-flow diagram of PV system. These findings provide valuable insight into the financial feasibility of implementing a stand-alone solar system for air-conditioning on passenger trains in Pakistan. It indicates that the proposed solar-powered air-conditioning system is financially feasible and viable.

Table 5. Breakdown of Investment Cost

Component	**Price (USD)**
PV Panels	12000
Battery Racks	6000
Inverter	2700
Controller	650
Accessories	2100
Total Investment Cost	**23450**

Table 6. Savings Per Month

Fuel Saved per Tour (Litres)	84.1
Estimated Tours per Month	12
Fuel Saved per Month (Litres)	1009.2
Diesel Price per Litre	$0.93
Amount Saved Per Month	**$942**

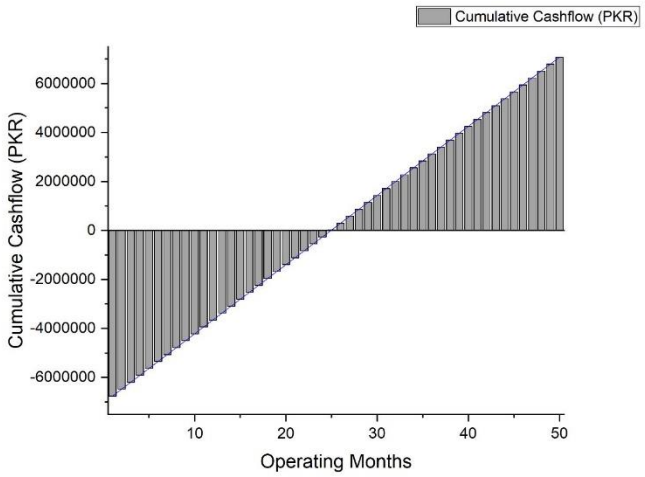

Figure 7. Cash Flow Diagram for PV System

4 CONCLUSION

To conclude, the main objective of this study was to determine the environmental and financial feasibility of solar-powered air-conditioning system for trains. The cooling load calculation for the train cabin was performed using HAP, and a maximum cooling load of 36.9 kW was determined for the city of Sahiwal in West and Northwest directions. A Danfoss VZH117CGM variable-speed scroll compressor was chosen with a factor of safety of 1.2 to provide maximum cooling of 44.3 kW while using a maximum of 9.95 kW of power. Using PVsyst, a PV system was designed for the air conditioning system, providing 10.95 kW of power while accounting for inverter losses. The appropriate PV panels, controller, and batteries were selected as per PVsyst recommendations. The simulation was conducted for the city with the minimum irradiance on the train route, i.e., Lahore. By utilizing the PV system, it was estimated that the carbon emissions could be reduced by 17.4 metric tonnes per year during usage months (Apr-Sep). The payback period for the system was determined to be 25 operating months that extends to 4 years and 4 months. This study presents a feasible solution to reduce carbon emissions and achieve financial feasibility through the implementation of a solar-powered air-conditioning system for trains.

ACKNOWLEDGEMENTS

The authors are thankful to Dr Muhammad Usman and Chairman Mechanical Engineering Department, UET Lahore for supporting this work.

CONFLICT OF INTEREST

The authors of this research study declare that they did not have any commercial or financial relationships that could potentially create a conflict of interest. Furthermore, all authors contributed equally to the preparation and revision of this manuscript, and there are no conflicts of interest to report.

REFERENCES

[1]. 'Pakistan Energy Demand Forecast (2021-2030)', Ministry of Planning, Development & Special Initiatives Government of Pakistan, IEP Report-1, Oct. 2021.

[2]. S. Akram, 'Petroleum Sector of Pakistan and its Trade Dynamics', Trade Development Authority of Pakistan, TDAP-PETROLEUM.

[3]. M. A. Shah, 'Exports, Imports and Balance of Trade', State Bank of Pakistan.

[4]. A. G. Bhatti, A. R. Bhatti, I. A. Chaudry, and M. N. Javed, 'Energy Crisis In Pakistan, Adaption And Mitigation Measures', *Journal of Faculty of Engineering & Technology*, vol. 19, pp. 67–82, 2012.

[5]. S. Jaffery, H. Khan, M. Khan, and S. Ali, *A study on the feasibility of solar powered railway system for light weight urban transport*. 2012.

[6]. W. A. W. Omar, G. Hayder, A. Aldrees, and A. T. B. Taha, 'Feasibility study on use of solar energy in Malaysia's light rail transit', *IOP Conf. Ser.: Earth Environ. Sci.*, vol. 708, no. 1, p. 012042, Apr. 2021, doi: 10.1088/1755-1315/708/1/012042.

[7]. B. Kilic and E. Dursun, 'Integration of innovative photovoltaic technology to the railway trains: A case study for Istanbul airport-M1 light metro line', in *IEEE EUROCON 2017 -17th International Conference on Smart Technologies*, Jul. 2017, pp. 336–340. doi: 10.1109/EUROCON.2017.8011131.

[8]. M. Shravanth Vasisht, G. A. Vashista, J. Srinivasan, and S. K. Ramasesha, 'Rail coaches with rooftop solar photovoltaic systems: A feasibility study', *Energy*, vol.

118, pp. 684–691, Jan. 2017, doi: 10.1016/j.energy.2016.10.103.

[9]. C. Nazir, 'Solar Energy for Traction of High Speed Rail Transportation: A Techno-economic Analysis', *Civil Engineering Journal*, vol. 5, pp. 1566–1576, Jul. 2019, doi: 10.28991/cej-2019-03091353.

[10]. R. Ioannidis *et al.*, 'Solar-powered bus route: introducing renewable energy into a university campus transport system', in *Advances in Geosciences*, Copernicus GmbH, Dec. 2019, pp. 215–224. doi: 10.5194/adgeo-49-215-2019.

[11]. S. H. I. Jaffery *et al.*, 'The potential of solar powered transportation and the case for solar powered railway in Pakistan', *Renewable and Sustainable Energy Reviews*, vol. 39, pp. 270–276, Nov. 2014, doi: 10.1016/j.rser.2014.07.025.

[12]. W. Liu, Q. Deng, W. Huang, and R. Liu, 'Variation in cooling load of a moving air-conditioned train compartment under the effects of ambient conditions and body thermal storage', *Applied Thermal Engineering*, vol. 31, no. 6, pp. 1150–1162, May 2011, doi: 10.1016/j.applthermaleng.2010.12.010.

[13]. 'Danfoss Scroll Compressor VZH117CGAMA 120G0309'. Danfoss. Accessed: Apr. 20, 2023. [Online]. Available: https://store.danfoss.com/ae/en_GB/Climate-Solutions-for-cooling/Compressors/Compressors-for-air-conditioning/Inverter-compressors/Scroll-compressor%2C-VZH117CGAMA/p/120G0309

[14]. 'POWER | Data Access Viewer'. NASA. Accessed: Apr. 20, 2023. [Online]. Available: https://power.larc.nasa.gov/data-access-viewer/

[15]. A. Q. Jakhrani, A. R. H. Rigit, A.-K. Othman, S. R. Samo, and S. A. Kamboh, 'Estimation of carbon footprints from diesel generator emissions', in *2012 International Conference on Green and Ubiquitous Technology*, Jul. 2012, pp. 78–81. doi: 10.1109/GUT.2012.6344193.

[16]. 'Emission Facts: Average Carbon Dioxide Emissions Resulting from Gasoline and Diesel Fuel', United States Environmental Protection Agency, EPA420-F-05–001, Feb. 2005.

INVESTIGATION OF FLUID ELASTIC INSTABILITY EFFECT ON GROOVED TUBE HEAT EXCHANGER USING IN-LINE SQUARE ARRANGEMENT

Hassan Shawar Shah[1,*], Muzaffar Ali[1], Muhammad Ammar Akram[2], Asif Durez[3], Fawad Yousaf Malik[4]

[1]Mechanical Engineering Department, University of Engineering & Technology, Taxila, Pakistan

[2] Mechanical Engineering Department, HITEC University, Taxila Cantt, Pakistan

[3] Mechanical Engineering Department, National University of Technology, Islamabad, Pakistan

[4] Mechanical Engineering Department, Swedish College of Engineering & Technology, Wah Cantt, Pakistan

[*]Corresponding author. Tel.: +92-334-5419249

E-mail address: Hassan.shawar@students.uettaxila.edu.pk (Hassan Shawar Shah)

ABSTRACT

This research paper is related to fluid elastic instability in the heat exchanger, which is taken from the groove tube an in-line square tube bundle arrangement with a P/D ratio of 1.28 and a subsonic wind tunnel is used with single-phase cross flow. The tube vibration is measured through an accelerometer which is attached to the groove tube. The streamwise and transverse direction instability is almost the same until reduce velocity is 28.5 m/s, however when the reduced velocity cross 35.5 m/s, the transverse direction amplitude response is indicated as higher than the streamwise direction for all rows. The maximum resultant amplitude response is 1.13 percent of the tube diameter indicated in the third row, which is higher than the fourth and second rows. The fourth and second rows of the resultant amplitude response indicated 0.593 percent of tube diameter and 0.497 percent of tube diameter at a reduced velocity is 69.8 m/s.

Keywords: *In-line Square Tube Arrangement; Fluid-Elastic Instability; Groove Tube; Reduce Velocity; Heat Exchanger*

1 INTRODUCTION

The nuclear industry has been extremely concerned about flow-induced vibration in heat exchangers for many years. There are several events of heat exchanger failures caused by apparent flow-induced vibration. There have been several reported cases of tube failure in commercial steam generators [1].

Flow velocity is higher through the tube bundle bank of the shell and tube-type heat exchanger. Three mechanisms are caused by flow-induced vibration in these structures. When the fluid flow across a bluff body, vortices shedding is produced due to fluid striking with the bluff body then two layers are created, one of the outer layers has a higher flow velocity than the inner layer which has a low velocity then these layer difference creates the vortex shedding, fluid elastic instability phenomenon occurs when fluid energy passing through the tube, there is some of the energy expended on the damping structure [2].

Many experiments have been conducted to analyse the flow-induced vibration of tubes, especially U-bend tubes and straight tubes [3]. Fluid elastic instability happened in the transverse direction to the flow at Reynold number 800 [4]. The experiment was performed on the U-tubes in a two-phase cross-flow analysis of the vibration. Fluid elastic instability was observed from an experiment in the transverse direction and parallel direction in the U-tubes [5].

Created a time domain model for fluid elastic instability forces in tubes with slack supports. The pattern may be used to determine the critical flow velocity, the tube reaction, and the force that would cause the tube to strike the support [6]. The fluid elastic instability experiment had been organized a multiply in tube array and understanding the phenomenon to helped. The experiment was conducted on the square array with a pitch-to-diameter ratio was 1.45 and recognizing that flow-induced dynamic coefficient and flow-induced vibrations in two configurations of the tube bundle

emanate were observed in the light of Tubular Exchange Manufacturers Association (TEMA) [7]. Chung and Che conducted the experiment of rotated square and normal square tube arrangement with a pitch-to-diameter ratio of 1.633. tube vibration measured through by strain gauge [8].

The fluid elastic instability of a U-tube array with P/D = 1.633 in two-phase cross flow was experimentally examined. To figure out Connor's equation instability constant, measured [9]. When the fluid pass the through the tube bundle fluid elastic instability occurs, when the threshold of the fluid elastic instability was lesser than the flow reduced velocity, then due to impact vibration between the support structures and tube bundle, it was the early harm of the tube bundles [10].

The experiment was performed on the tube bundle and the result of the experiment found that the amplitude of the turbulence-induced vibration of the tube increase constantly. When the reduce velocity is below the theshold of the fluid elastic instability [11]. In this paper, the crack produces due to cross flow and loose support, analysis that when the flow reduces velocity increases crack and loose support become more visible and when the vibration of the crack tube cause serious damage to the fretting wear [12]. When the fluid elastic instability was analysis in cross flow in parallel direction then it was static instability in the tube bundles and when the fluid flow reduce velocity greater than the critical value divergence of the system occurs, changing the position of static equilibrium and the two-phase flow the void fraction had an important result on the critical velocity of the streamwise fluid elastic instability. The fluid elastic instability of the tube bundles threshold was increased constantly in a parallel direction and resulted in the void fraction of the two phase flow increase [13]. When the void fraction was increased the total damping ratio in each tube bundle was also increased [14].

1.1 Tube Bundle Arrangements

Heat transfer from one fluid to another fluid is used heat exchanger device. Tube bundle arrangement is an important factor in the heat exchanger. The counter flow heat exchanger achieves maximum heat transfer. Tube bundle arrangement is an important to factor, however, four types of tube bundle arrangement, are shown in Figure 1 (a) and (b).

a) In-Line Square
b) Rotated Square
c) Parallel Tri-angular
d) Normal Tri-angular

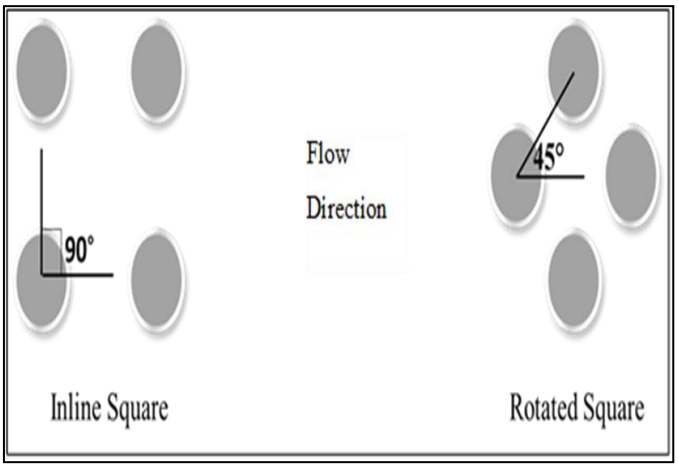

Figure 1. (a) Tube Array Geometry in Heat Exchanger [15]

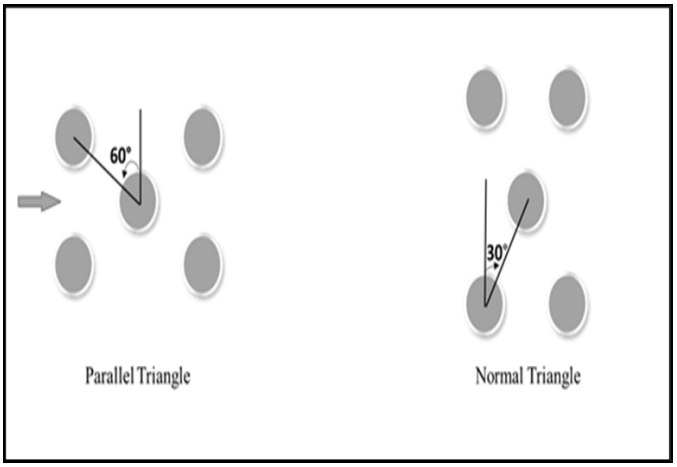

Figure 1. (b) Tube Array Geometry in Heat Exchanger [15]

To increase the heat exchanger efficiency, a high flow velocity is also preferred. When the high flow fluid pass through between the tubes is called pitch velocity, the pitch velocity can be determined by the given equation (1) [16]

$$U_p = \{P/(P-d)\}\ U \qquad (1)$$

The equation (1) represents the upstream velocity is U_p, the tube diameter d and P is the pitch.

1.2 Drag effect on groove cylinders

Drag is an aerodynamic force caused by fluid interaction with a solid body. Reynold number has influences on the force, and it is expressed in a non-dimensionalized version known as the drag coefficient. The force increases as the air velocity increase in the diameter of the cylinder.

The coefficient of drag on the circular cylinder from the following equation (2)

$$C_d = 2F_d/(A\rho\mu^2) \qquad (2)$$

Where the density of ρ, drag force F_d platform Area A, and velocity is μ.

The v-groove cylinder had shown a lower drag coefficient than the rough cylinder [17]. When the wedge-shaped longitudinal groove-type external flow was analysed, fractional drag had been decreased. When groove height was less than around 25 in terms of the law of the wall coordinates drag had been reduced [18]. When the grooves were at roughly 80 degrees, they were most effective. There was a closely observed in a shallow groove, they are nevertheless functional. The impact of dimples on golf balls is said to be similar to the effect of grooves [19].

The highest heat transfer enhancement attained for the grooved tube was as an until 63 percent, the trapezoidal groove 58 percent, and the rectangular groove 47 percent, in comparison with the smooth tube. The thermal performance of all existing grooved pipes was 1.28 to 1.24 for circular grooves, trapezoidal grooves for 1.25 to 1.22, and rectangular grooves for 1.26 to 1.13 at constant power with Reynold number ranges from 10,000 to 38,000. The ideal value for the entropy generation number was about Reynold number 17,000 for all types of grooved pipes [20].

The cactus model outperformed the circular model in terms of stream-wise turbulent velocity, vorticity attachment to the cylinder surface, and after the cylinder velocity deficit. The cactus wake had a lower shear than the circular model. Improve a heat can cause vorticity with strong greater effect and stretching as well as more severe vortex and vortex interactions and unsteadiness [21].

1.3 Experimental Work on Crossflow Induced Vibration

The experiment was conducted in a wind tunnel with a test section of dimensions 125 mm width, 125 mm height and 420 mm length. 28 tubes, 8-row parallel triangular array was tested. The other specification of the array were D_o= 13 mm, t_{wall}=1.3 mm, L= 125 mm, P/D =1375 and the Reynold number ranges from 0.63 to 12700. The result predicted that the mode change occurs instantaneously throughout the array. At certain flow velocities, each of the instrumented cylinder pressure signals were showed strong co-relation. Pressure changes in the array result in two stable state flow all over the array almost simultaneously (Koegh & Meskell, 2015) [22].

The test was conducted in a wind tunnel with a test section of dimensions 0.3 m width, 1.2 m height and 2.3 m length. Two cylinders were used to conduct a test with an aluminium shaft placed at the cylinder centre. The other specification of the cylinder is mass (m) = 0.241 *kg,* mass ratio (m^*) = m/m_f – 204.5, damping ratio (ζ) = 0.0035, mass*damping ratio (m*ζ) = 0.71, f_n= 10 Hz, T^* = T/D =0.1-3.2, Aspect Ratio =4.4, a polyethylene flexible sheet is attached with a mass(m) of 1.32 g and 0.02 mm thickness with the cylinder to suppress the flow induced vibrations. The conditions for free stream velocity vary from 0.6 to 40 m/s. reduced velocity range from 1.5 to 26 Reynolds number range from 4365 to 74200. The different characteristics of vibration patterns are observed (Kim & Alam,2015) [23].

I. $0.1 < T^* < 0.2$, both cylinder vibrates with maximum amplitude at the same reduced velocity (10.47 m/s).
II. $0.2 < T^* < 2.1$, both cylinder vibrates with maximum amplitude at the smaller reduced velocity.
III. $2.1 < T^* < 3.2$, Maximum amplitude produce each of the cylinder as an isolated cylinder.
IV. The FIV of both cylinder in patterns III and IV were successfully suppressed by the flexible sheet, and pattern I amplitude was minimized.

Table 1. Summary of the experimental work on drags and lift force

Researcher	Frequency	Model	Flow Type	Method	Remarks
(Javed Farrokhi and Derakh-shandeh, 2022) [24]	75≤Re ≤ 200	Square grooved shape ($\theta=45^0$ & 90^0)	Laminar Flow	Finite Volume Method (FVM) ANSYS-Fluent	Amplitude of lift and drag coefficient for the down-stream greater because it constantly the vortex shedding
(Afroz Sharif, 2021) [25]	Reynold numbers vary from 50 to 300	Circular cylinder triangular V-shaped the U-shaped and rectangular shaped grooves	Laminar cross flow	ANSYS Fluent Code	Reynold number, pressure drag is reduced more success-fully in U-grooves coefficient, lift coefficient, viscous drag coefficient, mean and maximum force

Derakhsha-ndeh and Gharib 2020) [26]	Reynold number varies from 50 to 200	Grooved circular cylinder square, triangular and dimple	2D viscous flow grooves are located at ($\theta = 0^0$, 30^0, 45^0, 60^0 and 90^0)	Finite volume method using ANSYS fluent	A triangular groove geometry at 46^0 decrease the drag coefficient by up to 100%

The research work concludes that the tube bundle arrangement and pitch ratio is an important factor for fluid elastic instability. The current research on the groove tube has revealed that the third row is found to be more unstable than all other rows.

2 EXPERIMENTAL SETUP

2.1 Wind Tunnel and Facility

The experiment has been carried out in the subsonic wind tunnel which was developed by GUNT and the model HM-170 which is shown in Figure 2. The tube bundle was mounted inside the test section. The test section was a square shape with dimensions was 300 mm length and 300 mm width.

Figure 2. Subsonic Wind Tunnel

Air is sucked from outside of the wind tunnel and which pass through the pre-chamber, which is also called the contraction section air flow enters this part airflow becomes laminar and parallel to the test section, it passes through the diffuser then the axial fan is delivered out to the surrounding area. The fluid flow speed can change from the valve. The subsonic wind tunnel schematic layout is shown in Figure 3.

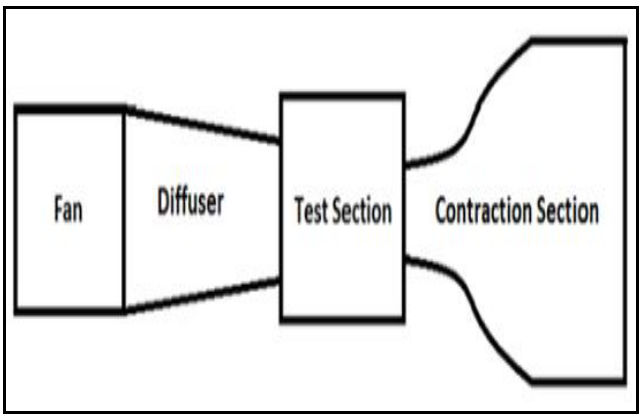

Figure 3. Subsonic Wind Tunnel Schematic Diagram

Studies by Ralston presented that when boundary layers on the test section front and rear walls are excluded, the flow in the test section was uniform to within 1 percent at the test section entry and 2.5 percent at the axial midway [27].

The parameter for tube bundle arrangement is shown in Table 2.

2.2 Accelerometer

The accelerometer was installed on the top of the flexible tube under observation shown in Figure 4 (a). when the tube vibrates because of the fluid flow, the sensor senses the deflection in the tube and transfers the signal to the wireless base station connected to PC where the signal was observed in a software Node commander. The data was analyzed by using another software known as SigView.

Accelerometer is devised which consists of G-Link Bluetooth tri-axial acceleration measuring node along with the WSDA Bluetooth USB Base station shown in Figure 4(b), which was connected with the PC through Node Commander. The accelerometer specification is shown in Table 2.

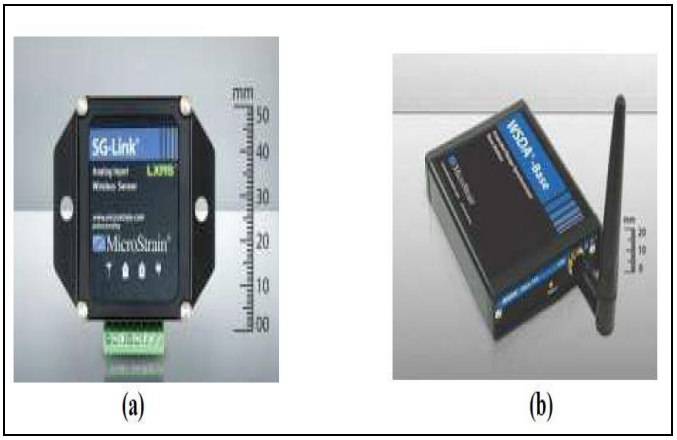

Figure: 4. (a) SG Wireless Node (b) WSDA Base Station

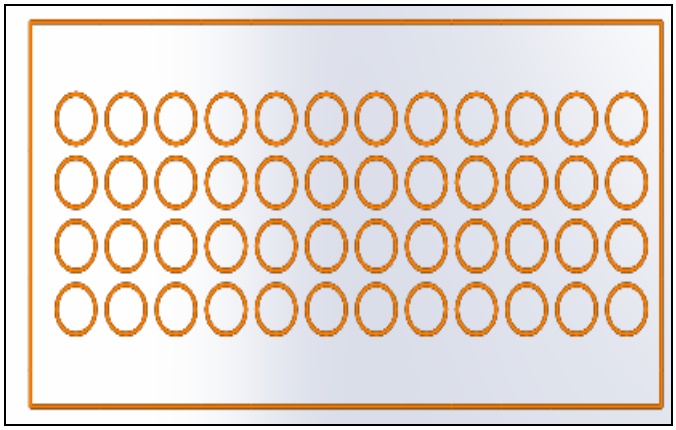

Figure 5. In-Line Square Arrangement Baffle Plate

Inline square tube arrangement of baffle plate is shown in Figure 5, which distance between one cylinder to another cylinder is 16.13 mm, this is called pitch distance. Tube diameter is 12.80 mm. This arrangement is kept constant for this experiment. When the arrangement is changed then all experiment result would be changed.

Table 2. Parameter of Tube Bundle

Pitch to Diameter Ratio	1.28
Tube Bundle Arrangement	In-Line square
Column x Row	12 x 4
Total Number of Tubes	48
Groove Tube Width and Depth	3 mm & 2 mm
Length of monitored groove tube	324 mm

Table 3. Parameter of Accelerometer

Specifications	
Accuracy	0.1%
Maximum Measuring Range	-98.1 to 98.1 m/s^2
Sampling Rate	317.5 per second

2.3 Signal Analysis

- The data acquisition is shown in Figure 6. To analyse the signal received from the accelerometer, which is attached to the groove tube in the in-line square tube bundle. The signal is monitored and saved using software i.e., "Node Commander."
- The software saves the data in the form of an excel file. To analyse the signal, the form of excel files is copied into text files and then "SIGView" software is used for data analysed.

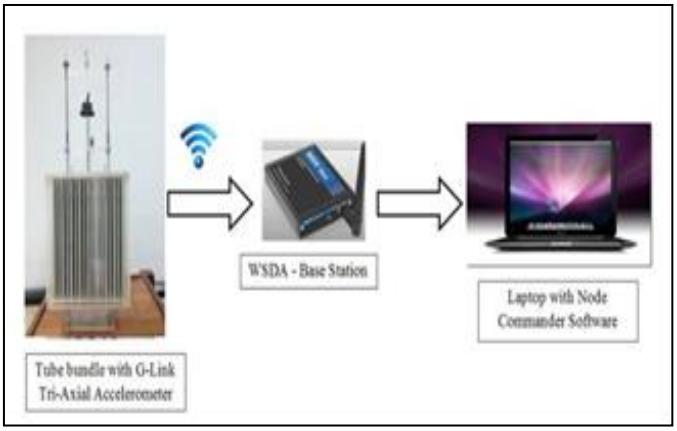

Figure 6: Data Acquisition Loop

3 RESULT AND DISCUSSION

Researchers conducted many experiments on circular tubes and examined the instability in single flexible tubes in a rigid array which strongly depends on the number of rows and the tube location.

In this experiment, four rows are used in the tube bundle and analysis of the groove tube instability where it is using varying fluid flow velocity, in which minimum flow velocity is taken 2.2 m/s and maximum flow velocity 10.2 m/s.

3.1 Groove tube natural frequency

The different heat exchanger has different natural frequency, so the heat exchanger of the tube bundle has a natural frequency that is taken 8 Hz to 25 Hz. Groove tube natural frequency is taken that, initially excited and then set free vibration for natural frequency. We have established a natural frequency between 9.5 Hz to 10.5 Hz of the in-line square tube bundle for the second row to the fourth row. Figure 7 (a) is shown the time Domain versus Amplitude of the third row which is taken at 9.92 Hz and Figure 7 (b) is shown the FFT signal of vibration where the maximum amplitude response is approximately 0.11 m/s^2.

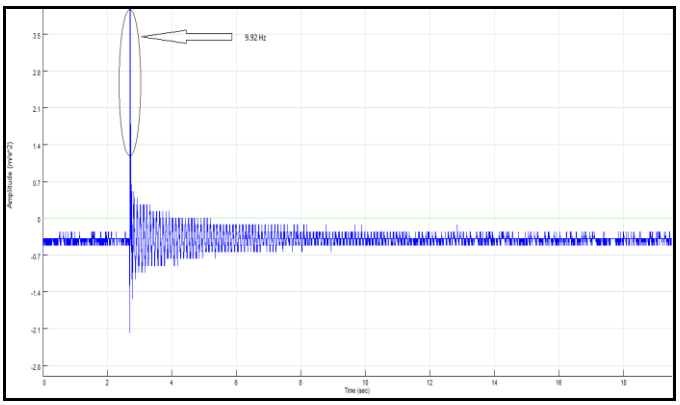

Figure 7. (a) Groove Tube Vibration Response

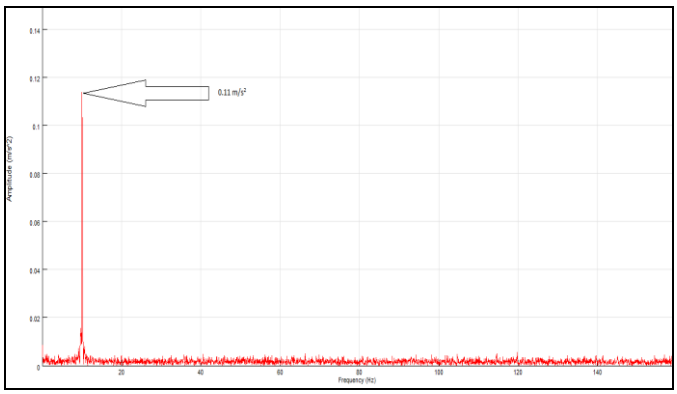

Figure 7. (b) FFT signal of vibration

3.2 Amplitude Response of Transverse and Stream-wise Direction of Groove Tube

Figure 8 represent the reduced velocity versus RMS amplitude (%d_o), it is indicated the amplitude response of streamwise and transverse direction of instability at different reduce velocity. However, at the start of until 15.0 m/s amplitude response is below approximately 0.05 percent of tube diameter at both transverse direction and streamwise direction. When the reduced velocity increased and reached 35.6 m/s, at that point transverse direction amplitude response is increased and the streamwise direction amplitude remains the same as previous of the reduced velocity. When the reduced velocity is 62.9 m/s, the amplitude response of transverse and streamwise directions are indicated a gap between them. It is revealed that the transverse direction amplitude response is higher compared to the streamwise direction. The maximum amplitude response of the transverse direction is 0.4402 percent of tube diameter, and the streamwise direction amplitude response is 0.231 percent of tube diameter, which is indicated at a reduced velocity of 69.8 m/s.

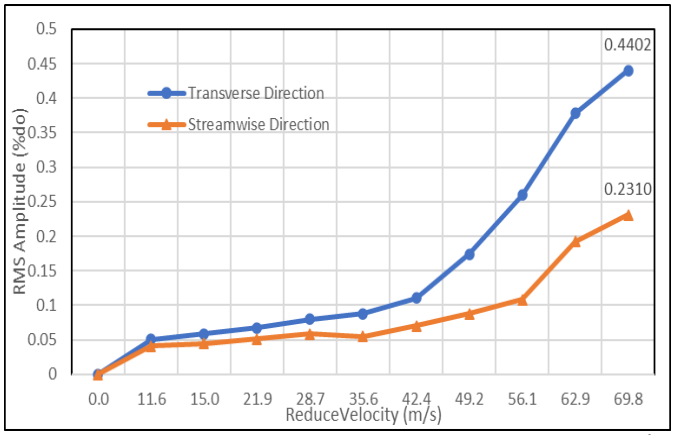

Figure 8. Single Flexible Groove Tube of 2nd Row

In Figure 9 graph is shown 3rd row of the groove tube where the stream-wise and transverse direction of instability is the same until at a reduced velocity of 35.6 m/s, however when the reduced velocity increased transverse direction amplitude response increased and the streamwise direction amplitude is lower than the transverse direction. The transverse direction maximum amplitude response is 1.13 percent of the tube diameter, and the streamwise direction maximum amplitude response is nearly 0.4615 percent of the tube diameter at a reduced velocity of 69.8 m/s.

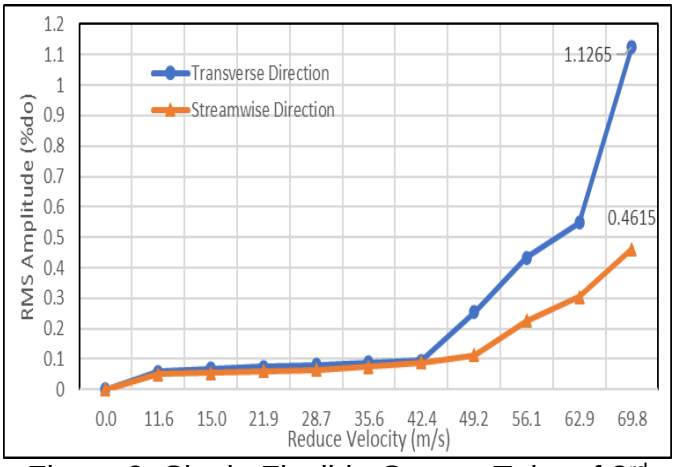

Figure 9. Single Flexible Groove Tube of 3rd Row

Figure 10 is shown that streamwise and transverse direction amplitude response is almost the same until 33.5 m/s, which is below 0.05 percent of tube diameter. The reduced velocity of 56 m/s at transverse amplitude is indicated as 0.29 percent of the tube diameter, which is higher than the streamwise direction amplitude response of 0.17 percent of the tube diameter.

The maximum amplitude response is 0.49 percent of the tube diameter in the transverse direction and the maximum amplitude response is 0.34 percent of the tube diameter in the streamwise direction both are at the reduced velocity of 69.7 m/s. From third row graph and fourth-row graph revealed that the in-line square tube bundle arrangement maximum instability is indicated in the third row and fourth row. The second row is indicated low instability.

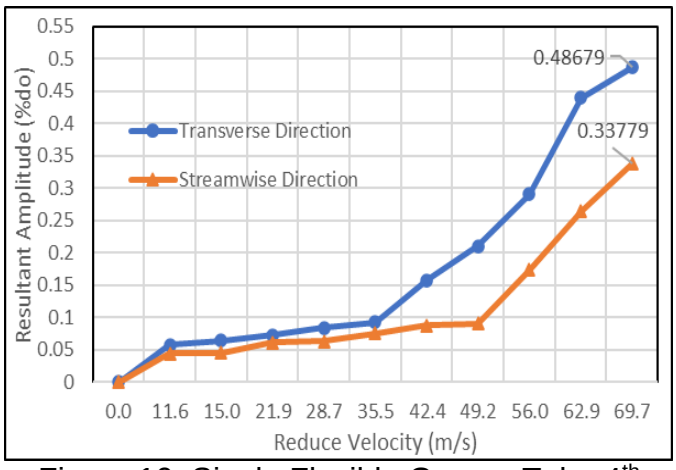

Figure 10. Single Flexible Groove Tube 4th Row

3.3 Comparison of the resultant response of rows

The resultant amplitude response versus the reduced velocity graph is shown in Figure 11, where it is indicated that the third row shows the highest instability compared to other rows.

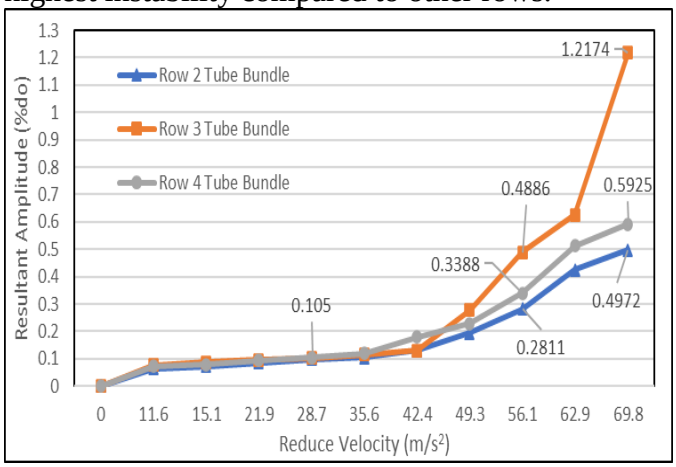

Figure 11. Resultant amplitude of a single flexible groove tube

However, when reduce velocity is 28.7 m/s, the amplitude response is 0.105 percent of tube diameter is the same for all rows, although when reduce velocity is above 35.6 m/s, the amplitude response is indicated differently for all rows, at a reduced velocity of 56.1 m/s, amplitude response for second row 0.2811 percent of tube diameter, third row 0.4886 percent of tube diameter and fourth row 0.3388 percent of the tube diameter. At the maximum reduce velocity of 69.8 m/s, the amplitude response of the third row is 1.22 percent of the tube diameter, the fourth row is 0.593 percent of the tube diameter, and the second row is 0.497 percent of the tube diameter. From the resultant amplitude of a single flexible groove, the graph revealed that the third row indicated maximum instability compared to the second and fourth rows. The fourth row has higher instability than the second row.

4 CONCLUSION

The fluid elastic instability is investigated on the groove tube with tube arrangement as an in-line square tube bundle of four rows and pitch to diameter ratio of 1.28. This experiment is performed on the subsonic wind tunnel apparatus. All rows have a natural frequency between 9.5 Hz to 10.5 Hz with ±0.05.

- Instability in the in-line square tube bundle is decreases when the grooved tube is used. The minimum resultant amplitude response is indicated in the second row, which is 0.497 percent of tube diameter, at a reduced velocity of 69.8 m/s.
- Instability is observed that 3rd row resultant amplitude response is 1.22 percent of tube diameter, at a reduced velocity of 69.8 m/s, which indicated that higher compared to other second and fourth rows. In the fourth-row resultant amplitude response is 0.593 percent of tube diameter, which is also indicated higher instability than the second row.
- From this experiment revealed that the transverse direction amplitude response is higher than the streamwise direction. However, at the start of the reduced velocity until 28.5 m/s streamwise and transverse direction amplitude responses are almost the same, which is less than 0.1 percent of the tube diameter.

REFERENCES

[1]. S. Khushnood, Z. M. Khan, M. A. Malik, Z. U. Koreshi, and M. A. Khan, "A review of heat exchanger tube bundle vibrations in two-phase cross-flow," *Nucl. Eng. Des.*, vol. 230, no. 1–3, pp. 233–251, 2004,

[2]. M. J. Pettigrew and C. E. Taylor, "Fluidelastic instability of heat exchanger tube bundles: Review and design recommendations," *J. Press. Vessel Technol. Trans. ASME*, vol. 113, no. 2, pp. 242–256, 1991,

[3]. T. Nakamura, Y. Fujita, and T. Sumitani, "Study on in-flow fluidelastic instability of triangular tube arrays subjected to air cross flow," *J. Press. Vessel Technol. Trans.*

ASME, vol. 136, no. 5, pp. 1–7, 2014,

[4]. T. Nakamura, K. Nishimura, Y. Fujita, and C. Kohara, "Study on in-flow vibration of cylinder arrays caused by cross flow," *Am. Soc. Mech. Eng. Press. Vessel. Pip. Div. PVP*, vol. 4, pp. 69–76, 2011,

[5]. V. P. Janzen, E. G. Hagberg, M. J. Pettigrew, and C. E. Taylor, "Fluidelastic instability and work-rate measurements of steam-generator U-tubes in air-water cross-flow," *J. Press. Vessel Technol. Trans. ASME*, vol. 127, no. 1, pp. 84–91, 2005,

[6]. A. Elhelaly, M. Hassan, A. Mohany, and S. Eid Moussa, "Effect of the flow approach angle on the dynamics of loosely-supported tube arrays," *Nucl. Eng. Des.*, vol. 368, no. March, p. 110802, 2020,

[7]. S. A. Al-Kaabi, Y. A. Khulief, and S. A. Said, "Prediction of flow-induced vibrations in tubular heat exchangers-Part II: Experimental investigation," *J. Press. Vessel Technol. Trans. ASME*, vol. 131, no. 1, pp. 1–7, 2009,

[8]. H. J. Chung and I. Chu, "Fluid-Elastic Instability of Rotated Square Tube Array in Air-Water Two-Phase Cross-Flow," *Nuclear Engineering and Technology*, vol. 38, no. 1. p. 69, 2006.

[9]. I. C. Chu, H. J. Chung, and C. H. Lee, "Fluid-elastic instability of rotated square array U-tubes in air-water flow," *J. Press. Vessel Technol. Trans. ASME*, vol. 131, no. 4, pp. 1–8, 2009,

[10]. J. Lai, T. Tan, S. Yang, L. Lu, L. Sun, and H. Ming, "Flow-induced vibration of tube bundles considering the effect of periodic fluid force in a rotated triangular tube array," *Ann. Nucl. Energy*, vol. 161, p. 108488, 2021,

[11]. J. Lai, S. Yang, T. Tan, L. Gao, L. Sun, and P. Li, "Turbulence-induced vibration of tube bundles subjected to cross-flow and loose support," *Int. J. Press. Vessel. Pip.*, vol. 195, no. January 2021, p. 104601, 2022.

[12]. J. Lai, L. Lu, S. Yang, T. Tan, and L. Sun, "Dynamic characteristics of tube bundles with crack subjected to cross-flow and loose support," *Ann. Nucl. Energy*, vol. 166, p. 108802, 2022,

[13]. J. Lai, T. Tan, S. Yang, and L. Sun, "Experimental and theoretical study on fluidelastic instability of tube bundles subjected to cross-flow in the parallel direction," *Ann. Nucl. Energy*, vol. 169, p. 108927, 2022,

[14]. C. Heung June, "fluid elastic instability of rotated sqaure tube array in an air water two phase cross flow." Nuclear Engineeering anf Technology, p. 12, 2005.

[15]. A. Aboushita, "Experimental Investigation of Streamwise Fluidelastic Instability in Tube Arrays," no. May, 2020.

[16]. S. Khushnood and L. A. Nizam, "Experimental study on cross-flow induced vibrations in heat exchanger tube bundle," *China Ocean Eng.*, vol. 31, no. 1, pp. 91–97, 2017,

[17]. N. W. M. Ko, Y. C. Leung, and J. J. J. Chen, "Flow past V-groove circular cylinders," *AIAA J.*, vol. 25, no. 6, pp. 806–811, 1987,

[18]. J. J. J. Chen, Y. C. Leung, and N. W. M. Ko, "Drag Reduction in a Longitudinally Grooved Flow Channel," *Ind. Eng. Chem. Fundam.*, vol. 25, no. 4, pp. 741–745, 1986,

[19]. T. Kimura and M. Tsutahara, "Fluid dynamic effects of grooves on circular cylinder surface," *AIAA J.*, vol. 29, no. 12, pp. 2062–2068, 1990,

[20]. K. Bilen, M. Cetin, H. Gul, and T. Balta, "The investigation of groove geometry effect on heat transfer for internally grooved tubes," *Appl. Therm. Eng.*, vol. 29, no. 4, pp. 753–761, 2009,

[21]. A. M. El-Makdah and G. F. Oweis, "The flow past a cactus-inspired grooved cylinder," *Exp. Fluids*, vol. 54, no. 2, 2013,

[22]. D. B. Keogh and C. Meskell, "DRAFT: Bi-stable flow in parallel triangular tube arrays with a pitch-to-diameter ratio of 1.375," *Nucl. Eng. Des.*, vol. 285, pp. 98–108, 2015,

[23]. S. Kim and M. M. Alam, "Characteristics and suppression of flow-induced vibrations of two side-by-side circular cylinders," *J. Fluids Struct.*, vol. 54, pp. 629–642, 2015,

[24]. Z. G.-T. Javad Farrokhi Derakhshandeh, "Computational fluid dynamics analysis of flow over a re-entry vehicle," *Phys. Sci. Educ. eJournal*, vol. 45, no. 16 Feb 2022, pp. 1–37, 2022.

[25]. F. Afroz and M. A. R. Sharif, "Numerical study of cross-flow around a circular cylinder with differently shaped span-wise surface grooves at low Reynolds number," *Eur. J. Mech. B/Fluids*, vol. 91, pp. 203–218,

2022,

[26]. J. F. Derakhshandeh and N. Gharib, "Laminar flow instabilities of a grooved circular cylinder," *J. Brazilian Soc. Mech. Sci. Eng.*, vol. 42, no. 11, 2020,

[27]. L. M. Ralston, "An experimental study on passive control of a reattaching shear layer behind a backward-facing step. Diss," Bucknell University, 1997.

COMPARATIVE STUDY FOR SELECTION OF SUPPLIERS USING MCDM TOOLS

S. Ali Imran Zaidi[1,*], Zaheer Ahmed[2], S. Jawad Hussain Zaidi[3], S. Adil Abbas Zaidi[4]
[1]Industrial Engineering Department, UET University of Engineering & Technology, Taxila, Pakistan

[*]Corresponding author. Tel.: +92-333-9112771;
E-mail adress: engineer.saiz@gmail.com (S. Ali Imran Zaidi)

ABSTRACT

Selection of suitable contractors according to the nature of the job remains a crucial problem in the construction industry. In most cases, the decision-makers are being criticized for wrong or biased qualification/selection of the contractor. There must be a standardized computational model for the selection of the contractor under a versatile and complex environment. Thus, the method is adaptable to the concerned stakeholders. This research prioritizes the selection criteria for Suppliers in Construction projects and develops a standardized computational model combining AHP and TOPSIS techniques for a robust selection of contractors for every edifice engineering. A case study of Supplier Selection (SS) at a renowned public sector organization i.e. Heavy Mechanical Complex of Pakistan, underneath the facility of the Public Procurement Regulatory Authority (PPRA) has been investigated in detail. By using the Analytic Hierarchy Process (AHP) the organized conferences were planned with the qualified experts in order to examine the comparative reputation weights against the particulars of the suppliers which have composed during the first phase. AHP is applied to create a precise result against the weights of contractor's parameters. Another tool i.e. Technique for Order Preference by Similarity to the Ideal Solution (TOPSIS) is used to assess and identified the suppliers attributes against engineering projects. Finally, the intimacy based on the suppliers' factors/numbers are calculated & assessed to get the best performance with regards to project execution. The main purpose of this research is to create such model by using the Multi Criteria Decision Making (MCDM) techniques which is helpful to scrutinize the appropriate contractor in every organization for the successful execution and completion of the projects in engineering field. Further, the planned methodology based on PPRA guidelines has been functioned in supplier selection to confirm the fruitful enactment against projects. The established methodology is constructed on the combination of AHP-TOPSIS, provided a standardized approach towards SS, thus adaptable to public sector organizations as well as private companies.

Keywords: MCDM, AHP, TOPSIS, Supplier Selection, Software, Hydro Power Plant, Research Methodology

1 INTRODUCTION

The finalization of contractor for any venture endures to be a part of rank and attention to organizations accountable for carrying project results successfully. Initially as far as Project execution is concern, it is the utmost considerate activities achieved by clients, the success of which is unswervingly associated to project feat and the accomplishment of quantified purposes [1][3][4]. The environmental conditions for making decisions around contractor and their aptitude to deliver is intricate spectacles. It encompasses high echelons of vagueness, competing sponsor standards and thorny associations as a consequence of numerous contradictory purposes [4][5][6].

Further snags ascend in classifying appropriate & pertinent measures and assigning suitable hefts which may differ as a function of several aspects, least of which are the organizational aims and skill of the assessor. Assumed the difficulties and fundamental questions arises against similarity for contractor selection and the diversity of norms accessible, then in what way do consumers elect contractors and what is the association between the criteria used for valuation? Criteria reassurance prime? Is financial cost a more significant criterion than skill, competency, proficiency, or recital?

Does the comparative rank diverge as a purpose of situation, experience, industry or project density? These queries form the source of our enduring research to examine which features effect the real choice of a contractor for key projects and the virtual status of the principles used. Disdain its status, this feature of supplier selection relics mainly uncharted, as evinced through rare revisions testified.

Since this era is full of technical mechanization where connoisseurs believe heftier on the erudite utensils and desire to weary the unadventurous methods. To support the clients, several scholars from eras trying to enhance the gap and bringing forth progressive verdict support selection replicas and outlines. Considering the quandary in the traditional lowest bid approach, numerous pronouncement sustenance models have been the part of this important research monarchy. The fundamental purpose of those replicas is to assist the clients in making lucid conclusions based on multi-criteria. Clients want to gates with a translucent and impartial decision for the contractor's selection. Due to the intricacy, it entails the provision of progressive decision-making methods to pact with this thorny delinquent and to make impregnable decisions.

One extensively used Multi-Criteria Decision Making (MCDM) technique is Analytic Hierarchy Process (AHP). AHP was anticipated by Saaty in the year 1980 [2].AHP is used to measure, order, rank and assess decree choices. Another MCDM technique used widely is TOPSIS. Recent research [49] has been carried out using TOPSIS technique for prequalification of contractor in Environmental System. The study also utilizes AHP technique in order to quantify the weighted average of controlling parameters in selection of the contractor.

This study aims to combine the AHP and TOPSIS scheme for assortment of contractor in construction industry under real and complex environment. A computational and robust model will be proposed for supporting decision makers.

2 LITERATURE REVIEW

2.1 MCDM In Supplier Selection

To keep a viable place in the worldwide marketplace, companies follow some important supplier selection methodologies to achieve quicker lead times, minimized prices and sophisticated advantages. Therefore, performers/vendors show an important part in gaining community support, so selecting the exact contractor for any project is a risk factor for these innovative approaches.

Many conflicting measurable and qualitative characteristics or criteria, such as price, value, shipping, etc., plague the dealer choice problem. Thus, this is a multi-criteria decision problem containing computable and qualitative aspects, few among them have conflict with each other. The surge and diversification of client needs, the advancement of statement and information system disciplines and technologies, the competition in the global atmosphere, the reduction of organizational agreements and the enhancement of ecological awareness have all made people involuntarily pay attention to Supply Chain Management (SCM). The term "supply chain management" has been in use for nearly 21 centuries and is well-defined as the activity of ensuring the transformation of supplies into intermediate, final, distribution to customers, scheduling projects for emerging suppliers. Coordination between builders and contractors is often a difficult but important link in terms of frequency of circulation in the supply chain. When a supplier becomes part of a well-organized and reputable supply chain process, this relationship can have a permanent impact on the reliability of the whole supply chain. Due to this, contractor selection errors have become one of the most significant topics in project execution and creating effective Supply Chain Systems.

Contractor assortment is a complex process because many criteria must be weighed in the decision-making process. The findings indicate that supplier selection method is the important variables that directly affect organizational performance. As organizations become more reliant on the suppliers, the shortest and incidental effects of judgment deprivation will convert extra risky. The nature of this conclusion is usually compound and amorphous. On the other hand, delinquent contractor assortment decisions involve adjustments between multiple criteria involving calculable and qualitative impacts, which can also be contradictory.

2.1.1 Analytic Hierarchy Process (AHP) Model

AHP was proposed by Saaty [2]. It is an MCDM that simplifies complex and ill-structured issues by arranging the criteria and options in a hierarchical

structure by using pairwise comparison metrics [3] [4]. The main advantage of AHP is its ability to rank options in the order of their effectiveness in meeting conflicting goals [3] [4].
In an AHP model, multiple paired comparison metrics are based on nine levels of a standardized comparison scale.

Let A = {Abb = 1, 2, . . ., m} be the set of number of criteria The pairwise comparison metric of the m factor will be presented in an m x m evaluation matrix C, in which every element dab is the quotient of weights of the factor, as shown in Equation (1):

$$C = (dab),\ a, n = 1, \ldots, m \quad (1)$$

The relative priorities are given by the vector (u) corresponding to the largest vector (max) as shown in Equation (2):

$$Cu = \lambda \max \mu \quad (2)$$

The consistency is determined by the relation between the entries of C and the consistency index (CI) is shown as Equation (3):

$$CI = (\lambda \max - m) / (m - 1) \quad (3)$$

The final consistency ratio (CR), calculated as the ratio of the CI and the RI, is shown in Equation (4):

$$CR = CI/RI \quad (4)$$

The upper limit for CR is 0.1. If the CR value exceeds 0.1, the evaluation procedure needs to be repeated to improve consistency.

The steps of the AHP process are as follows:

Step 1: Defining a research problem and goals.
Step 2: Building a hierarchy structure of the AHP model.
Step 3: Constructing of the target matrix of the supply network.
Step 4: Building the pairwise comparison matrices.
Step 5: Evaluating the consistency of the judgments and performing a consequence weights analysis through Equation (5):

$$C=(dab)=\begin{bmatrix} 1 & U1/U2 & U1/Un \\ U2/U1 & 1 & U2/Un \\ Um/U1 & Un/u2 & 1 \end{bmatrix} \quad (5)$$

Step 6: Check consistency. Calculate the vector of the matrix through Equation (6):

$$CR = CI/RI \quad (6)$$

Where:
CI: consistency index; RI: random index.
Calculating the consistency ratio (CR) through Equation (7):

$$CR = (CI/RI) \quad (7)$$

2.1.2 Technique for Order Preference by Similarity to Ideal Solution (TOPSIS)

The classical TOPSIS has been proposed by Hwang and Yoon [5] who explored that the best alternative should have the shortest distance from the positive ideal solution and the furthest distance from the negative one. Despite TOPSIS has a high weakness that it does not provide a good alternative [6], in contrast, that TOPSIS affords the decision-maker the nearest alternative which is considered the best one according to the score which has been illustrated by the judgement. As such, if one decision-maker gives a score for each alternative, the result will be an alternative ranking according to this score. If another decision-maker provides different scores, consequently the alternative ranking will be different. Hence, TOPSIS gives judgement the perfect solution with respect to the perspective of each decision-maker. TOPSIS decision-making technique is classified into five main steps. Converting performance attributes into non-dimensional ones is the first step, the decision matrix is normalized using Equation (8).

$$r_{ij} = = \frac{Xij}{\sum_{i=1}^{m} x^2 ij} \quad (8)$$

After normalization, the second step is to determine the normalized weighted decision matrix by multiplying the normalized decision matrix by its corresponding weights. The normalized weighted value Vij is taken using Equation (9).

$$V_{ij} = r_{ij} * w_j \quad (9)$$

The third step is to identify the positive or most ideal solutions and negative ideal solutions which are produced by using Equation (10) and Equation (11). A+ shows the most positive ideal solution. Conversely, A- shows the negative ideal solution. For benefit criteria, the decision-maker obtains the most extreme value of any alternatives. Meanwhile, for cost criteria, the decision-maker requires obtaining minimum value among all alternatives.

A+={(maxVij\€J),(minVij\€J'),i=1,2,3..M}={V+1, V+2..V+N} (10)

A-={(maxVij\€J),(minVij\€J'),i=1,2,3..M}={V-1,V-2..V-N} (11)

Where;
J = {j = 1, 2, 3……N/j associated with benefit criteria}
J'= {j = 1, 2, 3……N/j associated with cost criteria}
The fourth step is to measure the difference between each alternative to the positive ideal (PIS) A+ and negative ideal solutions (NIS) A-. Further, S + i describes the distance separating every alternative from the ideal positive solution in the Euclidean way. On the contrary, S-i illustrates the separation distance between each alternative in the Euclidean way from the optimal negative solution using equations (12) and (13) respectively.

$$S+_i = \sum_{j=1}^{n} (V_{ij} - V + j)2 \quad (12)$$

$$S-_i = \sum_{j=1}^{n} (V_{ij} - V - j)2 \quad (13)$$

Fifth step: measure the performance score by using Equation (14).

$$C+_I = Si/(S+i)+(S-i) 0 \leq C+_i \leq 10 \leq \quad (14)$$

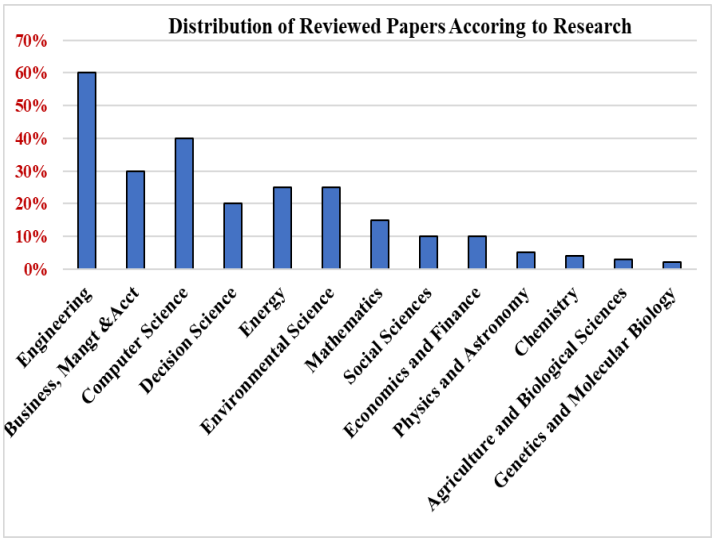

Figure 1. Distribution of Reviewed papers according to research areas

The above Fig. 1 defined the publication of papers with wide range areas. It has been clearly seen from the below grid that mostly comparison with regards to Engineering has been adopted, as engineering set up has versatile field of execution of projects having multiple combination factors regarding comparing attributes/tools. Second comes the Computer Science area having publication less than 40 and similarly the ratio for other turfs is describe as per above figure.

3 RESEARCH METHODOLOGY

3.1 Benchmark Paper

The main purpose of this study is to develop a prototype capable of selecting the most suitable supplier alternatives for industrial and construction organizations based on hydropower project indicators. The forecasting model takes into account the supplier pre-qualification process during the scheduling phase. The flowchart shown in Figure 3-2 illustrates the flowchart mechanism of how to identify and select suppliers based on their attributes under complex projects. Both techniques, AHP and TOPSIS were applied and they were used mostly due to their recompences [48][49]. Compensation for TOPSIS consists of submission, acceptance, and consideration of the prosperity of the distance from the ideal solution [49]. The advantages of AHP include accepting, reducing bias caused by human factors reflecting and confirming information differences.

3.2 Data Collection

For the Statistics of the suppliers, we have different techniques/methods which is illustrated in the below Fig. 2, however, here we have taken the Data of the Suppliers through; Literature review to develop the hypothetical context and execute a lean of project principles for contractor selection, second Through different Organization, Past Survey/references and then evolving the general grading of AHP model. Finally steering organised interviews to acquire the qualified position for each project principles and indicator.

Figure 2. Data collection methods

3.3 Structured Interviews

Here, organized conferences with suppliers are articulated as initial waft of the hierarchy in the arrangement of a formulating meeting during biding or tendering process.

After that, the proficient specialists are renovated the sorting of standards and are added some other characteristics such as the professional experiences, Skilled Manpower, Tools & Tackles and Financial states. It has comprehended that partaking a discussion with regards to project issues with suppliers as well as satisfying in the grading is the most suitable way to evade any misperceptions for the projects. Lastly, the broad cessation edifice hierarchy will be established grounded on semi-structured conferences, Past references and prose.

3.4 Parameters Identification

A literature review was performed to gather data. In this study, 10 criteria have found from the literature on Contractor selection. These criteria have divided into main four categories which classified according to gathering data from literature, Past references/survey and semi-structured interviews. Moreover, the main output from the documentation reviews and information collection is to identify the list of project criteria for selecting the supplier to support sustainability performance. This list is used in organised interviews to help the experts in understanding the research study.

3.5 Research Methodology flow chart

The below Fig. 3 is the methodology applied against supplier traits using MCDM techniques i.e (AHP and TOPSIS)

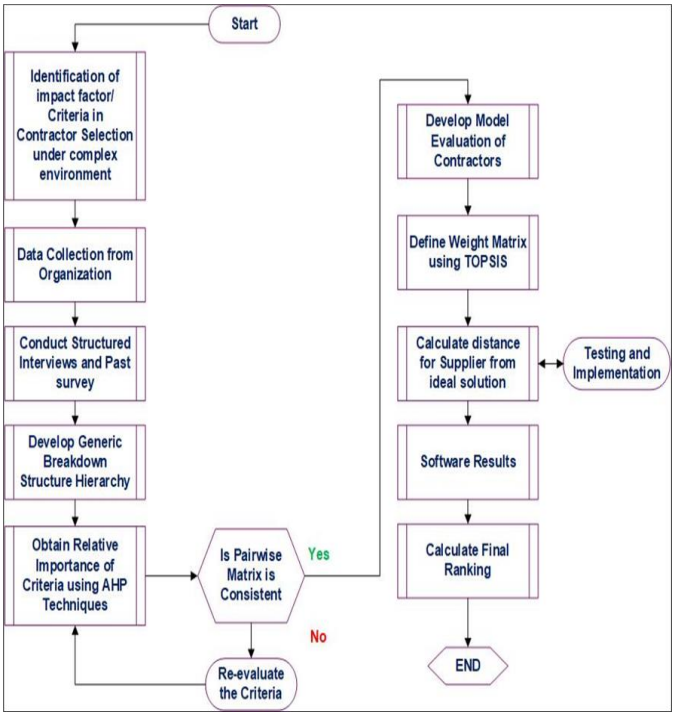

Figure 3. Research Methodology Flow Chart

4 IMPLEMENTATION STRATEGIES AND COMPUTATIONS

4.1 Description of the Cases

Supplier selection for the execution of any Projects plays a vital role in the public and private sector. Here we have selected Heavy Mechanical Complex (HMC) a public sector for the suitable supplier selection for the Projects.

HMC have variety of multi task projects to execute depending the scope, delivery, cost, quality and time and for the same appropriate supplier would have been a vigorous selection, so that the Projects could be closed in well mannered.

Following are the main core projects;

1. Hydro Power Plant (HPP).
2. Sugar Boilers.
3. Oil and Gas (OGDCL).
4. Overhead Pedestrian Bridges (OHPB).

Keeping in view the above projects, HPP has been selected and implemented the MCDM techniques i.e (AHP and TOPSIS) on HPP project for suitable supplier selection accordingly.

4.2 Application to Case

The execution working methodology of Hydro Power Plant is consider as most versatile and difficult, so here preference of suitable supplier based on their bidding documents/data should be selected using AHP and TOPSIS techniques.

4.3 Supplier Selection for Hydro Power Plant Project by Using AHP

A real time calculation data sheet of the supplier participated in the bidding documents has shown in figure 4-1. Now, for below pairwise comparison matrix, AHP technique has applied against traits of contractors for their selection and preferences regarding execution of the project.

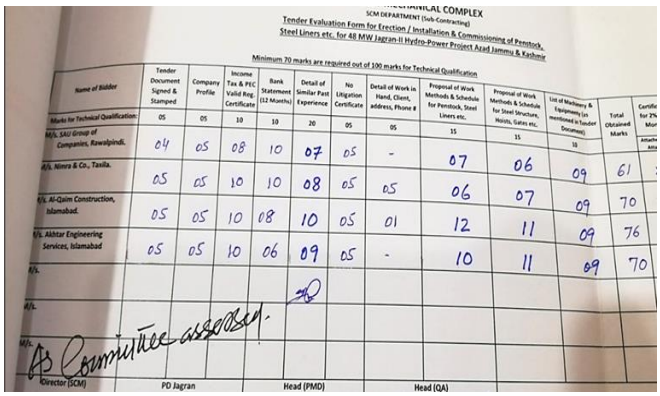

Figure 4. Comparison of Real Time Data of suppliers

From the above list of constituents, we have selected 04 main attributes which are;

a) Past Experience
b) Skilled Manpower
c) Detail of Machinery
d) Financial Statement

Now we will compare the above attributes with all suppliers by using AHP technique as below;

4.4 Past Experience

Comparison against supplier attributes has been made with regards to their technical and financial data as per table 1.

Table 1. Comparison of past experiences of the potential bidders

Supplier's	SAU Group of Companies	Nimra & Co.	Al-Qaim Construction	Akhtar Engg Services
SAU Group of Companies	1	2	0.25	0.25
Nimra & Co.	0.5	1	5	0.333
Al-Qaim Construction	4	0.2	1	3
Akhtar Engineering Services	4	3	0.333	1
Total Sum	**9.5**	**6.2**	**6.583**	**4.583**

Divide the value of each column of above matrix by its sum to get matrix in the form of table 2.

Table 2. Computed Comparison

Supplier's	SAU Group of Companies	Nimra & Co.	Al-Qaim Construction	Akhtar Engg Services
SAU Group of Companies	0.1053	0.3226	0.0380	0.0545
Nimra & Co.	0.0526	0.1613	0.7595	0.0727
Al-Qaim Construction	0.4211	0.0323	0.1519	0.6546
Akhtar Engineering Services	0.4211	0.4839	0.0506	0.2182

Taking row wise average to get the priorities of the suppliers as per table 3.

Table 3. Priorities of the bidders

	SAU	Nimra	Al-Qaim	Akhtar Engg	Total Sum	Avg	Priority
SAU	0.1053	0.3226	0.0380	0.0545	0.5204	4	**0.1301**
Nimra	0.0526	0.1613	0.7595	0.0727	1.0461	4	**0.2615**
Al-Qaim	0.4211	0.0323	0.1519	0.6546	1.2598	4	**0.3150**
Akhtar Engg	0.4211	0.4839	0.0506	0.2182	1.1737	4	**0.2934**

The above table shows the priorities of the suppliers against Past Experience. Similarly, the same procedure and comparison of supplier's attributes

against their bidding documents will be performed for Skilled Manpower, Detail of Machinery, Financial Statement.

4.5 Skilled Manpower

Table 4. Priorities of the bidders

	SAU	Nimra	Al-Qaim	Akhtar Engg	Total Sum	Avg	Priority
SAU	0.0702	0.3279	0.0331	0.0255	0.4567	4	**0.1142**
Nimra	0.0175	0.0820	0.0331	0.7693	0.9020	4	**0.2255**
Al-Qaim	0.4912	0.5738	0.2334	0.0512	1.3497	4	**0.3374**
Akhtar Engg	0.4211	0.0164	0.7003	0.1539	1.2916	4	**0.3229**

4.6 Detail of Machinery

Table 5. Priorities of the bidders

	SAU	Nimra	Al-Qaim	Akhtar Engg	Total Sum	Avg	Priority
SAU	0.1111	0.1035	0.0689	0.0908	0.3743	4	**0.0936**
Nimra	0.2222	0.2069	0.6207	0.0908	1.1407	4	**0.2852**
Al-Qaim	0.3333	0.0689	0.2069	0.5456	1.1547	4	**0.2887**
Akhtar Engg	0.3333	0.6207	0.1035	0.2728	1.3303	4	**0.3326**

4.7 Financial Statement

Table 6. Priorities of the bidders

	SAU	Nimra	Al-Qaim	Akhtar Engg	Total Sum	Avg	Priority
SAU	0.0455	0.0222	0.0263	0.0266	0.1206	4	0.0301
Nimra	0.3182	0.1564	0.7418	0.0374	1.2539	4	0.3135
Al-Qaim	0.3182	0.0391	0.1855	0.7488	1.2915	4	0.3229
Akhtar Engg	0.3182	0.7822	0.0464	0.1872	1.3340	4	0.3335

4.8 Overall Priorities of Suppliers

Multiply each value of Major Priority with supplier attributes row wise and add to get the overall priority of the supplier.

Table 7. Overall Priorities

Major Priority	Past Exp	SK/ MP	DOM	Fin/St	Overall Priority	Supplier
0.040	0.130	0.114	0.093	0.030	**0.100**	**SAU Group**
0.585	0.261	0.225	0.285	0.313	**0.252**	**Nimra & Co**
0.267	0.315	0.337	0.288	0.322	**0.321**	**Al-Qaim**
0.106	0.293	0.322	0.332	0.333	**0.325**	**Akhtar Engg**

Keeping in view the above matrix, it is concluded that by applying AHP technique against supplier attributes, Akhtar Engineering supplier has higher selection preferences.

4.9 Supplier Selection for Hydro Power Plant Project by Using TOPSIS

Now we will apply TOPSIS technique on supplier features and get the results;

4.10 Using Point Scale Criteria

In TOPSIS, first we have to define a point table criterion as per below table 8.

Table 8. Point Scale Criteria

Suppliers	Past Experience	Skilled Manpower	Detail of Machinery	Financial Statement
SAU Group of Companies	4	5	4	1
Nimra & Co	6	4	5	3
Al-Qaim Construction	8	7	7	4
Akhtar Engg Service	7	8	6	5

Here, the comparison between the supplier attributes with regards to Past Experience, Skilled Manpower, Detail of Machinery and Financial Statement are defined in terms of point rating. For low it is 1, for below average is 2, similarly for average, good and excellent it is 3, 4 and 5 respectively.

4.11 Vector Normalization is carried out;

Taking Square root of column wise values and further take submission.

For Past Experience = $\sqrt{(4)^2+(6)^2+(8)^2+(7)^2}$ = 12.84

For Skilled Manpower = $\sqrt{(5)^2+(4)^2+(7)^2+(8)^2}$ = 12.4

For Detail Machinery = $\sqrt{(4)^2+(5)^2+(7)^2+(6)^2}$ = 11.22

For Financial Statement = $\sqrt{(1)^2+(3)^2+(4)^2+(5)^2}$ = 7.14

The above Performance value of each Cell is divided by rooted submission of square

For Past Experience

0.3115	0.4673	0.6231	0.5452

For Skilled Manpower

0.4032	0.3226	0.5645	0.6452

For Detail Machinery

0.3565	0.4456	0.6239	0.5348

For Financial Statement

0.1401	0.4202	0.5602	0.7003

By putting these values in matrix, a matrix is called Normalized Decision Matrix.

Table 9. Normalized Decision Matrix

Past Experience	Skilled Manpower	Detail of Machinery	Financial Statement
0.3115	0.4032	0.3565	0.1401
0.4673	0.3226	0.4456	0.4202
0.6231	0.5645	0.6239	0.5602
0.5452	0.6452	0.5348	0.7003

Multiply each value of above matrix column wise by 0.25 weight. Now by multiplying weight the below matrix will be called weighted Normalized Decision Matrix.

Table 10. Weighted Normalized Decision Matrix

Weight	0.25	0.25	0.25	0.25
Criteria	**Past Experience**	**Skilled Manpower**	**Detail of Machinery**	**Financial Statement**
SAU Group of Company	0.0779	0.1008	0.0891	0.0350
Nimra & Co	0.1168	0.0806	0.1114	0.1050
Al-Qaim Construction	0.1558	0.1411	0.1560	0.1401
Akhtar Engg Service	0.1363	0.1613	0.1337	0.1751

4.12 Calculating Ideal Best and Ideal Worst by Euclidean Distance Formula

FORMULA: - Si+, Si-

$S_{+i} = \sqrt{\sum mj=1 \ (V_{ij} - Vj +)^2}$ - Ideal Best Values

$S_{-i} = \sqrt{\sum mj=1 \ (V_{ij} - Vj -)^2}$ - Ideal Worst Values

From the above table 10, maximum rating values will be considered as Vj+ and minimum rating values will be considered as Vj- shown in table 11.

Table 11. Results of TOPSIS Euclidean Distance Formula.

	Past Experience	Skilled Manpower	Detail of Machinery	Financial Statement
Vj^+	0.1558	0.1613	0.1560	0.1751
Vj^-	0.0779	0.0806	0.0891	0.0350

By applying the above equations of ideal best and ideal worst against table 10 and 11, we get the below Si+ and Si- values.

Table 12. Results of Ideal Best and Ideal Worst values.

S_{1i}^+	**0.183**	**S_{2i}^+**	**0.122**	**S_{3i}^+**	**0.04**	**S_{4i}^+**	**0.029**
S_{1i}^-	**0.02**	**S_{2i}^-**	**0.083**	**S_{3i}^-**	**0.158**	**S_{4i}^-**	**0.177**

4.13 Calculating Performance Score

The performance score is calculating as per below formula;

Formula: $\mathbf{P_i = Si^-/Si^+ + Si^-}$

The Performance score is basically calculated as the ratio of Ideal worst value by sum of Ideal Best and Ideal worst values.

Table 13. TOPSIS Results.

S_i^+	S_i^-	$S_i^+ + S_i^-$	P_i	100 (Rank x 100)	Rank Priority Basis
0.183	0.02	0.203	0.0985	9.8522	**SAU Group of Company**
0.122	0.083	0.205	0.4049	40.4878	**Nimra & Co**
0.04	0.158	0.198	0.7980	79.7980	**Al-Qaim Construction**
0.029	0.177	0.206	0.8592	85.9223	**Akhtar Engg Service**

From the above matrix, we conclude that by applying TOPSIS technique the supplier M/s Akhtar Engineering has higher percentage rank and selected accordingly.

5 MCDM TOOLS APPLICATION THROUGH SOFTWARE

5.1 Visual Studio2012

Supplier Selection software is developed using Visual Studio C# .NET (version 2012). The programming language used is C#. Visual Studio is the Combined Expansion Milieu in which inventers toil when making curricula in one of several languages, counting C# for the dot NET Framework. It is used to generate soothe and graphic user interface (GUI) submissions along with Windows Forms or WPF (Windows Presentation Foundation) bids, web applications and web services in both inherent ciphers composed with accomplished code for all platforms supported by Microsoft Windows, Windows Mobile, Windows CE,

5.2 AHP Working of Software

In AHP, pairwise comparison between the supplier's data will result two outcomes which normally defines as Outcome 1 and Outcome 2. The details of the software results are described below;

Software Outcome 1:

First, we have to check the AHP case, either it falls within the range of AHP defined parameters or not. The outcome of the software has, main group box of pair wise comparison between traits of the project supplier entailing the Past Experience, Skilled Manpower, Details of Machinery and Financial Statement. The group box comprises of 16 text boxes where the numeric values will be entered. At the end the total sum of each attribute will be exhibited.

After that we have next group boxes covering the Priority and Weighted sum where the row wise priorities and average weighted sum will be discrete.

Further, we have text boxes of Lamda Max, Consistency Index, Consistency Ratio and to calculate the results of qualities, we have calculated button by clicking on that the result will be showed.

For the acceptance of the supplier's comparison case in AHP is, if the final value of consistency ratio is below 0.1 value, then the case is acceptable otherwise not and as per AHP procedure to make case/criteria acceptable we again compare the values with new ones in case of not acceptable criteria.

Subsequently we further proceed to pair wise comparison of supplier. At the end, we have supplier selection combo box where we can select number of suppliers who partaken in the bidding process. By clicking ok button, the next form of suppliers will be opened. Software outcome 1 is shown in Fig 5.

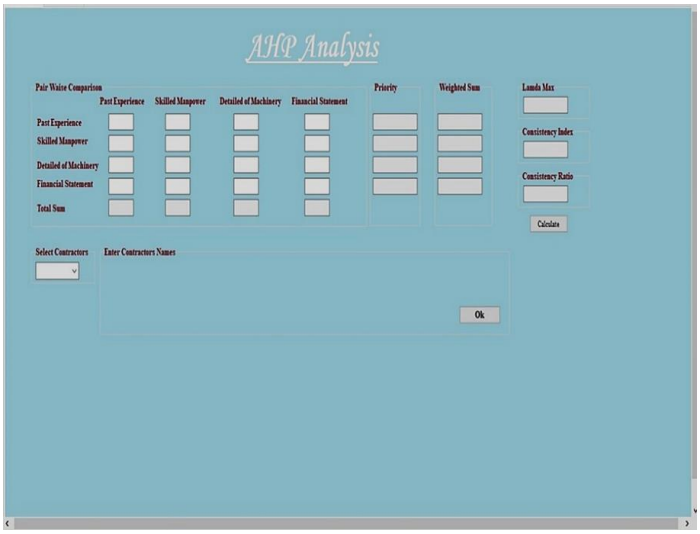

Figure 5. AHP Graphic User Interface.

Software Outcome 2:

After initial acceptance of supplier's criteria as defined in above outcome 1. Now the comparison between supplier's Past experience, Skilled Manpower, Details of Machinery and Financial Statement are performed. The screen display four group boxes of the above said attributes and by entering the numeric values based on the

comparison with regards to the submitted data of the suppliers, we have to calculate the priority of each attribute of the suppliers related to their Past experience, Skilled Manpower, Details of Machinery and Financial Statement.

At the end the overall priorities of the suppliers' attributes are calculated which shows the final selection results. Software Outcome 2 is shown in Fig 6.

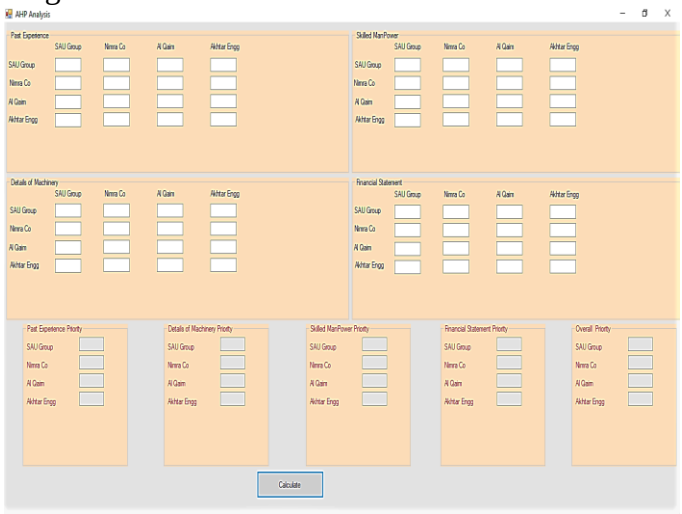

Figure 6. AHP Code GUI

5.3 TOPSIS Working of Software

In TOPSIS we have only single scheme, the details of the scheme are defined as under;

First, we have to define the number of suppliers in the supplier selection text box who participated in the bidding process and by clicking the ok button the results of the suppliers are generated in the next box. Then we have to enter the values in the text boxes against supplier's Past experience, Skilled manpower, Details of machinery and Financial Statement and make comparison accordingly. Based on this comparison we have next text boxes of each above said attributes for vector normalization process. By the putting these values in matrix, the same will be become Normalized Decision Matrix. As per TOPSIS procedure if we multiply the normalized decision matrix by 0.25 then the same matrix will be Weighted Normalized Decision Matrix which is defined in the next combo box and by clinking on calculate button the values will be displayed accordingly.

Then we have to calculate the Ideal Best/Worst as per Euclidean formula from the above matrix i.e Vj^{+} and Vj^{-}. By clicking on calculate button, we get the ideal best and ideal worst values of each supplier against Past experience, Skilled manpower, Details of machinery and Financial Statement.

On the basis of ideal best and worst, we have to calculate the priority index which is defined in the last combo box. From left to right, we have first table is of Ideal best (Si^{+}) values then we have Ideal worst values after that we have sum of Ideal best + Ideal worst then we have Priority Index table the details of which is already defined above. According to TOPSIS process, at last the result of Performance score index is then multiply with 100 to get final priority of the suppliers. Software outcome of TOPSIS is shown in figure 7.

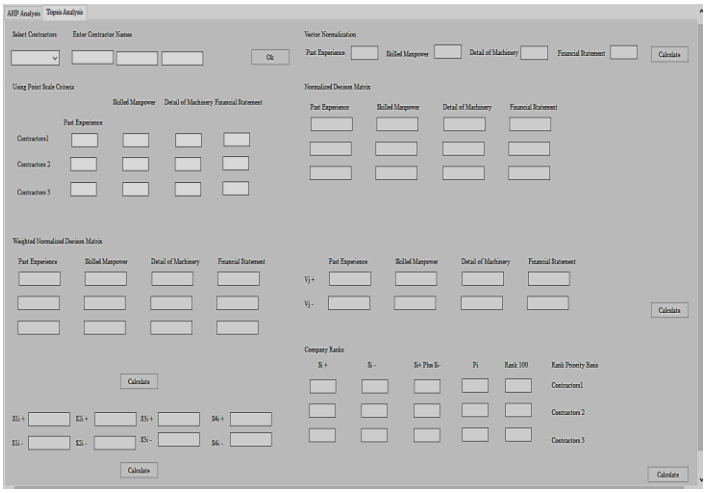

Figure 7. TOPSIS Graphic User Interface

6 RESULT AND DISCUSSION

6.1 AHP

The AHP technique has been applied individually against each comparison matrix for the supplier characteristics i.e. Past experience, Skilled Manpower, Detail of Machinery and Financial Statement and their final priorities/ results shows the rank of the supplier regarding most suitable selection with 1^{st}, 2^{nd}, 3^{rd}, 4^{th} accordingly. As from the above case, selection of supplier M/s Akhter Engineering Services has been nominated as most suitable choice for the employment of the HPP Project having ratio of 0.3254.

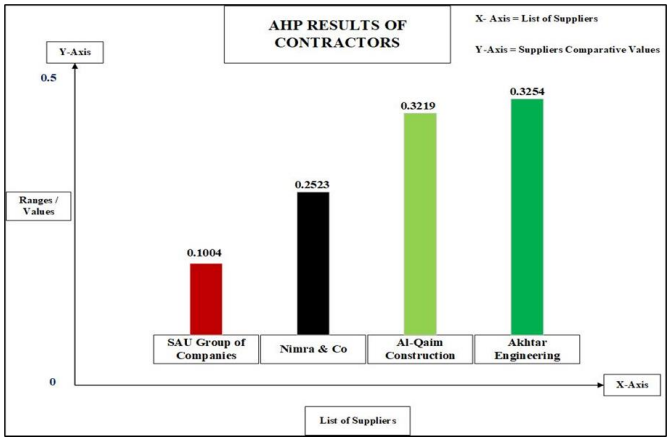

Figure 8. Graphical Display of AHP Results of Contractors

6.2 TOPSIS

By applying the another MCDM Technique i.e TOPSIS against attributes of the supplier, we found that M/s Akhtar Engineering Services has designated with Percentage of 85.92 among all suppliers for HPP Project. So, M/s Akhtar Engineering has been selected in TOPSIS case.

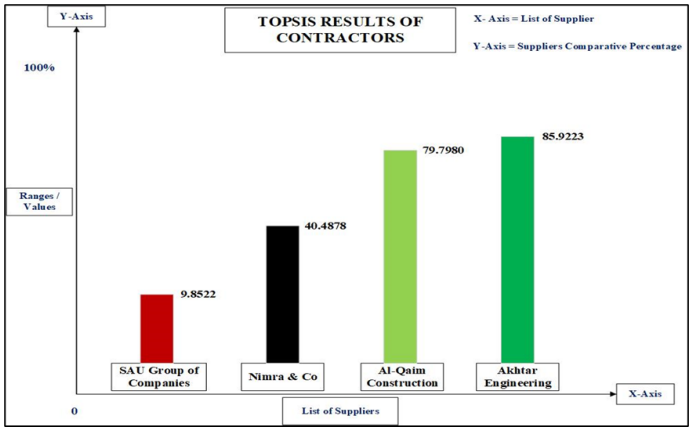

Figure 9. Graphical Display of TOPSIS Results of Contractors

6.3 Discussion

The assortment of appropriate contractors in the project execution is the most critical task and their must some approaches/criteria by adopting the same, the biasness with regards to selection of supplier could be avoided. Here two MCDM methods AHP and TOPSIS along with Software are applied to avoid discrimination of the contractor selection for the project. Further, the results of the supplier through above technique will also help out in such case if we have the identical figures/results of the suppliers. Their comparison between the technical and final attributes differentiates the overall results. Structures interviews, Past reference, Execution techniques of the project provided by the suppliers identifies and strongly support their selection point of view. The input of the supplier data/attributes through software not only curtailed the process time but also give better results of the suppliers without any biasness. The results of the supplier are based on the technical and financial bid. Only the Suppliers who have been technically qualified, the financial offers of the same suppliers are opened. The impact and selection of suppliers are most probably depended upon their financial strength once the supplier has been technically qualified, as in the above case financial quotation for the execution of the project of M/s Akhtar Engineering is lowest among all bidders so, he has been selected for the implementation of the project.

7 CONCLUSION AND RECOMMENDATIONS

7.1 Conclusion of applied AHP and TOPSIS results

The results derived from TOPSIS technique based on comparison related to Past experience, Skilled manpower, Detail of machinery, Financial Statement. It is concluded that by applying both technique i.e. AHP and TOPSIS the end results are identical. Keeping in view the above statistics of the contractors with regards to comparison between their norms, M/s Akhtar Engineering Services was considered as most suitable and appropriate contractor for the accomplishment of the Project tasks.

We have already discussed in the above selection criteria of HMC and mostly public sector organizations. Presently there is no MCDM technique is being followed in HMC. Whereas in the Public/Private sector also no such certain selection criteria related to the above methods have been implemented for the verdict of suppliers. Some organizations used their own structural process and in some sector they have already pre-qualified the suppliers by implementing their own organization rules.

In the light of above, here we have evaluated the results of the suppliers based on the bidding statistics and we come to conclude that by applying both techniques AHP and TOPSIS on the basic

features of the supplier for the execution of Projects the results from both MCDM techniques are same.

Different projects have different criteria depending on the scope, time, quality and delivery. To understand, we have considered a public sector project of Hydro Power Plant and for the execution of the HPP Project, a suitable supplier who has the competency regarding execution and completion of the same are selected based on their technical and financial bidding details through MCDM techniques.

We have compared the attributes of suppliers i.e. Past Experience, Skilled Manpower, Detail of Machinery & Financial Statement and achieved the results of suppliers by Appling the AHP and TOPSIS techniques.

By doing the above, will help in the future to make strong judgments and recommendations regarding the selection of apt suppliers with the impartial and satisfactory process using both AHP and TOPSIS techniques without predetermining or using partial intentions towards supplier selection in any public or private sector, as suitable and appropriate supplier selection is the main task for the organizations to execute/monitor and control any Project within the given timeline satisfactorily.

Further, the if we compare the results of both applied techniques i.e. AHP and TOPSIS with regards to excel data and software, we find appropriate and accurate results of the Suppliers for example as per above discussion the end results of Supplier (Akhtar Engineering) in case of AHP and TOPSIS are defined below, further graphic illustration of the contractors grades are also revealed as per Fig. 8 and 9.

AHP

Excel Data Sheet Result = 0.3254

Software Result = 0.32540

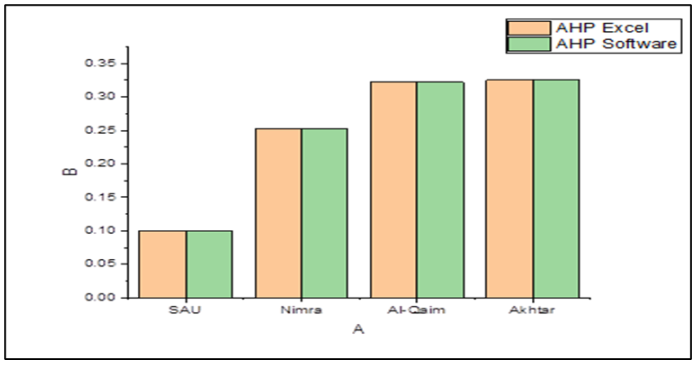

Figure 10. Comparison Results of AHP Excel Data and Software

TOPSIS

Excel Data Sheet Result = 85.9223

Software Result = 85.71

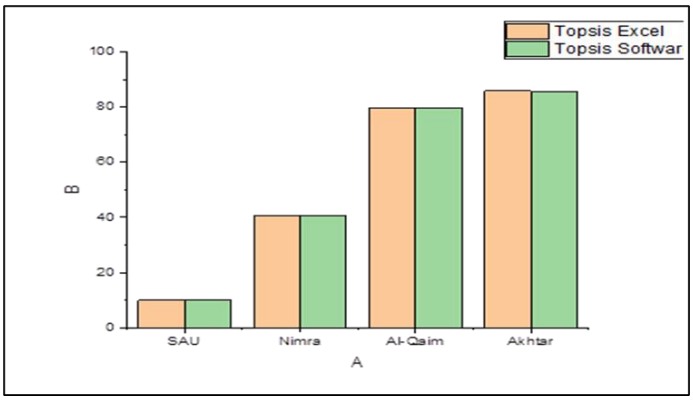

Figure 7-1: Comparison Results of TOPSIS Excel Data and Software

Single AHP technique in the supplier selection for the Projects has minimum assistance, so cater the condition integration of both AHP and TOPSIS approaches are very useful and helpful to achieve more accuracy, counter verification of end results, and strengthen the supplier selection process.

We strongly recommend that combination of both AHP and TOPSIS techniques in the contractor selection procedure not even screams the encrypting process but also improves counter results in the selection of dealers for the Projects. The study can be further extended in future for any other complex projects (Turnkey or EPC) for which execution of pertinent supplier/contractor is required. Here we have taken the Hydro Power Project (HPP) the execution hierarchy of the HPP is difficult from start till completion. In future any other project with similar complexity can be used to get the best results with regards to selection of supplier without any partialities. Further, different comparison of supplier traits based on environmental aspects, Health & safety or any other may be used for selection and timely completion of the projects. Jointly comparing the traits of the supplier and project data or any additional judgement of supplier based on project nature/completion we may conclude or extend the research accordingly.

REFERENCES

[1]. Vargas L.G and Whittaker R.W (1990). Decision Making by the AHP Theory and Applications.

[2]. Saaty T.L. The AHP Process, Mcgraw -Hill, New York, USA 1980.

[3]. Saaty T.L. An exposition of AHP in reply to the paper remarks on Analytical Hierarchy Process Management Science 1990.

[4]. Saaty T.L. Fundamentals of Decision Making and Priority Theory with AHP, RWS, Publications, Pittsburgh USA, 2000.

[5]. Hwang, Yoon. Multiple Attribute Decision Making Methods and Applications State of the Art Survey, Springer. Berlin/Heidelberg, Germany, New York, USA, 1981.

[6]. Chaharsooghi, S.K,Ashrafi, 2014. Sustainable Supplier Performance Evaluation and Selection with Neo Fuzzy TOPSIS Method. International Scholarly Research Notices,2014.

[7]. Alsugair A. Frame work for evaluating bids of Construction Contractors. Management Engg, 1999.

[8]. Shalke, Paydar, Hajiaghaei – Keshteli, 2018. Sustainable Supplier Selection and order allocation through quantity discounts. International Management halke, Science Engineering Management.

[9]. Muhammad A (2020). Towards a Sustainable Assessment of Supplier, an integrated Fuzzy TOPSIS Possibilistic multi-objective approach. Annals of Operations Research.

[10]. Memari A, Dargi, Akbari Joker, M.R, Ahmad, R,Abdul Rahim,2019 Sustainable Supplier Selection, a Multi Criteria Intuitonistic Fuzzy TOPSIS Method, J Manuf.

[11]. Bai and Sarkis (2018). Integrating Sustainability into Supplier Selection. A grey based TOPSIS Analysis. Technological and Economic Development of Economy.

[12]. Li, Fang and Song (2019). Sustainable Supplier Selection bases on SSCM Practices. A Rough Cloud TOPSIS approach. Journal of Cleaner Production.

[13]. Dos Santos, Godoy and Campos (2019). Performance Evaluation of Green Supplier Using Entropy TOPSIS Fuzzy. Journal of Cleaner Production.

[14]. Yu,C,Shao, Wang and Zhang (2019). A Group Decision Making Sustainable Supplier Selection approach using extended TOPSIS under interval valued Pythagorean Fuzzy Environment. Expert System with Applications.

[15]. Khoshfetrat , Rahim Nezhad Galankashi M and Almasi (2020). Sustainable Supplier Selection and order allocation. A Fuzzy approach, Engineering Optimiation.

[16]. Buyukozkan, G., & Çifçi, G. (2011). A novel fuzzy multi-criteria decision framework for sustainable supplier selection with incomplete information. *Computers in industry*, *62*(2), 164-174.

[17]. Laosirihongthong, T., Samaranayake, P., & Nagalingam, S. (2019). A holistic approach to supplier evaluation and order allocation towards sustainable procurement.

[18]. Badri Ahmadi, H., Hashemi Petrudi, S. H., & Wang, X. (2017). Integrating sustainability into supplier selection with analytical hierarchy process and improved grey relational analysis: a case of telecom industry.

[19]. Xu, Z., Qin, J., Liu, J., & Martínez, L. (2019). Sustainable supplier selection based on AHPSort II in interval type-2 fuzzy environment.

[20]. Pishchulov, G., Trautrims, A., Chesney, T., Gold, S., & Schwab, L. (2019). The Voting Analytic Hierarchy Process revisited: A revised method with application to sustainable supplier selection.

[21]. Ghadimi, P., Dargi, A., & Heavey, C. (2017). Making sustainable sourcing decisions: practical evidence from the automotive industry.

[22]. Demir, L., Akpınar, M. E., Araz, C., & Ilgın, M. A. (2018). A green supplier

evaluation system based on a new multi-criteria sorting method: VIKORSORT.

[23]. Lu, H., Jiang, S., Song, W., & Ming, X. (2018). A rough multi-criteria decision-making approach for sustainable supplier selection under vague environment. 2.

[24]. Qin, J., Liu, X., & Pedrycz, W. (2017). An extended TODIM multi-criteria group decision making method for green supplier selection in interval type-2 fuzzy environment. *European Journal of Operational Research*, *258*(2), 626-638.

[25]. Qin, J., Liu, X., & Pedrycz, W. (2017). An extended TODIM multi-criteria group decision making method for green supplier selection in interval type-2 fuzzy environment. *European Journal of Operational Research*, *258*(2), 626-638.

[26]. Jain, N., & Singh, A. R. (2020). Sustainable supplier selection criteria classification for Indian iron and steel industry: a fuzzy modified Kano model approach. *International Journal of Sustainable Engineering*, *13*(1), 17-32.

[27]. Wang, X., Cai, J., & Xiao, J. (2019). A novel decision-making framework for sustainable supplier selection considering interaction among criteria with heterogeneous information. *Sustainability*, *11*(10), 2820.

[28]. Osiro, L., Lima-Junior, F. R., & Carpinetti, L. C. R. (2018). A group decision model based on quality function deployment and hesitant fuzzy for selecting supply chain sustainability metrics. *Journal of Cleaner Production*, *183*, 964-978.

[29]. Foroozesh, N., Tavakkoli-Moghaddam, R., & Meysam Mousavi, S. (2018). Sustainable-supplier selection for manufacturing services: a failure mode and effects analysis model based on interval-valued fuzzy group decision-making. *The International Journal of Advanced Manufacturing Technology*, *95*(9), 3609-3629.

[30]. Foroozesh, N., Tavakkoli-Moghaddam, R., & Mousavi, S. M. (2019). An interval-valued fuzzy statistical group decision making approach with new evaluating indices for sustainable supplier selection problem. *Journal of Intelligent & Fuzzy Systems*, *36*(2), 1855-1866.

[31]. Igarashi, M., de Boer, L., & Fet, A. M. (2013). What is required for greener supplier selection? A literature review and conceptual model development. *Journal of Purchasing and Supply Management*, *19*(4), 247-263.

[32]. Rao, C., Goh, M., & Zheng, J. (2017). Decision mechanism for supplier selection under sustainability. *International Journal of Information Technology & Decision Making*, *16*(01), 87-115.

[33]. Rabbani, M., Foroozesh, N., Mousavi, S. M., & Farrokhi-Asl, H. (2019). Sustainable supplier selection by a new decision model based on interval-valued fuzzy sets and possibilistic statistical reference point systems under uncertainty. *International Journal of Systems Science: Operations & Logistics*, *6*(2), 162-178.

[34]. Park, K., Kremer, G. E. O., & Ma, J. (2018). A regional information-based multi-attribute and multi-objective decision-making approach for sustainable supplier selection and order allocation. *Journal of cleaner production*, *187*, 590-604.

[35]. Almasi, M., Khoshfetrat, S., & Galankashi, M. R. (2019). Sustainable supplier selection and order allocation under risk and inflation condition. *IEEE Transactions on Engineering Management*, *68*(3), 823-837.

[36]. El Mariouli, O., & Abouabdellah, A. (2019). A new model of supplier's selection for sustainable supply chain management. *Advances in Science, Technology and Engineering Systems*, *4*(2), 251-259.

[37]. A., Paydar, M. M., & Safaei, A. S. (2018). An integrated fuzzy MOORA method and FMEA technique for sustainable supplier selection considering quantity discounts and supplier's risk. *Journal of cleaner production*, *190* 577-591.

[38]. Azadnia, A. H., Saman, M. Z. M., & Wong, K. Y. (2015). Sustainable supplier selection and order lot-sizing: an integrated multi-objective decision-making process. *International Journal of Production Research, 53*(2), 383-408.

[39]. Gupta, P., Govindan, K., Mehlawat, M. K., & Kumar, S. (2016). A weighted possibilistic programming approach for sustainable vendor selection and order allocation in fuzzy environment. *The International Journal of Advanced Manufacturing Technology*, *86*(5), 1785-1804.

[40]. Hamdan, S., & Cheaitou, A. (2017). Dynamic green supplier selection and order allocation with quantity discounts and varying supplier availability. *Computers & Industrial Engineering*, *110*, 573-589.

[41]. Jauhar, S. K., & Pant, M. (2017). Integrating DEA with DE and MODE for sustainable supplier selection. *Journal of computational science*, *21*, 299-306.

[42]. Tavana, M., Yazdani, M., & Di Caprio, D. (2017). An application of an integrated ANP–QFD framework for sustainable supplier selection. *International Journal of Logistics Research and Applications*, *20*(3), 254-275.

[43]. Yazdani, M., Chatterjee, P., Zavadskas, E. K., & Zolfani, S. H. (2017). Integrated QFD-MCDM framework for green supplier selection. *Journal of Cleaner Production*, *142*, 3728-3740.

[44]. Babbar, C., & Amin, S. H. (2018). A multi-objective mathematical model integrating environmental concerns for supplier selection and order allocation based on fuzzy QFD in beverages industry. *Expert Systems with Applications*, *92*, 27-38.

[45]. Babbar, C., & Amin, S. H. (2018). A multi-objective mathematical model integrating environmental concerns for supplier selection and order allocation based on fuzzy QFD in beverages industry. *Expert Systems with Applications*, *92*, 27-38.

[46]. Babbar, C., & Amin, S. H. (2018). A multi-objective mathematical model integrating environmental concerns for supplier selection and order allocation based on fuzzy QFD in beverages industry. *Expert Systems with Applications*, *92*, 27-38.

[47]. Rabieh, M., Rafsanjani, A. F., Babaei, L., & Esmaeili, M. (2019). Sustainable supplier selection and order allocation: An integrated delphi method, fuzzy TOPSIS, and multi-objective programming model. *Scientia Iranica. Transaction E, Industrial Engineering*, *26*(4), 2524-2540.

[48]. Schramm, V. B., Cabral, L. P. B., & Schramm, F. (2020). Approaches for supporting sustainable supplier selection-A literature review. Journal of cleaner production, 273, 123089.

[49]. Marzouk, M., & Sabbah, M. (2021). AHP-TOPSIS social sustainability approach for selecting supplier in construction supply chain. *Cleaner Environmental Systems*, *2*, 100034.

DEVELOPMENT AND PERFORMANCE STUDY OF LAB SCALE CONTINUOUSLY STIRRED TANK REACTOR FOR BIOGAS PRODUCTION

Asad A. Zaidi[1,*], Abdul Hameed Memon[1], Rahool Rai[1], Muhammad Uzair[2]
[1]Mechanical Engineering Department, Faculty of Engineering Science and Technology, Hamdard University, Karachi, Pakistan
[2]Mechanicall Engineering Department, NED University of Engineering & Technology, Karachi, Pakistan

[*]Corresponding author. Tel.: +92-333-3561095; fax: +92-21-36440045
E-mail address: asad.zaidi@hamdrad.edu.pk (Asad A. Zaidi)

ABSTRACT

Anaerobic digestion is widely used technology for biogas production. Considering the current scenario of the Natural Gas scarcity in Pakistan, dire need to explore more substrates for their potential for biogas production is an urgent issue. In this study, a lab-scale Continuously Stirred Tank Reactor (CSTR) was developed for biogas production from anaerobic digestion with a five-litre capacity. In CSTR, anaerobic digestion (AD) was performed by using different substrates including cow dung, kitchen waste and fruit waste. Results showed that with cow dung and water as substrate in ratio 50:50, 465 ml of total biogas was produced in the total retention time of 18 day and the methane yield was 47.937%. The second experiment conducted contained kitchen waste, cow dung and water in the ratio 25:25:50, the total biogas yield was observed to be 520ml and the methane yield was 52.467%.The third experiment conducted contained Fruit waste, cow dung and water in the ratio 25:25:50 the total biogas yield was observed to be 384 ml and the methane yield was 53.747%.

Keywords: Anaerobic Digestion, Biogas, Renewable Energy, CSTR Reactor

1 INTRODUCTION

Anaerobic Digestion (AD) is a biological process that is normally utilized to convert heterogeneous biodegradable waste into suitable biogas with methane as the power source [1]. Progressively, AD is being consumed in agricultural, industrial, and municipal waste (water) management applications [2]–[4]. The practice of AD technology permits plant operators in moderating waste disposal costs and offset energy utility costs. While treating organic wastes, energy crops are also being converted into the consumable energy source methane. With the extension to application of AD in treating new substrates and co-substrates, the demand for a consistent testing methodology at the pilot- and laboratory-scale has also intensified [5], [6].

AD produces biogas when microorganisms break down (eat) organic materials in the absence of oxygen. Methane (CH_4) and carbon dioxide (CO_2) make up the majority of biogas, with very minute quantities of other gases and water vapor [7]. The carbon dioxide and other gases can be removed, leaving only the methane as the primary component of natural gas.

Besides biogas there are two other principal products at the completion of AD, the first being water and the second is called "digestate." Digestate is a wet mixture that is usually separated into a solid and a liquid. Digestate are nutrient-rich and may be applied to crops as fertilizer [8].

AD systems are in diverse configurations, including the anaerobic sequencing batch reactor (ASBR), plug flow (PF) and continuously stirred tank reactor (CSTR) [9]. The CSTR is recurrently utilized in research because of its uncomplicatedness in design and operation, but also for precedence that it provides in experimentation. In Comparison to most other configurations, the CSTR provides more stability to system's required parameters, such as substrate concentration, temperature, chemical concentration, and mixing. Eventually, when designing a full-scale reactor, the optimum reactor configuration will depend on the character of given substrate among many other

nontechnical considerations. However, all arrangements share essential design features and operating boundaries that make the CSTR appropriate for almost all preliminary evaluations. If researchers and engineers use an influent stream with usually high solid concentrations, lab-scale bioreactor setups cannot be fed continuously due to solids blocking difficulties in lab-scale pumps or solids settling in tubing. For that situation with constant mixing needs, lab-scale bioreactors are fed on a regular basis, and such arrangements are referred to as continuously stirred anaerobic digesters. (CSADs) [10].

Burning of fossil fuel emits in tremendous amounts of contaminants among which carbon tops the list. CO_2 and other GHGs, when released into the atmosphere, pollute air that we breathe which has become a cause of diseases like asthma, which has shortened life expectancy [11]–[13]. The other incommodities caused by burning of fossil fuel include increase in atmospheric temperature which became the reason of the loss of many human lives in Karachi and Pakistan in recent years [14]. These gases, when released into ocean, also cause damage to marine life. This gave rise to an energy source that does not spoil the atmosphere, hence, a greener environment.

Biomass produced by household, industries and agriculture possesses an incredible amount of potential for energy, majority of which is wasted [7], [15]–[17]. Overproduction of these has become a problem in many countries, especially in Pakistan. These can be utilized to overcome the need of electricity which will also decrease the amount of waste in the country.

The objective of this study is to develop laboratory scale CSTR biogas digester and analyze the performance of the Digester for duration of 15 to 20 days using cow dung, kitchen waste and fruit waste as substrates.

2 MATERIALS AND METHODS

2.1 Development of Biogas Digester

The complete experimental setup of Lab Scale Anaerobic Digester is shown in Figure 1. The 5 litre conical flask is the closed container used for digestion placed in the water bath which was used to maintain the mesophilic temperature for microbes. For the agitation an AC motor of 250 r.p.m is used which is connected through a shaft to a flat paddle blade stirrer. To hold the motor in place a simple laboratory stand is used. The stainless steel shaft is passed through a Teflon cork which is used to seal the container. An analogue thermometer was also used to measure the temperature in case of any error that might occur in the digital thermometer of water bath. In order to collect the biogas generated in the digester a gas pipe was placed on the cork. On the other end of the gas pipe a gas pouch is placed through a gas valve where the biogas is collected.

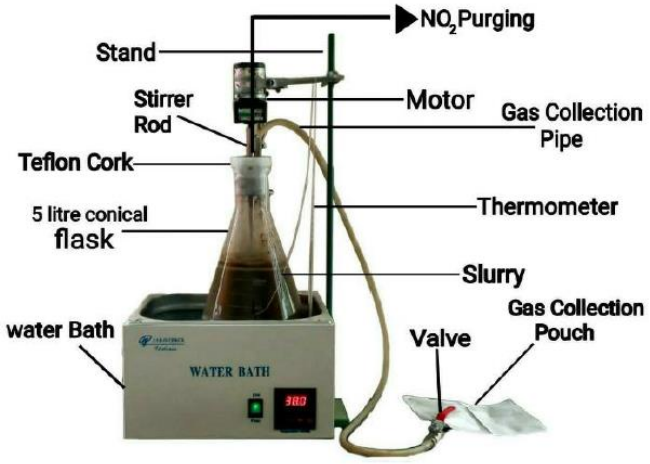

Figure 1. Lab Scale Anaerobic Digester

2.2 Gas Composition Measurement

For analysing the gas two tests were conducted in order to find the composition of different gases present in the biogas samples. The first test conducted was on Gas Chromatograph to find the composition of Methane (CH_4) and Carbon dioxide (CO_2) in the biogas sample. The second test was on Gas Detector Tube for the presence of hydrogen Sulphide (H_2S).

Gas chromatography (GC) is a typical analytical technique used to isolate and analyse volatile and semi-volatile compounds in a mixture [31]. GC Chromatec-Crystal 9000 was used for the purpose of gas chromatography by PRD Laboratory. Crystal 9000 is fully automated, flexible, versatile instrument features a wide range of detectors, injectors and external automatic samplers and other devices.

The GPA method 2261 was utilized for this purpose. For this particular required test, the components nitrogen/air, methane, carbon dioxide and ethane through n-pentane are eluted on forward flow of carrier gas through the partition column. The numerous heavy components of natural gas are grouped into a single peak using a precut column which is backflushed to elute the hexanes and heavier as the first peak in the chromatogram. This recommended approach to the hexanes and heavier separation has two distinct advantages: better

precision of measuring the peak area, and a reduction in analysis time over the non-precut (single) column approach.

3 RESULTS AND DISCUSSION

3.1 Anaerobic Digestion of Cow Dung

Figure 2 demonstrates the cumulative Biogas production for the first experiment. CSTR experiments were run at with cow slurry as substrate at mesophilic temperature of 37°C. For about 18 days that the experiment was conducted and monitored, It was determined that the first four days ,the long chain substances, carbohydrates, proteins and fats broke down into smaller fragments such as simple sugars, glycerol, fatty acids and amino acids, this step is known as hydrolysis [18]. From the graph it can be determined that from day 5 to day 15 the rest of the stages were carried out. The gas generation was maximum at day 9 and 10 and then it was observed to the gas production started to decline since them. Then at day 17 the gas production was negligible. The total biogas generated in this experiment was 465.4592 ml.

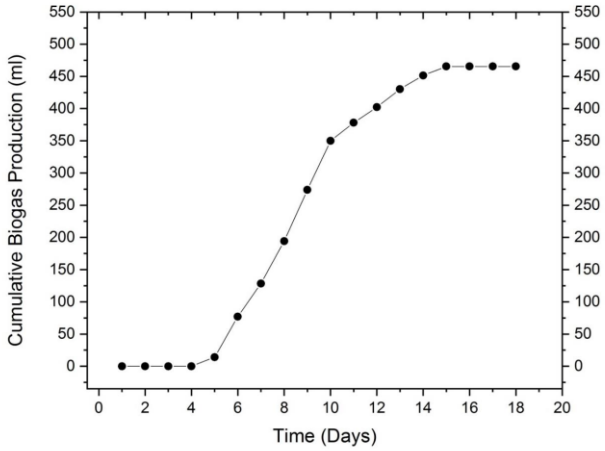

Figure 2. Cumulative Gas Production (for Cow Dung and Water in ratio 50:50)

3.2 Anaerobic Co-Digestion of Kitchen Waste and Cow Dung

Figure 3 demonstrates the daily cumulative Biogas production for the second experiment. The digester was run with kitchen waste and cow slurry along with water as substrate at mesophilic temperature. The kitchen waste is composed of corn; wheat and potato peel in equal ratios. This experiment was observed to be rather faster than the first one since it only lasted for four days (96 hours). Maximum gas production was observed between 36 and 48 hours, the gas production per 12 hours was observed to be reduced significantly since then and no gas was produced after 96 hours. The total biogas production in this experiment was 520 millilitres.

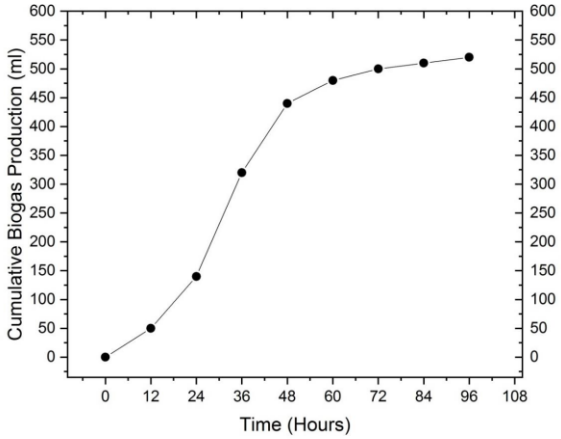

Figure 3. Cumulative Gas Production (for Kitchen waste + Cow Dung and Water in ratio 25:25:50)

3.3 Anaerobic Co-Digestion of Kitchen Waste and Cow Dung

Figure 21 demonstrates the daily cumulative Biogas production for the third experiment. The digester was run with fruit waste and cow slurry along with water as substrate at mesophilic temperature. The fruit waste composed of peel of banana, apple, mango and grapefruit in equal ratios. This experiment was also observed to be faster than the digestion of cow dung, as it only lasted for four days (96 hours). Maximum gas production was observed between 12 and 24 hours, the gas production per 12 hours was observed to be reduced significantly since then and no gas was produced after 96 hours. The total biogas production in this experiment was 384 millilitres.

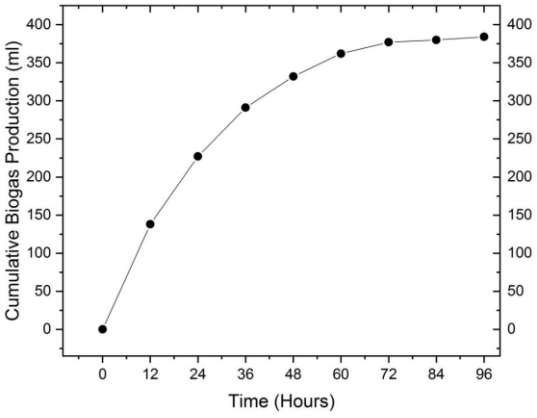

Figure 4. Cumulative Gas Production (for Fruit waste + Cow Dung and Water in ratio 25:25:50)

3.4 PRD Test Results

Table 1 represents the percentage of major elements found in the tests reports from the biogas sample of each report received from PRD laboratory. The maximum biogas yield in terms of volume comparative to the percentage of methane was from experiment 2 "Anaerobic Co-Digestion of Kitchen Waste And Cow Dung". Followed by first experiment "Anaerobic Digestion of Cow Dung" at second and the minimum being the third experiment "Anaerobic Co-Digestion of Fruit Waste and Cow Dung"

Table 1. Element Composition from Tests

Experiment	Element Composition (Mole %)			
	CH_4	CO_2	O_2	N_2
CD	47.932	23.270	2.403	26.389
CD + KW	52.467	18.735	1.723	27.069
CD + FW	53.747	17.735	2.463	26.049

4 CONCLUSION

The main objective for this project was development of lab scale biogas digester and performance study of the digester on different substrates. After the development of biogas three experiments were successfully performed. The substrates for each experiment were 'Cow Dung And Water', 'Cow Dung, Kitchen Waste and Water' and 'Cow Dung, Fruit Waste and Water' each in the ratios of 50:50, 25:25:50 and 25:25:50 respectively. The total biogas yield from each experiment was 465, 520 and 384 milliliters.

This digester could further by improved with the enhancement in technology and providing a more controlled environment to the anaerobic microbes with the help of continuous monitoring of certain parameters such as pH, Organic loading rate, Alkalinity etc. The experiments could also be improved by pre-treatment of substrates and then feeding them in the digester.

REFERENCES

[1]. A. J. F. Graef S P, "Mathematical modeling and control of anaerobic digestion.," *AIChE Symp. Ser.*, vol. 136, pp. 101–131, 1974.

[2]. A. A. Zaidi *et al.*, "Conjoint effect of microwave irradiation and metal nanoparticles on biogas augmentation from anaerobic digestion of green algae," *Int. J. Hydrogen Energy*, vol. 44, no. 29, pp. 14661–14670, 2019.

[3]. R. Feng, A. A. Zaidi, K. Zhang, and Y. Shi, "Optimisation of Microwave Pretreatment for Biogas Enhancement through Anaerobic Digestion of Microalgal Biomass," *Period. Polytech. Chem. Eng.*, vol. 63, no. 1, pp. 65–72, 2018.

[4]. A. A. Zaidi, S. Z. Khan, and Y. Shi, "Optimization of nickel nanoparticles concentration for biogas enhancement from green algae anaerobic digestion," *Mater. Today Proc.*, vol. 39, pp. 1025–1028, 2021.

[5]. A. Xia *et al.*, "Fermentative hydrogen production using algal biomass as feedstock," *Renew. Sustain. Energy Rev.*, vol. 51, pp. 209–230, 2015.

[6]. R. Ganesh Saratale, G. Kumar, R. Banu, A. Xia, S. Periyasamy, and G. Dattatraya Saratale, "A critical review on anaerobic digestion of microalgae and macroalgae and co-digestion of biomass for enhanced methane generation," *Bioresour. Technol.*, vol. 262, no. March, pp. 319–332, 2018.

[7]. B. Deepanraj, V. Sivasubramanian, and S. Jayaraj, "Effect of substrate pretreatment on biogas production through anaerobic digestion of food waste," *Int. J. Hydrogen Energy*, vol. 42, no. 42, pp. 26522–26528, 2017.

[8]. F. Han, S. Yun, C. Zhang, H. Xu, and Z. Wang, "Steel slag as accelerant in anaerobic digestion for nonhazardous treatment and digestate fertilizer utilization," *Bioresour. Technol.*, vol. 282, pp. 331–338, 2019.

[9]. Z. Liu, F. Lv, H. Zheng, C. Zhang, F. Wei, and X.-H. Xing, "Enhanced hydrogen production in a UASB reactor by retaining microbial consortium onto carbon nanotubes (CNTs)," *Int. J. Hydrogen Energy*, vol. 37, no. 14, pp. 10619–10626, 2012.

[10]. M. H. Zandvoort, E. D. van Hullebusch, S. Golubnic, J. Gieteling, and P. N. L. Lens, "Induction of cobalt limitation in methanol-fed UASB reactors," *J. Chem. Technol. Biotechnol.*, vol. 81, no. 9, pp. 1486–1495, Sep. 2006.

[11]. M. S. Kim, Y. Ahn, B. Kim, and J. I. Lee, "Study on the supercritical CO2 power cycles for landfill gas firing gas turbine bottoming cycle," *Energy*, vol. 111, pp.

893–909, 2016.

[12]. Y. M. Kim, C. G. Kim, and D. Favrat, "Transcritical or supercritical CO2 cycles using both low- and high-temperature heat sources," *Energy*, vol. 43, no. 1, pp. 402–415, 2012.

[13]. E. Alper and O. Yuksel Orhan, "CO2 utilization: Developments in conversion processes," *Petroleum*, vol. 3, no. 1, pp. 109–126, 2017.

[14]. M. M. Siddiqi *et al.*, "Evaluation of Municipal Solid Wastes Based Energy Potential in Urban Pakistan," *Processes* , vol. 7, no. 11. 2019.

[15]. S. Hu, X. Ma, Y. Lin, Z. Yu, and S. Fang, "Thermogravimetric analysis of the co-combustion of paper mill sludge and municipal solid waste," *Energy Convers. Manag.*, vol. 99, pp. 112–118, 2015.

[16]. Z. Huang, S. L. Ong, and H. Y. Ng, "Submerged anaerobic membrane bioreactor for low-strength wastewater treatment: Effect of HRT and SRT on treatment performance and membrane fouling," *Water Res.*, vol. 45, no. 2, pp. 705–713, 2011.

[17]. W. Ma *et al.*, "Enhanced nitrogen removal from coal gasification wastewater by simultaneous nitrification and denitrification (SND) in an oxygen-limited aeration sequencing batch biofilm reactor," *Bioresour. Technol.*, vol. 244, pp. 84–91, 2017.

[18]. B. Yang *et al.*, "Mechanism of high contaminant removal performance in the expanded granular sludge blanket (EGSB) reactor involved with granular activated carbon for low-strength wastewater treatment," *Chem. Eng. J.*, vol. 334, pp. 1176–1185, 2018.

THERMAL ANALYSIS OF SHELL AND TUBE HEAT EXCHANGER AND ITS OPTIMIZATION USING DIFFERENT MATERIALS

Usama Asghar[1,*], Abdullah Rafique[1], Muhammad Talha Aziz[1], Danyal Iqbal[1], Aymen Nadeem[1]

[1]Mechanical Engineering Department, University of Engineering & Technology, Taxila, Pakistan

[*]Corresponding author. Tel.: +92-307-6695221
E-mail address: usama.asghar@students.uettaxila.edu.pk (Usama Asghar)

ABSTRACT

Shell and tube heat exchangers are widely used in various industrial processes for heat transfer between two fluids. This paper presents an analysis of a shell and tube heat exchanger using a computational model created in ANSYS FLUENT. The model closely resembles a commercial heat exchanger, and various parameters such as average surface temperatures, surface heat transfer coefficient, surface area, surface heat flux, and amount of heat transfer are calculated. The efficiency of the heat exchanger largely depends on various parameters, such as the tube material, flow rate, and design, which need to be optimized for better performance. The heat exchanger system is optimized by changing the tube material from aluminum to copper and steel. The results indicate that copper tubes are 3% more effective for heat transfer, while steel tubes are the least effective. This study provides valuable insights for designing efficient heat exchangers and improving their performance.

Keywords: Shell and tube heat exchanger; computational model; heat transfer co-efficient; heat flux

1 INTRODUCTION

Heat exchangers are important devices used in many industrial and commercial applications to transfer heat from one fluid to another. The shell and tube heat exchanger is one of the most common types of heat exchangers used in industry. It consists of a cylindrical shell with a bundle of tubes inside. One fluid flow through the tubes, while the other fluid flows through the shell, with heat being transferred between them through the tube walls [1].

Ali et al. investigated the use of nanofluids in shell and tube heat exchangers and compared their performance to that of conventional fluids. The results showed that nanofluids can improve the heat transfer rate and overall efficiency of the heat exchanger [2].

Balaga, R et al. examined the effect of twisted tape inserts on the heat transfer rate in a shell and tube heat exchanger. The results indicated that twisted tape inserts can significantly enhance the heat transfer rate and reduced the overall size of the heat exchanger [3].

Zahid, H. *et al.* Studied the effect of baffle configurations on the heat transfer rate in a shell and tube heat exchanger. The results showed that different baffle configurations can significantly affect the heat transfer rate and pressure drop in the heat exchanger [4].

Alqarni, M.M. et al. experimentally investigated the use of nanofluids to enhance the heat transfer rate in shell and tube heat exchangers. The results showed that the use of nanofluids can improve the heat transfer rate and overall efficiency of the heat exchanger [5].

The goal of minimizing both capital and operating costs was considered by the authors as an objective function. Similar strategies based on genetic algorithms and traditional mathematical optimization algorithms have also been employed by other researchers [6-13] to optimize the design of heat exchangers for various objectives, including minimizing entropy generation [10,11] and minimizing the cost of STHEs [12-13].

In this research, a computer model made in ANSYS FLUENT is used to analyze a heat exchanger. Several parameters, including average surface temperatures, surface heat transfer coefficient,

surface area, surface heat flux, and amount of heat transfer, are computed using a model that closely matches a commercial heat exchanger. The design, flow rate, and other factors that must be tuned for improved performance have a significant impact on the heat exchanger's efficiency. By switching from aluminum to copper and steel for the tube material, the heat exchanger system is improved.

2 METHODOLOGY

In general, the thermal design analysis of a heat exchanger involves determining the size and geometry of the heat exchanger required to meet the desired heat transfer rate, while also ensuring that the pressure drop across the heat exchanger is within acceptable limits. Here are the general steps involved in the thermal design analysis of a heat exchanger:

2.1 Define the operating conditions

The first step is to define the operating conditions of the heat exchanger, including the flow rates, temperatures, and physical properties of both the hot and cold fluids.

2.2 Select the heat transfer surface

Based on the operating conditions and the desired heat transfer rate, a suitable heat transfer surface was selected. This may include a tube-and-shell, plate-and-frame, or finned-tube heat exchanger.

2.3 Determine the heat transfer coefficient

The heat transfer coefficient is a measure of the heat transfer rate per unit area of the heat transfer surface. It was determined using empirical correlations or through computational fluid dynamics (CFD) simulations.

2.4 Calculate the overall heat transfer coefficient

The overall heat transfer coefficient takes into account the heat transfer coefficient of the hot and cold fluids, as well as the resistance to heat transfer at the heat transfer surface. It was calculated using the log-mean temperature difference (LMTD) method.

2.5 Determine the heat transfer area

The heat transfer area is calculated based on the heat transfer rate and the overall heat transfer coefficient. This provides an estimate of the size of the heat exchanger required to meet the desired heat transfer rate. Mass

2.6 Evaluate pressure drop

The pressure drop across the heat exchanger is calculated based on the flow rates and the physical properties of the fluids. It is important to ensure that the pressure drop is within acceptable limits to prevent excessive energy loss and maintain fluid flow.

2.7 Optimize design

Based on the results of the thermal design analysis, the heat exchanger can be optimized to improve its performance. This may involve modifying the geometry, adjusting the operating conditions, or selecting a different heat transfer surface to achieve the desired heat transfer rate while minimizing pressure drop.

The following working steps have been followed during the simulation.

- Modeling a heat exchanger of the Shell and Tube type.
- Converting the file once more to ensure compatibility with the simulation process.
- Using Ansys Fluent to import the file and run the simulation.
- Choosing names for the various Shell and Tube type heat exchanger components.
- Carry out cross-flow heat exchanger meshing that is suitable for CFD analysis.
- Providing the appropriate boundary conditions.
- Giving the material qualities a name.
- Creating the ideal environment for the CFD analysis process.
- Analyzing the outcomes after the simulation work is complete.

3 GOVERNING EQUATIONS

In simulations, governing equations 1-7 are used to model and predict the thermal behavior of complex systems as well as the velocity produced by temperature gradients.

$$\rho\frac{DV}{Dt} = \rho g - \nabla P + \mu\nabla^2 V \quad (1)$$

$$\frac{DV}{Dt} = \frac{\partial V}{\partial t} + u\frac{\partial V}{\partial x} + v\frac{\partial V}{\partial y} \quad (2)$$

Where,

$$\nabla^2 V = \frac{\partial^2 V}{\partial^2 x} + \frac{\partial^2 V}{\partial^2 y} \quad (3)$$

$$\frac{\partial u}{\partial x} + \frac{\partial v}{\partial y} = 0 \quad (4)$$

$$\rho\frac{Du}{Dt} = \rho g_x - \frac{\partial P}{\partial x} + \mu\nabla^2 u \quad (5)$$

$$\rho \frac{Dv}{Dt} = \rho g_y - \frac{\partial P}{\partial x} + \mu \nabla^2 v \quad (6)$$

$$\rho \frac{Dw}{Dt} = \rho g_z - \frac{\partial P}{\partial x} + \mu \nabla^2 w \quad (7)$$

4 MODEL DESCRIPTION

The simulation is done on a counter flow, horizontal, shell and tube heat exchanger with a shell of 1-meter diameter and 3m depth. There are 19 hot water tubes of 0.1 m diameter and 4m length passing through the heat exchanger. The cold fluid enters the shell at the mass flow rate of 0.1 kg/s from a 0.3 m diameter opening at the top and exits through an equal-sized opening at the bottom. The tube material used for the simulation is Aluminium. The geometry of shell and tube heat exchanger is shown in Figure 1 and 2.

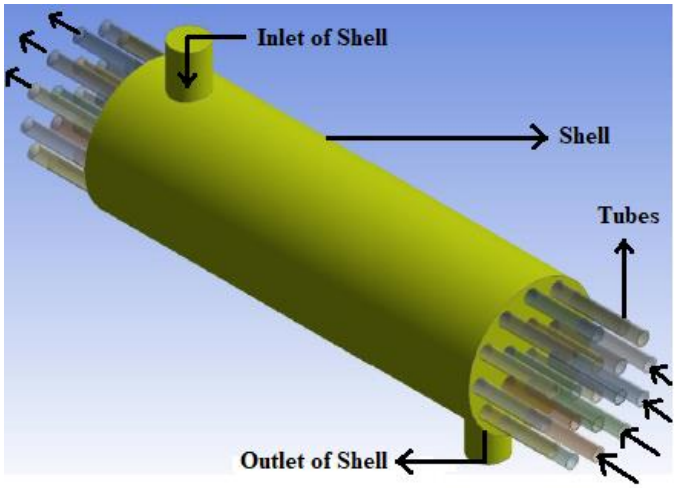

Figure 1. Geometry of shell and tube heat exchanger

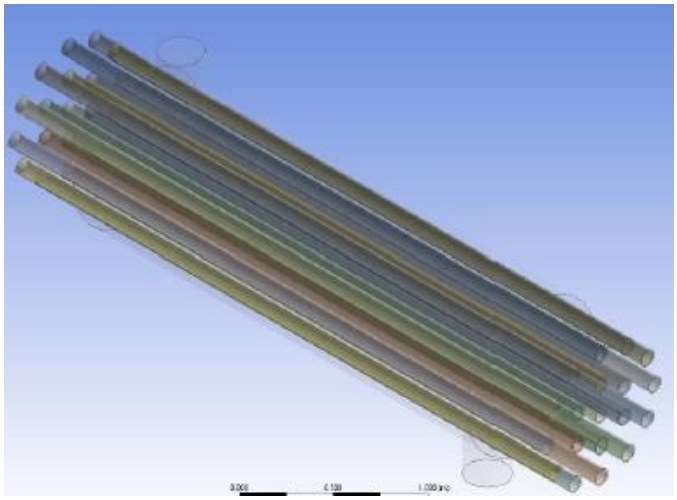

Figure 2. Tubes in the shell of the heat exchanger

5 MESHING

To make our simulation simple and less complicated it has already been established that since both conduction and convection processes would be considered in the simulation it is ideal to apply the Conformal meshing method. The heat is transferred from hot fluid in the tube-to-tube wall via convection, conduction in the wall tube and then convection from tube wall to shell fluid.

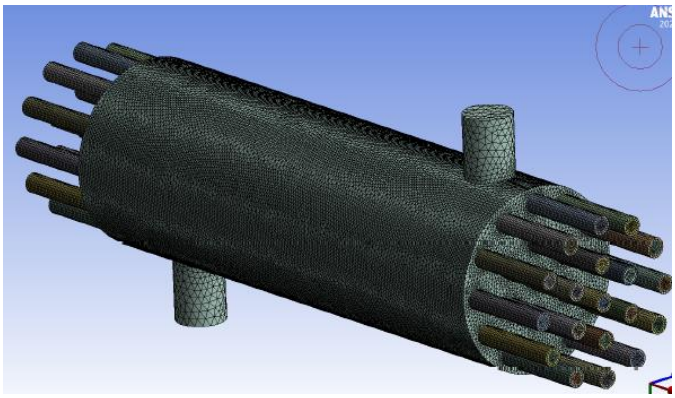

Figure 3. Meshing of STHE

Table 1. Meshing details

Values	Element Quality	Aspect Ratio	Skewness
Minimum	0.1596	1.1443	2.72e-008
Maximum	1	14.705	0.8448
Average	0.8259	1.8631	0.2394
Standard Deviation	0.1028	0.5015	0.1297

Number of Nodes = 1260000
Number of Elements = 4455925
The model used for simulation is Realizable k-Epsilon with Enhanced Wall Treatment**,** for all three materials since we want to capture turbulence in our results as well.

6 MATERIAL SPECIFICATIONS AND BOUNDARY CONDITIONS

The main goal of this simulation is to design and perform a thermal analysis of a heat exchanger by changing the tube material (Aluminium, Copper and, Steel), to see how it affects the heat transfer. This is done by finding out important parameters such as outlet temperatures at the tube (hot fluid) and shell side (cold fluid), heat transfer coefficient at tube surface, surface heat flux, surface area and

amount of heat transfer, and comparing them for each material.

The setup involves the definition of the boundary conditions for the simulation. This involves specifying the flow conditions, such as inlet velocity, pressure, temperature, and turbulence parameters, at the boundaries of the domain.

The fluid passing through the tube is taken to be water at 100 °C and shell fluid is taken to be also water at 20 °C.

Table 2. Properties of material used

Properties	Aluminum	Copper	Steel
Density (kg/m^3)	2719	8978	8030
Specific Heat (J/kg.K)	871	381	502.48
Thermal Conductivity (W/m.K)	202.4	387.6	16.27

Table 3. Appropriate Boundary Conditions

Boundary Conditions	Values
Hot Inlet temperature at tube	373 K
Cold Inlet temperature at shell	293 K
Mass Flow Rate	0.1 kg/s
Wall Flux	0 W/m^2
Initial Gauge Pressure	0 Pa
Turbulent Intensity	5%
Turbulent Viscosity Ratio	10

7 RESULTS AND DISCUSSION

The simulation results for Aluminium tubes are viewed on a midplane that is on an x-y plane and constitutes the center of the z-plane.

7.1 Pressure

Pressure contour refers to a graphical representation of pressure distribution in a fluid domain. It shows how pressure changes across the domain, with different colours indicating different pressure values. The contour lines connect points of equal pressure, like a topographical map.

The Figure 4 shows different pressure values at inlets, outlets, inside the shell and tube as well.

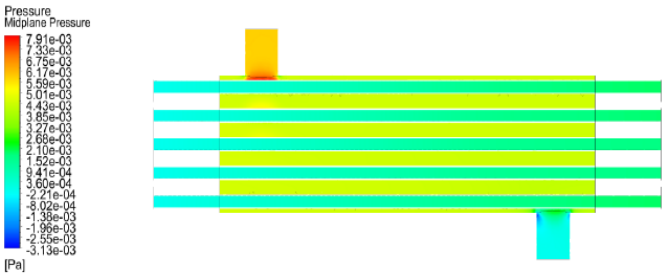

Figure 4. Pressure Contours of STHE

The cold water enters the shell at a relatively higher pressure of almost 6.17 mPa and leaves at 3.6 mPa from the bottom of the shell. Inside the shell, the Pressure maintains at 3.9 mPa.

The hot water enters the Aluminium tubes at the pressure of 1.52mPa and leaves the tubes at decreased pressure of 2.9 mPa.

It should also be noted that since there are no bends in tubes thus temperature drop is almost negligible.

7.2 Temperature

The temperature contours in the following figure show that the inlet temperature of the shell is 2 93.15 K. The temperature at the outlet of the shell is 307.51735 K. This shows that the water passing through the shell undergoes a temperature drop of 14.36735K.

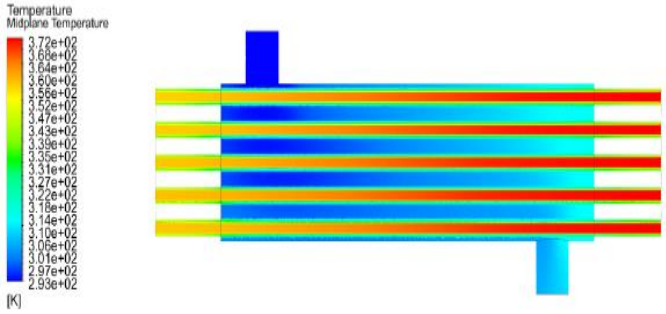

Figure 5. Temperature Contour of Shell and tube heat exchanger

However, the temperature of hot water at the inlet of the aluminum tubes is 373.15K. As the water passes through the tubes, it exchanges heat with cold water in shell. Thus, hot water in the tubes undergoes a temperature drop leaving the tubes at a lower temperature of 358.7269K. The Figure 6 shows how temperature varies in shell.

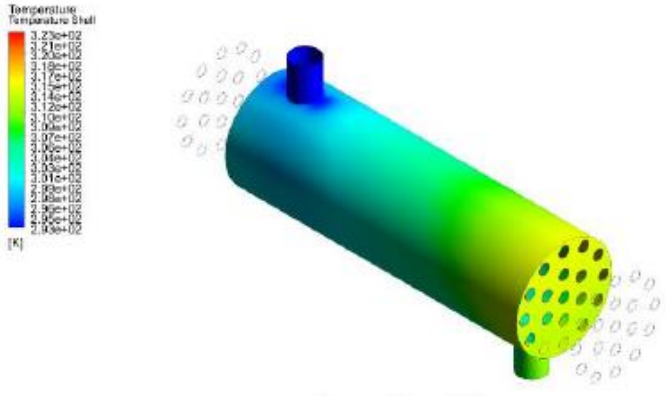

Figure 6. Temperature Contour of Shell Side

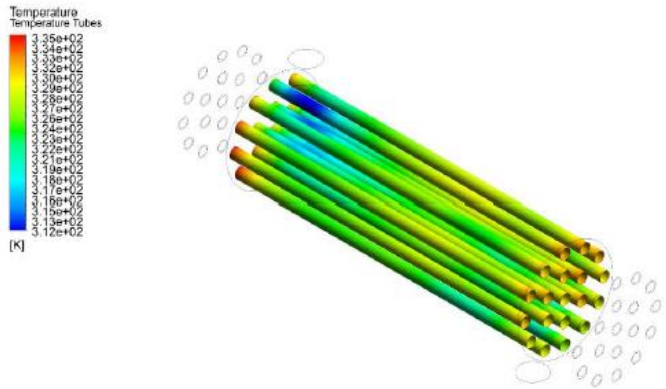

Figure 7. Temperature Contour of Tubes Side

The above Figure 7 show that the tube surface at which cold water strikes is comparatively very low in temperature since the temperature gradient is very high in this region and maximum heat transfer takes place here.

7.3 Velocity

Since the water is entering the shell at the mass flow rate of 0.1 kg/s a low velocity of 1.76mm/s is observed at the shell inlet which further drops to n even more low velocity near stagnation inside the shell. However, the velocity inside tubes almost remains unchanged.

It should be noted here the area where fluid enters the shell and hits the tubes, the backflow occurs, and turbulence is observed here. This appears in a rise in

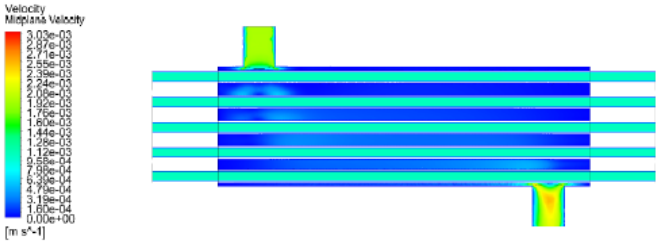

Figure 8. Velocity Contour of STHE

velocity of the fluid in this region. This can be seen as a light blue color appearing above the tubes.

Also, as the fluid leaves the shell at the bottom rise in velocity is observed in Figure 8.

7.4 Fluid Stream

Fluid streamlines are imaginary lines that represent the instantaneous direction of fluid flow at a particular moment in time. These lines are drawn in a fluid domain to visualize and analyze the flow patterns. Streamlines are derived from the velocity field of the fluid, which is a vector field that defines the velocity of the fluid at every point in the domain.

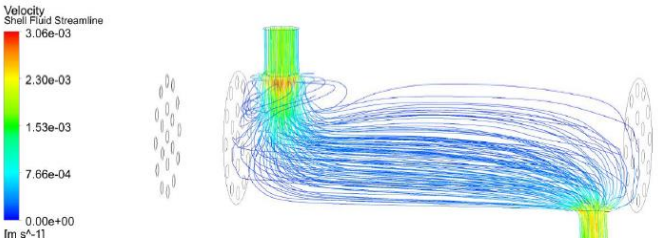

Figure 9. Fluid streamline of Shell Side

It can be observed from the Figure 10 that cold water at 293.1K is entering the shell from the top and makes its way to the outlet at the bottom. Some backflow is also observed at the location where fluid hits the tubes appearing as zigzag lines. However, the hot water flowing in the counter direction of the shell flow travels in a straight path and appears as a straight streamline.

Another important point to be noted here is that since the mass flow rate is very low i.e. 0.1 kg/s, therefore, the water leaves the shell before filling it.

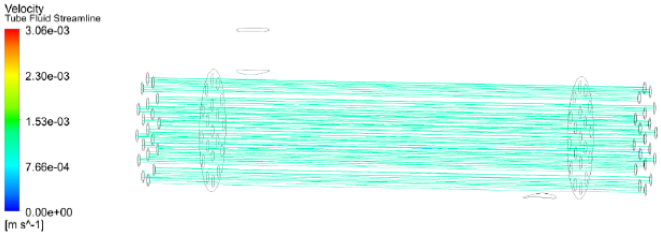

Figure 10. Fluid streamline of Tube Side

7.5 Central Tube Fluid Temperature

To see how the temperature changes across the 3m length of the Aluminium tubes, the Figure 11 is given below. It shows how the temperature is dropped along the length of the tube as it exchanges heat with cold water in the shell flowing in the counter direction.

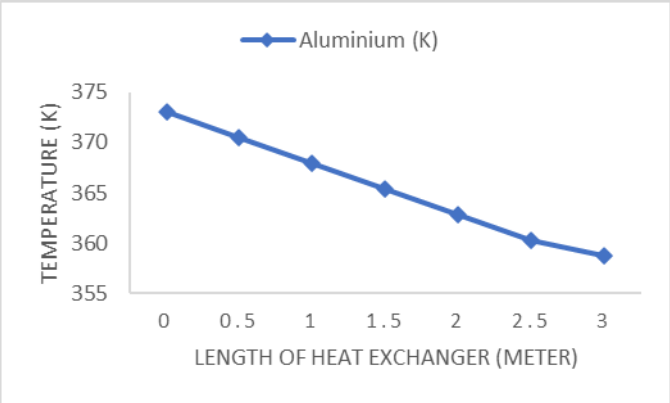

Figure 11. Temperature reduction profile in aluminium tubes

Table 4. Values of different parameters using Aluminium material

Parameters	**Location**	**Aluminum**
Tube Temperature (K)	Inlet Hot Outlet Hot Difference	373.15 358.7269 14.4231
Shell Temperature (K)	Inlet Cold Outlet Cold Difference	293.15 307.7173 14.3672
Surface Heat Transfer Coefficient (W/m^2K)	Shell Fluid Wall Boundary Tube Fluid Wall Boundary	-9.4261 8.3706
Surface Area (m^2)	Shell Fluid Wall Boundary Tube Fluid Wall Boundary	17.6190 19.0224
Heat Flux (W/m^2)	Shell Fluid Wall Boundary Tube Fluid Wall Boundary	-341.2548 315.7981
Heat Transfer (W)	Shell Fluid Wall Boundary Tube Fluid Wall Boundary	-6012.59 6007.248

8 OPTIMIZATION

The material optimization of fluid material is done by changing the material of tubes from Aluminum to copper and steel. The different thermal conductivities affect the rate of heat transfer. This pattern is observed by different outlet temperatures of fluid passing through tubes.

Thus, material optimization in CFD analysis involves selecting the optimal material for a given application to achieve desired performance. It typically involves selecting a material with the right properties that can withstand the thermal and mechanical stresses induced by the fluid flow.

The properties that are important for material selection include thermal conductivity, specific heat, density, viscosity, and other material properties that affect fluid flow and heat transfer. For example, in the case of a heat exchanger, selecting a material with high thermal conductivity and low thermal resistance can increase the efficiency of the heat transfer process.

For this simulation, the material of the tubes is changed from Aluminium to Copper and steel.

The simulation is run for these cases to see how the heat transfer is affected by changing the material of the tubes.

The results of all parameters calculated by simulation are compiled in the following figure table

Table 5. Value of parameters using copper and steel during optimization

Parameter	Location	Copper	Steel
Tube Temperature (K)	Inlet Hot Inlet Hot Difference	373.15 358.53 14.6178	373.15 359.531 13.618
Shell Temperature (K)	Inlet Cold Inlet Cold Difference	293.15 307.717 14.5673	293.15 306.697 13.547
Surface Heat Transfer Co-efficient, h (W/m2-K)	Shell Fluid Wall Boundary Tube Fluid-Wall Boundary	-9.4290 8.41883	-9.3242 8.37163
Surface Area (m2)	Shell Fluid-Wall Boundary Tube Fluid-Wall Boundary	17.6190 19.0224	17.6190 19.0224
Heat Flux (W/m2)	Shell Fluid-Wall Boundary Tube Fluid-Wall Boundary	-346.09 320.260	-321.48 297.526
Heat Transfer (W)	Shell Fluid-Wall Boundary Tube Fluid-Wall Boundary	-6097.8 6092.1	-5664.24 5659.68

Since the thermal conductivity of copper is higher compared to Aluminium its surface heat transfer coefficient across the Shell Fluid-Wall Tube boundary and Tube Fluid-Wall Tube boundary is high. However, due to the low thermal conductivity of steel, the value of h is also low. Thus, it can be established that due to the high value of k of copper, more effective heat transfer takes place and the amount of heat transfer is also high e.i around 6100 W and but in the case of steel, it is around 5600 approximately.

If we look at the temperature drop across the hot fluid passing through the center tube at the length of the shell body (3m), the following trend is observed.

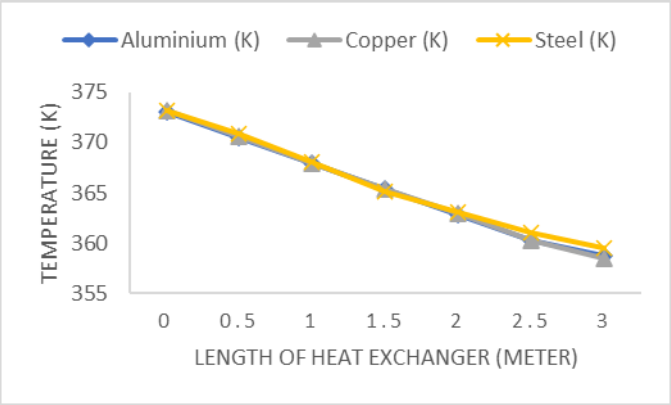

Figure 12. Comparison of temperature drop profiles for different tube materials

The plotted graph in Figure 12 shows that the most effective heat transfer takes place in the case of copper due to its high thermal conductivity and the least is in the case of steel, having the lowest thermal conductivity of all.

9 CONCLUSION

In conclusion, this paper has provided a comprehensive analysis of a shell and tube heat exchanger using a computational model created in ANSYS FLUENT. The study highlights the crucial role of various parameters such as tube material, flow rate, and design in determining the efficiency of the heat exchanger. By optimizing the heat exchanger system through changing the tube material from aluminium to copper and steel, the study has shown that copper tubes are more effective for heat transfer, while steel tubes are the least effective.

REFERENCES

[1]. Ghazanfari, V. *et al.* "Numerical Study on the thermal performance of the shell and tube heat exchanger using twisted tubes and al2o3 nanoparticles," Progress in Nuclear Energy, 155, 104526, 2023.

[2]. Ali, H.M., Hassan, A. and Wahab, A. Shell and tube heat exchanger," Nanofluids for Heat Exchangers, 1–23, 2022.

[3]. Balaga, R., Koona, R. and Tunuguntla, S., Heat transfer enhancement of the F-MWCNT- fe2o3/water hybrid nanofluid with the combined effect of wire coil with twisted tape and perforated twisted tape," International Journal of Thermal Sciences, 184, 108023, 2023.

[4]. Zahid, H. *et al.* Experimental and CFD Simulation Study of shell and tube heat exchangers with different baffle segment configurations, Thermal Science, 27(1 Part B), 843–853, 2023.

[5]. Alqarni, M.M. *et al.* Two-phase simulation of a shell and tube heat exchanger filled with hybrid nanofluid, Engineering Analysis with Boundary Elements, 146, 80–88, 2023.

[6]. Ozkol, G. Komurgoz, Determination of the optimum geometry of the heat exchanger body via a genetic algorithm. International Journal of Heat and

[7]. Mass Transfer 48, 283-296, 2005.

[8]. R. Hilbert, G. Janiga, R. Baron, D. Thevenin, Multi objective shape optimization of a heat exchanger using parallel genetic algorithm. International Journal of Heat and Mass Transfer 49, 2567-2577, 2006.

[9]. J.M. Ponce-Ortega, M. Serna-Gonzalez, A. Jimenez-Gutierrez, Use of genetic algorithms for the optimal design of shell-and-tube heat exchangers. Applied Thermal Engineering 29, 203-209, 2009.

[10]. M. Saffar-Avval, E. Damangir, A general correlation for determining optimum baffle spacing for all types of shell-and-tube exchangers. International Journal of Heat and Mass Transfer 38, 2501-2506, 1995.

[11]. S. Sun, Y. Lu, C. Yan, Optimization in calculation of shell-and-tube heat exchanger. International Communications in Heat and Mass Transfer 20, 675-685, 1993.

[12]. P.P.M. Lerou, T.T. Veenstra, J.F. Burger, H.J.M. Brake, H. Rogalla, Optimization of counter flow heat exchanger geometry through minimization of entropy generation. Cryogenics 45, 659-669, 2015.

[13]. B.V. Babu, S.A. Munawar, Differential evolution strategies for optimal design of shell-and-tube heat exchangers. Chemical Engineering Science 62 (14), 3720-3739, 2007.

[14]. F. Pettersson, J. Soderman, Design of robust heat recovery systems in paper machines. Chemical Engineering and Processing 46 (10), 910-917, 2007.

STRETCHING ANALYSIS OF COPPER THIN FILM WITH BS-8599 V7 RTV SUBSTRATE USING COMPUTER SIMULATIONS

Shahzaib Nazim[1,*], Murtuza Mehdi[1], Muhammad Saad Suleman[1]
Mechanical Engineering Department, NED University of Engineering & Technology, Karachi, Pakistan

[*]Corresponding author. Tel.: +92-312-5051284
E-mail address: shah111.sn@gmail.com (Shahzaib Nazim)

ABSTRACT

Microelectromechanical systems (MEMS) are the systems which has at least one dimension in the scale of micro meters. These are very sophisticated systems which are now extensively used in stretchable and flexible applications. Metal thin films with polymer substrate are being used in fabrication of multiple microelectronic devices, opto-electronics and optical devices. Polyethylene terephthalate (PET) and Polydimethyl siloxane (PDMS) have been extensively used as substrate for multiple stretchable and flexible microelectromechanical systems (MEMS) applications but now we can consider some other alternatives due to their increasing cost and availability issue. In this study, we are considering BS-8599 V7 Room Temperature Vulcanized elastomer as alternate substrate and Copper metallic thin film. FEA model of this laminate is studied numerically using commercial codes. Mesh independent results are obtained by applying uniaxial uniform strain on three different configurations. It will provide the estimates of stresses and strain for thin film materials. Results show that BS-8599 V7 RTV can be easily used as alternate of PDMS and PET because it generates approximately the same stresses by applying the specified strain.

Keywords: MEMS; Thin film; RTV; FEA

1 INTRODUCTION

In the last two decades, microelectromechanical systems (MEMS) have made a tremendous progress in the field of stretchable and flexible electronics [1-3]. Testing of free standing films with thickness less than 3 µm is difficult due to preparation and handling. A method to test these type of films uses Si support frames [4]. This method is complex in sample preparation, such as patterning and etching. Due to this reason, computer based simulations are better option to derive the results.

Polymers like Polyethylene terephthalate (PET) and Polydimethyl siloxane (PDMS) have long been used in stretchable and flexible microelectromechanical systems (MEMS) as substrate [5-8]. Due to high demand of these polymers, their cost has been increased and their frequent availability also has become more difficult. Thus, it has become inevitable to study an alternate polymer which should be cheaper in cost and also easily available [9].

Therefore, in this paper, we used BS-8599 V7 Room Temperature Vulcanized elastomer, which is commonly available and low-cost, silicone-based polymer alternative to PDMS and PET for stretchable and flexible MEMS applications [10].

A thin film of a functional material is an integral part of such a system in which the film may be subjected to mechanical stretching, bending, twisting, vibrations and even their combinations [11, 17]. These loadings can cause the film to crack open which ultimately results in device failure [18-20]. A FEA based model that can predict the failure for such thin film laminate s would therefore be of great significance as it can help the designers to gain more insight prior to the fabrication steps.

It will identify the limits of applicability on the basis of stress and strains for thin film lamina te used in MEMS applications.

Further studies for instance dynamic testing and parametric studies can be performed in future.
The model will be solved using computer based commercial code and validated by mesh independent results.

2 FEA SIMULATION

The present work is based on the FEA study of a thin film substrate laminate in three dimensions (3D). Firstly, the CAD models of the laminate are developed, in which the film and substrate physical dimensions are remained fixed during the entire analysis (usually thickness, width and length).
This geometry is now discretized by using appropriate mesh analysis and Boundary conditions are then applied by using commercial FEA package. During post processing, the tensile stress in the film material is studied and validated by mesh independent results.
The material properties used in the entire analysis are represented in Table 1.

Table 1. Material properties

S. no	Properties		Material	
	Name	Thin film Thickness (µm)	Copper	BS-8599 V7 RTV
1	Yield strength (MPa)	2.775	324	1.24
		2.025	366	
		0.95	502	
2	Tangent Modulus (MPa)	2.775	8000	-
		2.025		
		0.95		
3	Young's Modulus (MPa)	2.775	108800	0.74
		2.025		
		0.95		
4	Poisson's ratio	2.775	0.34	0.498
		2.025		
		0.95		

2.1 CAD Model

CAD model of the laminate is developed by using SolidWorks 2022 by Dassault systemes®, in which the physical dimensions of film and substrate are remained fixed during the entire analysis.

In total, 3 different configurations of Cu thin film and BS-8599 V7 RTV elastomer substrate are taken into consideration and the dimensions are mentioned in the Table. 2.

Table 2. Laminate dimensions

Setup	Layer	Dimension		
		Width (mm)	Length (mm)	Thickness (µm)
1	Thin film	8	45	2.775
	Substrate	8	45	12.7
2	Thin film	8	45	2.025
	Substrate	8	45	12.7
3	Thin film	8	45	0.95
	Substrate	8	45	12.7

Length and width in the model are taken as half i.e. 22.5 mm and 4 mm respectively because we can apply quarter symmetry command later to reduce the simulation time and cost as shown in Figure 1 and Figure 2.

Figure 1. CAD model

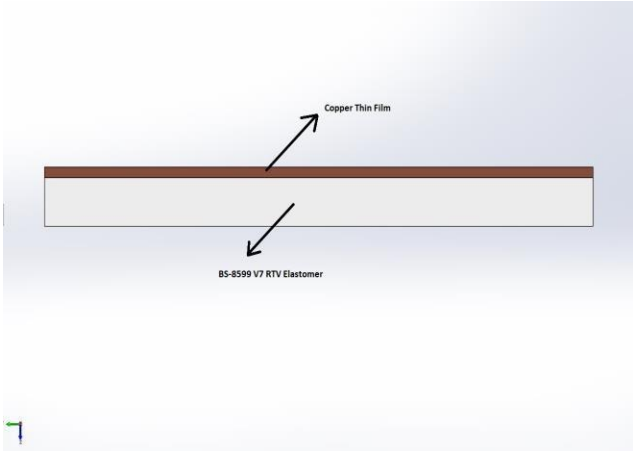

Figure 2. Laminate Cross-section

Model of laminate is also generated in such a way that the region in length can be eliminated from the results where stresses are artificially very high to avoid the singularities.

2.2 Meshing Analysis

Whole geometry is then divided into multip le elements and nodes. Very fine meshes are applied on metallic thin film and polymer substrate both by using Workbench 2020 R2 by ANSYS®. Element size is maintained in both meshes from initially 500 µm to 300 µm. Thickness of Copper thin film is divided initially into two number of divisions and subsequently raised to 4 and 6 divisions while number of divisions in substrate is fixed to 4. These inflated elements are denser in the vicinity of interface of thin film and substrate, as shown in Figure 3 and Figure 4.

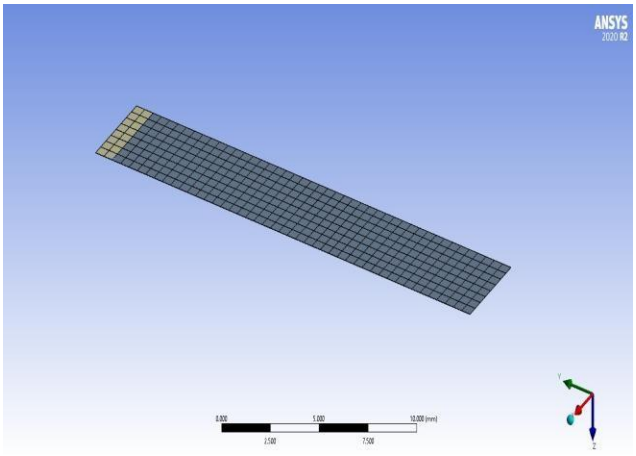

Figure 3. Element sizing

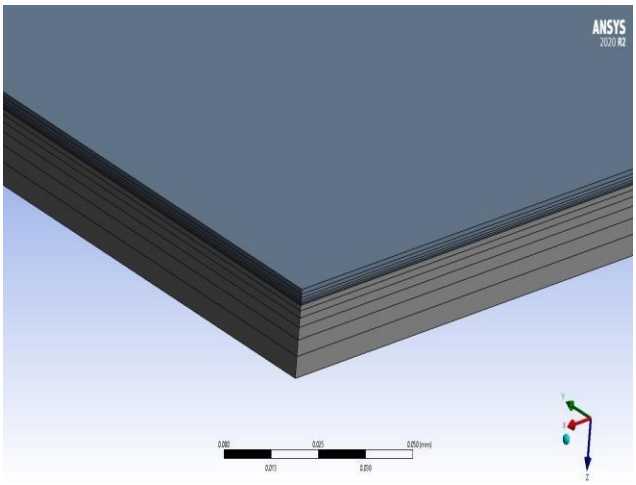

Figure 4. Elements division at interface

2.3 Boundary Conditions

Uniaxial strain of 1% is applied onto the substrate in the form of displacement of 0.225 mm in the direction of length of laminate while the other end is kept fixed, as shown in Figure 5.

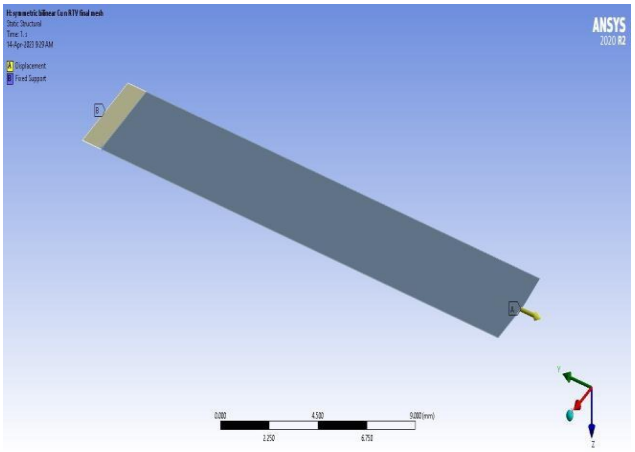

Figure 5. Boundary conditions

2.4 Solution

Solution is run considering bilinear model and by using above mentioned meshes and boundary conditions in Workbench 2020 R2 by ANSYS® for all the three configurations.

Firstly, element size is fixed to 500 µm and number of divisions in thin film and substrate is set to 2 each. Then, number of divisions are increased to 4, and finally to 6 each for thin film and substrate.

The same procedure is repeated by keeping the element size 300 µm to obtain the mesh independent results.

3 RESULTS AND DISCUSSION

Equivalent (Von-Mises) stress, total strain and interface shear stress are selected as solution results for all three configurations of laminate. Results can be seen in Figure .6 to Figure 14.

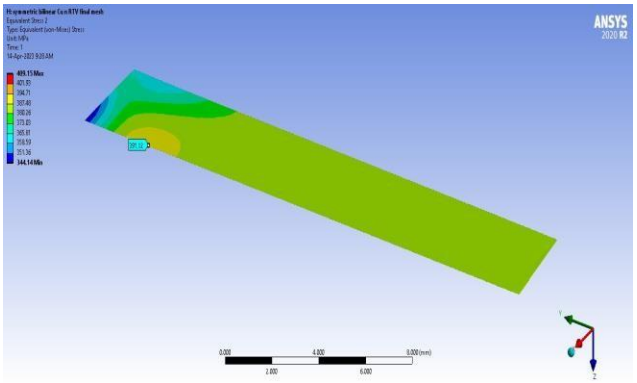

Figure 6. Von-Mises stress in 2.775 µm Copper thin film

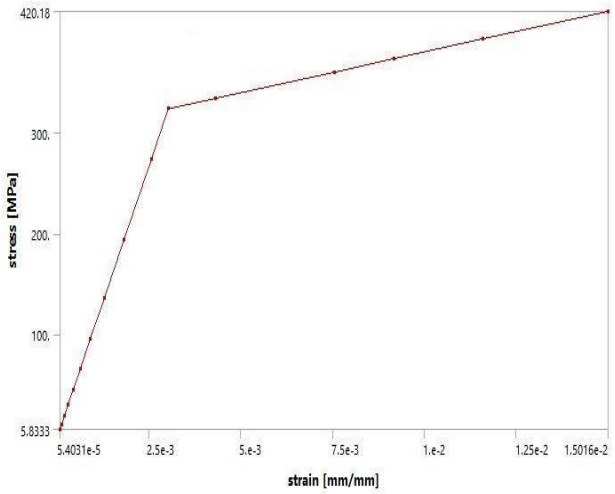

Figure 7. Stress Vs. strain of 2.775 µm Copper thin film

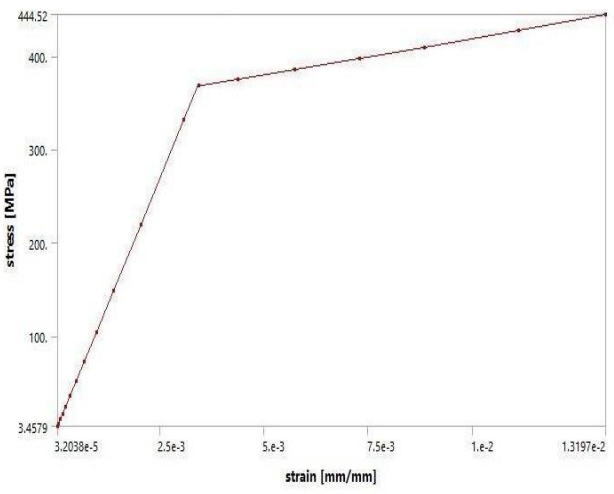

Figure 10. Stress Vs. strain of 2.025 µm Copper thin film

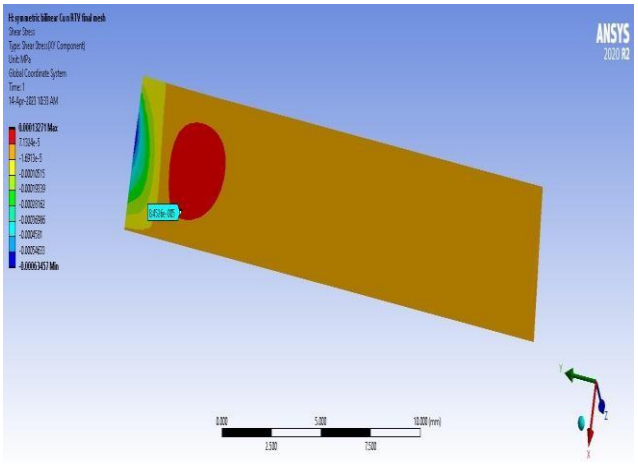

Figure 8. Interface Shear stress in 2.775µm Copper thin film

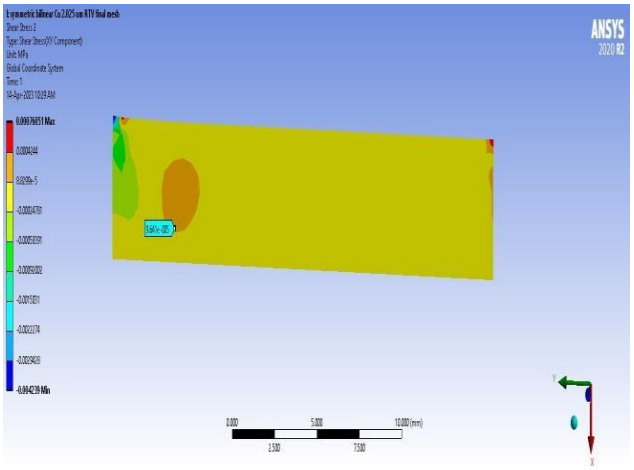

Figure 11. Interface Shear stress in 2.025µm Copper thin film

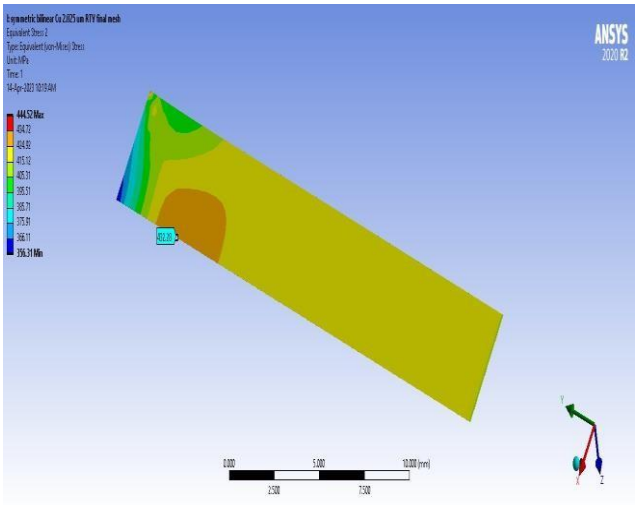

Figure 9. Von-Mises stress in 2.025 µm Copper thin film

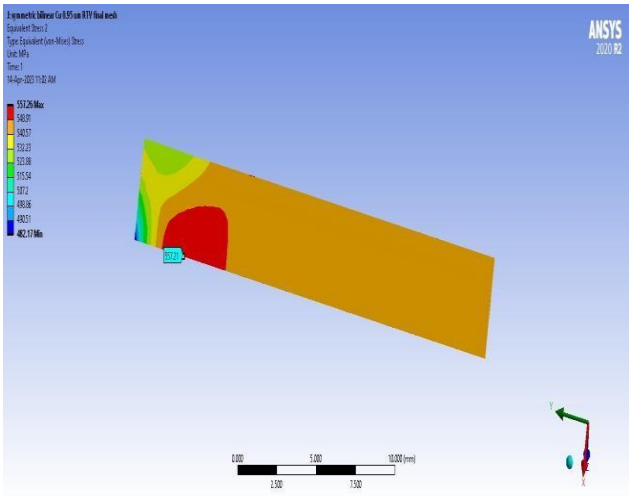

Figure 12. Von-Mises stress in 0.95 µm Copper thin film

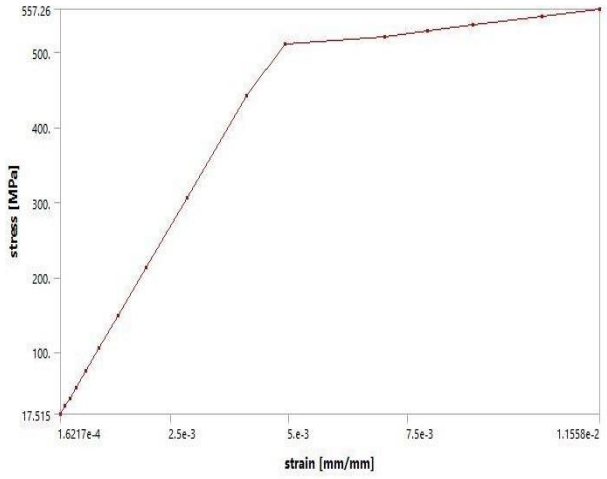

Figure 13. Stress Vs. strain of 0.95 µm Copper thin film

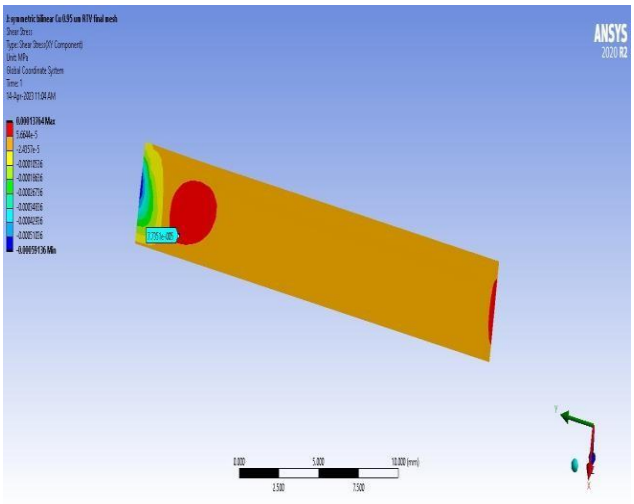

Figure 14. Interface Shear stress in 0.95 µm Copper thin film

Shear stress can be seen in above figures as almost Zero at the interface of thin film and substrate. Mesh independent results after excluding high artificial stresses due to singularities can be seen below in Table 3.

Table 3. Mesh Independent results

S. no	Film Thickness (µm)	Mesh size (µm)	Max Eq. stress (MPa)		
			No. of Divisions		
			2	4	6
1	2.775	500	392.88	392.08	391.57
		300	392.19	391.78	391.12
2	2.025	500	434.55	433.12	432.91
		300	433.65	432.38	432.38
3	0.95	500	560.39	559.02	558.11
		300	559.61	558.76	557.21

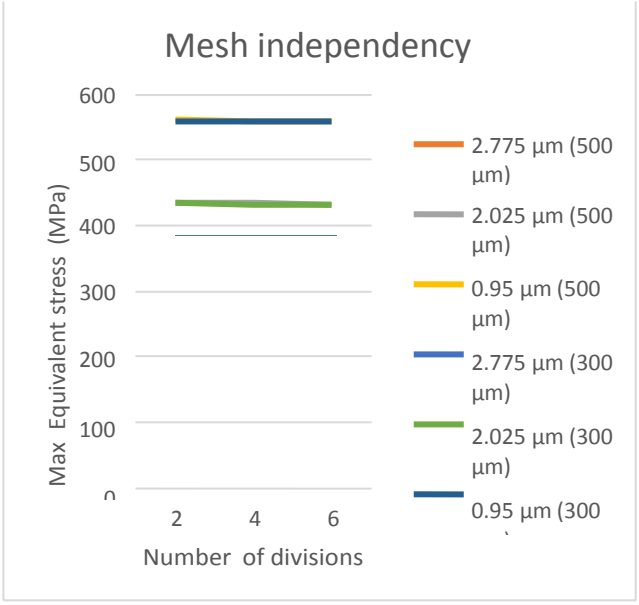

Figure 15. Mesh Independent results

The analysis of the above mesh independent numerical data reveals that the substrate BS-8599 V7 Room Temperature Vulcanized (RTV) elastomer is highly stretchable, flexible, and can be easily used as a low-cost alternate to PDMS and PET for various MEMS-based applications because it generates approximately the same stresses as in costlier above mentioned materials.

ACKNOWLEDGEMENTS

We would like to thank our teachers and parents for their continuous mentorship and support.

REFERENCES

[1] Y. Zheng, Y. Li, K. Dai, M. Liu, K. Zhou, G. Zheng, C. Liu, and C. Shen, Conductive Thermo plastic Polyurethane Composites with TunablePiezoresistivity by Modulating the Filler Dimensionality for Flexible Strain Sensors, *Applied Science and Manufacturing*, Composites Part A (101), 41–49, 2017.

[2] J. Yin, J. Kim, H. U. Lee, and J. Y. Park, Highly Conductive and Flexible Thin Film Electrodes Based on Silver Nanowires Wrapped Carbon Fibre Networks for Super capacitor Applications, *Thin Solid Films*, 660, 564–571, 2018

[3] M. Mehdi, M. Akhtar, A. Hussain, M. Nauman, D. S. Alothmany, I. Ahmed, and K. H. Choi, Dip Coated Stretchable and Bendable PEDOTPSS Films on Low Modulus Micro- bumpy PDMS Substrate, *Journal of Polymer Engineering*, 38(5) 469–474, 2017.

[4] Denis Y. W. Yu and Frans Spaepen, The yield strength of thin copper films on Kapton, *Journal of Applied Physics*, 95(6), 2991-2996, 2004.

[5] S. M. Mehdi, K. H. Cho, C. N. Kang, and K. H. Choi, Stretchability of Silver Films on Thin Acid-Etched Rough Polydimethylsiloxa ne Substrates Fabricated by Electrospray Deposition, *Journal of Electronic Materials*, 44(7), 2514–2521, 2015.

[6] A. Nakamura, T. Hamanishi, S. Kawakami, and M. Takeda, A Piezo-Resistive Graphene Strain Sensor with a Hollow Cylindrica l Geometry, *Materials Science and Engineering*, 219(B), 20–27, 2017.

[7] D. Chen, S. Yi, W. Wu, Y. Zhong, J. Liao, C. Huang, and W. Shi, Synthesis and Characterization of Novel Room Temperature Vulcanized (RTV) Silicone Rubbers Using Vinyl-POSS Derivatives as Cross Linking Agents, *Polymer*, 51(17), 3867–3878, 2010.

[8] I. D. Johnston, D. K. McCluskey, C. K. L. Tan, and M. C. Tracey, Mechanical Characterization of Bulk Sylgard 184 for Microfluidics and Micro engineering, *Journal of Micromechanics and Micro engineering* 24(3), 035017, 2014.

[9] S. T. Khan, M. Akhtar, M. Mehdi, N. Malik, S. Hashmi, and F. Butt, Characterizations of a Cost-Effective Single Component Polymer for Stretchable and Flexible Microelectromechanical Systems Applications, *Journal of Testing and Evaluation*, 51(2), 1-15, 2022.

[10] Bossil Technology Sdn. Bhd., *Safety Data Sheet, Kuala Lumpur, Malaysia*, Bossil Technology Sdn. Bhd., 2017.

[11] Roy, Sudesna, et al., Computational Analysis on the Thermal and Mechanical Properties of Thin Film Solar Cells, *Materials Today*, 44(1), 1207–1301, 2021.

[12] S. M. Mehdi, K. H. Cho, and K. H. Choi, Stretchability and Resistive Behavior of Silver (Ag) Nanoparticle Films on Polydimethylsiloxane (PDMS) with Random Micro Ridges, *Journal of Materials Science: Materials in Electronics*, 25(8), 3375–3382, 2014.

[13] S. Hong, H. Lee, J. Lee, J. Kwon, S. Han, Y. D. Suh, H. Cho, J. Shin, J. Yeo, and S. H. Ko, Highly Stretchable and Transparent Metal Nanowire Heater for Wearable Electronic s Applications, *Advanced Materials*, 27(32), 4744–4751, 2015.

[14] Y. J. Yang, S. Aziz, S. M. Mehdi, M. Sajid, S. Jagadeesan, and K. H. Choi, Highly Sensitive Flexible Human Motion Sensor Based on ZnSnO3/PVDF Composite, *Journal of Electronic Materials* 46(7), 4172–4179, 2017.

[15] S. Chun, Y. Choi, and W. Park, All-Graphene Strain Sensor on Soft Substrate, *Carbon*, 116, 753–759, 2017.

[16] S. Wang, Q. Liu, M. Li, T. Li, Y. Gu, Q. Li, and Z. Zhang, Property Improvements of CNT Films Induced by Wet- Stretching and Tension- Heating Post Treatments, *Applied Science and Manufacturing*, 103(A) 106–112, 2017.

[17] B. Hao, L. Mu, Q. Ma, S. Yang, and P. C. Ma, Stretchable and Compressible Strain Sensor Based on Carbon Nanotube Foam/Polymer Nano composites with Three-Dimensional Networks, *Composites Science and Technology*, 163, 162– 170, 2018.

[18] S. Choi, S. Lee, B. Lee, T. Kim, and Y. Hong, Selective Crack Formation on Stretchable Silver Nano-particle Based Thin Films for Customized and Integrated Strain-Sens ing System, *Thin Solid Films*, 707, 138068, 2020.

[19] Choi, Seongdae, et al., Selective Crack Formation on Stretchable Silver Nano-Particle Based Thin Films for Customized and Integrated Strain-Sensing System, *Thin Solid Films*, 707(1), 138068, 2020.

[20] Glushko, O., et al., Determining Effective Crack Lengths from Electrical Measurements in Polymer-Supported *Thin Films. Thin Solid Films*, 699(1), 137906, 2020.

PERFORMANCE EVALUATION OF MULTI-NOZZLE PESTICIDE SPRAYER WITH CHAIN & SPROCKET MECHANISM

Rahool Rai[1], Asad Ali Zaidi[1,*], Kashif Ahmed[1], Muhammad Uzair[2], Ali Mustafa Shah[3]

[1]Mechanical Engineering Department, Faculty of Engineering Science & Technology, Hamdard University Karachi, Pakistan

[2]Mechanical Engineering Department, NED University of Engineering & Technology, Karachi, Pakistan

[3]Mechanical Engineering Technology Department, The Benazir Bhutto Shaheed University of Technology and Skill Development Khairpur Mirs, 66020, Sindh, Pakistan

[*]Corresponding author. Tel.: +92-333-3561095;
E-mail address: asad.zaidi@hamdard.edu.pk (Asad Ali Zaidi)

ABSTRACT

Automation for spraying in the field of agriculture has increased the productive output of the farms. Owing to this, labour problem has been solved. But the scenario in the country like Pakistan is different. In the agriculture field, automation in such places is a difficult task also the economic condition of majority of Pakistani farmers is not well to do. Therefore, the manually operated sprayer finds wide application in such condition. Small scale farmers are very interested in manually lever operated knapsack sprayer because of its versatility, cost and design. In Pakistani farms two types of sprays are used: Hand operated and Fuel operated pump. The main drawn back of hand operated spray pump is that the user cannot use it for more than 5-6 hours continuously as he gets tired whereas fuel operated spray pump requires fuel which is expensive and availability of fuel is not easy at rural places. The suggested project of manually operated multi nozzle pesticides sprayer pump which will perform spraying at maximum rate in minimum time without necessity of fuel to operate and also reduce the fatigue to the farmer.

Keywords: Chain & Sprocket mechanism; Mechanical Advantage; Multi-nozzle sprayer; Pesticide

1 INTRODUCTION

More than seventy-five percent of Pakistan's population is reported to be directly or indirectly reliant on agriculture. Farming has been done this way for centuries, yet our farmers continue to do it now. Effort and time are required to spray pesticides and fertilizers in the conventional manner, which necessitates the development of new spraying methods. There is a pressing need to modernize agriculture in order to keep up with the expanding population and fast industrialization. Delays in planting, incorrect distribution of herbicides and fertilizers, harvesting, etc. are common problems on many farms. There is a lack of electricity and inadequate agricultural mechanization to blame for reduced output on the farms [1].

Low production may be solved entirely by automating the process; a better and more equitable allocation of effort is achieved as a result. It minimizes the amount required for a better response and prevents input losses and waste. As a consequence, farmers may get more production out of their equipment while also saving money. Vegetables, grains, pulses, and spices make up the bulk of Pakistan's agricultural output. Wheat production and exports are going to be booming in Pakistan in the near future. In Pakistan, rice, cotton, and sugarcane are among the country's most significant crops and spices. Pakistan is a major exporter of all of these commodities, as well as other agricultural products. Potato, tomato, and onion are Pakistan's most important vegetable crops, together accounting for 11.2% of world vegetable output. For both revenue and nutrition, tomato is a vital vegetable crop. In this concern people are transforming from conventional systems to Renewable power systems, the same transformation is also required in agriculture sector as well [2].

Protecting crops from pests and disease is critical to maximizing yields. Many crops are harmed by agricultural pests. To reduce losses and maximize the value of other production inputs, effective plant

protection is necessary. To be effective, chemical application in pest management must be managed carefully, rationed, and sprayed efficiently. As the only completely automated agricultural activity, chemical application necessitates specialized equipment. It's a vital part of farming to use pesticides. A specialized instrument called a "Sprayer" is used to apply these herbicides, insecticides, and fertilizers to agricultural crops. Using the sprayer, you may get the best results with the least amount of work. An agricultural revolution was brought about by the discovery of a pesticide, a fertilizer, as well as the development of a sprayer. Chemical application machines including knapsack sprayers, ultra-low volume sprayers, and tractor boom sprayers have all been produced in the past [3]. Most often used pesticide and herbicide spraying equipment includes large tractor-mounted sprayers, as well as smaller backpack devices that may be handled by hand. In view of the above constraints, a manually operated wheel driven sprayer was proposed which is mainly designed to reduce human effort. It is focused on spraying pesticides at maximum rate in minimum time by using wheel operated mechanism. The target of users is smaller industries and small gardens. Usually, gardeners will use the manual knapsack sprayer that is heavy and need to carry on their back to do spraying session. But proposed wheel sprayer needs only a forward push to operate it in field. Besides this, with a single operator, the proposed wheel sprayer can apply spray solution on both sides of its forward motion. So that the time taken is less, more area can be covered and effort is less than that of normal knapsack sprayer [4].

However multiple problems are faced due to conventional sprayer such as; Heavy weight of sprayer causes difficulty in carrying on backside or shoulder of operator, Fatigue due to heavy weight, Heavy weight reduces the efficiency of the operator, big size of pump cause inconvenience to the operator, Poor selection and quality of equipment. Due to above stated problems following solutions were taken into account as to select the placement and size of nozzles, design of the sprayer with proper adjustment facility with respect to crop size & height, the performance analysis of the developed wheel sprayer, calculate the area covered with respect to the flow rate of pesticides and time [5].

2 LITERATURE REVIEW

Joshua has worked on "Solar Sprayer - An Agriculture Implement". This research shows how they can be changed to utilize solar sprayers instead of fossil fuels. Solar PV technology was utilized to power solar sprayers as an alternative to power sprayers [6].

Poratkar and Raut [7] carried out their work in "Development of Multi nozzle Pesticides Sprayer Pump". The manual lever-operated knapsack sprayer is a popular choice for small-scale farmers due of its flexibility, low cost, and simple construction. Using a manual multi-nozzle pesticide sprayer pump, this study proposes a design for a device that can provide maximum spray output in the shortest amount of time [8] . Raut have worked on agricultural sprayer with weeder. This study proposed the mechanization of agriculture to meet the growing demand of food. Mechanization facilitates the conservation of resources. To maximize human, animal, and other power sources, agricultural mechanizations have been one of the selected mechanical operation [9].

Subbarayudu and Venkata chala pathi [10] have worked on "Modelling and Development of Pedal Operated Agricultural Sprayer". It is the goal of this research to reduce the amount of effort required by the user while increasing the pedal-to-pump reciprocation and discharge rate ratio. The crank mechanism is used to transform rotational motion into linear motion in this pedal-operated sprayer. In the next step, the frame and reciprocating pump was developed. Pesticide and insecticide spraying in fields and orchards made it easier [11]. Deshpande, has worked on "Agricultural Reciprocating Multi Sprayer" in order to reduce time of spray.

It has a precision-made nozzle tip for a customizable stream and the ability to spray fog depending on the situation, making it ideal for spreading chemicals evenly. Spraying time, weeding time, and human efforts may be greatly reduced by employing an agricultural sprayer, which also reduces costs [8]. Shiva raja Kumar, have done work on "Development of wheel driven sprayer". It uses a reciprocating pump that is powered by the wheel of this sprayer [12]. Wayzode [13] carried out their work in "Design and Fabrication of Agricultural sprayers, weeder with cutter" Wheel-and-pedal-operated sprayers have been presented in this study; they are simple to move and spray pesticides by turning the wheel and pedalling the equipment, which is effective and fuel-free. Harendra carried out their work on "Mechanical Agricultural Sprayer Vehicle". In order

to improve spraying methods and boost spraying efficiency, experimental research of setup is carried out using a mechanism devised and built to promote agricultural development. The majority of people use this for gardening and flower arranging [14].

3 DESIGN & FABRICATION

3.1 Equations for Design

For Wheel

$$S=2\pi r \quad (1)$$

For Motion Transmission

$$i = \frac{T_2}{T_1} \quad (2)$$

$$CD = 30P \text{ or } 50P \quad (3)$$

$$L=Kp \quad (4)$$

$$x = \left[k - \frac{T_1+T_2}{2} + \sqrt{\left(k - \frac{T_1+T_2}{2}\right)^2 - 8\left(\frac{T_2-T_1}{2\pi}\right)^2}\right] (SEQ\ Equation \ * ARABIC)$$

$$PD = \frac{P}{Sin\left[\frac{180}{N}\right]} \quad (5)$$

Since the above equations are utilized for designing chain and sprocket mechanism to increase the transmission and work power [15].

3.2 Fabrication

After the analysis of different parameters, the final model was fabricated. As the project is shown in figure 1 & 2 in its semi-finished condition.

Figure 1. MMPS with Pump

Figure 2. Semi Finished Product

4 RESULTS & DISCUSSION

For result parameters and calculations. A performance test was carried out with the manually operated multi nozzle sprayer; it was used to spray on a cultivated piece of land of 2m x 30m as shown in figure 3, and repeated same experiment for five consecutive times. The time taken to spray was recorded with stop watch. The same procedure was carried out using the knapsack hand sprayer; the time used was also recorded. The results were evaluated and compared. The developed wheel sprayer in the field was evaluated by spraying solution on the selected field. The actual discharge was determined. The readings are observed, the theoretical field capacity as well as actual field capacity were calculated. Field efficiency is calculated in order to analyse and evaluate the performance of wheel sprayer with chain and sprocket mechanism.

Figure 3. Field Selected for Testing

Figure 4 Comparison of Average Working Speed of Conventional and MMPS

Figure 4 clearly depicts that the average speed of conventional sprayer is less than that of fabricated manually operated multi nozzle sprayer. In this figure series 1 denotes conventional sprayer and series 2 denotes fabricated one.

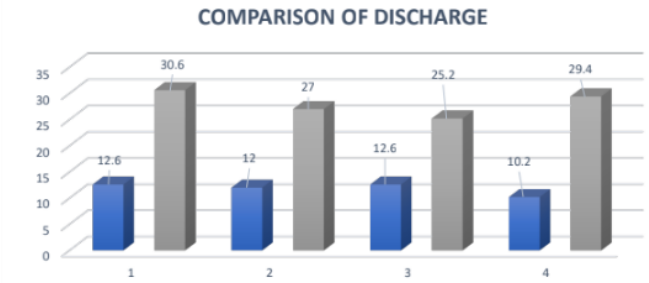

Figure 5: Discharge Comparison between MMPS and Knapsack Sprayer

In the figure 5, it is represented that the overall discharge in the chain and sprocket mechanism is higher than that of hand pumped sprayer. The chain and sprocket mechanism increases the efficiency of the system.

5 CONCLUSION

The multi-nozzle mobile compression pump sprayer was fabricated. It was tested, evaluated and test results were compared to those of a knapsack sprayer; the following parameters were used for evaluation; working speed, flow rate and the rate of application. Test result shows that the MULTI NOZZLE SPRAYER had a mean working speed of 0.4675 m/sec and mean discharge rate of 28.05m^3/s while the knapsack sprayer had a mean working speed of 0.19 m/s and mean discharge rate of 11.85 m^3/s. The working speed ratio of both suggests that the approximately Multi nozzle sprayer is five times faster than the knapsack sprayer. Also, the mean field efficiency of MMPS is 44% which according to comparison with research paper is good and efficient.

ACKNOWLEDGEMENTS

The authors acknowledge the support of Mechanical Engineering Department workshops Hamdard University for their support in carrying out this study.

REFERENCES

[1]. M. A. Hasan, M. Mia, M. A. S. Sagor, M. Rana, and M. Masum, “Analysis of Newly Developed Agricultural Multi Nozzle Wheel Sprayer,” 2022.

[2]. R. Rai, A. R. Larik, K. Ahmed, S. Kumaramasy, and A. A. Zaidi, “Comparative Analysis of finned absorber plate with and without black paint in Solar Air Heater,” presented at the 2023 4th International Conference on Computing, Mathematics and Engineering Technologies (iCoMET), IEEE, 2023, pp. 1–4.

[3]. J. Adedipe *et al.*, “Development And Performance Evaluation Of A Simple Multi-Nozzle Mobile Compression Pump (MMPC) Sprayer,” *Development*, vol. 7, no. 12, 2020.

[4]. P. Bante, S. Munshi, S. Gawai, H. Pote, S. Mawande, and S. Nimkarde, “Design and Fabrication of Spraying Machine”.

[5]. T. C. Mashongedza and H. R. Beem, “Design and Testing of a Low-Cost Wheel-Driven Crop Sprayer,” presented at the 2022 IEEE Global Humanitarian Technology Conference (GHTC), IEEE, 2022, pp. 184–187.

[6]. R. Joshua, V. Vasu, and P. Vincent, “Solar sprayer-an agriculture implement,” *International Journal of Sustainable Agriculture*, vol. 2, no. 1, pp. 16–19, 2010.

[7]. S. H. Poratkar and D. R. Raut, “Development of Multinozzle Pesticides Sprayer Pump,” *International Journal of Modern Engineering Research (IJMER)*, vol. 3, no. 2, p. 365, 2013.

[8]. M. Gaodi, A. Lonkar, A. Wankhede, and S. Gandate, “Development of Multipurpose Sprayer-A Review,” *International Research Journal of Engineering and Technology (IRJET) Volume*, vol. 3, 2016.

[9]. L. P. Raut, S. B. Jaiswal, and N. Y. Mohite, “Design, development and fabrication of agricultural pesticides sprayer with weeder,” *International Journal of Applied Research and Studies*, vol. 2, no. 11, 2013.

[10]. T. Subbarayudu and D. N. Venkatachalapathi, "Modeling And Development Of Pedal Operated Agricultural Sprayer," *Australian Journal of Basic and Applied Sciences*, 2017.

[11]. M S Engineering College, A. M, M. A, V. M, V. G, and R. V J, "Solar Powered Semi-automatic Pesticide Sprayer for use in Vineyards," *IJECE*, vol. 4, no. 4, pp. 55–58, Apr. 2017, doi: 10.14445/23488549/IJECE-V4I4P111.

[12]. Department of Mechanical Engineering R.T.M.N.U, Nagpur and S. Thombare, "Design and Development of Man Driven Pesticides Spraying Machine," *ijmeit*, vol. 05, no. 03, pp. 1851–1854, Mar. 2017, doi: 10.18535/ijmeit/v5i3.02.

[13]. P. B. Wayzode, S. R. Umale, R. R. Nikam, A. D. Khadke, and H. More, "Design and Fabrication of Agricultural Sprayer, Weeder with Cutter," 2016.

[14]. R. H. Singh, A. Akodiyawala, J. Khokar, and G. Ingole, "Mechanical agriculture sprayer vehicle (MASV)," *Int J Adv Res Ideas Innov Technol*, vol. 5, no. 1, pp. 476–479, 2019.

[15]. V. Turdaliyev, S. Komilov, A. Ismoilov, and X. Akbaraliyev, "A dynamic study of a chain transmission with a variable centre distance is performed (on the transmission of rotational motion)," presented at the IOP Conference Series: Earth and Environmental Science, IOP Publishing, 2022, p. 012024.

PERFORMANCE AND EMISSION ANALYSIS OF A DIESEL ENGINE USING DIESEL MIXTURES WITH BIODIESEL AND CARBON NANOTUBES

Muhammad Sarfraz Ali[1,*], Sadia Saleem[2], Rozeena Aslam[1], Hamza Akhtar[1], Muhammad Imran[1], Talha Nadeem Hassan[1], Abdul Rehman[1]

[1]Mechanical Engineering Department, Swedish College of Engineering & Technology, Rahim Yar Khan, Pakistan

[2]Institute of Computer Science and Information Technology, The Women University, Multan, Pakistan

[*]Corresponding author. Tel.: +92-345-8329528

E-mail address: sarfrazali@piet.edu.pk (Muhammad Sarfraz Ali)

ABSTRACT

The current study explored how the performance and emission characteristics of a diesel engine would change if carbon nanotubes (CNTs) were added to diesel-biodiesel fuel. The B5 biodiesel blend was combined with the CNTs nanoparticles. The CNTs nanoparticles were dissolved into B5 using a magnetic stirrer at concentrations of 40, 60, and 80 ppm. Engine testing was done under varied conditions with a full load at 1200, 1400, 1600, 1800, 2000, and 2200 rpm. Investigations were made into performance and emission parameters, such ssas brake-specific fuel consumption (bsfc), torque, brake power, NOx, CO2, and CO. In comparison to D and B5, the results revealed that adding CNTs to B5 enhanced power by 8.95% and 9.29%. Additionally, compared to the D and B5, the average torque rose by 18.17% and 20.38%, respectively. Brake-specific fuel consumption dropped in comparison to D and B5 fuels by 6.25% and 8.57%, respectively. Despite the presence of CNTs in the fuel blends, for B5 the CO emissions were on average lower than the D by 2.37%. Additionally, compared to the D, CO2 emissions dropped by 11.61% for the B5 fuel blend.

Keywords: Engine Performance; Engine emissions; carbon nanotubes; biodiesel.

1 INTRODUCTION

The damaging effects of pollutants on the environment brought on by the burning of fuels are one of the most crucial challenges in transportation. More than 25% of all greenhouse gas emissions are caused by land- and sea-based transportation. In the current energy situation, finding a substitute for diesel fuel requires lowering exhaust emissions without sacrificing thermal efficiency [1]. Biofuels are recognized as renewable, non-toxic, and ecologically favourable fuels. They are also the ideal diesel fuel substitute since they emit fewer greenhouse emissions and are cleaner than diesel fuel [2]. Since it offers a high level of energy security, a variety of supply sources, and much lower carbon emissions than diesel fuel, biodiesel, which is made from animal fat or vegetable oils, is an excellent substitute for diesel fuel. Its utilization is however constrained by several factors, including high NOx emissions, low energy output, and increased fuel consumption [3]. According to research, using additives can lessen issues with biodiesel fuel. One method utilized to enhance the fuel's ability to burn is the addition of water, nanoparticles, and other additives. According to earlier research, nanoparticles have a high surface area, high heat conductivity, and high reactivity [4]. Additionally, adding nanoparticles to biofuels raises the cetane number and enhances the engine's overall fuel efficiency. Due to their chemical and physical characteristics, such as electric, optical, thermal, and magnetic conductivity, carbon nanotubes (CNTs) are among the nanoparticles that are of great significance [5]. The impact of adding nanoparticles to pure diesel fuel on the efficiency and emissions of a diesel engine has been the subject of much investigation. Recently, carbon nanotubes have been proposed as a viable fuel additive to boost diesel engine efficiency and cut emissions.

To increase the efficiency of diesel engines and decrease CO, HC, NOx, and soot, M. Mirzajanzadeh et al. [6] employed a hybrid catalyst that includes sodium oxide nanoparticles and CeO2-CNTs hybrid nanocatalyst. The concentrations of 30, 60, and 90

ppm of a nanocatalyst with a diesel fuel combination (B5 and B20) were employed in this investigation. According to their findings, the catalyst would reduce soot, NOx, HC, and CO by 26.3%, 18.90%, 71.4%, and 38.80%, respectively, when nanoparticles were added. H. Jumaa et al. [7] investigated how nanoparticles affected a single-cylinder, four-stroke, air-cooled CI engine's performance. When the nanoparticles were introduced to diesel fuel, the consumption of brake-specific energy was reportedly reduced by about 3%. In a four-stroke, six-cylinder diesel engine, Ghanbari et al. [8] investigated the effects of carbon nanotubes (40, 80, and 120 ppm) and nano-silver particles (40, 80, and 120 ppm) on engine performance and emissions characteristics. The outcome showed that UHC and CO were dramatically reduced by the use of carbon nanotubes. In comparison to diesel fuel, power and torque were increased by up to 2%, while brake-specific fuel consumption fell by roughly 7.08%.

Many previous researchers have used carbon nanotubes and biodiesel with pure diesel to assess the performance and exhaust emissions of a diesel engine [9]. It can be observed, adding carbon nanotubes to pure diesel would enhance engine performance while lowering diesel engine exhaust emissions. Numerous research on engine performance and emissions have been conducted recently, with an emphasis on nano fuel additives. But there are still a lot of unanswered questions regarding the impacts of carbon nanotubes (CNTs) and biodiesel additives on the performance and emission characteristics of diesel engines when they are blended with pure diesel.

The surveys of the literature indicate that no studies on the emission and performance characteristics of diesel engines employing CNTs and biodiesel blends with pure diesel have been published. The goal of the current work is to determine the impacts on the performance and exhaust emissions of a four-stroke, single-cylinder diesel engine due to the characteristics of CNTs and the mixtures of biodiesel and pure diesel fuel. Thus, biodiesel is employed as an oxygenated fuel and multi-walled carbon nanotubes as a combustion accelerator ingredient. A combination of biodiesel and diesel was combined with CNTs at three distinct concentrations: 40, 60, and 80 ppm. It also looked at how the engine's bsfc, torque, and brake power as well as NO_X, CO2, and CO emissions increase or decrease.

2 MATERIALS AND METHODS

2.1 Fuel Preparation

In the current study, the transesterification process was used to create biodiesel from used cooking oil. There are no contaminants or water in the oil used to make biodiesel. An essential problem is the absence of water and contaminants necessary for a good transesterification process. Then, B5 (5% biodiesel and 95% diesel) was combined with carbon nanotubes (CNTs) at concentrations of 40, 60, and 80 ppm. The design of the experiment is shown in Table 1. To create a homogeneous emulsion fuel, the CNTs introduced to any fuel bend were stirred using a magnetic stirrer for 30 minutes. The addition of carbon nanotubes (CNTs) to pure diesel can improve its quality. Amido group-containing carbon nanotubes (CNTs) are highly reactive and may interact with a variety of substances [10].

Table 1. Design of the experiment

Name	Diesel (%)	Biodiesel (%)	CNTs (ppm)
D	100	0	0
B5	95	5	0
B5CNT40	95	5	40
B5CNT60	95	5	60
B5CNT80	95	5	80

2.2 Experimental Setup

A water-cooled, four-stroke, single-cylinder diesel engine was used for the trials. To load the engine, the crankshaft is linked to the eddy current dynamometer. A rotameter is used to maintain the coolant flow rate regularly. The schematic diagram of the experimental setup is shown in Figure 1, and the details are provided in Table. By keeping track of how long it takes for a certain amount of fuel to be used in the burette, the fuel flow is calculated. Two measurements are made, and the average value is recorded. A thermocouple attached to the setup is used to determine the temperature at the exhaust. The concentrations of NOx, CO2, and CO are measured by connecting the engine exhaust to an exhaust gas analyzer. For all the CNTs Concentrations, the experiments were performed under default conditions at engine speeds of 1600, 1800, and 2000 rpm without changing the injection timing or pressure. At full engine load, the engine performance and exhaust emissions were observed.

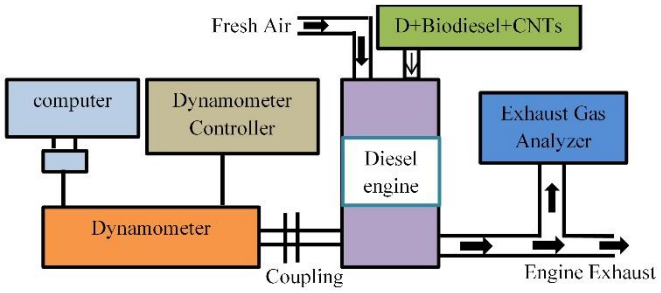

Figure 1. Schematic diagram of the experimental setup

2.3 Experimental Procedure

For the experiments in the current investigation, pure diesel (D) was blended with biodiesel B5 and various quantities of carbon nanotubes, such as 40, 60, and 80 ppm. The tests were conducted under full load conditions at engine speeds of 1200, 1400, 1600, 1800, 2000, and 2200 rpm. Brake-specific fuel consumption (bsfc), torque, braking power, NOx, CO2, and CO were all recorded for each fuel blend, and data was stored in a computer. To assure the elimination of remnants of earlier fuel mixtures in the fuel line, the engine was run for several minutes with pure diesel before each test. The data-collecting process then got underway. The same method was used for the testing of all fuel blends. Each experiment was repeated three times.

3 RESULTS AND DISCUSSIONS

3.1 Brake-Specific Fuel Consumption

It can see in Figure 2, by adding biodiesel to the pure diesel fuel brake-specific fuel consumption increases. But when we added the carbon nanotubes to the B5 fuel blends the brake-specific fuel consumption decreases. Also, the brake-specific fuel consumption of the engine increases with an increase in engine speed. For the B5CNT80 fuel blend the bsfc of the engine decreases by an average of 5.59%, 4.62%,5.95%, 5.15%, 6.25%, and 3.99% at the engine speeds of 1200, 1400, 1600, 1800, 2000, and 2200 rpm respectively when it was compared to pure diesel. This is because friction rises as engine speed rises, and as a result, fuel consumption rises. Low biodiesel fuel heating and viscosity values can be used to explain why bsfc in B5 fuel is higher than in pure diesel. According to some writers, the decline in heating value for biodiesel compared to diesel is essentially equivalent to the rise in fuel usage. In general, a reduced combustion delay, a larger heat release, and a faster burning rate, which result in a lower viscosity and full combustion, which in turn results in an increase in engine power, are the reasons for enhancing bsfc by adding CNTs to fuel. The findings of this investigation agreed with the researchers' earlier publications [11].

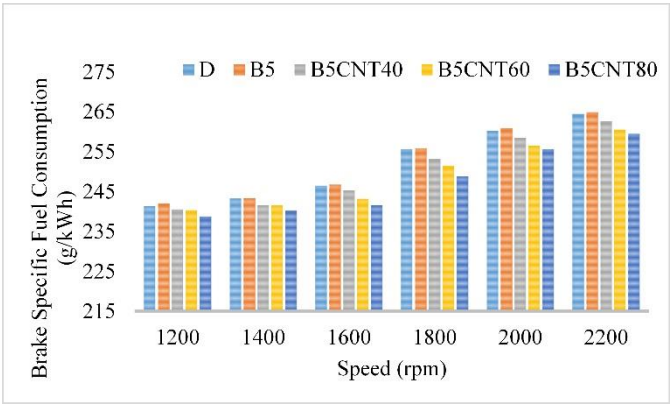

Figure 2. Brake-specific fuel consumption at different engine speeds

3.2 Brake Power and Torque

The rate of engine work is defined as the brake power. The viscosity, lubrication, and thermal properties of biodiesel, in particular, have a significant impact on the brake power of the engine. Figures 3 and 4, illustrate how introducing CNTs to diesel biodiesel fuel mixtures affects engine power and torque. As can be observed, because biodiesel has a lower heat rate than diesel, B5 fuel has less brake power and torque than pure diesel [12]. Therefore, the brake power and torque of the engine are decreased while mixing biodiesel with pure diesel. The quantity of carbon nanotube utilization directly correlates to brake power and torque, and their connection is practically linear. Compared to pure diesel, the use of carbon nanotubes enhances the power and torque.

The B5CNT80 fuel blend has the greatest brake power at all speeds. When compared to pure diesel, the brake power for the B5NT80 fuel blend improves by 8.95%, 6.24%, 8.91%, 7.81%, 7.36%, and 4.92% at engine speeds of 1200, 1400, 1600, 1800, and 2200 rpm, respectively. At 1400 rpm, the engine torque is the highest level. Similar to braking power, engine torque drops for biodiesel while increasing for carbon nanotubes.

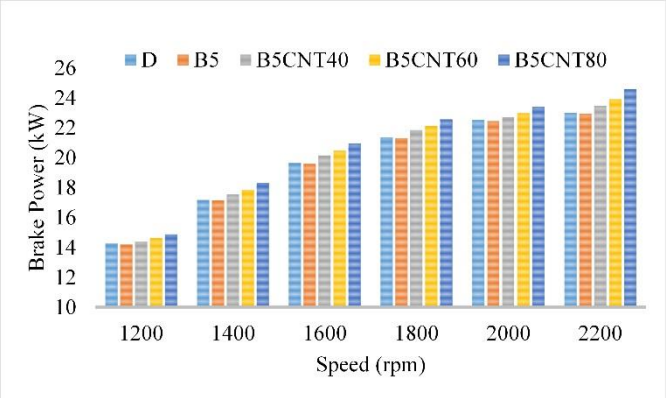

Figure 3. Brake power at different engine speeds

When compared to pure diesel, the engine torque for the B5NT80 fuel mix improves by 16.89%, 15.43%, 14.68%, 18.17%, 15.83%, and 16.57% at engine speeds of 1200, 1400, 1600, 1800, and 2200 rpm, respectively. One justification for this is to improve the combustion process while achieving more complete combustion. Additionally, full combustion is caused by enough oxygen in the fuel blends, which boosts engine power. The catalytic activity of the CNTs nanoparticles, which shortens the ignition delay and the duration of fuel combustion, is one of the other factors contributing to the improvement in engine brake power and torque. In addition, by improving the surface-to-volume ratio, carbon nanotubes improve heat transmission. Additionally, lowering the viscosity of fuel blends by adding CNTs to B5 boosts engine power [13].

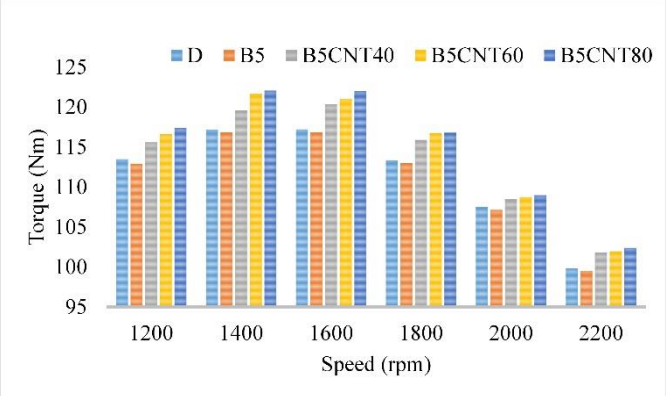

Figure 4. Torque at different engine speeds

3.3 NO_x Emissions

Peak combustion temperature, speed reduction, and temperature rise all affect NO_x emissions. Fuel quality and cetane number have a relationship with the combustion temperature. The formation of nitrogen oxide occurs at high temperatures. Nitrogen oxide emissions decrease as the temperature drops [14]. Additionally, where the fuel blend is weaker in the combustion chamber, nitrogen oxide is created. Figure 5 illustrates how NO_x is affected by the addition of carbon nanotubes to B5 fuel. In comparison to pure diesel, the NO_x reduction rate for B5 at 1200, 1400, 1600, 1800, 2000, and 2200 rpm was 3.27%, 4.35%, 2.85%, 4.95%, 5.81%, and 7.63%, respectively. Also mentioned is the fact that emissions rose as a result of carbon nanotubes. This increase for B5CNT80 was 4.76%, 5.91%, 6.82%, 5.45%, 4.25%, and 3.53%, respectively, compared to pure diesel at speeds of 1200, 1400, 1600, 1800, 2000, and 2200 rpm.

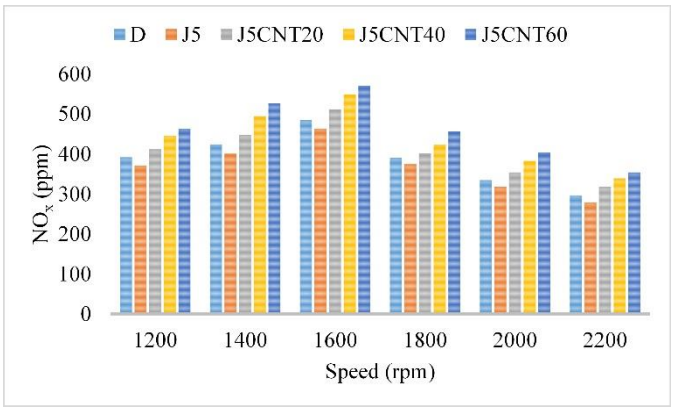

Figure 5. NO_x emissions at different engine speeds

3.4 CO_2 Emissions

Figure 6 displays how adding carbon nanotubes to B5 fuel affects CO_2 emissions. As can be seen, adding carbon nanotubes to B5 fuel causes CO_2 emissions to increase. The decrease in CO_2 emissions by adding biodiesel is due to the availability of excessive oxygen at the time of combustion [15]. The highest CO_2 emission took place at the speed of 2200 rpm and the lowest took place at the speed of 1600 rpm. The decrease in CO_2 emissions for the B5 fuel blend at the speeds of 1200, 1400, 1600, 1800, 2000, and 2200 rpm was 4.58%, 4.14%, 5.49%, 6.82%, 5.13%, and 6.37%, respectively. While the CO_2 emissions increased with an increase in the concentration of carbon nanotubes. Increase in CO2 emissions for B5CNT80 fuel blend at the speeds of 1200, 1400, 1600, 1800, 2000, and 2200 rpm was 9.24%, 11.61%, 10.52%, 9.37%, 7.26%, and 8.29%, respectively. The maximum increase in CO_2 emissions was recorded with the B5CNT80 fuel blend. The increase in CO_2 emissions with CNTs is due to the presence of excessive carbon in the carbon nanotubes.

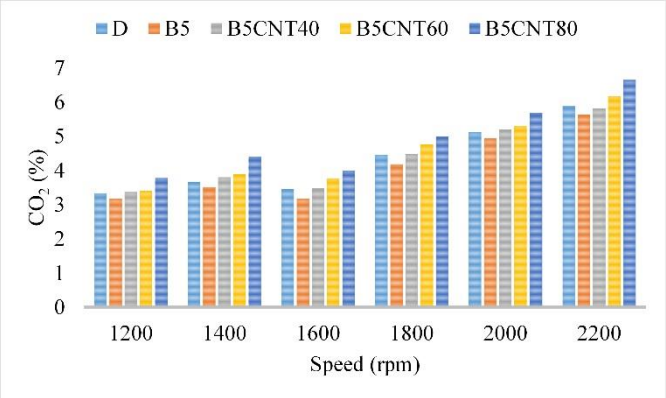

Figure 6. CO_2 emissions at different engine speeds

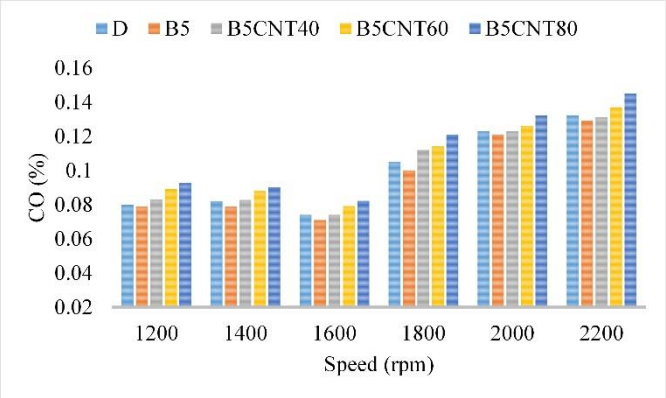

Figure 7. CO emissions at different engine speeds

3.5 CO Emissions

In general, poor combustion of diesel, particularly a lack of oxygen and a low flame temperature, results in the production of CO, which, in one of the aforementioned situations, occurs in place of CO_2. More than 38% of the additional air is still accessible in the diesel engine's combustion chamber even when it is operating at maximum power. Although it is not anticipated that carbon monoxide will be created, some of it can be discovered in exhaust gases. The oxygen is largely consumed before the fuel in particular sections of the combustion chamber, which leads to fuel spillage. In these places, diesel engines are therefore not entirely in contact with carbon dioxide. The result of adding CNT nanoparticles to B5 fuel is shown in Figure. The B5 has the lowest CO emission across all engine speeds, per the findings. At engine speeds of 1200, 1400, 1600, 1800, 2000, and 2200 rpm, the CO decrease for B5 was 1.32%, 1.73%, 1.86%, 2.26%, 1.95%, and 2.37%, respectively, compared to D. The presence of nanoparticles and their advantageous effect on the combustion process may be responsible for this decrease in CO emission. The tested fuel's higher oxygen content expedited combustion and reduced CO emissions [16]. More specifically, the addition of nanoparticles caused complete combustion by improving the degree of fuel-air mixing and shortening the ignition delay [14].

4 CONCLUSION

In this experimental study, the emission and performance characteristics of the engine which was fueled with diesel mixture with waste cooking biodiesel and carbon nanotubes with a concentration of 40, 60, and 80 ppm. The experiments were conducted on a single-cylinder, four-stroke diesel engine at the speeds of 1200, 1400, 1600, 1800, 2000, and 2200 rpm under full load conditions. The major conclusions from the experiments could be summarized as follows:

- Engine brake power and improved by the addition of carbon nanotubes.
- Brake-specific fuel consumption of the engine also decreases with the addition of carbon nanotubes.
- Due to the addition of biodiesel in the pure diesel NOx, CO2, and CO were decreased.
- In comparison to D and B5, the results revealed that adding CNTs to B5 enhanced power by 8.95% and 9.29%.
- Additionally, compared to the D and B5, the average torque rose by 18.17% and 20.38%, respectively.
- Brake-specific fuel consumption dropped in comparison to D and B5 fuels by 6.25% and 8.57%, respectively.
- Despite the presence of CNTs in the fuel blends, for B5 the CO emissions were on average lower than the D by 2.37%.
- Additionally, compared to the D, CO2 emissions dropped by 11.61% for the B5 fuel blend.

ACKNOWLEDGEMENTS

The Authors would like to thank the management of the Swedish College of Engineering and Technology, Rahim Yar Khan, for supporting this experimental study.

REFERENCES

[1]. D. Balasubramanian, A. T. Hoang, I. Papla Venugopal, A. Shanmugam, J. Gao, and T. Wongwuttanasatian, "Numerical and experimental evaluation on the pooled effect of waste cooking oil biodiesel/diesel blends and exhaust gas recirculation in a twin-cylinder diesel engine," *Fuel*, vol. 287, no. August 2020, p. 119815, 2021, doi: 10.1016/j.fuel.2020.119815.

[2]. A. Pourahmadiyan, P. Ahmadi, and E. Kjeang, "Dynamic simulation and life cycle greenhouse gas impact assessment of CNG, LNG, and diesel-powered transit buses in British Columbia, Canada," *Transp. Res. Part D Transp. Environ.*, vol. 92, no. February, p. 102724, 2021, doi: 10.1016/j.trd.2021.102724.

[3]. M. Kapetanović, A. Núñez, N. van Oort, and R. M. P. Goverde, "Reducing fuel consumption and related emissions through optimal sizing of energy storage systems for diesel-electric trains," *Appl. Energy*, vol. 294, no. November 2020, 2021, doi: 10.1016/j.apenergy.2021.117018.

[4]. S. H. Hosseini, A. Taghizadeh-Alisaraei, B. Ghobadian, and A. Abbaszadeh-Mayvan, "Performance and emission characteristics of a CI engine fuelled with carbon nanotubes and diesel-biodiesel blends," *Renew. Energy*, vol. 111, pp. 201–213, 2017, doi: 10.1016/j.renene.2017.04.013.

[5]. B. Arora and P. Attri, "Carbon nanotubes (CNTs): A potential nanomaterial for water purification," *J. Compos. Sci.*, vol. 4, no. 3, pp. 1–20, 2020, doi: 10.3390/jcs4030135.

[6]. M. Mirzajanzadeh *et al.*, "A novel soluble nano-catalysts in diesel-biodiesel fuel blends to improve diesel engines performance and reduce exhaust emissions," *Fuel*, vol. 139, no. x, pp. 374–382, 2015, doi: 10.1016/j.fuel.2014.09.008.

[7]. H. Jumaa and M. A. Mashkour, "The Effect of Variable Engine Parameters on Performance and Emissions of DI Diesel Engine Running on Diesel-Biodiesel Blended with Nano Additives," *IOP Conf. Ser. Mater. Sci. Eng.*, vol. 1094, no. 1, p. 012122, 2021, doi: 10.1088/1757-899x/1094/1/012122.

[8]. M. Ghanbari, G. Najafi, B. Ghobadian, T. Yusaf, A. P. Carlucci, and M. Kiani Deh Kiani, "Performance and emission characteristics of a CI engine using nano particles additives in biodiesel-diesel blends and modeling with GP approach," *Fuel*, vol. 202, pp. 699–716, 2017, doi: 10.1016/j.fuel.2017.04.117.

[9]. H. Solmaz, S. M. S. Ardebili, A. Calam, E. Yılmaz, and D. İpci, "Prediction of performance and exhaust emissions of a CI engine fueled with multi-wall carbon nanotube doped biodiesel-diesel blends using response surface method," *Energy*, vol. 227, 2021, doi: 10.1016/j.energy.2021.120518.

[10]. A. Heidari-Maleni, T. M. Gundoshmian, B. Karimi, A. Jahanbakhshi, and B. Ghobadian, "A novel fuel based on biocompatible nanoparticles and ethanol-biodiesel blends to improve diesel engines performance and reduce exhaust emissions," *Fuel*, vol. 276, no. April, p. 118079, 2020, doi: 10.1016/j.fuel.2020.118079.

[11]. A. F. Chen, M. Akmal Adzmi, A. Adam, M. F. Othman, M. K. Kamaruzzaman, and A. G. Mrwan, "Combustion characteristics, engine performances and emissions of a diesel engine using nanoparticle-diesel fuel blends with aluminium oxide, carbon nanotubes and silicon oxide," *Energy Convers. Manag.*, vol. 171, no. June, pp. 461–477, 2018, doi: 10.1016/j.enconman.2018.06.004.

[12]. V. Arul Mozhi Selvan, R. B. Anand, and M. Udayakumar, "Effect of cerium oxide nanoparticles and carbon nanotubes as fuel-borne additives in diesterol blends on the performance, combustion and emission characteristics of a variable compression ratio engine," *Fuel*, vol. 130, pp. 160–167, 2014, doi: 10.1016/j.fuel.2014.04.034.

[13]. G. R. Kannan, R. Karvembu, and R. Anand, "Effect of metal based additive on performance emission and combustion characteristics of diesel engine fuelled with biodiesel," *Appl. Energy*, vol. 88, no. 11, pp. 3694–3703, 2011, doi:

10.1016/j.apenergy.2011.04.043.

[14]. A. Taghizadeh-Alisaraei and A. Rezaei-Asl, "The effect of added ethanol to diesel fuel on performance, vibration, combustion and knocking of a CI engine," *Fuel*, vol. 185, pp. 718–733, 2016, doi: 10.1016/j.fuel.2016.08.041.

[15]. A. I. EL-Seesy and H. Hassan, "Investigation of the effect of adding graphene oxide, graphene nanoplatelet, and multiwalled carbon nanotube additives with n-butanol-Jatropha methyl ester on a diesel engine performance," *Renew. Energy*, vol. 132, pp. 558–574, 2019, doi: 10.1016/j.renene.2018.08.026.

[16]. O. M. I. Nwafor, G. Rice, and A. I. Ogbonna, "Effect of advanced injection timing on the performance of rapeseed oil in diesel engines," *Renew. energy*, vol. 21, no. 3, pp. 433–444, 2000, doi: 10.1016/S0960-1481(00)00037-9.

OPTIMIZATION AND PERFORMANCE ANALYSIS OF NATURAL GAS-BASED COMBINED CYCLE POWERPLANT USING POST COMBUSTION PROCESS

Abdul Rehman[1, *], Abid Hussain[1], Muhammad Mubashir Iqbal[1], Haris Khan[1], Ahmed Usman [1]
[1]Mechanical Engineering Department, University of Engineering & Technology, Taxila, Pakistan

[*]Corresponding author. Tel.: +92-309-0374448
E-mail address: ar8330239@gmail.com (Abdul Rehman)

ABSTRACT

The major contribution to global warming and air pollution is the carbon dioxide emissions emitted from the thermal power plants that operate on hydrocarbon-based fuels. The use of fossil fuels in power plants and various industrial processes significantly increases carbon dioxide emissions to the atmosphere. The methodology used for this research is such that first of all the model of a combined cycle power plant is developed in ASPEN HYSYS software using a post-combustion process for CO_2 capture. Furthermore, the model is integrated using the literature parameters and industrial operating data. The model is validated with the reference model of literature. Based on the results of this research, it was determined that 87% of CO_2 was captured using a combined cycle power plant based on natural gas. Furthermore, the obtained result presents that by varying the temperature across compressor the maximum power generation value is 19.52 MW at gas turbine 1, 16.83 MW at steam turbine and 14.58 at gas turbine 2. The results is also obtained by varying the pressure across compressor. The output results highlights that maximum power generation is 5.99 MW at gas turbine 1, 1.775 MW at steam turbine and 1.20 MW at gas turbine 2. The model is further integrated by changing the mass flow rate across the source component (compressor). The obtained output results displays a maximum power generation of 742.2 MW at gas turbine 1, 102.3 MW at steam turbine and 92.98 MW at gas turbine 2. In last it is also concluded from this research, the amount of exhaust gas recirculation in the absorber and the pressure in the absorber both have a great impact on the requirement of energy.

Keywords: ASPEN HYSYS, CO_2 capture, Gas turbine, Steam turbine

1 INTRODUCTION

The modern lifestyle and increase in population, the role of electricity is essential in human life as things go rising energy demand. In past decades for enhancing the efficiency of electricity production various methods are being proposed in power cycles. Across the world, the Combine cycle are mostly used to produce electricity. Open cycle power plants are the demand for Gas turbines due to low-priced natural gas. The closed cycle power plant is a demand of the Combine cycle in which water or steam is mostly used as a working fluid which is a proposed method for energy sources like coal, nuclear etc. For achieving higher efficiencies combined cycles are used. Fossil fuels are utilized by non-renewable resources like conventional cycles which help to pollute the environment and not sustainable systems.

Using photovoltaic cells with solar irradiation and wind energy in a wind turbine is an effective method of producing electricity. These ones are reliable choices, but they meet many challenges and limitations like storage issues, high cost etc. For that reason, the best choice is to make use of sustainable and renewable energy sources such as solar, thermal and waste heat with the power cycles at medium temperatures and low temperatures. Without the demand for high temperatures and the burning of fossil fuels extensively the Combine cycle is a more suitable choice for producing a large amount of electricity. The working fluid used in this is organic fluids instead of water or steam. Nowadays Combine cycle is a flourishing technology just because of its self-governing operation, low maintenance required, more efficient and vital operational pressures [1].

Carbon dioxide (CO_2) is a greenhouse gas that absorbs and emits thermal radiation, and its concentration in the atmosphere has rapidly increased since the industrial revolution. CO_2 is mainly produced by industries such as coal and gas-fired power plants, steel production, cement production, chemical and petrochemical production, among others, making it the main anthropogenic contributor to the greenhouse effect and temperature rise. Scientists have proposed several methods to

mitigate CO_2 emissions, including switching to green energy sources, improving power plant efficiency, and capturing and storing CO_2 emissions. However, carbon capture and storage (CCS) is currently the most viable option to maintain a green environment in the coming decades.

Post-combustion CO_2 capture in combined cycle power plants can lead to larger removal systems and increased energy requirements for amine regeneration due to the high exhaust gas flow rates and low CO_2 concentrations. The integration of a CO_2 capture system within combined cycles can help minimize the energy and economic costs associated with carbon capture. In summary, incorporating CO_2 capture in combined cycles can aid in reducing emissions while simultaneously minimizing the drawbacks related to its implementation.

Exhaust gas recirculation (EGR) is a conventional approach used to boost the CO_2 concentration of exhaust gases while simultaneously reducing the flow rate of flue gas that must be handled by the post-combustion capture system. This technique helps to increase the energy efficiency of the system by decreasing the amount of energy required for CO_2 capture. EGR is a tried and tested method that has been used in the past to optimize energy efficiency and minimize the costs associated with carbon capture. In summary, EGR can effectively enhance the CO_2 concentration of exhaust gases while also minimizing the amount of flue gas that needs to be processed by the capture system, resulting in significant energy savings.

Various management technologies have been developed to capture carbon dioxide from flue gases, and the storage and utilization of captured carbon dioxide into methanol has been proposed, along with an energy analysis of the process.

Human-caused emissions of greenhouse gases peaked in 2010 [14] at 49.45 $GtCO_2$-eq/year. The majority of the increase in GHG emissions from 1970 to 2010 may be ascribed to CO_2 emissions from the combustion of fossil fuels and industrial activity. The Climate Change Act requires a decrease of 80% in overall emissions by the year 2050 [15]. To address the challenge of climate change and the increasing global temperatures, it is necessary to adopt a combination of new, renewable technologies and improvements to the existing infrastructure. This approach will facilitate the transition towards a low-carbon, and ultimately, a zero-carbon society, which is crucial in mitigating the impact of climate change. The use of fossil fuel power plants is increasing due to their adaptability in meeting fluctuating demand [15] and minimizing the intermittent character of contemporary renewable energy sources. Power plants normally use coal and natural gas as their principal fuel sources, although coal's share has decreased from 22% in 2015 to 16% in the second quarter of 2018 [16]. Despite being commonly perceived as a cleaner fuel than coal, natural gas contributes to 42% of all electricity generation and produces about 350 $kgCO_2$/MWh [6]. Lowering the carbon intensity of this swiftly growing industry is crucial to ensure that the global temperature increase remains significantly below 2 degrees Celsius. Achieving this goal is essential to mitigate the impact of climate change caused by greenhouse gas emissions. Monoethanolamine (MEA) is the most preferred solvent for amine-based CCS because of its low material costs [18], however, a significant energy penalty is associated with solvent regeneration for the power plant. Optimization of post-combustion CCS facilities is required to decrease greenhouse gas emissions from power plants.

Using MEA and a 400 MW combined-cycle gas turbine, Alhaja et al. [12] assessed the technology economics of a compression and post-combustion capture (PCC) plant. The study revealed that an optimal lean loading of 0.31 $molCO_2$/molMEA could be achieved, resulting in the reduction of specific reboiler duty (SRD). This finding highlights the importance of optimizing the lean loading in the PCC process to minimize the energy consumption required in the reboiler.

Here, both the sensible heat required to get the solvent to the temperature of the reboiler and the latent heat required to evaporate water and produce stripping steam is satisfied. A higher stripping column pressure decreased SRD as well as the solvent degradation limits. With such a large initial expenditure, it is essential to comprehend every step of the capture process, and the addition of packing volume as a studied factor accomplishes this. The MEA-based unit demonstrated that the SRD was concentration-dependent; thus, Masoudi Soltani et al. [20] revealed that a lean solvent loading reduced the SRD. With a 30% MEA solution and 0.19–0.21 $molCO_2$/molMEA lean loading, the SRD achieved 3.98 GJ/tonneCO_2. As a result of fluctuating CO2 partial pressure within the flue gas stream, SRD varies as a function of EGR; employing more EGR caused a greater decrease in SRD. There are strong relationships between L/G ratio, lean loading, and

reboiler duty found in the optimization of an MEA-based PCC system [19]. By varying the lean CO_2 loading, we were able to calculate the optimal flow rate of the lean solvent required to gain 90% capture; at low L/G ratios, the majority of the heat required in the reboiler is used to strip steam, whereas at high L/G ratios, it's used to raise the rich stream's temperature, providing further evidence that the reboilers sensible and latent heats are in equilibrium [17,18]. At a lean loading of 0.23, the specific reference demand (SRD) was lowered by 15%, from 7.1 MJ/kgCO_2 to 5.13 MJ/kgCO_2. The model used 30 wt% MEA and was validated against the pilot plant at the UK CCS research center [19]. As noted by Lindquist et al. [17], raising the stripper pressure from 1.25 to 2.50 bar lowered the SRD by an additional 17%. However, in order to minimize thermal degradation of the solvent, it was established that a pressure of 1.80 bar was optimal. The SRD was 4,4 MJ/kgCO_2 with an ideal lean loading of 0.21, which is consistent with the findings of Masoudi Soltani et al. [14] Optimizing the logarithmic mean temperature difference (LMTD) between the packing material and the heat exchanger may result in a 40% reduction in SRD. For a 90% capture rate, Xiaobo Luo [17] reported a 9.58 percent decrease in the NGCC's net power efficiency while using an optimal lean loading of 0.26 to 0.28, which is marginally higher than previous trials. This research [17] differs from the others since the column size is constant and the best operation is to decrease operating costs, allowing for a larger lean loading to be utilized.

2 METHODOLOY

2.1 Combined Cycle Power Plant Model Development

In this research the model of combined cycle powerplant is developed in ASPEN HYSYS software. For Chemical process, Petroleum process and industries based on power plant this software is a most powerful tool that are used for both modelling and simulating these processes. There are several different processes involved in developing the model of combined cycle powerplant. This software facilitates individual to design and build these different processes by using various common equipments and devices like chemical reactors, distillation column, pumps, mixers, separator etc. Hysys has ability to deal with various calculations especially for chemical engineering that are based on heat transfer, mass and energy balance, design of reactor and chemical kinematics as well. In process industries Aspen Hysys is a more practical tool for finding the effect of different parameters.

2.2 Component List

When creating a model for a natural gas-based combined cycle power plant, the first step is to compile a list of components that will be involved in the simulation process. This list includes all the necessary equipment and machinery required to model the power plant accurately. Figure 1 displays the comprehensive list of components used in the development of the simulation model for the natural gas-based combined cycle power plant.

Component List View: Component List - 1 [HYSYS Databanks]

Source Databank: HYSYS

Component	Type	Group
Propene	Pure Component	
H2O	Pure Component	
CO2	Pure Component	
Oxygen	Pure Component	
Methane	Pure Component	
Ethane	Pure Component	
Propane	Pure Component	
n-Butane	Pure Component	
n-Pentane	Pure Component	
Nitrogen	Pure Component	
CO	Pure Component	
Hydrogen	Pure Component	

Figure 1. (a) Component list 1

Component List View: Component List - 2 [HYSYS Databanks]

Source Databank: HYSYS

Component	Type	Group
H2O	Pure Component	
CO2	Pure Component	
Nitrogen	Pure Component	
Oxygen	Pure Component	
H2S	Pure Component	
Piperazine	Pure Component	
H2O2	Pure Component	

Figure 1. (b) Component list 2

Component List View: Component List - 3 [HYSYS Databanks]

Source Databank: HYSYS

Component	Type	Group
Methane	Pure Component	
Oxygen	Pure Component	
CO2	Pure Component	
H2O	Pure Component	

Figure 1. (c) Component list 3

2.3 Fluid Packages

When using process simulation software like Aspen Hysys, it is required to select a fluid package. A fluid package is a set of equations and correlations that are used to calculate properties during the process simulation. Here, Peng Robinson (PR) is a selected thermodynamic model for component list 1 and 3. PR has the almost same accuracy as Soave Redlich Kwong (SRK) thermodynamic model. The Peng

Robinson equation of state is used to find out the volume of 100% methane gas as a function of temperature and pressure. Figure 2 displays a Peng Robinson property package.

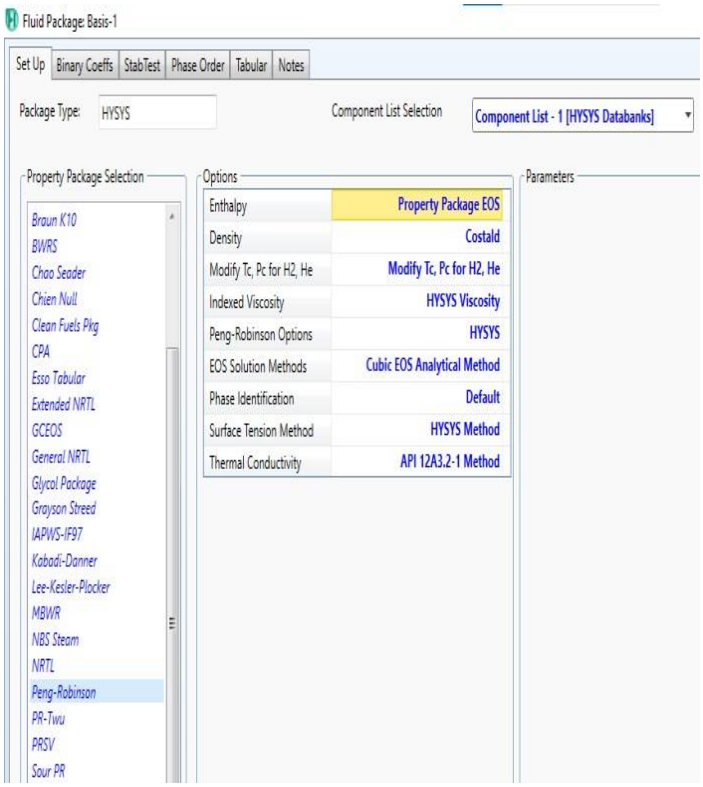

Figure 2. Property PackagePeng Robinson

Figure 3 displays an "acid gas-chemical solvents" fluid package. This fluid package is basically used for simulating the components of post combutsion process like piperazine, H_2S, H_2O_2 etc.

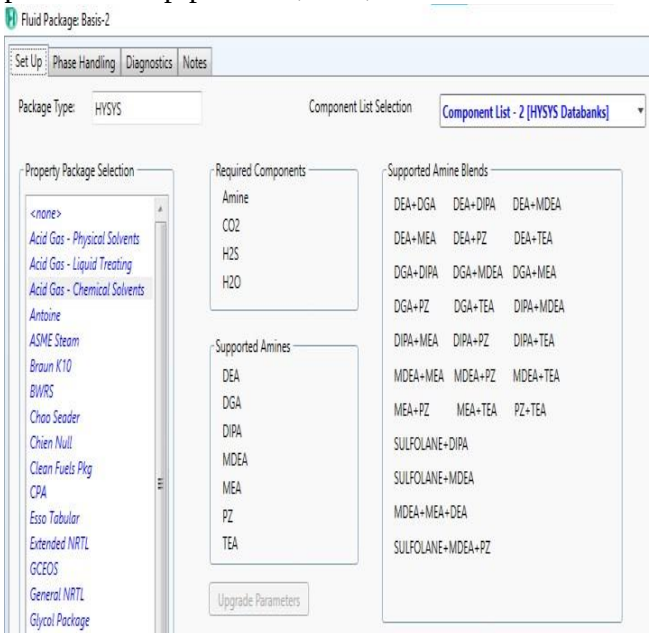

Figure 3. Property package Acid Gas-Chemical Solvents

2.4 Combined Cycle Power Plant

In a combined cycle powerplant there is a heat exchanger/heat recovery steam generator next to the turbine of simple gas powerplant. The waste heat gases of gas turbine enters in a heat exchanger. Water is also entering in a heat exchanger from point 3. Waste heat gases and water makes a steam in a heat exchanger. There are two outlets at the end of heat exchanger. First one is termed as Tube Side Outlet (TSO) and second one is termed as Shell Side Outlet (SSO). The Shell Side Outlet is used as an input to steam turbine. The steam turbine is running and generating a 700 KW of power generation. The outlet of steam turbine (stream 4) is used as an inlet to the cooler 1 to cool down the temperature of waste gases while the Tube Side Outlet (TS0) of heat exchanger is used in a cooler 2 to cool down the temperature of waste gases. Figure 4 displays all the above discussed phenomena.

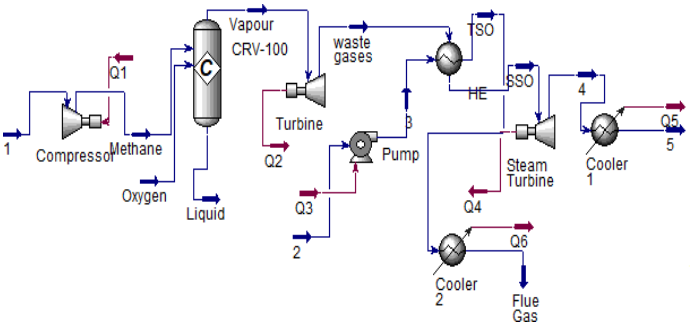

Figure 4. Combined Cycle Power Plant

2.5 Post Combustion Process

Absorber

Figure 5 highlights the absorber simulation along with the combined cycle powerplant. The waste flue gases enter in an absorber through the outlet of cooler 2 and the piperazine solution is entering in the absorber through the solvent stream. The piperazine and flue gases reacts together and generates a rich amine solution

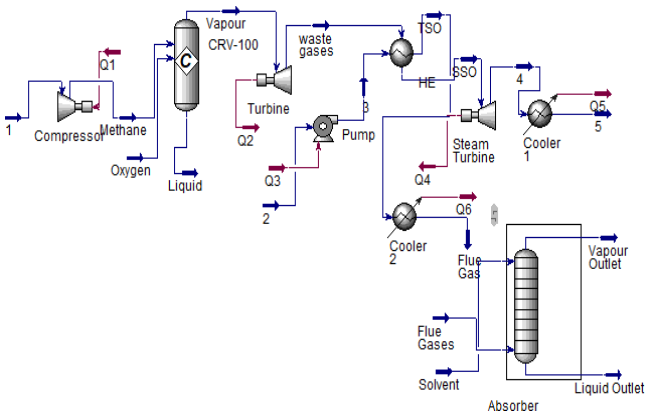

Figure 5. Simulation of absorber with combined cycle powerplant

Distillation Column

Next to the absorber column there is a distillation column. The rich amine solution from the absorber enters in a distillation column. The bond between the flow gases and piperazine breaks down in the distillation column. The lean solution returns back to the absorber column after the removal of CO_2 from this rich amine solution. Figure 6 presents the simulation of distillation column.

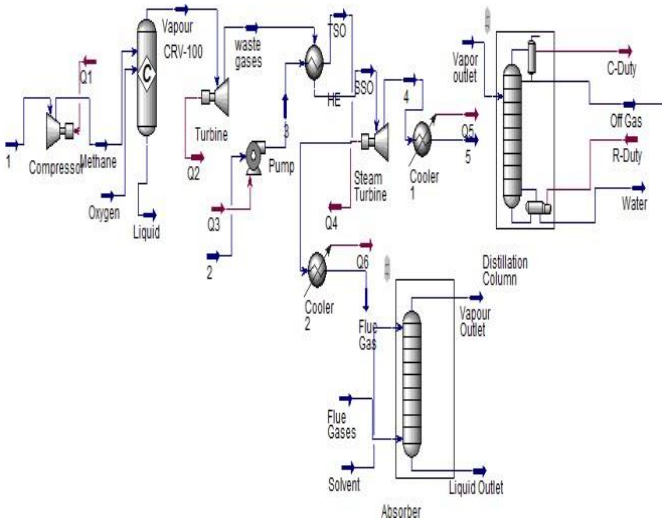

Figure 6. Absorber and Distillation Column simulation with CCPP

Gibbs Reactor

The Gibbs reactor is used for the formation of methane. Figure 7 reflects the inlet and outlet conditions of a Gibbs reactor.

Gibbs Reactor: GBR-100 - Set-5

Design | Reactions | Rating | Worksheet | Dynamics

Worksheet | Conditions | Properties | Composition | PF Specs

Name	Off Gas	6	Methane Outlet	Vap outlet
Vapour	0.1910	1.0000	0.0000	1.0000
Temperature [C]	-204.1	50.00	33.56	33.56
Pressure [kPa]	100.0	20.00	20.00	20.00
Molar Flow [kgmole/h]	18.06	9.921	0.0000	23.02
Mass Flow [kg/h]	700.0	20.00	0.0000	720.0
Std Ideal Liq Vol Flow [m3/h]	0.8177	0.2863	0.0000	0.9079
Molar Enthalpy [kJ/kgmole]	-2.704e+005	711.3	-2.118e+005	-2.118e+005
Molar Entropy [kJ/kgmole-C]	22.56	138.8	193.3	193.3
Heat Flow [kJ/h]	-4.883e+006	7057	0.0000	-4.876e+006

Figure 7. Inlet and outlet conditions of GibbsReactor

Figure 8 presents the combined simulation of distillation and gibbs reactor. Methane is produced at the outlet of gibbs reactor.

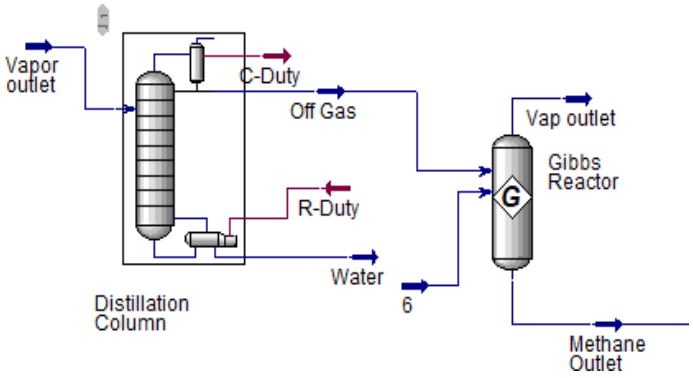

Figure 8. Simulation of Distillation column and Gibbs reactor

Figure 9 presents the power generation using post combustion process. 500 KW power is generation at turbine

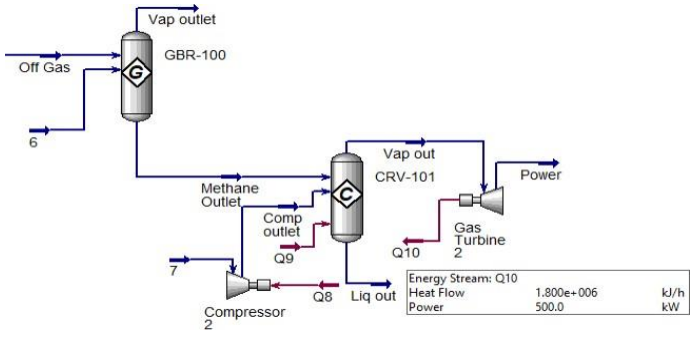

Figure 9. Compressor simulation

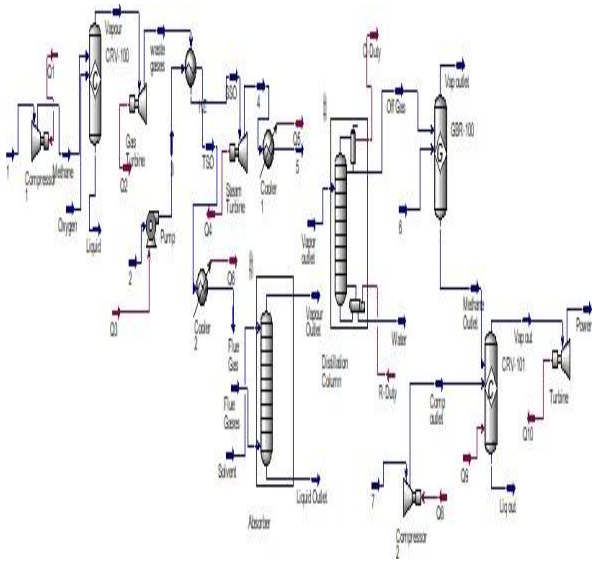

Figure 10. Simulation of Distillation column andGibbs reactor

3. Result and Discussion

This current phase of research includes results and discussion section. Table 1. shows all the components/equipments used in developing model. The working fluid at inlet of these components are also defined in this table. There are some nominal values at which this model of waste heat recovery is developed.

Table 1. Influence of the compressor temperatureon the net power production

Compressor Temperature (°C)	Power Generation at Gas Turbine 1 (MW)	Power Generation at Steam Turbine (MW)	Power Generation at Gas Turbine 2 (MW)
100	3.505	0.765	0.639
200	4.898	1.288	0.93
300	6.425	2.020	1.63
400	8.069	3.033	2.7
500	9.814	4.443	3.62
600	11.640	6.482	5.29
700	13.530	9.780	8.36
800	15.480	11.250	10.87
900	17.480	14.567	12.74
1000	19.520	16.839	14.58

Table 2. Influence of the compressor mass flowrate on the net power production

Compressor Mass Flow Rate (kg/s)	Power Generation at Gas Turbine 1 (MW)	Power Generation at Steam Turbine (MW)	Power Generation at Gas Turbine 2 (MW)
500	74.35	10.25	7.32
1000	148.6	20.47	16.37
1500	222.8	30.70	27.72
2000	297	40.93	35.52
2500	371.2	51.15	45.13
3000	445.4	61.38	54.43
3500	519.6	71.61	65.332
4000	593.8	81.83	72.541
4500	668	92.06	80.123
5000	742.2	102.3	92.987

Table 3. Influence of the compressor temperatureon the net power production

Compressor Pressure (bar)	Power Generation at Gas Turbine 1 (MW)	Power Generation at Steam Turbine (MW)	Power Generation at Gas Turbine 2 (MW)
60	5.994	1.775	1.20
65	4.978	1.071	0.835
70	4.317	0.778	0.723
75	3.829	0.614	0.551
80	3.449	0.509	0.415
85	3.142	0.435	0.388
90	3.116	0.429	0.349
95	3.289	0.415	0.325
100	3.454	0.392	0.254
105	3.521	0.39	0.248

The presented result in Figure 11 shows that when the compressor inlet temperature is increased, there is a corresponding increase in net power generation. This can be explained by the fact that there is a direct relationship between the two variables.

$$Q = m * C_p * \Delta T \qquad (1)$$

The amount of heat content (Q) is directly related to the temperature at the compressor inlet. This means that raising the temperature at the compressor inlet will also increase the heat content (Q) and subsequently raise the temperature at the turbine inlet. This raise in temperature at the turbine inlet leads to an increase in the temperature of the hot gases being exhausted, resulting in a higher net power generation of the system. In one study, it was found that increasing the temperature from 100°C to 1000 °C resulted in a 16 MW increase in power output at gas turbine 1, a 16.57 MW increase at steam turbine, and a 13.34 MW increase at gas turbine 2. These results were achieved with a constant pressure of 60 bar and a mass flow rate of 3000 kg/sec.

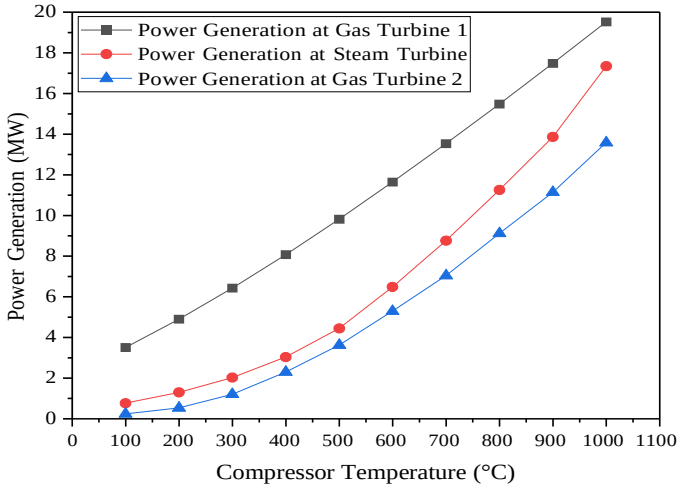

Figure 11. Parametric evaluation between net power output vs compressor temperature

Figure 11 Parametric evaluation aimed to observe how the net power output was affected by compressor temperature

Figure 12 shows a graph that demonstrates the relationship between pressure and net power output. Net power generation is not significantly affected by pressure according to the graph. Raising the pressure from 60 bar to 105 bar results in only a minor increase in net power output, specifically a 2.97 MW increase at gas turbine 1, a 1.085 MW increase at steam turbine, and a 1.067 MW increase at gas turbine 2. Other literature also shows similar trends, with only minor increases in power generation resulting from increased pressure [11]. These results were obtained with a constant temperature of 1273 °C and a constant mass flow rate of 96.98 kg/sec. Therefore, it is evident that a system with low source pressure is still capable of efficiently.

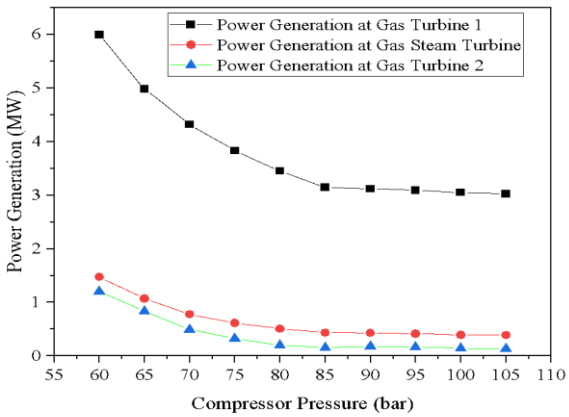

Figure 12. Parametric Assessment to note the influence of compressor pressure on the net power.

Figure 1 3 depicts the relationship between mass flow rate and net power generation. The graph indicates that increasing the mass flow rate leads to higher net power output. This trend can be attributed to the fact that an increase in mass flow rate results in a higher heat content (Q), which in turn enables the recovery of more waste heat and leads to a higher net power output at the turbine [12]. Specifically, in one study, the rise in net power generation resulting from a raise in mass flow rate was approximately 668 MW at gas turbine 1, 92 MW at the steam turbine, and 82.66 MW at gas turbine 2. These results were obtained with a constant temperature of 270 °C and a constant pressure of 60 bar. Therefore, it is evident that increasing the mass flow rate can lead to a substantial increase in net power output.

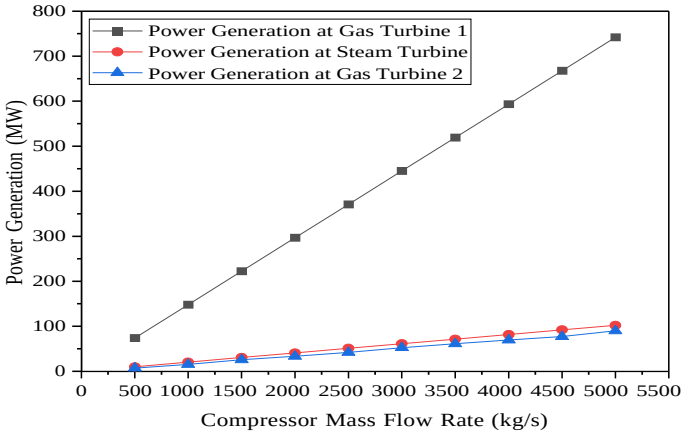

Figure 13. Parametric Evaluation aimed to observe how the net power output was affected by mass flowrate.

3.1 Validation

The validation of this current research is developed at different parameters. Each parameter is discussed below and validated with the results of literature.

Circulation Rate

With the increase in circulation rate the rate of CO_2 removal increases. The minimum amount of steam that is calculated is 3.42 MJ/Kg CO_2. The obtained results are presented in below figure compared with the results of literature [21].

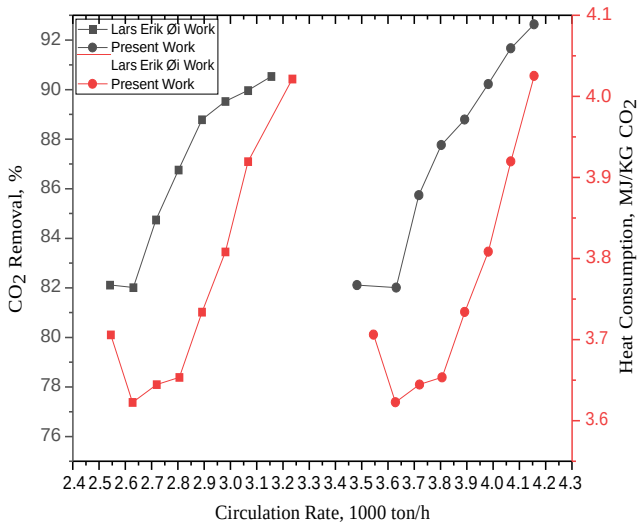

Figure 14. Circulation rate dependence

Number of absorption stages

By changing the number of stages, the absorber column height changes. The efficiency value is kept constant at 0.25. The results compared with the literature [21].

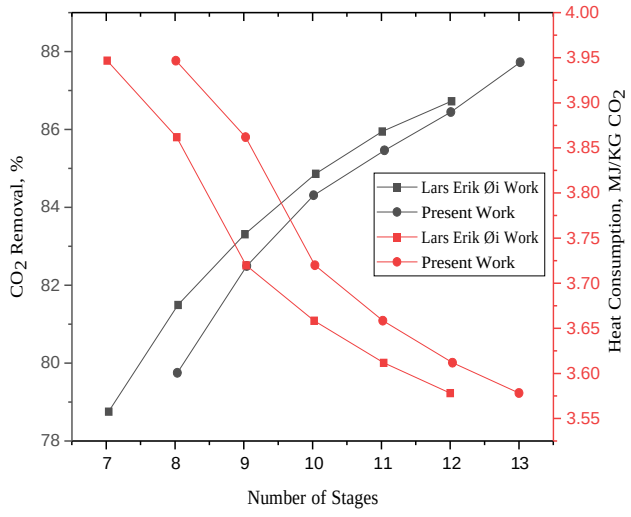

Figure 15: Number of stages dependence

Absorption temperature

At equilibrium the value of absorption decreases with the increase in value of liquid inlet temperature and gas. The results of simulation are obtained at constant efficiency value. The results are compared with the already published results [21].

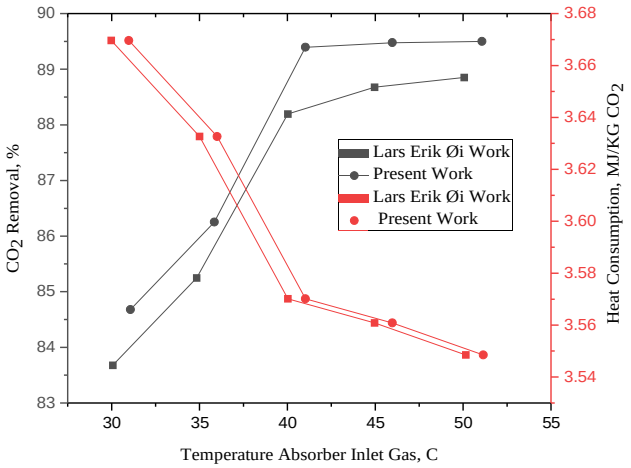

Figure 16. Absorber temperature dependence

Absorption pressure

The pressure drop plus atmospheric pressureis set to the atmospheric pressure at the inlet while at the outlet the absorption pressure is taken as atmospheric pressure. Results validated with the reference results of literature [21].

Reboiler Temperature

Pure amine solution with a great CO_2 removal efficiency is obtained by increasing the reboiler temperature. At above 120 C the problems of amine degradation occur. The presented results are compared with the reference results [21].

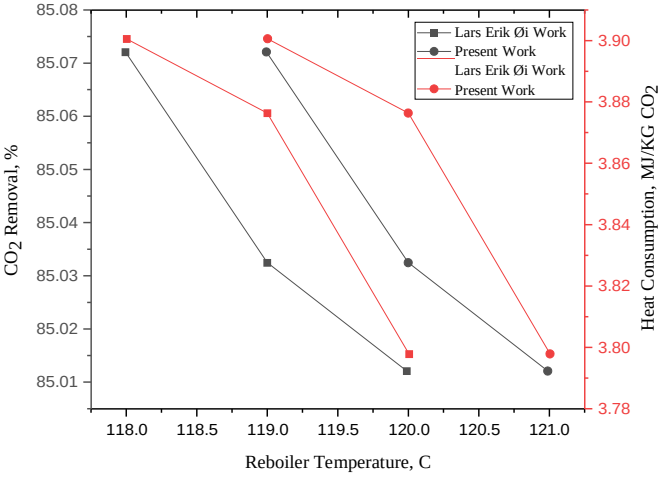

Figure 17. Reboiler temperature dependence

4 CONCLUSION

ASPEN HYSYS has proven to be the most appropriate tool for analysing CO2 capture from combined cycle power plants based on all of the research conducted thus far. The Capture of CO_2 is well calculated under HYSYS simulation along with the industrial processing data. The effects of varying the circulation rate of amine, height of absorption column, absorption temperature and the reboiler temperature are evaluated under ASPEN HYSYS software. The reduction in efficiency from a combined cycle power plant operating on natural gas could be calculated.

For upgrading the amine absorption process this developed model can be further modified for the CO_2 capturing.

REFERENCES

[1]. Udara SPR Arachchige, Dinesh K, Morten CM. Simulation of carbon dioxide capture for aluminium production process. Int J Model Optim2019;(4–1):43–50.

[2]. Sholeh Ma'mun. Selection and characterization of new absorbents for Carbon Dioxide capture (Ph.D thesis), Norway: NTNU; 2018

[3]. Udara SPR Arachchige. Carbon dioxide capture by chemical absorption: energy optimization and analysis of dynamic viscosity of solvents (Ph.D. thesis), University of South-Eastern Norway; ISBN: 978-82-7206-516-3, 2019

[4]. Anderson S, Newell R. Prospects for carbon capture and storage technologies. discussion paper.In: Resources for the future. 2016

[5]. Botero C., Finkenrath M., Bartlett M., Chu R., Choi G., Chinn D., Redesign, Optimization, and Economic Evaluation of a Natural Gas Combined Cycle with the Best Integrated Technology CO2 Capture, Energy Procedia 1 (2014) 3835M3842.

[6]. K., Sammak M., Genrup M., Post-combustion CO2 capture for combined cycles utilizing hot- water absorbent regeneration. Journal of Engineering for Gas Turbines and Power-ASME; 2012.

[7]. Li H., Haugen G., Ditaranto M., Berstad D., Jordal K., Impacts of exhaust gas recirculation (EGR) on the natural gas combined cycle integrated with chemical absorption CO2 capture technology, Energy Procedia 4 (2011) 1411-1418.

[8]. Shelton W., Black J., Kyle A., Yang W., Kuehn N., Woods M., Carbon Capture Approaches for Natural Gas Combined Cycle Systems, NETL Report, Jan 2016, DOE/NETL-2011/1470.

[9]. Li H., Ditaranto M., Yan J., Carbon capture with low energy penalty: Supplementary fired natural gas combined cycles, Applied Energy 97 (2012) 164-169

[10]. Dumee L., Scholes C., Stevens G., Kentish S., Purification of aqueous amine solvents used in post combustion CO2 capture: A review. International Journal of Greenhouse Gas Control 10 (2015) 443-455.

[11]. (Ramdin et al., 2012; Venkatraman and Alsberg, 2017; Rubin et al., 2012; Das and Meikap,2018).

[12]. Sultan, T., Zabiri, H., Ali Ammar Taqvi, S., Shahbaz, M., 2020. Plant-wide MPC control scheme for CO2 absorption/stripping system.

[13]. Mater. Today Proc

[14]. Sreedhar, I., Nahar, T., Venugopal, A., Srinivas, B., 2017. Carbon capture by absorption – path covered and ahead. Renew. Sustain. Energy Rev

[15]. Intergovernmental Panel on Climate Change, (IPCC). Climate Change 2014: Synthesis Report. Contribution of Working Groups I, II and III to the Fifth Assessment Report of the Intergovernmental Panel on Climate Change; IPCC: Geneva, Switzerland, 2014.

[16]. The UK Government. Climate Change Act2008; The UK Government: London, UK, 2008. Boot-Handford, M.E.; Abanades, J.C.; Anthony, E.J.; Blunt, M.J.; Brandani, S.; Mac Dowell, N.; Fernández, J.R.; Ferrari, M.-C.; Gross, R.; Hallett, J.P.; et al. Carbon capture and storage update. Energy Environ. Sci. 2014, 7, 130–189. [CrossRef]

[17]. Department for Business Energy & Industrial Strategy. Energy Trends September 2018; Department for Business Energy & Industrial Strategy: London, UK, 2018.

[18]. National Energy Technology Laboratory (NETL). Bituminous Coal (PC) and Natural Gas to Electricity. Cost and Performance Baseline for Fossil Energy Plants 2015; National Energy Technology Laboratory (NETL): Pittsburgh, PA, USA, 2015.

[19]. Popa, A.; Edwards, R.; Aandi, I. Carbon capture considerations for combined cycle gas turbine. Energy Procedia 2011, 4, 2315–2323.

[20]. Wang, M.; Lawal, A.; Stephenson, P.; Sidders, J.; Ramshaw, C. Post-combustion CO2 capture with chemical absorption: A state-of-the-art review. Chem. Eng. Res. Des. 2011, 89, 1609–1624.

[21]. Chen, P.; Luo, Y.X.; Cai, P.W. CO2 Capture Using Monoethanolamine in a Bubble-Column Scrubber. Chem. Eng. Technol. 2015, 38, 274–282.

[22]. Lars Erik Øi. Aspen HYSYS Simulation of CO2 Removal by Amine Absorption from a Gas Based Power Plant. SIMS2007 Conference, Gøteborg, October 30-31st 2007

DESIGN AND DEVELOPMENT OF COMPACT EQUIPMENT FOR THE GRADING OF MATERIAL COMPOSED OF DRY MICRO SIZE PARTICLES

Tariq Jamil[1], Muhammad Saad Jamali[1], Ghufran Ullah[1], Muhammad Ahmed[1], Sheikh Fahad Ahmed[1]

[1]Mechanical Engineering Department, NED University of Engineering & Technology, Karachi, Pakistan

[*]Corresponding author. Tel.: +92-332-8225815;
E-mail address: mtariqjamil@gmail.com (Tariq Jamil)

ABSTRACT

Solid-Solid micro particle separation from a carrying flow is a widely used industrial technique, which facilitates the separation of solid-solid mixtures. Literature suggests that Vibratory Sifters are used worldwide on a laboratory scale but it involves several drawbacks like, it requires regular cleaning. On the other hand, a cyclone separator is a particle separation apparatus that uses centrifugal force to sort particles based on their size. They are better than the devices which involve sieves for the separation since they are simple, continuous, and economical to use. The design of the equipment consists of two cyclone separators (Inverse and Conventional in series). The inverse cyclone separates the particles according to the size while the conventional is used to separate the fine particles from the airflow. Kaolin clay was used as the input feed, and the objective was to separate particles having size < 149 microns. 3D model of the final design was designed on AutoCAD. The Separators were fabricated using Polyvinyl Chloride (PVC) while wooden planks and Steel were used for the manufacturing of the frame. Experiments were performed on a fabricated prototype which concludes that the separation the fine particles from the clay sample at 97% accuracy of which ~75% fine particles are <74 microns and ~23% fine collected passes through 100 mesh size sieves (<149 microns).

1 INTRODUCTION

Micro particle separation is one of the most widely used processes in various industries. This technique basically involves selective sorting of micro particulates as per the requirement [1]. Moreover, the separation of solid or liquid particles from a fluid flow also comes under this process. This is an important topic in the field of material engineering because micro particles have several applications due to the fact that they offer numerous advantages based on their structural and functional abilities. Their size ranges from 1-1000 µm (micrometre or microns) [2]. Separation and sampling aerosol particles (<100 microns) from the carrying flow is an important topic in the field of ambient sampling and industrial particulate control [3]. One problem that is common in almost all separation processes is the emissions of micro particles. Matter of this fine size is found in huge amounts in our atmosphere. Their sources are man-made activities such as fuel combustion, industrial emissions, and the burning of agricultural waste. This causes a number of concerns like air pollution, global warming, fog, haze, etc. which adversely affects human health, vegetation, materials, and the environment [4]. Consequently, several micro particle separation techniques were previously designed to execute this process in industries and to control particulate emissions into the air [5].

The design includes a combination of cyclone separators connected in series. Cyclone separators are generally used in the separation of Gas-Solid mixtures but they can also be used in the separation of Solid-Solid mixtures by mixing the solid sample in the flowing fluid. The benefit of using a cyclone separator is that it has, generally, fewer or no moving parts consequently making it more resistive against wear and tear [1]. Furthermore, its development is very economical as compared to other types of separation equipment.

2 NEED OF PROJECT

Generally, particle sampling in laboratories is done using Vibratory Sifters Screen Separators. It uses different mesh of sieves to separate particles but it has several downsides as the separation process is a non-continuous process due to the fact that clogging

of the sieve is a major issue found in high number mesh sieves. Either they are needed to be cleaned again and again to function properly or they are damaged by the grain sample and needed to be replaced thus increasing the cost of the equipment [6].

This project will significantly contribute to several laboratory experiments comprising of micro particle sampling since our device has a continuous mode of separation due to its compact size and elementary design having less mechanical complexities.

In Pakistan several number of industries import particle grading equipment on large scale, that are uneconomical and expensive. However, the designed apparatus has the potential to be replicated on a large/commercial scale, empowering the local industries in Pakistan, producing it locally will decrease the equipment cost by 50% thus facilitating the local industries, and resulting in sustaining the country's needs as well.

Particulate pollution is global concern that can cause major environmental risk for the global society. The pollutants can manifest into the air and cause serious harm to the human health and environment. Breathing in particle pollutants may be dangerous to the human fitness in this kind of manner that coarse particles, referred to as PM10, can cause irritation in eyes, nose, and throat. Dust from roads, farms, dry riverbeds, production sites, and mines are forms of PM10.

Fine particles, referred to as PM2.5, are greater risk due to the fact they are able to get into the deep elements of our lungs and into our blood [7].

Therefore, these particles are needed to be subjected to particle separators so that, fine pollutant can be concealed and not directly released into the environment. Particle separating equipment such as Series of cyclone system can be used to achieve that goal.

3 APPLICATION OF CONCEPT

Cyclone separators are the most commonly used in industries to separate dust from gas or for product recovery. Cyclone separators are mechanically simple device. The geometric simplicity of this device makes them relatively cheap to purchase, install, and run as compared to other separator devices. They are compact and require little maintenance. In many industries, cyclone separators are used for gas-solid and gas-liquid separations. Major industrial applications include:

- For powder recovery in **pharmaceutical cleaning processes**
- Used in production process of blended spices in **Food Industry** and for product restoration in milk powder, coffee and cereal plants.
- Cyclone separators are used as dust collector for **metallurgical process** mills, smelters and kilns fine particulate recovery
- In Cement Manufacturing Industries cyclone systems are used in significant numbers to separate the fine particles from the coarse particles having high volumetric flow rates
- In Power Sector Cyclone separation is used in fluidized bed combustors, hot gas cleaning in coal gasifier and activated carbon plants.
- Cyclone separator mechanism is used for NPK & DAP fertilizer dust collection in coolers & dryers.
- Cyclone separators are used for reducing emissions in fluidized bed boilers.
- Cyclone separators are used as dust collector for dryer and cooler processes such as hot gas cleaning and product recuperation separation in spray dryers.

4 NUMERICAL AND ANALYTICAL APPROACH

We have designed our cyclone separators using the 2D-2D standard created by Lapple. The cyclone separators are designed when two parameters are assumed i.e., diameter and air flowrate.

4.1 Inverse Cyclone Separator

Flow Pattern of inverse cyclone separator is shown in Figure 1. The inverse cyclone separator is the main component of our device due to the fact that our equipment is a sampling/grading device for micro particles and inverse cyclone is solely responsible for separating fine particles from the feed sample. During the separation, the heavy coarse particles move to the bottom outlet while the fine, after separation, moves toward the top and exit the component through the tangential outlet. Its axial inlet is connected with the feed blower by a pipe from which feed sample enters our equipment.

Table 1. Dimension of Inverse Cyclone Separator

Inverse Cyclone Separator		
Dimensions	**Ratio**	**Value (m)**
Diameter	D	0.1524
Length of Barrel	2D	0.3048
Length of Cone	2D	0.3048
Diameter of Inlet pipe	D/2	0.0762
Diameter of the vortex finder	D/2	0.0762
Length of vortex finder	5D/8	0.0953
Diameter of dust outlet	D/4	0.0381

4.2 Conventional Cyclone Separator

The conventional cyclone separator is connected with the inverse cyclone in a series arrangement and this component is the second most significant component. Its function is to separate the fine particles from the air flow with negligible amount of sample loss. The fine particle enters the component via tangential inlet with air. Then, a cyclone effect is created which pushes the fine towards the bottom outlet while the air, which still contains minor fine dust particles, leaves the component through the axial outlet called the vortex finder.

Table 2. Dimension of Conventional Cyclone Separator

Conventional Cyclone Separator		
Dimensions	**Ratio**	**Value (m)**
Diameter	D	0.1016
Length of Barrel	2D	0.2032
Length of Cone	2D	0.2032
Diameter of Inlet pipe	D/2	0.0508
Diameter of the vortex finder	D/2	0.0508
Length of vortex finder	5D/8	0.0635
Diameter of dust outlet	D/4	0.0254

4.3 Calculations of Conventional Cyclone Separator

Maximum volumetric flow rate of Blower (Q) = 7.5 m^3/min = 0.125 m^3/s

Velocity of air:

$$V_i = Q/A \quad (1)$$

Where,
A = Area of the inlet pipe of the conventional cyclone separator

$$V_i = 0.125/(\tfrac{\pi}{4}(0.0508)^2)$$
$$V_i = 61.672\ m/s$$

Cut point diameter:

$$d_{pc} = \sqrt{\left[\frac{9\mu W}{2\pi N_e V_i(\rho_p - \rho_g)}\right]} \quad (2)$$

We know that,
Air viscosity = μ = 0.0000183 kg/ (m.s)
Width of Inlet = W = 0.0508 m
Number of Effective Turns = N_e = 6
Inlet velocity = V_i = 61.672 m/s
Density of solid = ρ_p = 2650 kg/m^3
Density of Air = ρ_g = 1.293 kg/m^3

$$d_{pc} = \sqrt{\left[\frac{9(0.0000183)(0.0508)}{2\pi(6)(61.672)(2650-1.293)}\right]}$$

$$d_{pc} = 1.165\ \mu m$$

Gas residence time:

$$\Delta T = \frac{path\ length}{speed} = \frac{\pi DN}{V_i} \quad (3)$$

$$\Delta T = \frac{path\ length}{speed} = \frac{\pi DN}{V_i}$$

$$\Delta T = \frac{\pi(0.1016)(6)}{61.672}$$

$$\Delta T = 0.0310\ s$$

4.4 Prototype Design

Prototype Design is displayed in figure 5. Materials such thermoplastics, rubber and PVC were used in the Fabrication Process. While performing the hit and trial testing on the prototype it was found that the device was working very effectively. A series of trials at different pressures were performed and the sample separated from the prototype was collected, the sample was then taken to the laboratory to find the concentration of the required size of the particles (<149 Microns) separated. The results were indicating that the number of particles (<149 Microns) was good but still not capable to maintain the flow rate of ~1 Kg/Hour, which is the aim of this design. Also, increasing the pressure results in increasing the flow rate of the collecting particles. But, at the same time increasing pressure results in greater losses of the feed into the environment. So there were some necessary refinements required in our design to reach the optimum results.

In order to counter the losses and to distribute the pressure equally one more cyclone was installed to the design, this time at a relatively larger scale. Multiple experimentations were conducted listed in table and observed that i.e., separated particles (<149 Microns) were in greater quantity maintaining the flowrate of ~1 Kg/Hr making the device more efficient. The losses can be further reduced by changing the density of air by increasing the temperature with the help of a heating coil which can be installed at the inlet and appropriate baffles were also installed to make sure the air must be preheated before entering into the cyclone. Also at the outlet, there will be multiple collection points separated by multiple routes and baffles. Whereas some design refinements will take place to counter the mentioned problem.

A 3D model was then drafted of our equipment design using AutoCAD. All the components of our equipment were acquired from the local market. The components include PVC fittings & joints, Blower, Inverter, wooden planks, metal beams and more. The manufacturing was done in local workshops. Finally, the equipment was tested in a controlled environment and the final performance and separation efficiency were monitored and noted.

4.5 Figures and Tables

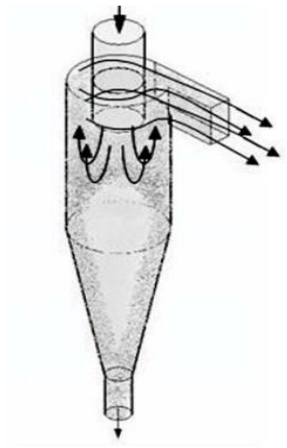

Figure 1. Inverse Cyclone Flow Pattern [8]

Table 1. List of Experiments

S. no	Blower Settings			Weight % of Kaolin Clay Sample		
	RPM	Frequency (Hertz)	Current (Amperes)	Losses	Fine Collected	Coarse Collected
1	3600	60	1.00	4.334	5.66	90.0
2	3300	55	1.30	5.01	5.34	89.65
3	3000	50	1.65	5.50	4.83	89.66
4	2700	45	1.92	7.57	4.47	87.96
5	2400	40	2.31	9.60	4.16	86.16
6	2100	35	2.40	9.89	3.81	86.3
7	1800	30	2.45	10.2	3.50	86.3
8	1500	25	2.52	10.9	3.30	85.8
9	1200	20	2.57	12.0	3.06	84.9

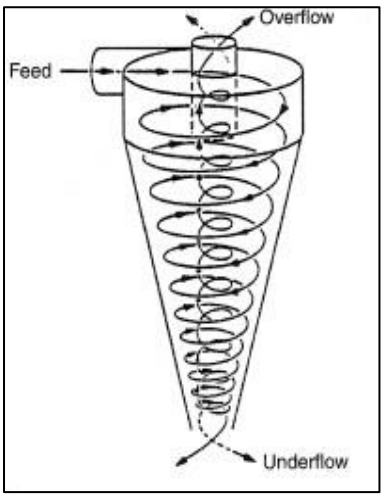

Figure 2. Hydro cyclone Flow Pattern [9]

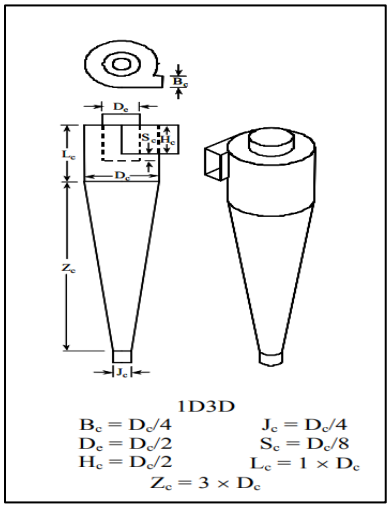

Figure 3. 1D2D Cyclone Configuration [10]

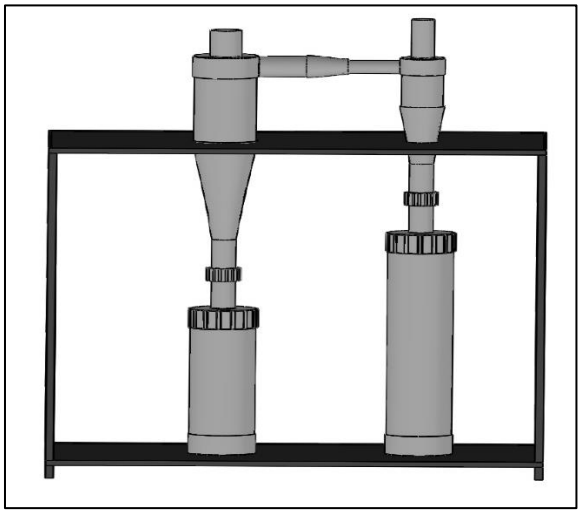

Figure 4. 3D Model of Cyclone Separator Assembly

Figure 5. View of Particle Grading equipment with VFD and Blower on Left

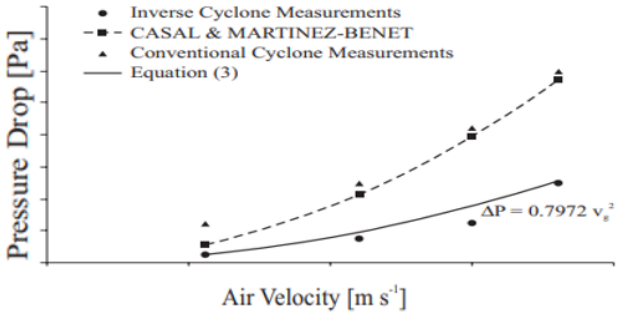

Figure 6. Comparison of Pressure Drop Rate B/w Conventional and Inverse Cyclone [8]

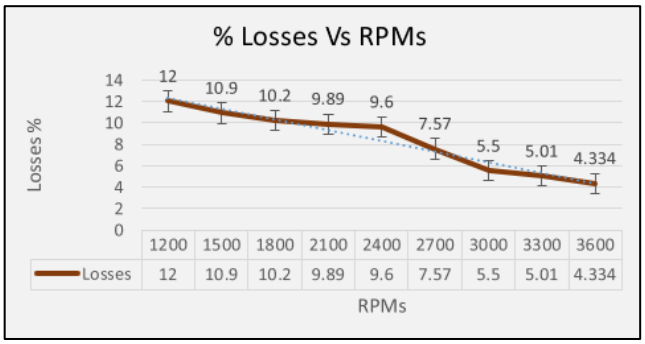

Figure 7. 2.8% Losses vs RPM Curve

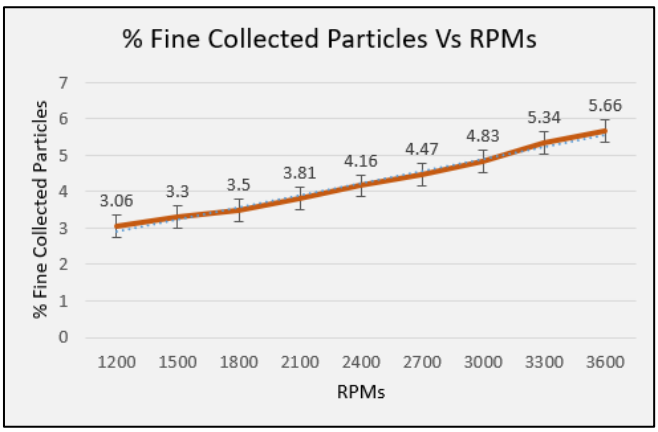

Figure 8. 29% of Fine Sample Collected vs RPM Curve

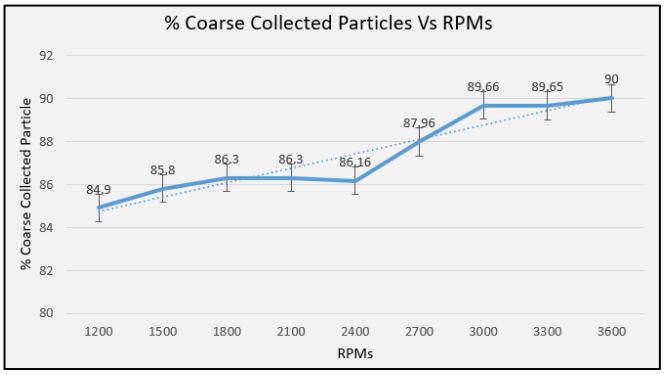

Figure 9. 30% of Coarse Sample Collected vs RPM Curve

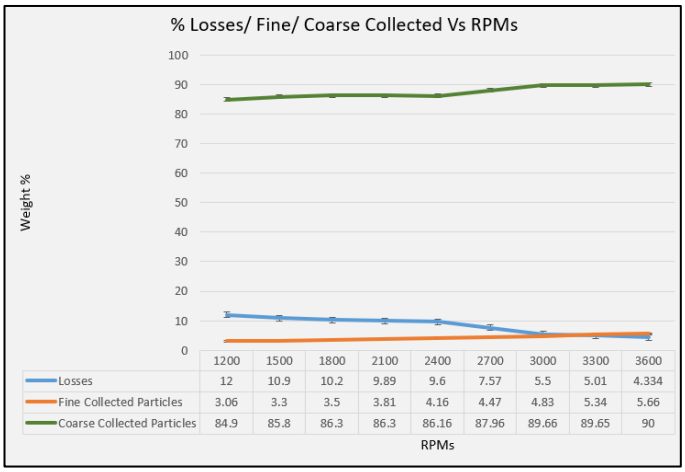

Figure 10. 31% of Losses/ Fine/ Coarse Collected Particle vs RPM Curve

5 CONCLUSION

From the results of the series of experiments, one can conclude that the micro particle separation is a very descriptive and detailed field and sometimes it becomes very complex to achieve the desired results. The reason behind all the work of this project is to eliminate that complexity by making such a device that can do the job on one's behalf. The device will facilitate the industries and the laboratories working in the relevant field of study. The equipment has a high collection efficiency with low-pressure drop. The design includes two cyclone separators connected in series. The first cyclone separator, separates the fine kaolin clay from the overall sample. The fine clay travels to the second cyclone separator, separating the fine clay from the airflow. As there are no moving parts in the system, the device requires less maintenance and operating cost. The fabricated device is easily detachable and easy to relocate at different locations. On operating on full RPM capacity with a flowrate of 7.5 m^3/min, the device gives around 5 % losses and the desired fine sample collected which is <149 microns is ~6% of the feed sample. After performing the particle size distribution of the given calcined clay sample, we found out that ~20% of the sample is <149 microns. So if we compare this with our tested results, we are extracting ~25% of fine clay from the total fine in the sample. As shown in Figure 7, On decreasing RPM periodically our loss percentage gradually increase, simultaneously decreasing the separation efficiency. The fabricated device is designed to separate the treated sample, i.e the feeding sample, must be dehumidified and contains no moisture content. Else, the material would contribute in the degradation of the equipment and also it will affect the working efficiency of the cyclone separator. The prototype has the potential to be replicated on the larger scale, and could be commercialized and implemented in any relevant industry. The Equipment will bridge the gap in present and the current market by replacing the Sifters and the final performance and separation efficiency were monitored and noted.

ACKNOWLEDGEMENTS

We would like to express our sincere gratitude to our project supervisor, Dr. Tariq Jamil, for his devotion, patience, helpful information, practical advice, and innovative ideas that have helped us tremendously during the experimentation. His enormous knowledge, intense experience, and professional expertise in the field of Materials Engineering have enabled us to take this project so far successfully. Without his support and guidance, this project would not have been possible.

REFERENCES

[1]. Pandya, D., *A low cost micro scale cyclone separator-design and computational fluid dynamics analysis*. 2010, The University of Texas at Arlington.

[2]. M.lengyel, N.K.-S., V.Antal, A.J.Laki, *Microparticles, Microspheres, and Microcapsules for Advanced Drug Delivery.* 2019. **87**(3).

[3]. Karagoz, I., et al., *Design and performance evaluation of a new cyclone separator.* Journal of Aerosol Science, 2013. **59**: p. 57-64.

[4]. Nwigbo, M., *Design, Fabrication and Performance Evaluation of a Cyclone System for Saw Dust Emission Control.* Int. J. Eng. Mod. Technol., 2019. **5**.

[5]. M.T.Kanojiya, N.M., V.Kalbande, C.Padole, *Design and fabrication of cyclone dust collector for industrial Application.* 2022. **49**: p. 378-382.

[6]. Wikipedia. *High-frequency vibrating screens*. Available from: https://en.wikipedia.org/wiki/High-frequency_vibrating_screens.

[7]. Pope 3rd, C., *Particulate pollution and health: a review of the Utah valley experience.* Journal of exposure analysis and environmental epidemiology, 1996. **6**(1): p. 23-34.

[8]. Herrera, C.A., M.E. Rosillo, and A. García, *Cassava flour separation using inverse cyclone.* Revista Brasileira de Engenharia Agrícola e Ambiental, 2007. **11**: p. 515-520.

[9]. Bradley, D. *HYDROCYCLONES*. Available from: https://thermopedia.com/content/862/#:~:text=The%20hydrocyclone%20is%20a%20simple,droplets%20from%20a%20liquid%20medium.&text=This%20reverse%20flow%20continues%20to,at%20the%20axis%20of%20rotation.

[10]. Bashir, K., *Design and fabrication of cyclone separator.* China University of Petroleum, 2015.